



PhD-FSTM-2022-160  
The Faculty of Science, Technology and Medicine

## DISSERTATION

Defense held on 07/12/2022 in Esch-sur-Alzette

to obtain the degree of

DOCTEUR DE L'UNIVERSITÉ DU LUXEMBOURG

EN PHYSIQUE

by

**Alexander Dimitri OST**

Born on 22 February 1994 in Luxembourg (Luxembourg)

## INVESTIGATION OF SURFACE SPUTTERING AND IONIZATION PROCESSES UNDER NON- REACTIVE LIGHT ION IRRADIATION: TOWARDS 4D SIMS IMAGING

### Dissertation defense committee

Dr. Tom Wirtz, dissertation supervisor

*Head of Unit, Luxembourg Institute of Science and Technology*

Dr. Jean-Nicolas Audinot

*Senior Researcher, Luxembourg Institute of Science and Technology*

Prof. Dr. Alex Redinger, Chairman

*Professor, Université du Luxembourg*

Dr. Carmen Höschen

*Research Scientist, Technical University of Munich*

Dr. Michael Wiedenbeck

*Group Leader, GFZ Helmholtz Center Potsdam*



## Abstract

The progressive trend to miniaturize samples presents a challenge to materials characterization techniques in terms of both lateral resolution and chemical sensitivity. The latest generation of focused ion beam (FIB) platforms has allowed to advance in a variety of different fields, including nanotechnology, geology, soil, and life sciences. State-of-the-art ultra-high resolution electron microscopy (EM) devices coupled with secondary ion mass spectrometry (SIMS) systems have enabled to perform in-situ morphological and chemical imaging of micro- and even nanosized objects to better understand materials by studying their properties correlatively.

However, SIMS images are prone to artefacts induced by the sample topography as the sputtering yield changes with respect to the primary ion beam incidence angle. Knowing the exact sample topography is crucial to understand SIMS images. Moreover, using non-reactive primary ions ( $\text{Ne}^+$ ) produced in a gas field ion source (GFIS) allows to image in SIMS with an excellent lateral resolution of  $< 20$  nm, but it comes with a lower ionization probability compared to reactive sources (e.g.,  $\text{Cs}^+$ ) and due to small probe sizes only a limited number of atoms are sputtered, resulting in low signal statistics.

This thesis focused first on taking advantage of high-resolution in-situ EM-SIMS platforms for applications in specific research fields and to go beyond traditional correlative 2D imaging workflows by developing adapted methodologies for 3D surface reconstruction correlated with SIMS (3D + 1). Applying this method to soil microaggregates and sediments allowed not only to enhance their visualization but also to acquire a deeper understanding of materials' intrinsic transformation processes, in particular the organic carbon sequestration in soil biogeochemistry.

To gain knowledge of the influence of the topography on surface sputtering, using model samples the change of the sputtering yield under light ion bombardment ( $\text{He}^+$ ,  $\text{Ne}^+$ ) for different ranges of incidence angles of the primary ion beam was studied experimentally. This data was compared to Monte Carlo simulation results and fitted with existing sputtering model functions. We showed thus that these models developed and studied for heavier ions ( $\text{Ar}^+$ ,  $\text{Cs}^+$ ) are also applicable to light ions ( $\text{He}^+$ ,  $\text{Ne}^+$ ). Additionally, an algorithm used to correct

SIMS images with respect to topographical artefacts resulting from local changes of the sputtering yield was presented.

Finally, the contribution of oxygen on positive SI yields was studied for non-reactive primary ions (25 keV Ne<sup>+</sup>) under high primary ion current densities (up to  $10^{20}$  ions/(cm<sup>2</sup> · s)). It was shown that in order to maximize and maintain a high ionization probability oxygen needs to be provided continuously to the surface. Secondary ion signal enhancement of up to three orders of magnitude were achieved for silicon, opening the doors for SIMS imaging at both highest spatial resolution and high sensitivity.

## Acknowledgements

First of all, I would like to thank both of my supervisors, Dr. Tom Wirtz and Dr. Jean-Nicolas Audinot, for their continuous support, their time, availability for discussions, and feedback throughout the 4 years of my PhD. I would also like to acknowledge Prof. Dr. Alex Redinger for his support and advice during the yearly thesis committee meetings.

I would like to thank Tianyi Wu, Dr. Carmen Höschen, and Prof. Dr. Carsten W. Mueller for their scientific support, for carrying out NanoSIMS measurements, for many constructive discussions during our regular project meetings, and for their kind reception during our visits at the Technical University of Munich and the University of Copenhagen.

I would also like to thank Dr. Patrick Philipp for his kind support for the SDTrimSP simulations.

I would like to express my gratitude to current and former LIST members, Olivier De Castro, Jennifer O. Usiobo, Kishor Acharya, Edyta Niemczyk, Charlotte Stoffels, Chérif Coulbary, Saba Tabean, Grégoire Defoort, Luca Cressa, Pablo Delfino, Atulya U. Kumar, Jules Lagrave, Kilian Huber, Alvar T. Massana, and Marco Moreira for many and long fruitful discussions at as well as outside of work.

Last but not least, I would like to thank my family and close friends for their support and for listening to me during some challenging moments of these 4 years of PhD.

## Acronyms and Abbreviations

Atomic Force Microscopy	AFM
Atomic percent	at%
Copper Indium Gallium Selenide	CIGS
Counts	cts
Counts per second	cps
Electron Microscopy/Microscope	EM
Energy Dispersive X-ray Spectroscopy	EDX
Everhart-Thornley	ET
Focused Ion Beam	FIB
Gas Field Ion Source	GFIS
Helium Ion Microscopy/Microscope	HIM
Liquid Metal Ion Source	LMIS
Mass Resolving Power	MRP
Monte Carlo	MC
Organic Matter	OM
Red Green Blue	RGB
Region of Interest	ROI
Radio Frequency	RF
Scanning Electron Microscopy/Microscope	SEM
Secondary Electron	SE
Secondary Ion	SI
Secondary Ion Mass Spectrometry/Spectrometer	SIMS

Sputtering Yield	SY
Stopping and Range of Ions in Matter	SRIM
Synthetic Seawater	SSW
Time-of-Flight	ToF
Total Ion Count	TIC
Transmission Electron Microscopy/Microscope	TEM

## Preface

This thesis was carried out at the Luxembourg Institute of Science and Technology (LIST) in the Materials Research and Technology (MRT) Department with affiliation at the Doctoral Program in Physics and Materials Science at the University of Luxembourg under the supervision of Dr. Tom Wirtz and Dr. Jean-Nicolas Audinot. The thesis supervision committee consisted of Dr. Tom Wirtz, Dr. Jean-Nicolas Audinot, and Prof. Dr. Alex Redinger. This PhD project was supported by the Luxembourgish National Research Fund (FNR) via the project SOIL3D (grant no. INTER/DFG/17/11779689).

Some of the work described in this thesis was presented at the following conferences and published in the following journals.

### Conference participation

1. **SIMS-22** Conference, Kyoto (Japan), October 2019: oral and poster presentations
2. **LIST PhD Day**, Belval (Luxembourg), November 2019: oral and poster presentations
3. **Materials Research Society** (MRS) Fall Meeting, remote (due to Covid-19 restrictions), November 2020: oral presentation
4. **European Materials Research Society** (EMRS) Spring Meeting, remote (due to Covid-19 restrictions), May 2021: oral presentation
5. **IBA** (Ion Beam Analysis)/**PIXE** (Particle Induced X-Ray) & **SIMS** Joint Conference, remote (due to Covid-19 restrictions), October 2021: oral presentation
6. **LIST Soil Workshop**, Belval (Luxembourg), December 2021: poster presentation
7. **Microscopy and Microanalysis** (M&M) Meeting, Portland (USA), July 2022: oral and poster presentations
8. **German Soil Science Society** Meeting, Trier (Germany), September 2022: oral presentation

## Publication list

1. Bengasi, G.; Quéту, L.; Baba, K.; **Ost, A.**; Cosas Fernandes, J. P.; Grysan, P.; Heinze, K.; Boscher, N. D. **Constitution and Conductivity of Metalloporphyrin Tapes.** *Eur. J. Inorg. Chem.* 2020. <https://doi.org/10.1002/ejic.202000243>.
2. **Ost, A. D.**; Wu, T.; Höschen, C.; Mueller, C. W.; Wirtz, T.; Audinot, J.-N. **4D Surface Reconstructions to Study Microscale Structures and Functions in Soil Biogeochemistry.** *Environ. Sci. Technol.* 2021, 55 (13), 9384–9393. <https://doi.org/10.1021/acs.est.1c02971>.
3. Wu, T.; **Ost, A. D.**; Audinot, J.; Wiesmeier, M.; Wirtz, T.; Carmen, H.; Buegger, F.; Werner, H. **Association of Fresh Low-Molecular-Weight Organic Compounds with Clay-Sized Mineral Fraction in Soils of Different Organic Carbon Loading.** *Geoderma* 2022, 409. <https://doi.org/10.1016/j.geoderma.2021.115657>.
4. Bredal, T. V.; Zimmermann, U.; Madland, M. V.; Minde, M. W.; **Ost, A. D.**; Wirtz, T.; Audinot, J.-N.; Korsnes, R. I. **High-Resolution Topographic and Chemical Surface Imaging of Chalk for Oil Recovery Improvement Applications.** *Minerals* 2022, 12 (3), 1–10. <https://doi.org/https://doi.org/10.3390/min12030356>.
5. De Castro, O.; Audinot, J.-N.; Hoang, Q. H.; Coulbary, C.; Bouton, O.; Barrahma, R.; **Ost, A.**; Stoffels, C.; Jiao, C.; Dutka, M.; Geryk, M., Wirtz, T. **Magnetic sector secondary ion mass spectrometry on FIB-SEM instruments for nanoscale chemical imaging.** *Anal. Chem.*, 2022, 94 (30), 10754-10763. <https://doi.org/10.1021/acs.analchem.2c01410>.
6. **Ost, A. D.**; Vollnhals, F.; Philipp, P.; Wirtz, T.; Audinot, J.-N. **Improvement of SIMS analyses under Ne<sup>+</sup> bombardment by oxygen flooding.** *Beilstein J. Nanotechnol.*, 2022 (submitted).

7. Bredal, T. V.; **Ost, A. D.**; Wirtz, T.; Audinot, J.-N.; Zimmermann, U.; Madland, M. V.; Minde, M. W.; Puntervold, T. **4D surface reconstruction of micron-sized organic calcite for characterization of chemical heterogeneity of chalk surfaces.** *Energy Fuels* (currently in preparation).

## Contents

<b>Abstract</b> .....	<b>3</b>
<b>Acknowledgements</b> .....	<b>5</b>
<b>Acronyms and Abbreviations</b> .....	<b>6</b>
<b>Preface</b> .....	<b>8</b>
<b>Contents</b> .....	<b>11</b>
<b>Introduction</b> .....	<b>14</b>
<b>Chapter 1: Background</b> .....	<b>18</b>
1. Introduction to SIMS.....	18
1.1 Fundamentals.....	18
1.2 Sputtering process .....	19
1.3 Ion beam irradiation dose.....	21
1.4 Ionization .....	21
1.5 Secondary Ion Intensity.....	22
2. SIMS Instrumentation.....	23
2.1 Ion sources .....	24
2.2 Primary ion optics .....	24
2.3 Mass analyzers .....	24
2.4 Analysis modes.....	26
3. Correlative microscopy and spectroscopy .....	29
4. SIMS on state-of-the-art electron microscopes .....	33
4.1 HIM-SIMS .....	34
4.1.1 Instrument design .....	34
4.1.2 Performance demonstration.....	37
4.1.2.1 Mass spectrum recording .....	37
4.1.2.2 Depth profiling .....	38
4.1.2.3 2D imaging .....	39
4.1.2.4 3D imaging .....	41
4.2 FIB-SEM-SIMS.....	43
4.2.1 Instrument design .....	43
4.2.2 Performance demonstration.....	45
4.2.2.1 Mass spectrum recording .....	45

4.2.2.2	Depth profiling .....	46
4.2.2.3	2D imaging .....	48
4.2.2.4	3D imaging .....	49
5.	Problem statements and thesis objectives .....	51
5.1	Sputtering.....	51
5.2	Ionization .....	54
6.	Chapter summary .....	56
<b>Chapter 2: Methodological development for surface reconstruction .....</b>		<b>57</b>
1.	Workflow description .....	57
1.1	Photogrammetry.....	57
1.2	Data acquisition .....	59
1.3	3D SE reconstruction.....	61
1.4	Photogrammetry software performance evaluation.....	62
1.5	3D + 1 reconstruction.....	69
2.	Application of the 3D + 1 method for sediments and soils.....	70
2.1	Diatoms .....	70
2.2	Chalks .....	73
2.3	Soils .....	75
3.	Chapter summary .....	81
<b>Chapter 3: Advanced topographical and chemical sample characterization .</b>		<b>83</b>
1.	Topography induced sputtering yield variation .....	83
1.1	Introduction .....	83
1.2	Sputtering models and Monte Carlo simulations .....	86
1.2.1	Flat surfaces .....	86
1.2.2	Rippled surfaces .....	89
1.3	Experimental and simulative study on He <sup>+</sup> and Ne <sup>+</sup> sputtering yields.....	93
1.4	Numerical algorithms for topographical artefact analysis in SIMS images .....	100
1.4.1	Ion beam incidence angle and sputtering yield estimation.....	100
1.4.2	Investigation of the SIMS signal variation in photovoltaic materials .....	104
1.4.3	Topographical artefact SIMS image correction.....	108
2.	Evaluation of the mass spectrometer transmission dependency from the ion emission direction .....	112
2.1	Introduction .....	112
2.2	Ion trajectory simulations .....	113

2.3	3D + 1 reconstruction to study directional dependency of the transmission .....	114
3.	Chapter summary .....	117
<b>Chapter 4: Optimization of positive secondary ion yields in Ne<sup>+</sup> by reactive gas flooding .....</b>		<b>118</b>
1.	Introduction.....	118
2.	Investigating the flooding process by Monte Carlo simulations.....	119
2.1	Simulation setup .....	119
2.2	Preliminary calculations .....	120
2.3	Quantification of surface absorbed residual and flooded oxygen.....	121
3.	Experimental investigation for sensitivity optimization .....	123
3.1	Preliminary experiments: isotopic oxygen-18 flooding .....	123
3.2	Depth profiling .....	124
3.3	Imaging.....	126
3.3.1	Maintaining high ionization yields for 3D imaging .....	126
3.3.2	Perspectives for high-resolution imaging .....	128
4.	Chapter summary .....	130
<b>General conclusions and perspectives.....</b>		<b>131</b>
<b>References.....</b>		<b>135</b>
<b>Appendices .....</b>		<b>150</b>

## Introduction

The development of high-performance sample characterization techniques has emerged from the need to better understand materials' properties at the relevant spatial scales. The trend to miniaturize samples requires analysis of very small volumes. Analyzing very small quantities of micro- or even nanoscopic samples requires not only high spatial resolution, but also detectability of low concentration elements present in the material.

Secondary Ion Mass Spectrometry (SIMS)<sup>1,2</sup> is a powerful surface analysis technique, excelling in a high sensitivity, the ability to detect all the elements (and isotopes) of the periodic table, and a high dynamic range. In SIMS, an energetic primary ion beam (e.g., Ga<sup>+</sup>, Cs<sup>+</sup>, O<sup>-</sup>) beam is accelerated toward the sample, leading to sputtering of the surface. Fractions of those sputtered atoms are ionized, extracted, and directed towards the mass spectrometer (quadrupole, time-of-flight, or magnetic field sector) to separate them according to their mass-to-charge ratio. Typical SIMS analysis modes are depth profiling, 2D, and 3D imaging.

Recent development on SIMS devices enabled to visualize specimens with high spatial resolution and chemical sensitivity, allowing to work on cutting-edge science in a variety of different applications including materials science,<sup>3,4</sup> life sciences,<sup>5,6</sup> and geology.<sup>7-9</sup> Correlating microscopy and spectroscopy techniques has the advantage to overcome limitations of each technique and to combine complementary information to provide a deeper topographic and chemical understanding of the sample. In the framework of this thesis, focused ion beam (FIB) platforms, including Helium Ion (HIM, also referring to Helium Ion Microscope depending on the context) and FIB-Scanning Electron Microscopy (FIB-SEM) equipped with state-of-the-art SIMS instruments (referred here as "HIM-SIMS" and "FIB-SEM-SIMS", respectively) were used to analyze samples correlatively with ultra-high resolution structural with analytical surface information.

Besides traditional SIMS data analysis modes, such as depth profiling and 2D imaging, 3D reconstruction workflows of micro- and nanoscopic objects are emerging nowadays with increasing computational performance and development of 3D visualization software. Visualization of chemical distribution was mostly done in 2D so far, but 3D analysis is needed for a deeper comprehension of the sample in all spatial directions.

The interpretation of the signal intensity variation can be challenging in SIMS, as besides the material's concentration the secondary ion (SI) intensity depends on intrinsic parameters related to the sputtering and ionization processes, often leading to artefacts in SIMS images and to misinterpretation of data. In order to understand the origin of SI intensity gradients, sputtering and ionization processes should be considered when inspecting SIMS data.

In the past, it has been shown that surface sputtering is strongly dependent on surface bombardment parameters, such as primary ion impact energy, its mass and incidence angle, and the density of the target.<sup>10,11</sup> Thus, in particular for SIMS imaging, the SI intensity will vary according to the local topography as the sputtering yield changes with the primary ion bombardment incidence angle.<sup>12</sup> To better understand SI intensity variations in SIMS images 3D topography information needs to be extracted from the sample. This thesis focused on the development of a novel methodology to reconstruct the 3-dimensional sample topography and correlate it with SIMS. In a first step, this 3D + 1 method was applied for soils and sediments and the benefits of these reconstructions were discussed. Then algorithms were provided to process 3D topographical and chemical information numerically to perform statistical analysis of the reconstructions. This was done here for soil microaggregates to investigate organic matter sequestration in soil biogeochemistry. In a next step, this 3D + 1 method was used to study experimentally and with simulations sputtering yields vs. the ion beam incidence angle for light ions ( $\text{He}^+$ ,  $\text{Ne}^+$ ). These datasets were discussed and fitted with existing models on surface sputtering of flat and rippled surfaces. Finally, algorithms were discussed used to localize and correct SIMS image artefacts resulting from variations of the sputtering yield caused by sample topography.

The HIM-SIMS instrument, equipped with a Gas Field Ion Source (GFIS), allows imaging with an excellent lateral resolution ( $< 20 \text{ nm}$ ) thanks to the high brightness of the GFIS. However, using  $\text{Ne}^+$  as primary ions comes with a lower ionization probability compared to reactive primary ion sources (e.g.,  $\text{Cs}^+$  or  $\text{O}^-$ ). Moreover, the number of sputtered atoms is typically very low due to the small probe/voxel sizes, resulting often in relatively low SI signal statistics. A known method to increase the detection limit of electropositive elements is by flooding the sample with oxygen. However, reactive gas flooding has not yet been explored under high-energetic non-reactive ion bombardment ( $25 \text{ keV Ne}^+$ ) with high current densities (up to  $10^{20} \frac{\text{ions}}{\text{cm}^2 \cdot \text{s}}$ ). In this thesis, sputtering of oxygen from a native oxide layer as well as oxygen surface

adsorption and implantation were studied by Monte Carlo (MC) simulations to quantify oxygen on the sample surface under high  $\text{Ne}^+$  current densities. Then, depth profiling experiments were conducted on the HIM-SIMS for two different materials (silicon wafer and cobalt binder in cemented carbide) to discuss the change of the SI intensity for different oxygen fluxes. Eventually, SI improvement under oxygen flooding was studied for imaging applications.

The 1<sup>st</sup> chapter of this thesis will be focusing on a brief introduction to the fundamentals about SIMS and related instrumentation. Recent developments on methods for microscopy and spectroscopy image correlation will be discussed. State-of-the-art electron microscopy and SIMS devices used for this thesis will be shortly presented and examples of applications will be shown.

The 2<sup>nd</sup> chapter consists of a presentation of the workflow of the 3D + 1 methodology, including data acquisition and processing. A simulative study on the reconstruction of known geometric structures, by comparing the reconstructions of commercial software and an own photogrammetry algorithm, was done to estimate the origin of reconstruction artefacts and to assess a quality of a 3D reconstructed object. Moreover, case studies will be presented to use the developed methodology to solve specific scientific questions for soils and sediments where both sample microstructural topography and chemical information are needed.

In the 3<sup>rd</sup> chapter, the presented 3D + 1 methodology will be used to study variations of the sputtering yield according to the incidence angle in simulations and experimentally on model samples, and discuss the results according to existing theoretical models in literature. The aim was to show here that theoretical models developed originally for sputtering developed for heavy ions, such as  $\text{Cs}^+$  or  $\text{Ar}^+$ , can be also applied to light ions ( $\text{He}^+$ ,  $\text{Ne}^+$ ). Finally, a methodology to “correct” topographical artefacts in SIMS images by estimating the sputtering yield change according to the primary beam incidence angle from 3D reconstructions will be presented.

The 4<sup>th</sup> chapter is dedicated to applied studies on the improvement of the ionization probability by oxygen flooding of the sample with non-reactive primary ions under high bombardment densities. MC simulations were done first to study the change of the oxygen surface concentration resulting from sputtering of the native oxide as well as deposition and

implantation from residual and flooded oxygen. Oxygen flooding was applied then for depth profiling, 2D imaging, and 3D SIMS imaging to demonstrate its applicability for a routine use in SIMS with  $\text{Ne}^+$  primary ions produced in a GFIS.

## Chapter 1: Background

### 1. Introduction to SIMS

Secondary Ion Mass Spectrometry (SIMS)<sup>1-3,13</sup> is a surface analysis technique where by impinging primary ion projectiles (e.g., Ga<sup>+</sup>, Cs<sup>+</sup>, O<sup>-</sup>) on the material secondary ions are created and separated by a mass analyzer to acquire chemical information. Advantages of SIMS are high sensitivity and high dynamic range. The latest development of SIMS techniques focused on improvement of lateral resolution and acquisition of molecular information with cluster primary ions to address new analytical challenges.<sup>14,15</sup> SIMS is used nowadays in a broad spectrum of applications, ranging from nanotechnology, geology, soil and sediment, to life sciences.

SIMS has been a widely addressed topic in scientific publications and theses for multiple decades. Reviewing and discussing in depth fundamental sputtering and ionization processes in SIMS as well as related instrumental parts is going certainly beyond the scope of this thesis. More information on each topic can be found in the given references. In this section, the aim is to give a brief overview of the fundamentals of SIMS and related systems as well as the key components of the technique.

#### 1.1 Fundamentals

Surface atom sputtering and ionization phenomena are the most crucial processes in SIMS. These are highly complex processes and, even though several theoretical models, and experimental and simulative studies have been made in the last decades, they are not fully understood up to now. Here basic concepts about sputtering and ionization will be introduced.

## 1.2 Sputtering process

In SIMS, primary ions are accelerated towards the material. During the primary ion impact particles are emitted from the surface (electrons, atoms, and ions). The process of material erosion by highly energetic ion bombardment (ranging typically from hundreds of eV to tens of keV), thus to expel atoms from the surface (which will be analyzed later in the mass spectrometer), is referred as sputtering.

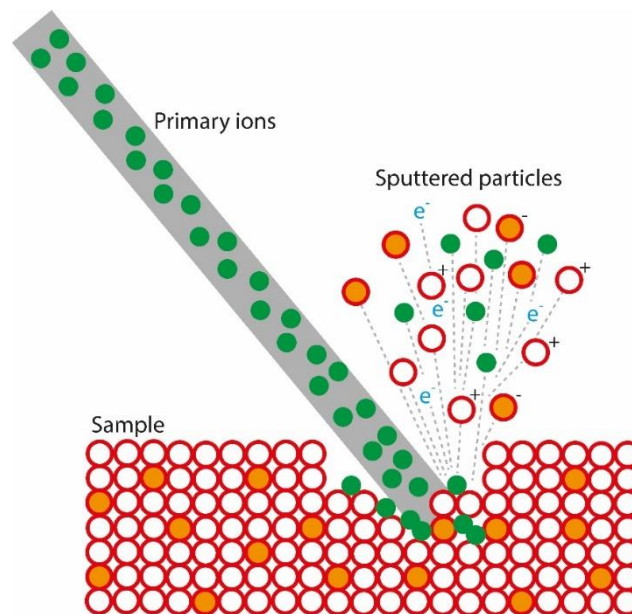


*Figure 1: Schematic illustration of the surface sputtering and secondary ion emission process by high energetic primary ions, creating emission of neutrals, positive and negative ions, electrons, and recoil of incident projectiles.*

Once the projectile has entered the material, a series of elastic collisions between the atomic nuclei of primary ion and material atoms is taking place, leading eventually to sub-surface implantation of the primary projectile and ejection of matrix atoms. Energy loss of the incident ion is determined either by electronic or nuclear stopping power. After collision of the primary ion with a matrix atom, the latter recoils and creates further random collisions of matrix atoms. This process is known as collision cascade and includes a high number of random atom-atom collisions and deflections.<sup>2</sup> For imaging applications with very finely FIBs in SIMS the spatial extend of the collision cascade (in the order of 8 nm for a 20 keV – 30 keV

Ne<sup>+</sup> beam)<sup>16</sup> determines the origin of sputtered ions with respect to the location of incident ion probe, and thus the lower limit of the lateral resolution of an acquired image, because the distance between the ion impact point and the SI emission is much larger than the radius of the ion beam.<sup>17,18</sup>

The number of sputtered atoms per incident ion is defined as the sputtering yield (SY). The SY is a highly specific quantity and depends on the target material, the probe energy, mass, and incidence angle. P. Sigmund<sup>10</sup> was the first to develop a theoretical description of the sputtering process based on Boltzmann's equation of transport and provided a solid base for further theoretical (and experimental) investigations of the sputtering yield.<sup>19,20</sup>

For the sputtering yield only the fraction of atoms receiving a significant amount of energy close to the surface are important. Thus, in general the deposited energy close to the surface will increase with impact energy. However, for instance He<sup>+</sup> presents an exception as the penetration depth is much larger compared to Ne<sup>+</sup>, Ga<sup>+</sup>, or Cs<sup>+</sup> and hence the energy is deposited deep in the material. For higher mass ions, such as Ga<sup>+</sup> or Cs<sup>+</sup> (nuclear stopping power dominating), the sputtering yield increases with the impact energy. For He<sup>+</sup> (electronic stopping power) the opposite is the case, because He<sup>+</sup> ions are implanted further into the material and the contribution to the surface sputtering is very low then. For Ne<sup>+</sup> the sputtering yield increases for a range between 5 keV and 10 keV and decreases for larger impact energies.<sup>16</sup> When studying the influence of the incidence angle, the sputtering yield increases with the incidence angle, as with oblique impact angles the energy deposition is shallower. However, for grazing incidence angles the sputtering yield drops as the incidence particle bounces back failing to break the surface binding forces. Sample topography has also a major impact on sputtering events, leading for instance to bombardment with a non-constant incidence angle and/or ion redeposition effects.<sup>21</sup>

The target surface binding energy influences the sputtering yield, as it determines the height of the potential barrier that an incident ion needs to overcome after its final collision to sputter an atom out of the material. The sputtering yield thus increases with lower materials' surface binding energies.<sup>22</sup> Additionally, crystallography of the target material was shown to influence the sputtering yield, as for crystalline targets projectiles shot along crystallographic planes are guided through the material and lead to less collision events than for a random target.<sup>23,24</sup>

Sputtering has long been considered as an undesired phenomenon, e.g., responsible for destroying diaphragms and targets in high-voltage EMs or for thinning of vessel walls in high-temperature plasma experiments being an important issue in fusion research.<sup>12,25</sup> However, nowadays sputtering is used for a variety of applications in physics and nanotechnology.<sup>26</sup> Sputtering with a well-focused ion beam enables the controlled erosion of atomic layers from a surface. Besides for surface analysis techniques, such as SIMS or SNMS (Sputtered Neutral Mass Spectrometry), sputtering is used to remove material to structure (i.e., pattern)<sup>27</sup> and polish surfaces<sup>28</sup> on the atomic scale, and to deposit thin films on a variety of different substrates, for example on microelectronics or even large areas of multiple m<sup>2</sup>.<sup>29</sup>

### 1.3 Ion beam irradiation dose

Depending on the primary ion dose, one can distinguish between two modes in SIMS. Static SIMS describes the process of gaining elemental and organic distribution information from the uppermost atomic surface layer by using low primary ion doses to limit atomic mixing and breaking of chemical bonds (by definition  $\leq 10^{13}$  ions/cm<sup>2</sup>). Typically, it is operated with a pulsed ion beam in combination with a time-of-flight mass spectrometer.<sup>17</sup>

In dynamic SIMS, a direct current (DC) primary ion current is used to irradiate the surface with a high ion dose (typically  $\geq 10^{16}$  ions/cm<sup>2</sup>) to create fast erosion used for elemental information. Dynamic SIMS is usually operated using a magnetic sector or quadrupole mass spectrometer for depth profiling or imaging applications.

### 1.4 Ionization

Through a charge exchange event between the sputtered atom and the surface, a fraction of the sputtered atoms is ionized. The ionization yield is highly dependent on the chemical environment (e.g., Si<sup>+</sup> yield orders of magnitude higher from SiO<sub>2</sub> compared to Si matrix) and can vary over several orders of magnitude within a single matrix consisting of different atomic species. This dependence of the ionization with the material environment is the so-called

matrix effect, which makes quantification challenging in SIMS. However, using reference samples matrix trace elements can be quantified with high accuracy,<sup>30</sup> which is a very common method to quantify dopants in semiconductors.<sup>2</sup> The yield of ionization is defined as the number of produced secondary ions per sputtered atoms.

Several theoretical models about ionization mechanisms of sputtered materials have been developed and reviewed in the past.<sup>31</sup> The most common ones are the electron tunneling model, used for metals and semiconductors, and the bond breaking model for ionic solids. A brief description of the electron tunneling and the bond breaking models can be found in the Appendices.

### 1.5 Secondary Ion Intensity

The SI signal intensity  $SI_A$  for a given species A is given by:

$$SI_A = \tau \cdot Y_i \cdot I_p \cdot S \cdot SY_A \cdot c_A \quad (1)$$

where  $\tau$  is the instrumental transmission (= ratio of detected ions versus produced SIs),  $Y_i$  the ionization probability,  $I_p$  the primary ion beam density,  $S$  the sputtered area,  $SY_A$  the sputtering yield,  $c_A$  the concentration of species A. Typically, the signal is monitored in number of counts per second (cps). One of the advantages of SIMS is a high dynamic range, i.e., it allows to measure signals over large ranges, which can extend up to  $\sim 10^9$  with multiple detectors.<sup>2</sup> As the SI signal is highly sensitive for slight variations of one of these parameters, direct quantification is not possible in SIMS. Quantification is possible in SIMS by determining the relative sensitivity factor (RSF) of a reference sample with known concentration (of an element of interest in a given matrix) and by applying it to the data of the unknown sample (RSF Method).<sup>2</sup> The detection limit DL refers to minimal detectable atomic concentration given by the following expression:<sup>32</sup>

$$DL = \frac{1}{N_{sputter} \cdot UY} \quad (2)$$

Where  $N_{sputter}$  is the number of sputtered atoms and  $UY$  the useful yield referring to the ratio of the number of detected ions (i.e., ionized atoms which passed through the SI optics) versus sputtered atoms of the same element. Thus, the analyzed voxel size and the ionization

probability have an impact on the detection limit of the species. With larger voxel sizes larger volumes and thus more atoms are sputtered, improving the detection limit. On the other hand, with a higher ionization probability more ions are created, resulting in better detection limits. In SIMS, detection limits can extend down to parts per billion (ppb) along with the related sensitivity (i.e., ability to measure small concentration differences).<sup>2</sup>

## 2. SIMS Instrumentation

SIMS instruments consist of different components, while the key parts are the focused ion source and the mass spectrometer, both kept under (ultra) high vacuum. The primary ion irradiates the sample surface, leading to atomic sputtering and ionization processes.<sup>17</sup> The secondary ions are collected, accelerated, and directed towards the mass spectrometer, where they are filtered by their mass-to-charge ratio and detected (Figure 2).

In this section, the key components for a SIMS instrument will be briefly described.

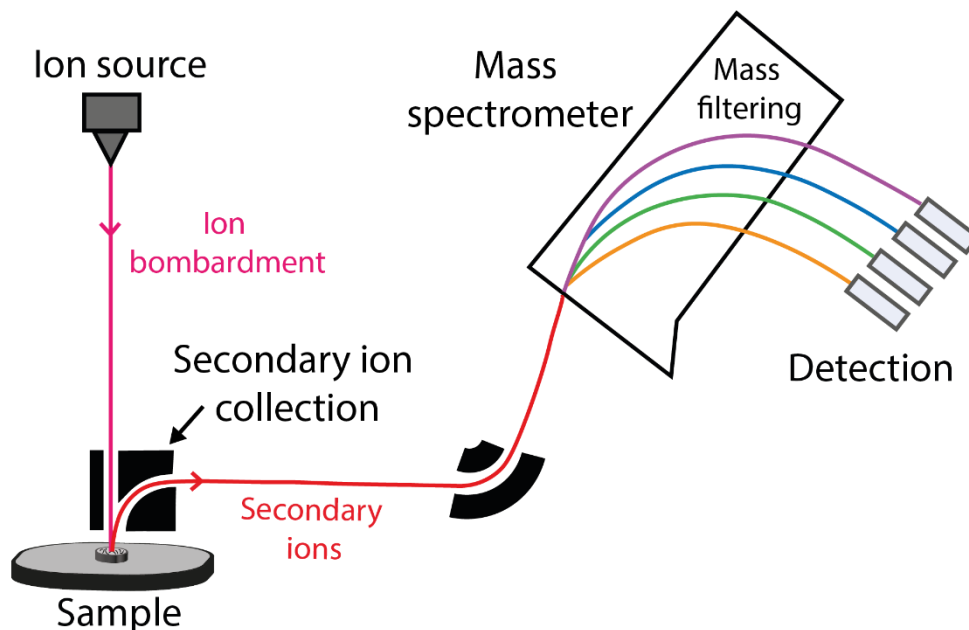


Figure 2: Schematic illustrating the main steps in SIMS (here with a magnetic field sector as mass spectrometer, figure adapted from Bredal et al.).<sup>33</sup>

### 2.1 Ion sources

A variety of different types of ion sources are used on SIMS instruments and the choice of a source impacts (among others) the beam current, the sputtering/ionization yield, and most importantly the probe size, thus the outcome of a SIMS acquisition. The most common ion sources used in SIMS are the electron impact, duoplasmatron, surface ionization, RF-plasma, and liquid metal ion sources (LMIS).<sup>16</sup> A brief description of the mentioned ion sources with their key characteristics can be found in the Appendices.

### 2.2 Primary ion optics

The primary ion optics is typically consisting of a system of stigmators, focusing lenses, and deflectors and is used to guide as well as to shape, focus, and raster the primary ion beam onto the sample. After being produced in the source, the primary ion beam is prone to energy and spatial spread.<sup>17</sup> A carefully designed primary optics system, consisting of combinations of stigmators, lenses, and deflectors, allows to control the shape and the deviation of the primary ion beam. The stigmators are quadrupoles or octopoles allowing to modulate the beam to attain circular shape, i.e., to correct astigmatism. The first lens (condenser lens) is used to image the source in the column to a cross-over. The second lens (objective lens) focusses the beam onto the sample.<sup>34</sup> Plate deflectors are positioned above the last lens and enable scanning of the primary beam over the surface of the sample.

### 2.3 Mass analyzers

Once the SIs are formed, these are collected by the secondary ion optics and transferred to the mass spectrometer.

The key parameters defining the performance of a mass spectrometer are: 1. the transmission (ratio of ions detected versus emitted ones from the sample surface), 2. the highest detectable charge-to-mass ratio, 3. the duty cycle, and 4. the mass accuracy and resolution

(ability to distinguish ions of different masses, typically referred as mass resolving power of the mass spectrometer). The mass resolving power (MRP) is defined as:<sup>2</sup>

$$\text{MRP} = \frac{m}{\Delta m} \quad (3)$$

where  $m$  is the average mass of the considered masses and  $\Delta m$  their mass difference. The MRP varies from values slightly above one to several thousands (and even hundreds of thousands), while the higher the value of  $R$  the better the mass resolution of the mass spectrometer. SIMS instruments with a high MRP are capable of distinguishing between ions with the same nominal mass, for instance to separate  $^{56}\text{Fe} = 55.93493 \text{ u}$  and  $^{40}\text{Ca}^{16}\text{O} = 55.9575 \text{ u}$  at least a mass resolving power of  $\approx 2500$  is required. Working at lower than the required MRP will result in the so-called mass interferences, where both (or multiple) peaks will not be distinguishable from one another.<sup>3</sup>

In SIMS, three types of mass analyzers are very common: the quadrupole, the time-of-flight, and the magnetic sector.

The quadrupole mass spectrometer (Figure 3 a) is based on four rod-like electrodes, placed in a square pattern. An oscillating frequency voltage is applied with the same sign for each opposite rod pair to create a stable path only for ions with a given mass-to-charge ratio, allowing these to reach the detector. Ions of higher or lower mass are subjected to unstable oscillations and are expelled out of the spectrometer, and thus filtered out. While quadrupoles present a low-cost solution, they do not allow simultaneous detection of multiple ion species and have a lower mass resolution compared to the other two types of spectrometers.

The time-of-flight spectrometer (Figure 3 b) measures the time which ions need to go from the sample surface to the detector. At the same energy, ions with a lower mass need less time to pass through the spectrometer compared to those with a higher mass which allows hence to perform mass separation. To create a signal, the primary ion beam is pulsed with a duration of a few ns, while the waiting time between two pulses is a few  $\mu\text{s}$ , leading to some duty cycle. The advantage of this system is that it offers an unlimited mass range and hence allows to detect full molecules and molecular fragments. Reflectron systems are used to reduce energy spread of the emitted ions. However, using pulses instead of continuous irradiation means

that the sample is irradiated with lower doses (leading to lower signal statistics) and results in overall longer acquisition times than for DC acquisitions.

The magnetic sector (Figure 3 c) is typically preceded by an electrostatic sector, in a double focusing (called "Herzog-Mattauch") configuration, to compensate for the ion energy of the secondary ions. In the magnetic sector, the trajectory of the ions bended by a magnetic field with path radii associated to their charge-to-mass ratio. Thus, for a specific magnetic field, SIs are separated and can be detected simultaneously. Magnetic sector-based spectrometers have the advantage to operate in DC mode (high duty cycle up to 100 % in contrast to a ToF spectrometer) and allow parallel mass detection which avoids loss of information since for a quadrupole spectrometer serial sputtering cycles are needed to detect multiple masses in a single ROI.

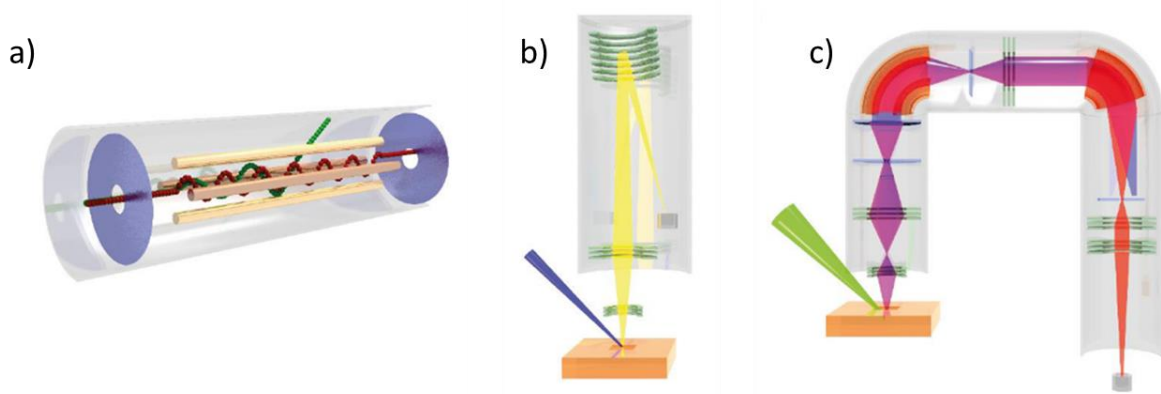


Figure 3: Schematic representation of the three types of mass analyzers used for SIMS: a) quadrupole, b) time-of-flight, and c) magnetic sector (Figure adapted from Audinot et al.).<sup>16</sup>

#### 2.4 Analysis modes

Ions can be detected in different modes in SIMS to acquire chemical (surface and depth) distribution information (Figure 4).

In the mass spectrum mode (Figure 4 a), the signal is collected over a given mass range by detecting SIs along the focal plane using one or multiple detectors. The detected masses in dynamic SIMS range from hydrogen to uranium, while in static mode masses of up to  $\sim 10,000$  m/z can be detected.<sup>35</sup> The mass spectrum provides a very specific chemical fingerprint of the analyzed sample. The differentiability of each peak in the mass spectrum depends on the MRP

of the spectrometer (see section 2.3). Spectral identification is relatively straight forward for single atomic or small molecular ions. Manual identification tends to become more complicated for large organic molecules with heavy fragmentation. Molecular fragmentation can be tuned for the emission of smaller, respectively larger, molecular fragments by choosing the right projectile and surface chemistry (e.g., by gas flooding or cationization by gold deposition). However, pattern recognition algorithms with spectral libraries present nowadays a more practical solution for spectral identification.<sup>2</sup>

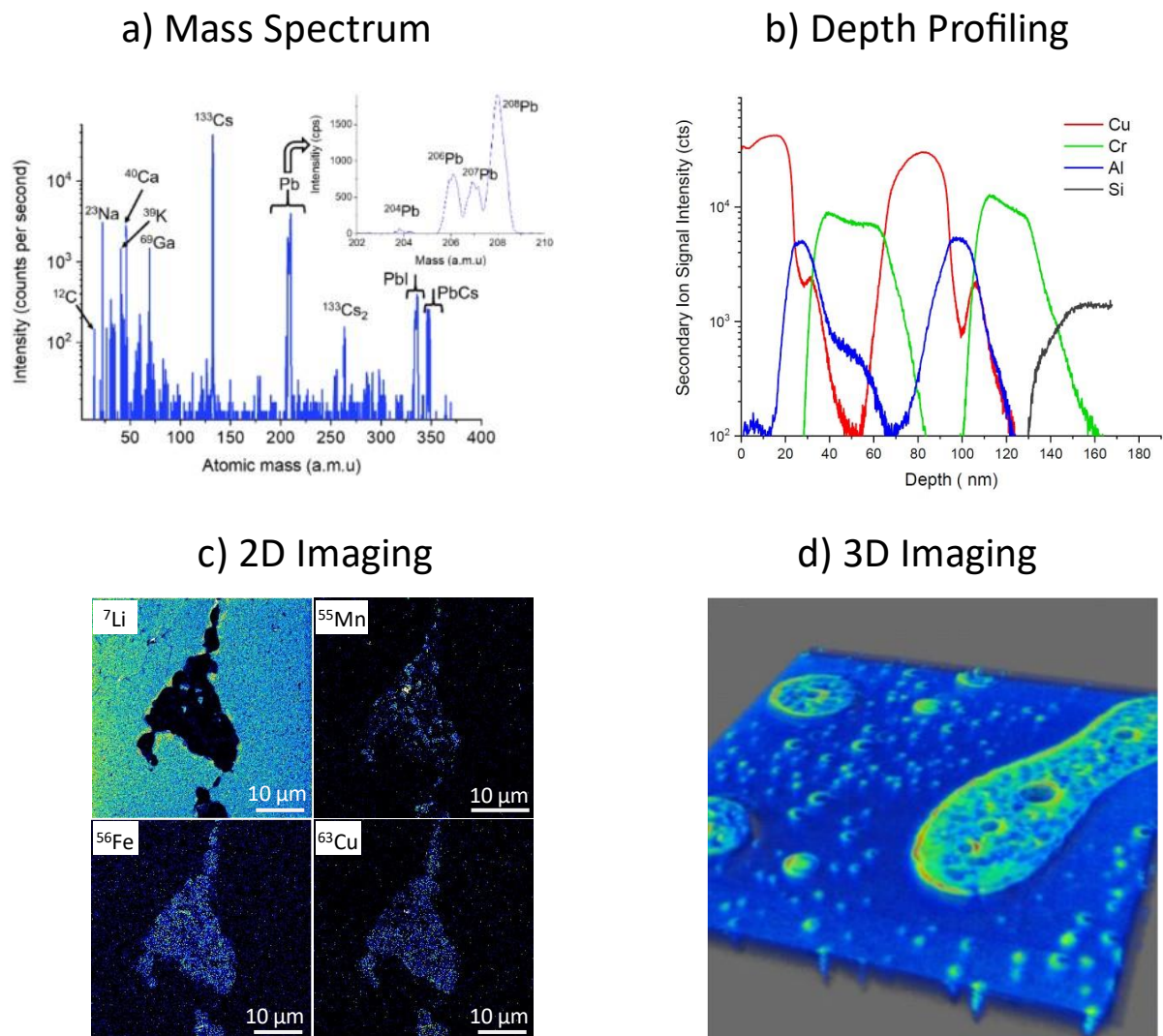


Figure 4: Examples illustrating the analysis modes in SIMS: a) mass spectrum of an organic-inorganic halide lead perovskite, b) depth profile of a copper-aluminum-chromium thin film sample, c) images of an Al-Li alloy, and d) 3D reconstruction of a polymer blend showing the  $^{12}\text{C}$  signal (Figures a-c adapted from De Castro et al.<sup>14</sup> and d from Wirtz et al.).<sup>18</sup>

The depth profiling mode (Figure 4 b) allows to monitor the SI intensity as a function of depth while scanning a defined surface of the sample with a primary ion beam. Analysis depths from 10 nm up to more than 10  $\mu\text{m}$  are assessed routinely in the depth profiling mode.<sup>2</sup> This mode is of particular interest for the analysis of semiconductor and thin film samples, as it allows to detect as well as determine the distribution of dopants and identify the composition of different layers, respectively. The ability to resolve a layer of a given thickness in a depth profile depends on the depth resolution, typically expressed as the change in nm per decade of signal (influenced by the primary ion type, its impact energy, incidence angle, and nature of the substrate).<sup>16</sup>

In the imaging mode (Figure 4 c), micrographs are obtained by pixel-wise raster scanning a surface with a primary ion beam and summing up the number of SI counts for each pixel. SIMS images allow to visualize spatially the distribution of the detected ions of the analyzed Region of Interest (ROI). Typical fields of view (FOVs) in SIMS can vary from  $1 \times 1 \text{ mm}^2$  down to  $1 \times 1 \mu\text{m}^2$ , depending on the instrument's performance and the application.<sup>16,36</sup> The spatial resolution of the SIMS image depends mainly on the probe size defined by the source performance, e.g., brightness, energy dispersion (see Appendices for more details about the characteristics of each source), and the primary ion optics. The sensitivity and the concentration of the analyzed element also have an impact on the lateral resolution. Additionally, for very fine FIBs, as it is the case for  $\text{Ne}^+$  in a GFIS, the resolution is not limited by the size of the beam, but by the distance of the ion impact and area of emission of the sputtered particle, i.e., the collision cascade. The latter imposes a minimal lateral resolution for SIMS of 10 nm.<sup>18</sup>

Sequential acquisition of 2D SIMS images provides 3D information (Figure 4 d), because due to progressive sputtering of the surface each image contains the spatial elemental information at the sputtered depth. These images can be compiled into a stack to create a volumetric 3D reconstruction of the analyzed zone representing the evolution of the signal as function of the sample depth. Novel data treatment algorithms allow then to visualize signal gradients in all three spatial directions and to perform further numerical analyses, e.g., cropping of the reconstruction to zoom on a sub-ROI and/or depth profile reconstruction by frame signal integration. It is worth noting that in "classical" 3D SIMS, the original surface topography of the sample and its evolution is not taken into account, as different materials

exposed to the primary ion beam at varying incidence angles sputter at different rates. More detailed discussions on topographical artefact correction will follow in chapter 3.

### 3. Correlative microscopy and spectroscopy

Correlative microscopy and spectroscopy is used to study a same ROI with multiple (typically two or even more) techniques to acquire complementary information for a deeper understanding of the sample and its properties. The latter can include morphological aspects, such as topography, connectivity, ordering, and physical or chemical properties, for instance chemical composition, distribution of chemical compounds, trace elements or dopant concentration, work function, magnetism, or optical properties.<sup>37</sup>

As mentioned earlier, SIMS is a highly sensitive surface analysis technique able to distinguish all elements and isotopes. Therefore, SIMS complements common analytical techniques including energy-dispersive x-ray spectroscopy (EDX) and electron energy-loss spectroscopy (EELS), available in common electron microscopes such as scanning electron (SEM) and transmission electron microscopes (TEM). As the lateral resolution in SIMS is defined by the ion source performance (mostly brightness), the sensitivity, the primary ion optics, and the spatial extend of the collision cascade, in the last years developments of SIMS instruments allowed to perform imaging at a lateral resolution close to the physical limit ( $\sim 10$  nm).<sup>18</sup> However, electron microscopy (EM) techniques (SEM or TEM) allow imaging at lateral resolutions far beyond the physical limit in SIMS (ranging from a few nanometers to atomic scale), but detection of trace elements and isotopes is not possible with EDX and EELS. Therefore, SIMS has been correlated with EM techniques, including SEM, TEM,<sup>38</sup> and also FIB platforms,<sup>39–41</sup> to combine lower resolution analytical information with ultra-high resolution structural information from EM acquired on the same ROI.

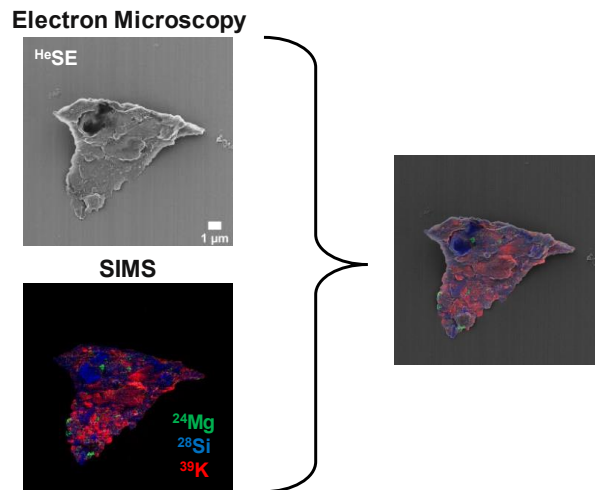
To improve data visualization and facilitate its interpretation, the EM-SIMS workflow is extended by performing image overlays and fusion. The simplest and most common procedure to perform image correlation is an image overlay, i.e., overlaying one image with the other (Figure 5 a) with a defined transparency of the overlaid image to observe the structure and chemical information in a single image. However, more sophisticated

algorithms from remote sensing and medical diagnostics are emerging in the last years, including the hue-saturation-intensity (HSI) principle component analysis and the Laplace fusion method.<sup>37</sup>

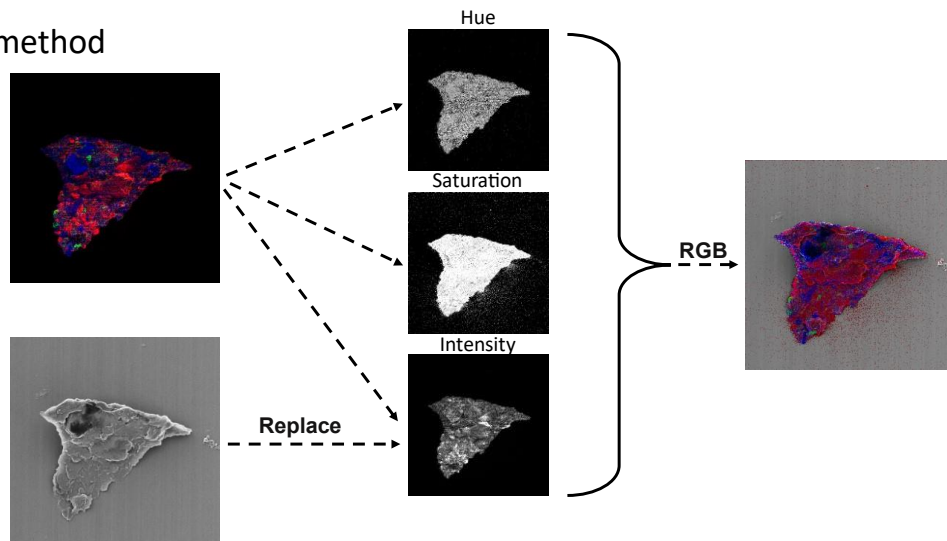
For the HSI-based image correlation method (Figure 5 b) the pre-processed RGB SIMS image is first converted into a HSI colormap. The hue (H) component carries the position on the color wheel and the saturation (S) component represents the amount of gray. The intensity (I) component contains the image contrast information. In the following, the intensity component is replaced by the high-resolution EM image. Finally, the HS-EM stack is converted again into an RGB image. The fused image presents both, EM and SIMS, datasets, as the SIMS information is visualized with the RGB colormap while the EM structural information is in grayscale, which allows an easy chemical identification of sub-ROIs and structural features. While the HIS-method is simple and fast, it suffers from severe drawbacks, for instance the restriction to process SIMS data in RGB format (SIMS intensity mapped in 8-bit range [0-255]) instead of raw image data. Furthermore, contrast related artefacts, as very dark or bright features (e.g., due to charging effects) in the EM image will suppress the color intensity of the SIMS information in the fused image.<sup>37</sup>

For the Laplace fusion method (Figure 5 c), high frequencies of the high-resolution EM image are extracted and added stepwise with the lower resolution SIMS image. The concept is based on the Laplacian pyramid introduced by Burt and Adelson.<sup>42</sup> The methodology was adapted by Vollnhals et al. studying it for EM and SIMS images. A brief description of the workflow adapted for the image processing software ImageJ/Fiji is given in the following: 1. A Gaussian blur filter with a radius of 2.0 is applied to the EM image (typically 2048 pixels × 2048 pixels). 2. The high frequencies from EM image are extracted by subtracting the blurred EM from the pristine EM (referred as EM<sub>1</sub>) image. The high-frequency image is named L<sub>1</sub> (2048 pixels × 2048 pixels). 3. The EM image is downscaled to 1024 pixels × 1024 pixels (EM<sub>2</sub>) and 512 pixels × 512 pixels (EM<sub>3</sub>), and steps 1. and 2. are repeated for EM<sub>2</sub> and EM<sub>3</sub> to obtain the high-frequency images L<sub>2</sub> (1024 pixels × 1024 pixels) and L<sub>3</sub> (512 pixels × 512 pixels), respectively. 4. Then the high-frequency L<sub>3</sub> image is added to the SIMS image (512 pixels × 512 pixels) and the resulting image (referred as LF<sub>3</sub>) is upscaled to 1024 pixels × 1024 pixels. 5. Step 4 is repeated twice by adding image L<sub>2</sub> to LF<sub>2</sub>, upscaling the resulting image to 2048 pixels × 2048 pixels and adding L<sub>1</sub>, which gives the final result.

a) Image overlay



b) HSI method



c) Laplace fusion

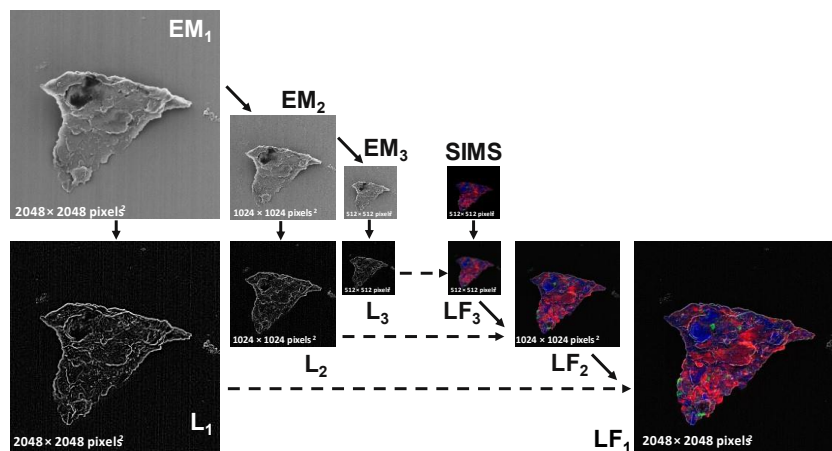
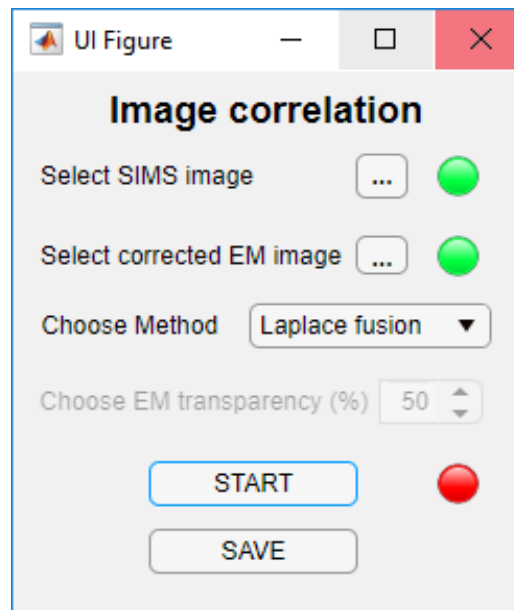


Figure 5: Workflow visualization of common image correlation methods applied to EM and SIMS images of a soil microaggregate: a) image overlay, b) HSI method, and c) Laplace fusion.

In contrast to the HSI method, the Laplace fusion method does not require to operate with RGB SIMS image data and overcomes color intensity artefacts, because only high frequencies (i.e., contours/edges) are retained from the EM image while information from plain surfaces is not included, which could mask the information from SIMS. Therefore, Vollnhals et al.<sup>37</sup> described the Laplace fusion method as the more reliable and robust correlation method compared to HSI. However, the workflow of the Laplace fusion method is relatively complex and time-consuming.

Therefore, for workflow efficiency improvement, in the framework of this work a MATLAB program and graphical user interface was written, which allows (after manual alignment of the EM and SIMS images in ImageJ/Fiji) fully automatic and fast correlation of EM and SIMS images (Figure 6). The user can choose among the image overlay (with the desired transparency of the EM image), the HSI method, and the Laplace fusion method, export, and save the final image in a desired format (.tiff or .png).



*Figure 6: Capture of the graphical user interface for image correlation of EM and SIMS images. The user can choose among the overlay (with a chosen transparency of the EM image), the HSI, and the Laplace fusion methods.*

#### 4. SIMS on state-of-the-art electron microscopes

In the framework of this thesis, two microscopes were used to carry out the research work. In both cases commercial microscopes for high-resolution microscopy and FIB patterning were upgraded with a SIMS system developed at LIST, allowing to add analytical capabilities to these FIB platforms (Figure 7).

A HIM (Zeiss ORION Nanofab) was the first instrument equipped with this compact mass spectrometer, allowing in-situ EM and SIMS analyses. The HIM generates primary He<sup>+</sup> and Ne<sup>+</sup> ion beams with a GFIS (see chapter 1 section 2.1) allowing to achieve in Secondary Electron (SE) imaging mode an ultra-high spatial resolution of down to 0.3 nm (with He<sup>+</sup>).<sup>40</sup> In the following, this instrument will be referred as the “HIM-SIMS”.

The second microscope is a FIB-SEM Dual-beam platform (Thermo Fisher Scientific Scios) equipped with a SIMS. The vertical SEM column is based on a field emission source and offers a lateral resolution of 1-2 nm. A LMIS-based Ga-FIB column is positioned at 52° with respect to the vertical axis. Here it will be referred as the “FIB-SEM-SIMS”.

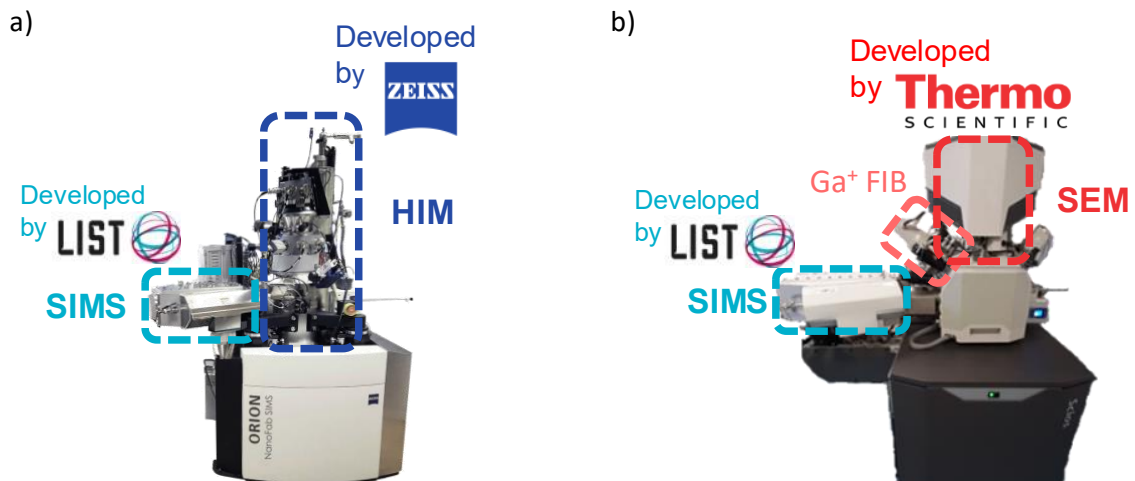


Figure 7: State-of-the art SIMS devices a) Zeiss ORION Nanofab HIM and b) Thermo Fisher Scientific FIB-SEM DualBeam coupled with an add-on SIMS systems developed at LIST.

## 4.1 HIM-SIMS

## 4.1.1 Instrument design

The helium ion microscope is a multipurpose instrument for ultra-high resolution EM imaging and FIB nano-patterning first introduced in 2006.<sup>40</sup>

The key technology of them HIM allowing to achieve very small probe sizes ( $\text{He}^+$ :  $< 0.5 \text{ nm}$ ,  $\text{Ne}^+$ :  $< 2 \text{ nm}$ ) is the gas field ion source. In the upper part of the HIM, the GFIS is acting as a source of the primary ( $\text{He}^+$  or  $\text{Ne}^+$ ) ion beams. It consists of a sharp tungsten tip (Figure 8) having only three atoms on its apex (“trimer”). The tip is cooled down to cryogenic temperatures to favor adsorption of injected He or Ne gas atoms. An electric field, created by a bias applied between the extractor electrode and the source, allows to extract and field ionize the adsorbed gas atoms. These are shot through the ion column towards the sample at acceleration energies ranging from 10 keV to 35 keV through the GFIS column kept under ultrahigh vacuum ( $10^{-6} \text{ mbar}$  with the gas injected). Emission takes place from one of the three beamlets, while one atom is selected as the main emitter, thus optimal source brightness ( $4 \cdot 10^9 \text{ A cm}^{-2} \text{ sr}^{-1}$ ) is achieved with primary currents ranging from 0.1 up to 100 pA.<sup>39,40</sup>

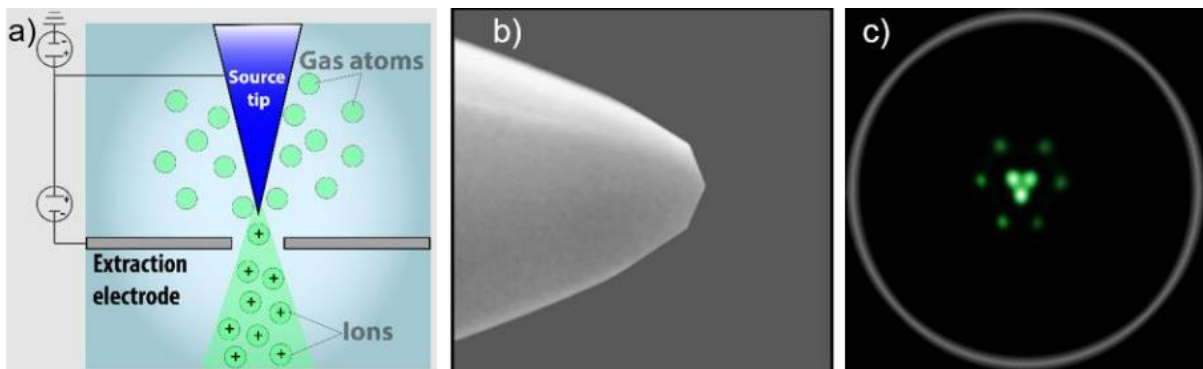


*Figure 8: Visualization of the primary ion beam production process and components in a GFIS. a) Schematic illustration of the ion production and extraction in the vicinity of the GFIS tip. b) Image of the tungsten tip with the three atoms on its apex, shown in c) in source view mode (Figure a from Audinot et al.,<sup>16</sup> b and c from Wirtz et al.).<sup>39</sup>*

After having passed a system of electrostatic lenses and apertures (more details about primary ion optics of the HIM can be found in the Appendices), used to focalize the ion beam, the primary ions hit the sample (see schematic in Figure 9). Among others, SEs are produced which are detected by an Everhart–Thornley (ET) detector located above the sample in the

analysis chamber (maintained at  $10^{-7}$  mbar). Typically,  $\text{He}^+$  ions are used in the SE image mode in order to reduce surface sputtering during the image acquisition process (lower sputtering yield of  $\text{He}^+$  vs.  $\text{Ne}^+$ )<sup>32</sup> and better lateral resolution in  $\text{He}^+$  (0.5 nm vs. 2 nm in  $\text{Ne}^+$ ).<sup>39</sup>

The advantages of a HIM compared to a conventional Scanning Electron Microscope (SEM) are: 1. A shorter wavelength of  $\text{He}^+$  and  $\text{Ne}^+$  ions vs. electrons (30 keV  $\text{He}^+$  has 83 fm as De Broglie wavelength) allowing to achieve very small probe sizes, i.e., spatial resolution (0.3 nm in  $\text{He}^+$ , 2 nm in  $\text{Ne}^+$  in SE imaging mode). 2. The surface area of the interaction volume of  $\text{He}^+/\text{Ne}^+$  ions is smaller compared to electrons, allowing to collect SEs closer to the beam impact point with a higher SE yield, and thus more surface details can be imaged. 3. With a lower (5-10 times) convergence angle of the primary ion beam a higher depth of field can be achieved, i.e., the image is in focus over a large range of working distances. 4. Charge compensation can be done using an electron flood gun, having the advantage to image samples directly without the need of a conductive surface coating, which could mask nm- (or sub-nm) sized features.

In order to perform SIMS analyses, a retractable SI extraction box is introduced between the primary ion column and the sample in the analysis chamber. While the height of the extraction box is 16 mm, the distance between the extraction box and the sample is 0.5 mm, allowing to perform analyses at a working distance of about 18.5 mm, i.e., significantly larger than for typical imaging with a HIM in SE mode. Although working at this relatively large working distance resulting in broadening of the probe size (to 3-4 nm), this does not affect the lateral resolution in SIMS as the SI emission area for both, helium and neon, is larger ( $\sim 10$  nm).<sup>16,18</sup>

Typically,  $\text{Ne}^+$  primary ions are used in this case to enhance sputtering of the surface and therefore increasing the SI signal. The sample stage is biased at  $\pm 500$  V for positive, respectively negative ion extraction (positive and negative ions in separate runs). The secondary ions are then collected by the SIMS extraction system and post-accelerated from (post-acceleration voltage typically 3 kV) to reduce angular spread of the beam and chromatic aberration of the beam. The SI beam is then focused and aligned with electrostatic lenses and quadrupoles. A modified Mattauch-Herzog-type magnetic field sector (double focusing condition) is filtering the SIs according to their charge-to-mass ratio and directing the analyzed species towards one of the four (three movable and one fixed) channeltron

detectors and a total ion count (TIC) detector in the SIMS system. More details about the primary and secondary ion optics of the HIM-SIMS can be found in the Appendices.

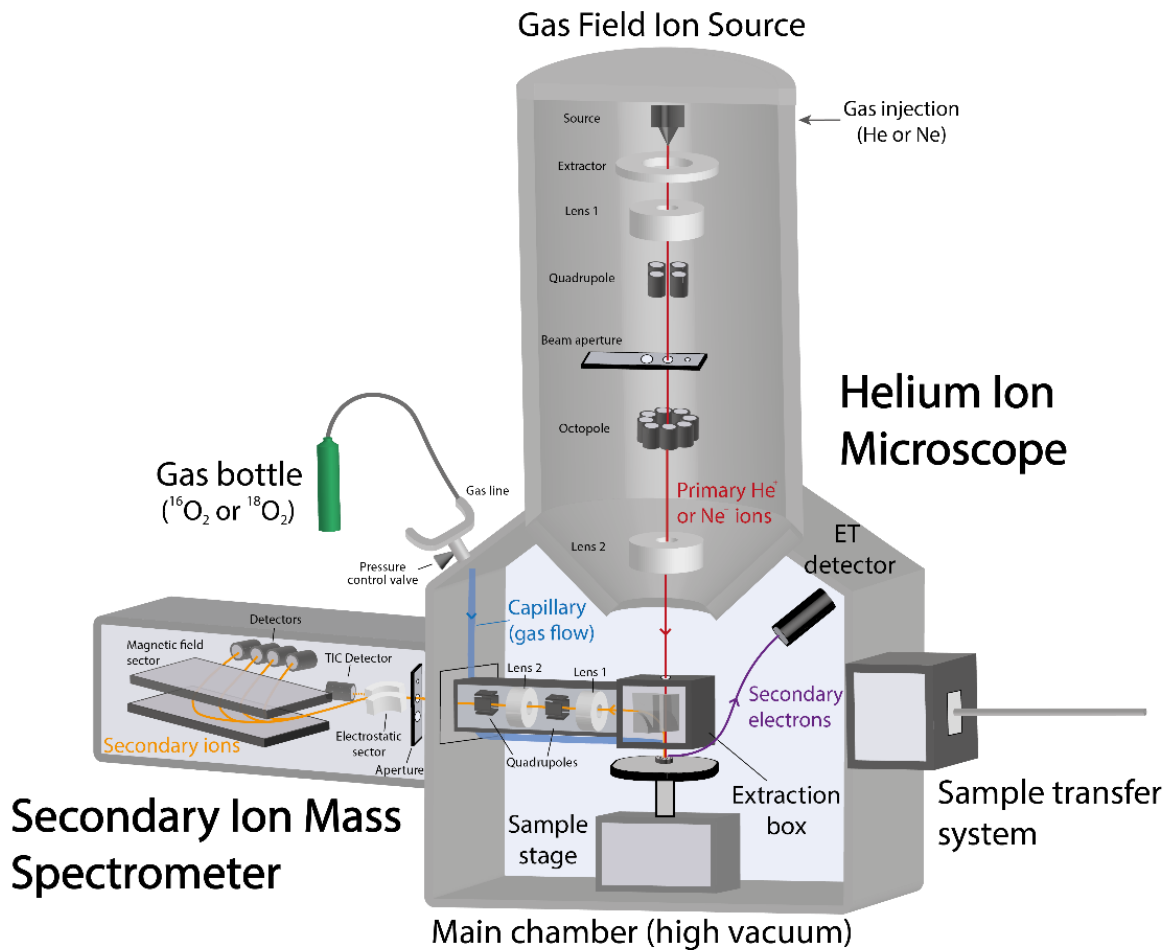


Figure 9: Schematic overview of the HIM-SIMS instrument. The central part of the instrument consists of the HIM, where  $\text{He}^+$  or  $\text{Ne}^+$  ions are used for SE imaging. The add-on SIMS system on the left part allows to acquire in-situ analytical information.

The typical imaging workflow consists of acquiring in a first step SE images (SIMS extraction box withdrawn, i.e. positioned at a storage position close to the chamber wall) and in a second step the SIMS images of the same ROI (extraction box inserted). It is worth noting that SE imaging while the extraction box is inserted is in principle possible but doing so leads to a lower SE detection and thus poorer SE image quality.

With the double focusing configuration, the SIMS system allows to achieve a MRP of more than 400 and a transmission above 40 %. Using a post-acceleration voltage of 3 kV (kinetic energy of 3.5 keV) and a magnetic field of 750 mT, a mass range of up to 500 m/z can be

measured. SIMS imaging can be performed routinely with sub 20 nm lateral resolution as demonstrated by Dowsett and Wirtz<sup>43</sup> (see Appendices for more details).

The HIM-SIMS is equipped with an oxygen flooding system allowing to enhance useful yields by improving the ionization probability of electropositive elements by a constant surface adsorption of oxygen changing the chemical environment of the surface. An oxygen bottle is connected to a gas line equipped with a highly sensitive leak valve which allows to regulate manually the oxygen flow the analysis chamber. In order to avoid air contaminations, the gas line is purged with an external pump before each set of flooding experiments according to a defined protocol.

A capillary passes through the SIMS extraction box with an orifice just above the sample surface. Experiments with up to  $4.5 \cdot 10^{-5}$  mbar pressure in the analysis chamber are possible. At higher pressures the system security intervenes by closing the valve between the main chamber and the GFIS to avoid contamination and damage of the source.

#### 4.1.2 Performance demonstration

In the recent years since its development, the HIM-SIMS has demonstrated its ability to face a variety of analytical challenges in materials, life, and soil sciences where both high spatial resolution and the sensitivity were needed. Here the key performances of the HIM-SIMS will be demonstrated on some examples for common SIMS analysis modes (mass spectrum, depth profiling, 2D, and 3D imaging).

##### 4.1.2.1 Mass spectrum recording

Figure 10 shows a mass spectrum recorded on a copper indium gallium selenide (CIGS) solar cell sample acquired on the HIM-SIMS in both positive and negative modes. The main elements, copper, indium, gallium, selenide and their most abundant isotopes are faithfully represented in the mass spectrum. A mass resolving power  $\frac{m}{\Delta m}$  of 550 was determined from this spectrum.<sup>39</sup>

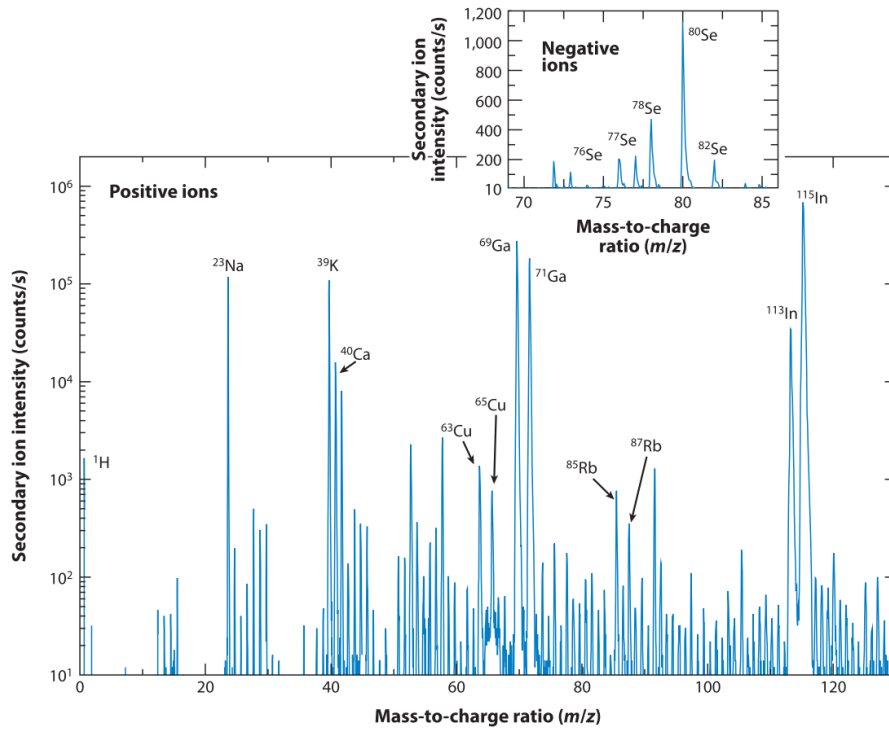


Figure 10: Mass spectrum recorded on a copper indium gallium selenide (CIGS) solar cell in positive (large graph) and negative (smaller graph on the upper part) analysis modes on the HIM-SIMS instrument at 25 keV Ne<sup>+</sup> with 20 pA (Figure from Wirtz et al.).<sup>39</sup>

#### 4.1.2.2 Depth profiling

Here a depth profiling study was performed on an aluminum-copper thin film sample. To do so, the acceleration energy of the Ne<sup>+</sup> ions was reduced to 10 keV. The signals of the most abundant isotopes of aluminum and copper, <sup>27</sup>Al and <sup>63</sup>Cu, respectively were monitored.

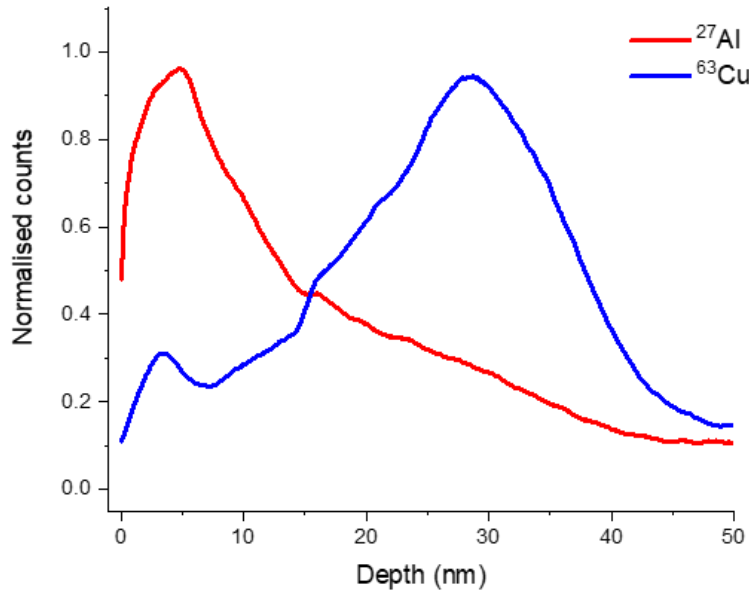


Figure 11: Depth profiling analysis on an aluminum-copper thin film sample (10 keV  $\text{Ne}^+$ , 15 pA).

As the thickness of each layer was known from previous measurements on a well-calibrated stand-alone SIMS (SC Ultra)<sup>44,45</sup> instrument, the time-scale was converted to depth-scale by imposing the thickness of each layer to the x-axis.

#### 4.1.2.3 2D imaging

In the following application, a coccolithophore structure was analyzed in the HIM-SIMS instrument in imaging mode. As mentioned in section 4.1.1, SE imaging can be done with a spatial resolution of down to 0.3 nm and SIMS imaging with < 20 nm.

Coccolithophores are microorganisms largely found in marine sedimentary chalk rock material surrounding hydrocarbon reservoirs. Studying this material is crucial to improve the efficiency of the oil recovery process. Here oil reservoir sample material was exposed to synthetic sea water (SSW) to alter calcite surfaces, which is a known method to gain more oil from existing reservoirs.<sup>33</sup>

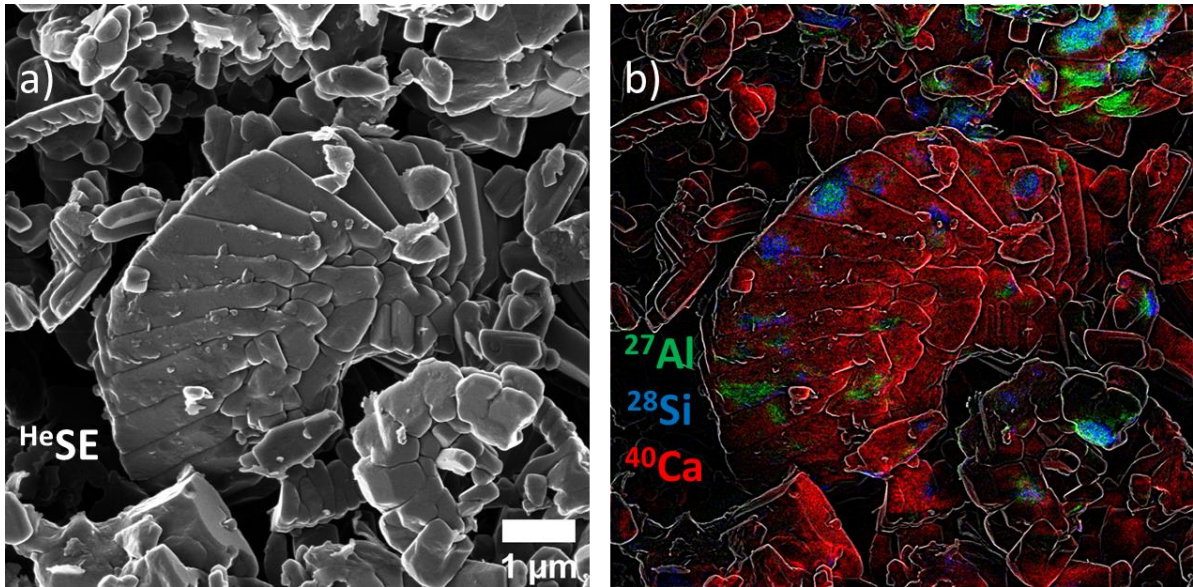


Figure 12: High-resolution imaging study on a coccolithophore structure on the HIM-SIMS. a) HIM SE image (25 keV  $\text{He}^+$ , 2 pA, 2048 pixels  $\times$  2048 pixels, 10  $\mu\text{s}/\text{pixel}$ , 8 lines average). b) Laplace image fusion of the SE image (a) and the RGB image SIMS image (25 keV  $\text{Ne}^+$ , 10 pA, 512 pixels  $\times$  512 pixels, 2 ms/pixel) containing  $^{27}\text{Al}$  (green),  $^{28}\text{Si}$  (blue), and  $^{40}\text{Ca}$  (red).

The coccolith structure was imaged here first in HIM SE mode (Figure 12 a). In the following, SIMS analyses in positive and negative modes were performed on the same area to show the distribution of clay minerals and calcite on the surface of the ROI. Using the Laplace fusion method, the RGB image containing the clay mineral information ( $^{27}\text{Al}$ : green,  $^{28}\text{Si}$ : blue) and the calcite ( $^{40}\text{Ca}$ : red) images was fused with the HIM SE image (Figure 12 a), showing the topography information and the clay mineral and calcite images in a single micrograph (Figure 12 b). The clay minerals present a very localized distribution whereas calcite is homogeneously distributed over the entire surface of the coccolith. Thus, with the high-resolution images it was possible to faithfully distinguish different phases covering the coccolith surface and allowed us to publish an article on fluid-rock interactions (Bredal et al.).<sup>33</sup>

### 4.1.2.4 3D imaging

In the next example, sequential 2D imaging on the HIM-SIMS instrument was done on a transistor sample. A series of SIMS images (in total 20 images) showing the silicon-28 distribution was acquired (Figure 13 a). A 3D volumetric representation was created from the SIMS 15 images allowing to visualize signal gradients inside the reconstruction as well as for vertically oriented surfaces.

To do so, in the framework of this thesis an algorithm was written in MATLAB. First, all the images were stacked above one another. The borders of the images were connected vertically by creating vertical surfaces while the SIMS counts were linearly interpolated over the distance from one image to the other. A box-like reconstruction was created then and plotted in a 3D space (Figure 13 b). A cuboid piece on the side of the reconstruction was cut out to show the interior structure of the transistor.

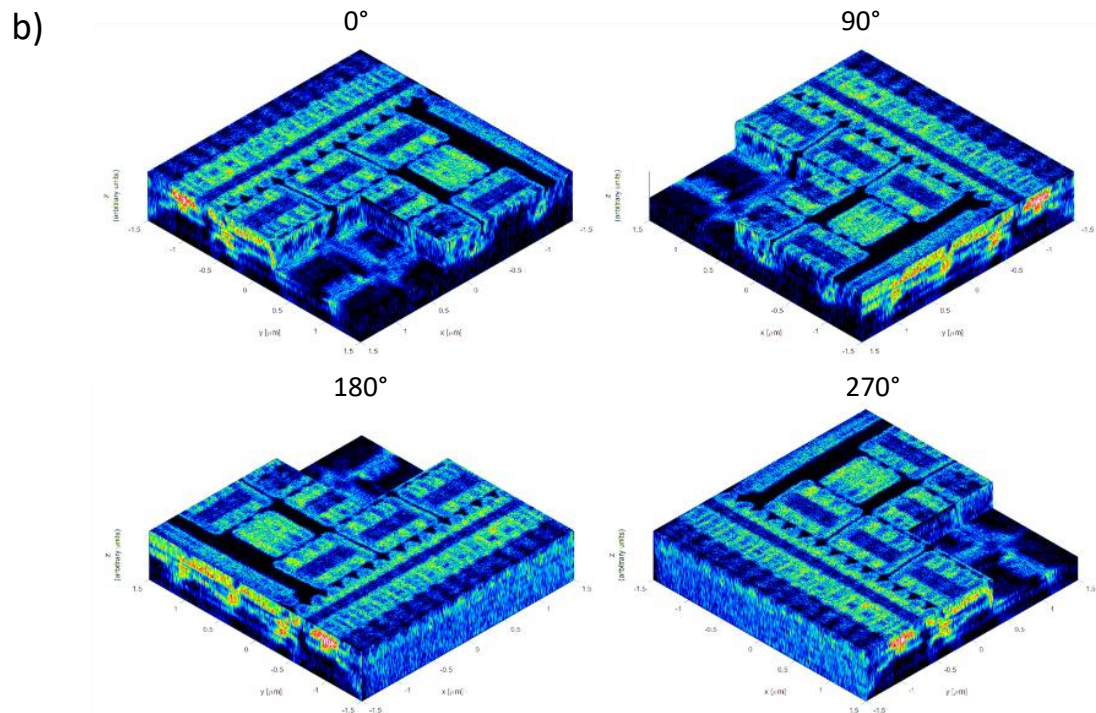
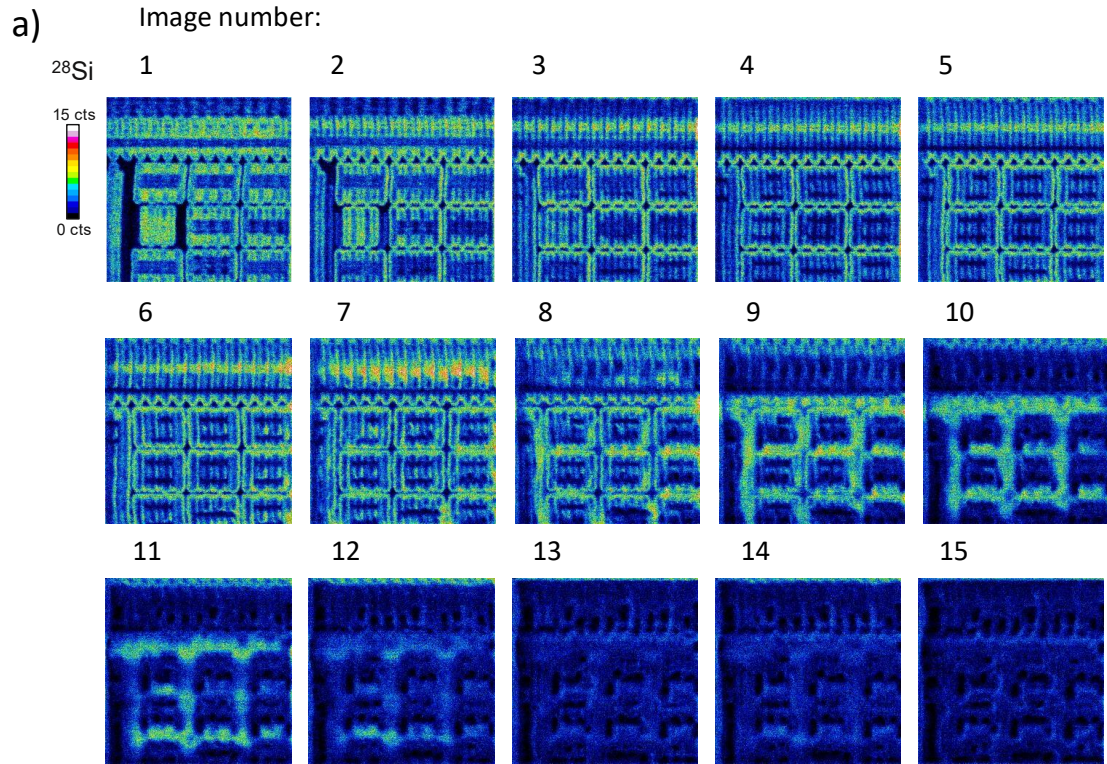


Figure 13: 3D SIMS imaging of a transistor ( $^{28}\text{Si}$  signal). a) SIMS images acquired sequentially on the same zone (25 keV  $\text{Ne}^+$ , 2 ms/pixel, FOV:  $3\ \mu\text{m} \times 3\ \mu\text{m}$ , 512 pixels  $\times$  512 pixels, in total 15 images). b) 3D volume reconstruction made of the stack of all the SIMS images shown in different perspectives (polar angle:  $45^\circ$ , azimuthal rotation:  $0^\circ$ ,  $90^\circ$ ,  $180^\circ$ ,  $270^\circ$ ). A cuboid was cut of the representation out to visualize the interior structure of the transistor.

## 4.2 FIB-SEM-SIMS

## 4.2.1 Instrument design

The DualBeam FIB-SEM instrument (Thermo Fisher Scientific), also called “Scios”, combines both an electron and a Ga<sup>+</sup> FIB column and is a widely used solution for high-resolution EM imaging and sample preparation by nano-patterning.<sup>46</sup>

The electron acceleration from a field emission source in the SEM column can be varied from 0.2 keV to 30 keV and it can be operated in SE and back scattered electron (BSE) detection modes. The Ga<sup>+</sup> column uses a liquid metal ion source (see Appendices for more details about the LMIS) and allows landing energies going from 0.5 keV to 30 keV with primary currents varying from 1.5 pA to 65 nA, while the smallest probe (3 nm) is achieved with 30 keV acceleration energy. The Ga<sup>+</sup> FIB can be used either in electron microscopy or in milling/patterning modes.

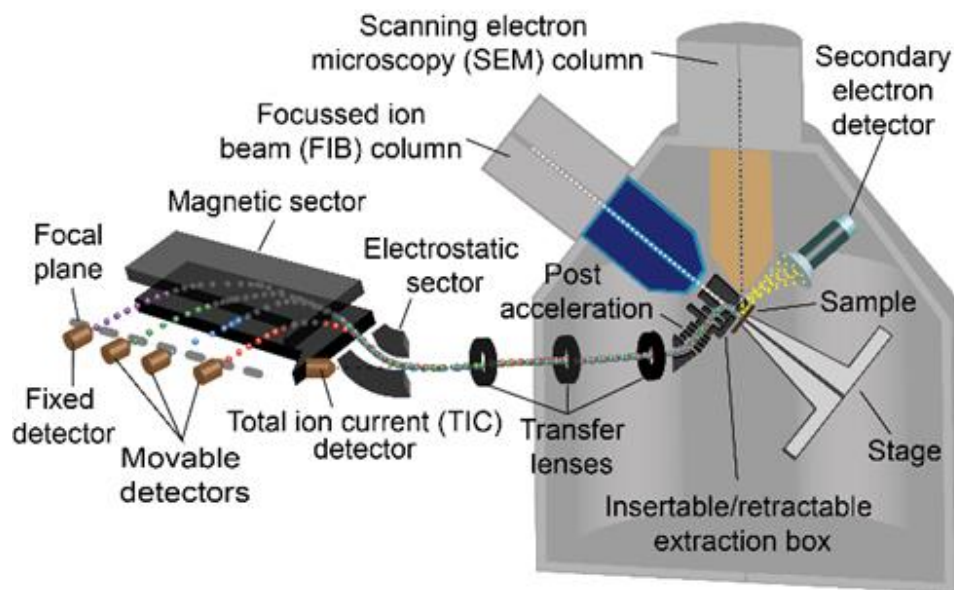


Figure 14: Schematic representation of the FIB-SEM-SIMS instrument. The main body consists of the analysis chamber with the electron column (vertical direction) for SEM imaging applications and the FIB column (installed at 52° with respect to the electron column). For SIMS analyses, the extraction box is inserted while the sample stage is tilted (Figure from De Castro et al.).<sup>14</sup>

A compact magnetic sector-based SIMS system designed at the LIST was installed for analytical measurements (Figure 14).<sup>14</sup> As the Ga<sup>+</sup> FIB is installed with a 52° angle with respect to the electron column oriented in the vertical direction and due to limited space between the SEM column, the FIB column, and the sample, the design of the SI extraction and transfer optics needed to be adapted with respect to the design of the HIM-SIMS. This included the addition of an electrostatic sector with a bending angle of 52° to orient the SI beam to the horizontal direction (Figure 15) and a third transfer lens. More details on this can be found in our recently published article (De Castro et al.).<sup>14</sup>

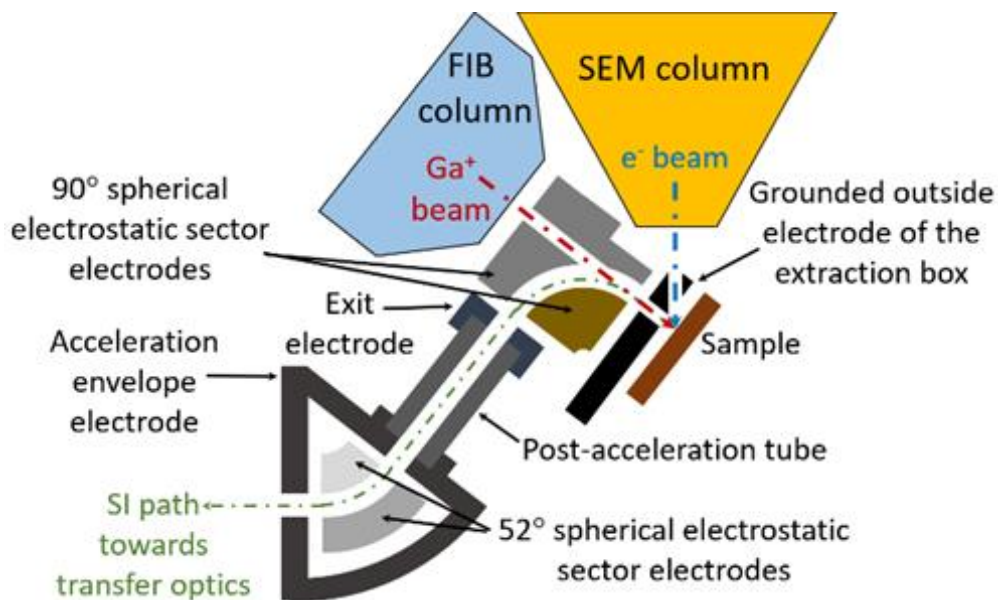


Figure 15: Schematic zoomed view on the SI extraction optics and the post-acceleration region in the FIB-SEM-SIMS instrument (Figure from De Castro et al.).<sup>14</sup>

To operate the SIMS system, the sample stage is tilted first at 52° with respect to the horizontal direction (Figure 15). Then the retractable SI extraction box is inserted in the analysis chamber between the Ga<sup>+</sup> FIB and the sample and approached at a distance of about 0.5 mm above the sample, allowing optimal SI collection at a working distance of the FIB of 19 mm. Using this configuration allows the primary ion beam to hit the sample at normal incidence and optimal collection of the SIs from the sample. It is worth noting that in order to operate the instrument in regular analysis modes, EM imaging and FIB patterning, the

extraction box can be retracted using piezo-positioners to a storage position close the wall of the main chamber.

During the SIMS analysis, a + or – 500 V sample bias is applied to maximize the yield of positive, respectively negative, SI collection. SI extraction is induced by the electric field produced by the sample bias and the first electrode grounded outside the extraction box. To transport the SIs towards the mass spectrometer, their trajectory is bent by spherical electrostatic sectors first by 90° and then by 52°. Using three electrostatic lenses (instead of two for the HIM-SIMS) and four quadrupole deflectors the SI beam is aligned and guided outside the analysis chamber. The SI beam enters then the mass analyzer (Mattauch-Herzog configuration based magnetic sector).

The magnetic sector allows detection of masses of up to 400 m/z (with four channeltron and a TIC detector) and a MRP of above 400 is attained (transmission: > 40 %). In SIMS imaging mode, a spatial resolution of sub 20 nm can be achieved (see Appendix). Reducing landing energies of the primary ion beam to 3 keV, allows to perform depth profiling with a depth resolution (decay length/decade) of ~ 4 nm.<sup>14</sup>

It is worth noting that a new detector system, a focal plane detector, was developed allowing simultaneous detection of the full mass range, i.e. recording of a full mass spectrum for each frame in depth profiling and each pixel in imaging mode.<sup>47</sup> A replacement of the multi-channeltron detectors with the focal plane detector is currently taken into consideration.

### 4.2.2 *Performance demonstration*

#### 4.2.2.1 *Mass spectrum recording*

A hybrid organic–inorganic halide lead perovskite absorber was analyzed in mass spectrum mode on the FIB-SEM-SIMS (Figure 16). The main elements constituting this perovskite solar cell were detected with some clusters (Cs<sub>2</sub>, Pbl, and PbCs). The isotopes of lead (<sup>204</sup>Pb, <sup>206</sup>Pb, <sup>207</sup>Pb, and <sup>208</sup>Pb) were detected and their signal ratios corresponds to the theoretical values of the isotopic abundances (1 %, 24 %, 22 %, and 52 %, respectively). A MRP of 410 was estimated from the <sup>208</sup>Pb peak.

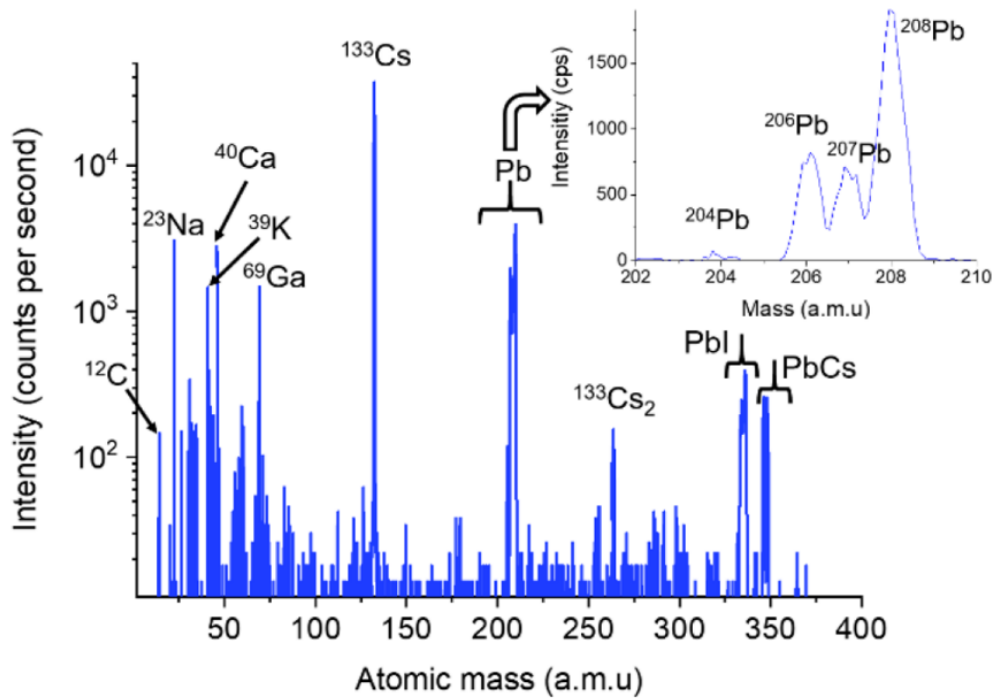


Figure 16: Mass spectrum (30 keV  $\text{Ga}^+$ , 6 pA, FOV:  $50 \mu\text{m}^2 \times 50 \mu\text{m}^2$ , magnetic field: 5 mT – 700 mT) of a hybrid organic–inorganic halide lead perovskite absorber. The enlarged mass spectrum on the upper right-side shows the isotopes of lead (Figure from De Castro et al.).<sup>14</sup>

#### 4.2.2.2 Depth profiling

The FIB column of the FIB-SEM-SIMS instrument is particularly suitable for depth profiling analysis as in practice it allows to reduce at landing energies down to 0.5 keV. To investigate the effect of the beam energy on depth profiling results on the FIB-SEM-SIMS, a thin film sample, consisting of copper, aluminum, and chromium (layer thicknesses: Cu (23nm)/Al (11nm)/Cr (34nm)/Cu (27nm)/Al (14nm)/Cr (27nm)/Silicon substrate) was analyzed in depth profiling mode setting the FIB column beam energies at 3.5 keV, 5 keV, 8 keV, 17 keV, and 30 keV (Figure 17). With a sample bias at + 500 V (for the extraction of positive ions), the aforementioned beam energies correspond to impact energies of 3 keV, 4.5 keV, 7.5 keV, 16.5 keV and 29.5 keV, respectively. The lowest beam landing energy used here was 3 keV to ensure both good signal statistics and depth resolution.

The SIMS detectors were aligned to measure the most abundant isotopes, i.e.  $^{63}\text{Cu}$ ,  $^{27}\text{Al}$ , and  $^{52}\text{Cr}$ . A 6 pA  $\text{Ga}^+$  beam was scanned over a surface of  $5 \times 5 \mu\text{m}^2$  at 256 pixels  $\times$  256 pixels integrating the total number of counts for each frame with a counting time of 1 s/frame. To

limit the crater edge effects during the depth profiling, an electronic gate corresponding to 60 % of the sputtered crater length and centered with respect to this area is applied, hence limiting the analyzed area to  $3 \times 3 \mu\text{m}^2$ .

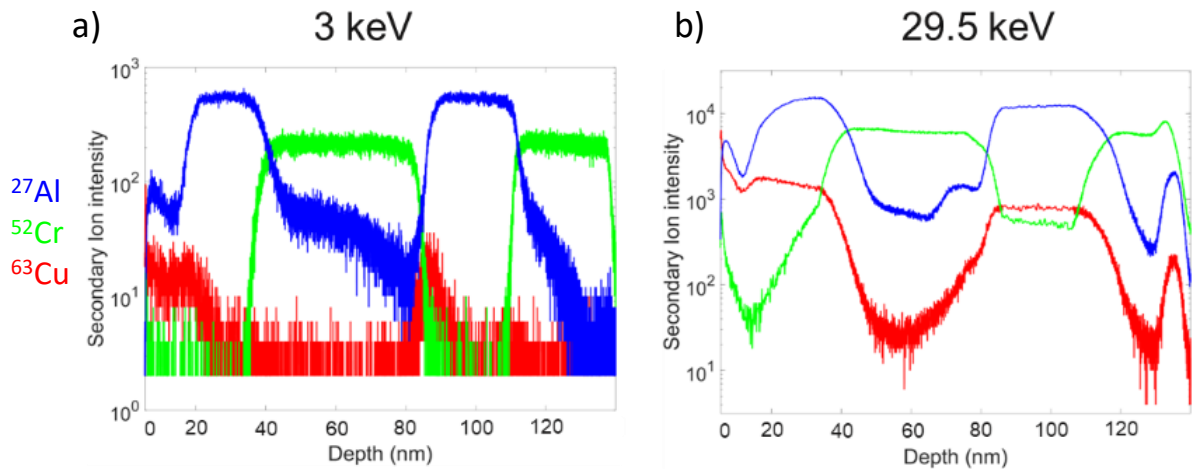


Figure 17: Depth profiles on a thin-film sample using the FIB-SEM-SIMS instrument, acquired at a) 3 keV and b) 29.5 keV Ga<sup>+</sup> landing energies.

Depth resolution (decay length in nm/decade) was extracted from the different depth profiles by taking the average between the front- and backside value for the aluminum and chromium layers (copper was not taken into account due to the high sputter rate compared to the other two elements). The results are reported in Figure 18.

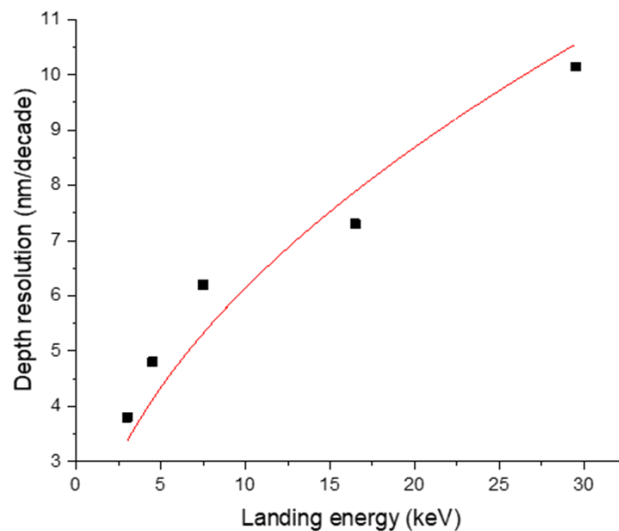


Figure 18: Study on the depth resolution of the FIB-SEM-SIMS instrument using a Cu-Al-Cr thin film sample measured at different landing energies. A square root variation (red line) of depth resolution with respect to the landing energy was found.

Optimal depth resolution of down to 3.8 nm is achieved at 3 keV landing energy. The depth resolution was found to vary with the square root of the impact energy, which is in accordance with the simulation studies made by Likonen et al.<sup>48</sup> The improvement in depth resolution by reducing the beam landing energy is due to a reduction of atomic mixing effects from one layer to another.

#### 4.2.2.3 2D imaging

Lithium-ion batteries are nowadays in high demand and improvement of their efficiency as well as lifetime are required to meet the increasing needs for energy storage. To study the degradation at the interface of a battery, after multiple charging and discharging cycles a LiMnNiCo cathode sample was taken from a battery cell and imaged in the FIB-SEM-SIMS (Figure 19). As mentioned previously in section 4.2.1, the FIB-SEM offers nanoscale imaging resolution in SE mode and sub 20 nm spatial resolution in SIMS.

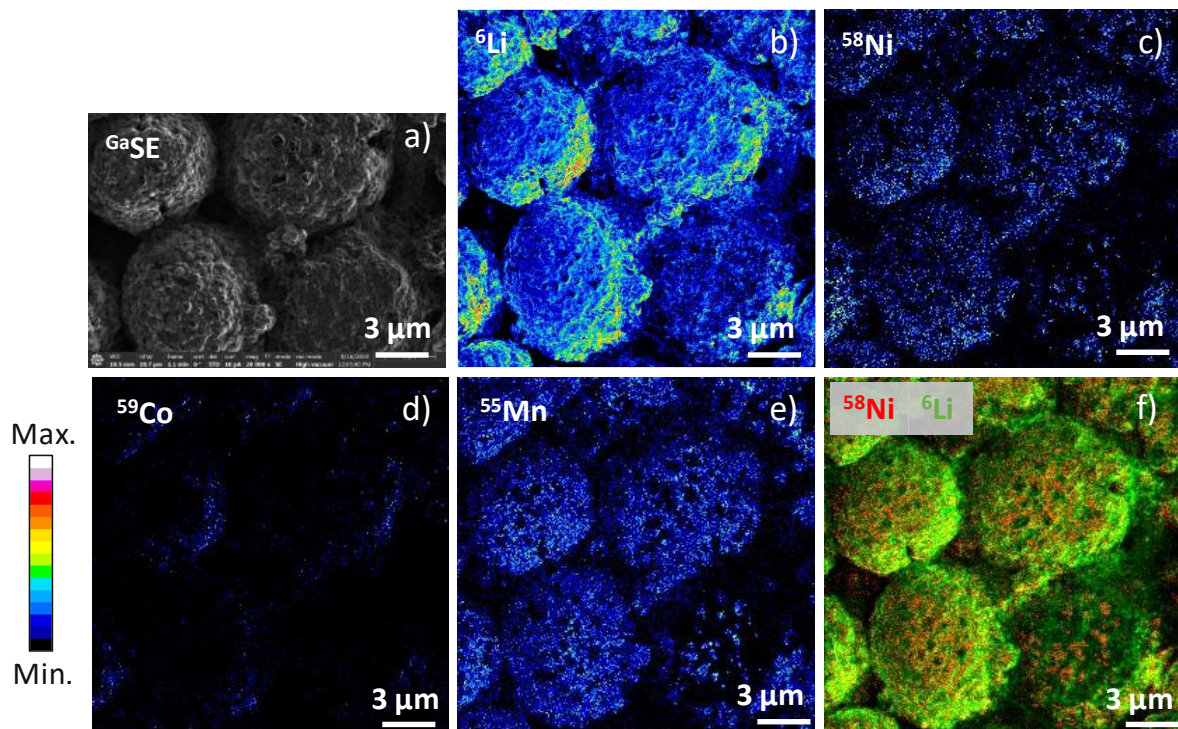


Figure 19: FIB-SEM-SIMS images of a LiNiCoMn cathode used for Li ion batteries. a) SE image (30 keV Ga<sup>+</sup>, 10 pA, 1536 pixels × 1092 pixels), b)-e) SIMS images (30 keV Ga<sup>+</sup>, 3 pA, 512 pixels × 512 pixels) of <sup>6</sup>Li, <sup>58</sup>Ni, <sup>59</sup>Co, and <sup>55</sup>Mn, respectively. f) Overlay of the <sup>6</sup>Li (green) and <sup>58</sup>Ni (red) images (Figure adapted from De Castro et al.).<sup>14</sup>

The cathode was first imaged with the Ga<sup>+</sup> FIB in SE mode. For SIMS analyses, the detectors were aligned with respect to the most abundant isotopes of manganese (<sup>55</sup>Mn), nickel (<sup>58</sup>Ni), and cobalt (<sup>59</sup>Co), while for lithium the less abundant isotope was chosen (<sup>6</sup>Li) to avoid saturation of the detector. In Figure 19 it is possible to see the degradation of the cathode, which was contact with the electrolyte before the analysis. Besides a granular topography, the distribution of manganese is quite homogeneous, while nickel and cobalt present a more heterogeneously distributed. A possible explanation for the degradation of the cathode could be the diffusion of nickel and cobalt into the electrolyte, creating a solid layer at the electrolyte interface.<sup>14</sup>

### 4.2.2.4 3D imaging

In this study, the thin film sample from section 4.2.2.2 was analyzed in the FIB-SEM-SIMS to create a 3D volume reconstruction (Figure 20 and Figure 21).

First, a cuboid structure was patterned using the Ga<sup>+</sup> FIB (Figure 20 a). Patterning of a structure will simplify during data processing the correction for positional sample stage drifts. For the SIMS analysis, detectors were aligned to the most abundant isotopes <sup>63</sup>Cu, <sup>27</sup>Al, <sup>52</sup>Cr, and <sup>69</sup>Ga and image frames were taken (Figure 20 b). The gallium signal was monitored for normalization purposes. After aligning all the images, the total counts were summed up and normalized with respect a linear function fitted to the gallium intensity to compensate for signal reduction resulting from an instrumental drift of the beam alignment, the sample stage position, or variation of FIB column parameters, because of the long acquisition time (12 h). A program written in MATLAB was used to create a depth profile (Figure 20 c) by taking the sum of all the counts for each image and by imposing the correct thickness of each layer (determined in an SC Ultra SIMS<sup>44,45</sup> instrument previously).

For 3D visualization, an algorithm in MATLAB was written to represent the SIMS image stack as a 3D point cloud. The SIMS images were first imported in MATLAB and 3D coordinates of each pixel of the image series were assigned. The pixels were then converted into a colored point cloud in a 3D space. The correct thickness of each layer was attributed to the 3D reconstruction. The point cloud was plotted and can be also exported as a text file, allowing it to import in other 3D visualization software (e.g., MeshLab).

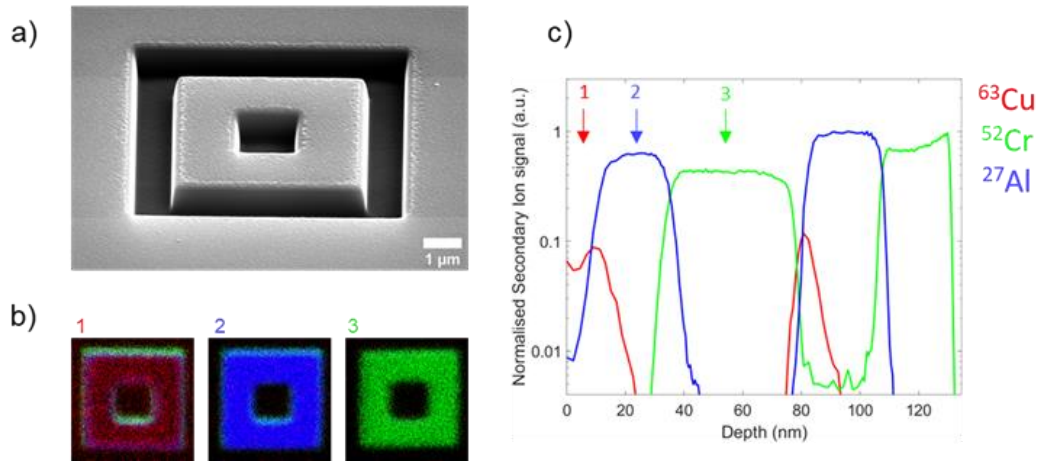


Figure 20: Depth profile reconstruction of a thin film sample from SIMS image frame integration FIB-SEM-SIMS instrument. a) Patterning of a cuboid structure. b) Exemplary SIMS images of the copper (red), aluminum (blue), and chromium layers (green). c) Reconstruction of a depth profile. The arrows indicate the depth where the SIMS images in b) were acquired. (Figure adapted from De Castro et al.).<sup>14</sup>

While this conventional method for 3D reconstruction in SIMS is appropriate for samples with well-defined layers, it becomes considerably more challenging for complex samples, e.g., with pronounced topography or/and with a mixed distribution of elements in the matrix. In this case, different elements and structures will sputter at different rates, due to a different sputtering yield of each material and locally different incidence angles of the primary ion beam. Thus, for this category of samples a more appropriate method for 3D topography reconstruction needs to be used. In this thesis, a photogrammetric methodology was developed, which will be presented in detail in chapter 2 section 1.

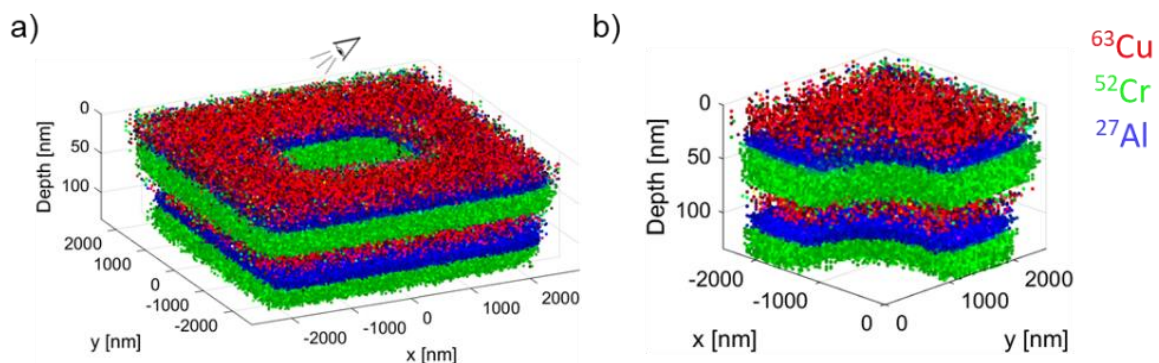


Figure 21: a) 3D volume reconstruction from serial SIMS images acquired on a thin film sample using the FIB-SEM-SIMS instrument. b) Cross-sectional view of the reconstruction (viewing direction indicated by a schematic eye in a) showing the distinguishability of each layer (Figure adapted from De Castro et al.).<sup>14</sup>

## 5. Problem statements and thesis objectives

As we discussed earlier (section 1.5), the signal intensity in SIMS depends (among others) on two fundamental processes: sputtering and ionization. Studying the sputtering yield for structures with a complex 3-dimensional morphology is crucial to understand sources of artefacts in SIMS imaging and to correct them. On the other hand, optimizing the ionization under non-reactive high density ion bombardment allows to achieve higher secondary ion yields and to improve both depth profile and image quality.

### 5.1 Sputtering

Surface sputtering phenomena in SIMS are highly complex processes strongly linked to sample topography can lead easily to confusion or even erroneous conclusions about signal intensity variations. Here the most common topographical imaging artefacts will be discussed and practical solutions to better evaluate and to correct these artefacts will be provided. The sputtering yield is a highly specific quantity and depends on probe and sample properties, including target material (e.g., chemical composition, density), the probe energy and mass, and sample topography related aspects, involving the incidence angle, edge effects, and sample height variations. In the following three paragraphs, we will briefly introduce these topographical aspects. More detailed discussions about the influence of the topography on the secondary ion intensity will follow in chapter 3.

The influence of the incidence angle on the sputtering yield has been studied extensively in the SIMS community.<sup>10,19,20,24,49</sup> For oblique incidence angles, atomic collisions are taking place in shallow regions of the surface, thus more surface atoms are emitted, compared to normal incidence. Therefore, the SI intensity changes purely due to variations in the sample topography, i.e. the local incidence angle. This effect becomes even more crucial in imaging, because the SI intensity changes locally (i.e., pixelwise) with the incidence angle.

Figure 22 a) shows model samples with two different slopes (40° and 60° incidence angle) and the schematic representations of the corresponding SIMS images, presenting a higher secondary ion intensity for the sample with the 60° slope (vs. the 40° case). Interpreting SIMS

data presents thus in many cases a challenge, as in many cases it is unclear whether signal variations result from material's concentration or topographic gradients.

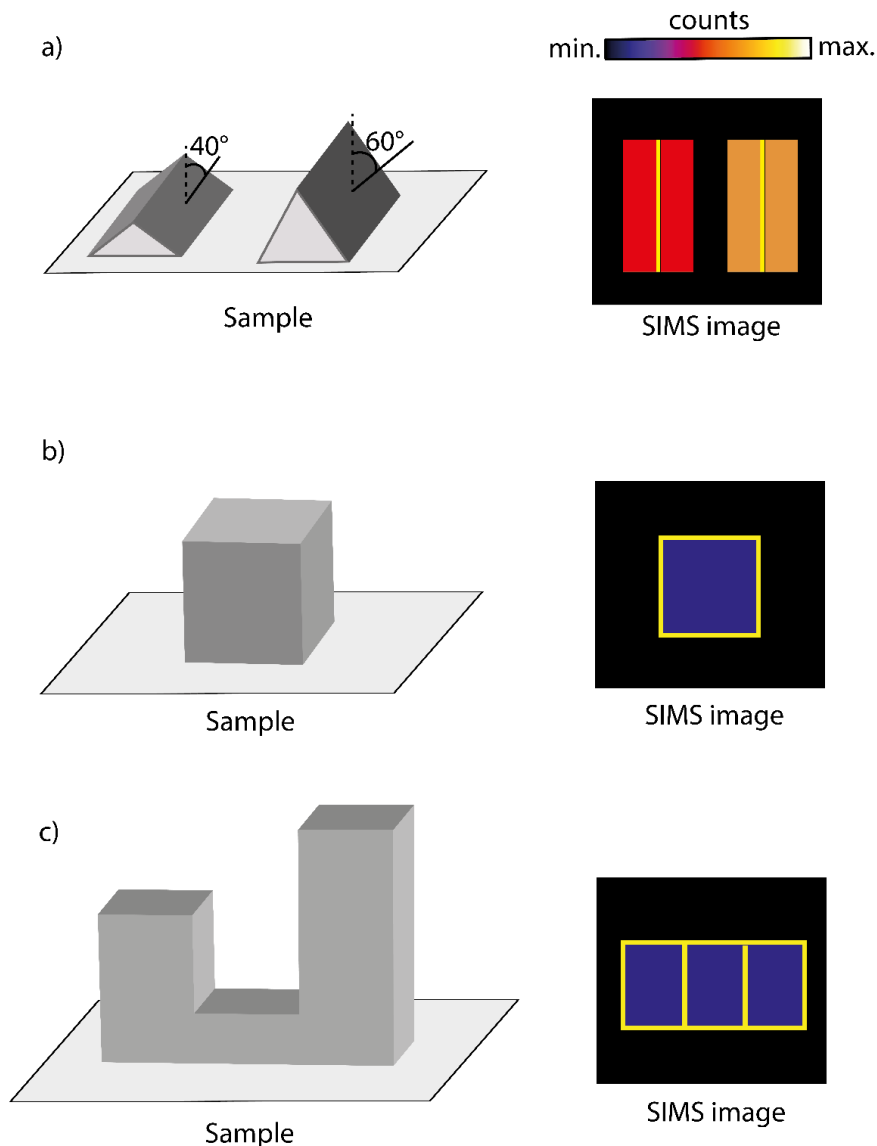


Figure 22: Common topographical artefacts in SIMS imaging, illustrated by showing exemplary samples (left column) and their corresponding (schematic) SIMS image in top view (right column). The signal intensity is color-coded with a colorbar. a) Sputtering yield variations due to different primary ion beam incidence angles. b) Preferential sputtering on sample edges (“edge effect”). c) Absence of sample height variation information in SIMS images.

The so-called “edge effect”<sup>34,50</sup> is responsible for increased SI intensity close to sample edges, due to preferential sputtering taking place on edges and borders. In fact, in these sites atoms

are chemically bound/surrounded by less matrix atoms, compared to a plain area sites, leading locally to a more effective surface erosion, thus sputtering yield. As shown in Figure 22 b), the SI signal on the edges of the cube is much higher than on the plain area, which is purely due to the edge effect. When analyzing SIMS images, it is thus crucial to know the exact 3D topography to identify and distinguish between concentration or topography gradients (or even both at the same time).

Understanding a 2D SIMS image (in top view) of a sample with a complex 3D topography presents a very challenging task. Since the primary ion beam is sputtering the sample in the shallowest region of the surface, the surface topography information is not captured in the image. The example in Figure 22 c) shows that, while the sample has a 3D topography, the latter is not represented in the SIMS image, as just by inspection of the SIMS image it is not possible to estimate local height changes in the sample.

Imaging samples with a highly pronounced topography leads to the appearance of at least one of the three described artefacts above. An accurate surface reconstruction of the sample will allow to understand their extend (and even to correct them). Previously, Atomic Force Microscopy (AFM) has been widely used for 3D surface reconstruction. In this case, AFM analyses were made before, after,<sup>51,52</sup> but also in-between<sup>53,54</sup> SIMS measurements to perform a topography correction. However, working on high aspect ratio particles,<sup>55</sup> especially in the micrometer size range and above, becomes very challenging for AFM, because of the tip collision with the sample using too high scanning speeds. Additionally, concave and very steep structures cannot be represented accurately, since the AFM tip is scanning vertically over the surface.

A recently proposed solution is photogrammetry which has been widely used as a 3D surface reconstruction method from optical images and is not restricted in terms of the aspect ratio of the analyzed structure. Recent studies were focusing on the development of workflows for 3D surface reconstruction from microscopy images and have successfully shown the applicability of the method and commercial photogrammetry software for high-resolution SE images.<sup>56,57</sup>

The first objective of this thesis is to develop and use a photogrammetry workflow for 3D surface reconstruction and to correlate these reconstructions with analytical information

from SIMS (referred here as the 3D + 1 method), allowing to enhance the visualization of samples as well as to study correlatively intrinsic properties of the sample. The second objective is to use the 3D + 1 workflow to study changes of the sputtering yield with respect to the incidence angle first on model samples and then on concrete examples of SIMS images.

## 5.2 Ionization

The second fundamental process in SIMS is related to the ionization. During the sputtering process ionization of a fraction of the sputtered atoms takes place. The ionization probability depends on the chemical environment and the reactivity of the implanted primary ion.<sup>17,30</sup>

High brightness ion sources, such as the GFIS (with a brightness of  $10^9 \text{ A cm}^{-2} \text{ sr}^{-1}$ ) allow to attain very small probe sizes.  $\text{Ne}^+$  primary ions produced in a GFIS, as in the case for the HIM-SIMS, provide both adequate sputtering yields (on average 1 atom/ion)<sup>58,59</sup> and allow to achieve high imaging resolution ( $< 20 \text{ nm}$ , see section 4.1.2.3). However, using non-reactive primary ions comes with a lower ionization probability, compared to reactive ions, e.g.  $\text{Cs}^+$ ,  $\text{O}_2^-$ . Moreover, because of the small probe and voxel size only a very small amount of atoms is sputtered.<sup>18,32,59</sup> Reactive gas flooding is a known method to strongly enhance the ionization probability and presents a practical solution to increase SI yields with non-reactive primary ion sources. Flooding the sample with a reactive species changes the chemical state of the analyzed surface and it has been shown previously that it can have a significantly positive effect on the SI yield, by up to several orders of magnitude.<sup>32,59</sup>

Oxygen flooding has been used to enhance the detection of electropositive elements<sup>60</sup> for depth profiling<sup>61–63</sup> and imaging<sup>64</sup> applications on SIMS systems with lower bombardment densities as well as lower brightness ion sources compared to the GFIS (e.g., duoplasmatron<sup>65</sup> or liquid metal ion sources).<sup>64</sup> The effect of oxygen flooding on SI detection combined with a GFIS under high bombardment densities (of up to  $10^{20} \frac{\text{ions}}{\text{cm}^2 \cdot \text{s}}$ ) of non-reactive primary ions has not been studied in-depth in the past.

Thus, the third objective of this thesis is to use the HIM-SIMS instrument to investigate the improvement of useful yields by oxygen flooding under high  $\text{Ne}^+$  current densities using a GFIS and to study the stability of the GFIS at high pressure conditions.

## 6. Chapter summary

In this section, a brief overview of the SIMS technique and instrumental parts were given. Two microscopes, a HIM and a FIB-SEM, both equipped with SIMS add-on systems developed at LIST were introduced. Their performances in terms of mass, depth, and spatial resolution, and with the possibility to correlate EM and SIMS in a single instrument the potential of these FIB-platforms for correlative microscopy was demonstrated.

While in a first step we have shown “traditional” correlative methodologies and applications of SIMS, we will present in the following a novel methodology allowing to reconstruct the 3D sample topography and to correlate this information with analytical maps from SIMS. This methodology will allow us then to study variations of the sputtering yield resulting from topography related changes of the primary ion beam incidence angle.

## Chapter 2: Methodological development for surface reconstruction

### 1. Workflow description

#### 1.1 Photogrammetry

Photogrammetry has become a common method to 3D reconstruct objects, monuments, and buildings in architecture, civil engineering, and geography.<sup>66</sup> By shape capture, size, and volume analysis, photogrammetry cannot only be used for better visualization of objects, but also to study topographical changes with respect to time, e.g. for ageing of buildings<sup>67</sup> or soil erosion.<sup>68</sup>

A large number of photographs (varying typically from a few tens taken to several hundreds) covering in the optimal case most of the outer areas of the object are taken by hand or by drones around the object of interest at varying polar and azimuthal angles. From the serial 2D images, photogrammetry software solutions allow to reconstruct the surface of the object in 3D and to observe the reconstruction at all angles and magnifications. An example of a photogrammetric reconstruction is shown in Figure 23.

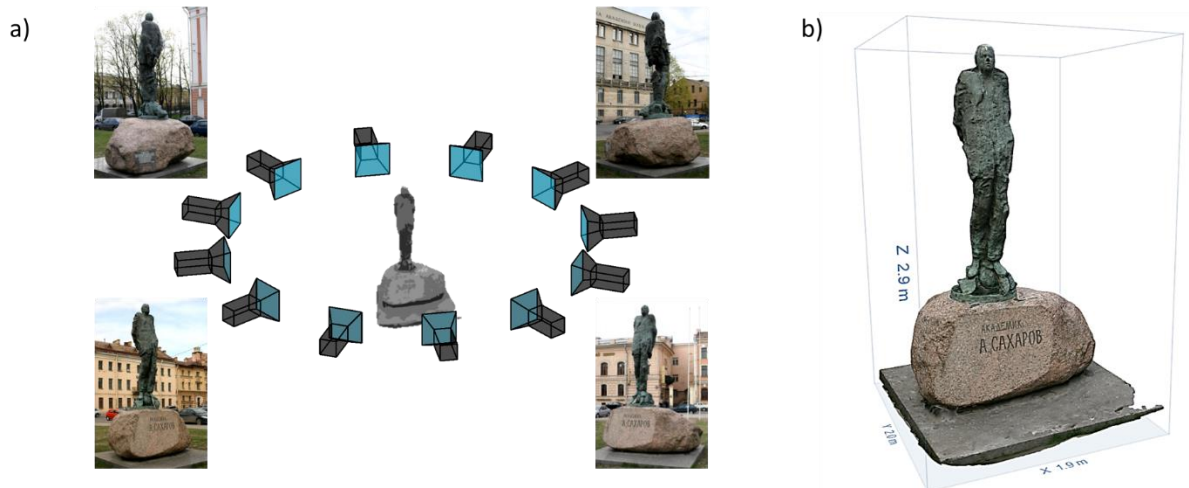


Figure 23: Photogrammetric 3D surface reconstruction of a statue. a) Sequential image acquisitions around the statue with exemplary images shown here.<sup>69</sup> b) 3D surface reconstruction and visualization in the photogrammetry software (here: Autodesk ReCap Photo).

In the photogrammetry software, after implementation of the images, features are searched (for instance using the SURF algorithm)<sup>70</sup> and matched throughout all the images (Figure 24). Based on this, the software estimates the original positions at which each image was taken with respect to the object, by computing the so-called fundamental matrix. In a second step, from the pixel coordinates of the matched features the 3D points in the world coordinates are calculated. In the simplified case of a stereoscopic system of two parallel, spatially translated images, the calculation of the 3D coordinates of the matched points is brought down to a simple geometrical calculation.<sup>71</sup> For more complex systems with cameras rotated and translated in space with respect to one another, a triangulation process is performed: for a given feature matched in two (or more) images, the 3D intersection point of the rays projected from the camera position to the matched image points is calculated. Mathematically speaking, this triangulation process comes back to solve a system of linear equations describing the translation from the 2D pixel coordinates of the matched features to the world coordinates of the corresponding 3D point in space with given camera positions using the camera matrix derived from the fundamental matrix.<sup>72</sup> A complete mathematical description of the triangulation process in the context of photogrammetric surface reconstruction is provided by Hartley and Zisserman,<sup>66</sup> and Hartley and Sturm.<sup>72</sup>

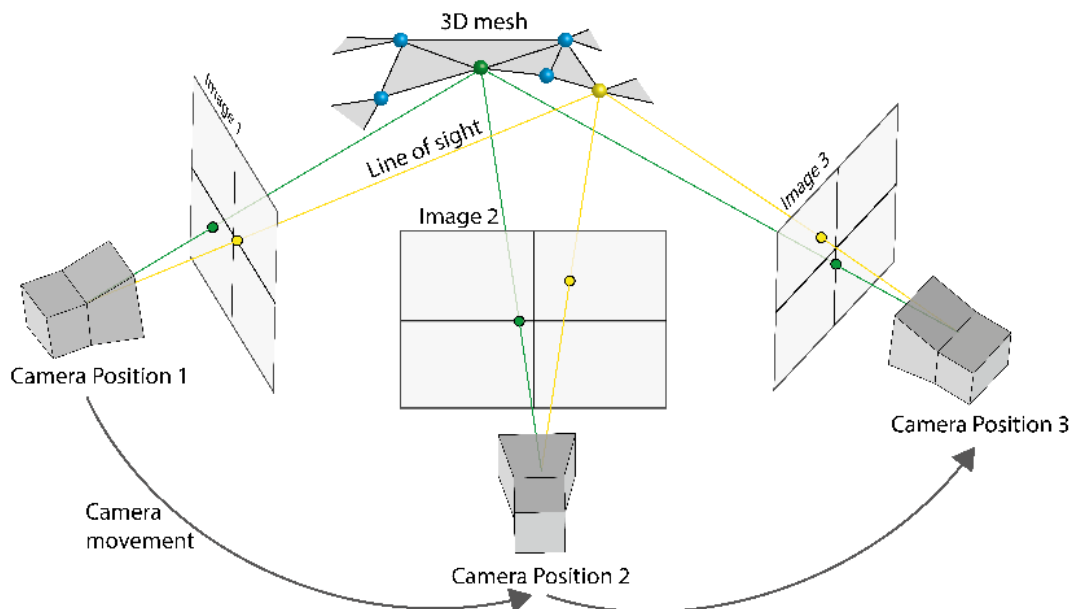


Figure 24: The basic working principle of a photogrammetry software. The reconstruction algorithm is first searching for features through the images acquired around the object. Then it is matching them and by performing a triangulation process a 3D point cloud is created.

*Points are connected to create a mesh and a texture is projected onto the 3D model. Matches on at least two images are required to perform triangulation.*

The triangulation process is repeated for all the matches allowing to create a 3D point cloud from the 2D matches in the images and the estimated camera position. Eventually, based on the point cloud a mesh (i.e., surface) will be created. A texture generated from the matched images is projected onto the reconstructed mesh.

While photogrammetry was originally developed to reconstruct macroscopic objects, its principles have started to be successfully applied in electron microscopy for micro- or even nanosized objects. First, photogrammetry workflows were applied using optical, followed by scanning electron,<sup>56</sup> then by helium ion microscopy,<sup>73</sup> mainly for demonstration of the methodology. Additionally, by correlating 3D surface reconstructions from this photogrammetric approach with SIMS images on the same ROI, Vollnhals and Wirtz<sup>73</sup> have provided a 3D + 1 workflow (projection of SIMS images on 3D SE surface reconstructions) demonstrated on indium phosphorus particles and gave an outlook to study the sample's chemical distribution and structure correlatively using a single representation.

In the following sections, we will present the 3D + 1 reconstruction workflow adapted to micro- and nano-sized objects and the application of this method to case studies with a focus on sediments and soils. In fact, in the framework of this thesis, a collaboration between the LIST and the Research Department Life Science Systems at the Technical University of Munich (TUM), Germany, with specialization in soil biogeochemistry was initiated. Hence, a strong focus on soil sample analyses was made throughout the PhD project, which lead to multiple collaborative measurements on the HIM-SIMS at the LIST and a CAMECA NanoSIMS 50L<sup>74-76</sup> instrument at the TUM (see also correlative imaging study in the Appendices).

## 1.2 Data acquisition

In the framework of this thesis, mainly the HIM-SIMS instrument was used for photogrammetric SE reconstruction, but the methodology is applicable to any electron microscope with a tiltable and rotatable sample stage. For photogrammetric 3D SE

reconstruction, SE images are taken in a series of sample stage rotations in a tilted position (Figure 25 a). The rotational stage movements are equivalent to a camera movement, here the ET detector (position fixed in the microscope), around the ROI (Figure 25 b). Optimal results were achieved when two series of images were recorded at two different polar angles (typically  $45^\circ$  and  $36^\circ$ ), hence two different tilt angles of the stage (the latter polar angles corresponding to  $45^\circ$  and  $54^\circ$  stage tilt). Thus, features below overhanging structures are covered as well, as they might not be exposed to the detector at a single stage tilt angle.

Subsequently, the stage is tilted back to a horizontal position, as for instrument design reasons, SIMS acquisitions can only be performed in the horizontal stage orientation. After finding back the same ROI, SIMS images are acquired after inserting the SIMS extraction box and aligning the detectors to the chosen masses.

Optimal reconstruction results were obtained by acquiring SE images using a 25 keV  $\text{He}^+$  primary ion beam with currents of 1 pA – 2 pA with high quality image parameters, choosing  $2048 \times 2048$  pixels with a counting time of 10  $\mu\text{s}/\text{pixel}$ , and averaging 4 lines. (HIM-)SIMS image analyses parameters were chosen depending on the application, but in most instances a 25 keV  $\text{Ne}^+$  primary ion beam with currents ranging from 4 pA to 10 pA with at least 2 ms/pixel counting time was used.

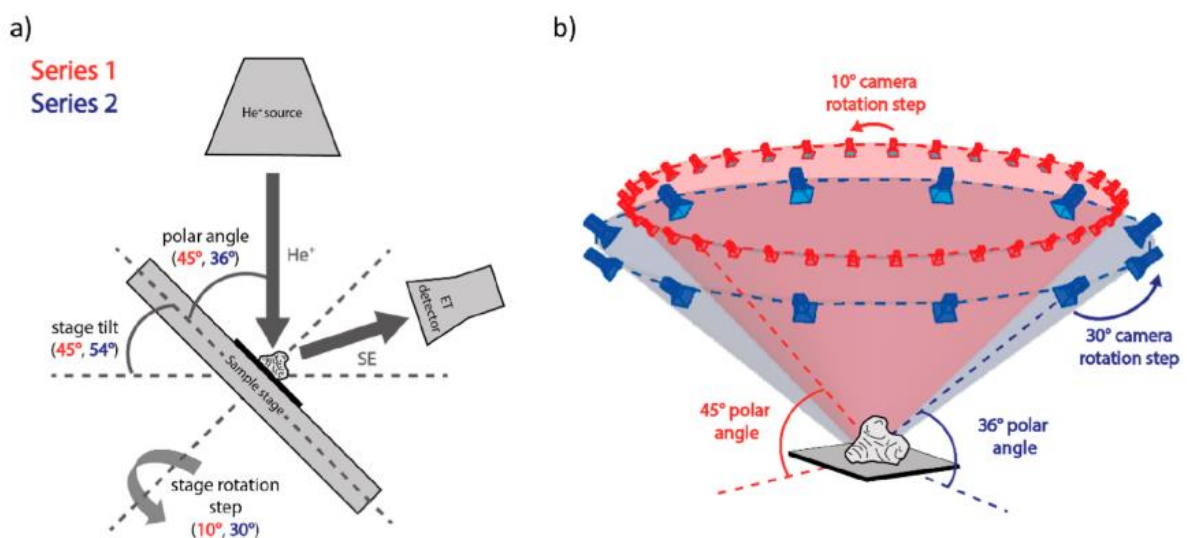


Figure 25: Workflow for photogrammetric SE image acquisition in a HIM. a) The sample stage is tilted at different angles (here  $45^\circ$  and  $54^\circ$  stage tilt, corresponding to  $45^\circ$  and  $36^\circ$  polar angle). Image acquisitions are performed in two series by varying the stage rotation in each case. b) Visualization of the “camera”, respectively ET detector positions at which SE images are taken with respect to the sample (Figure from Ost et al.).<sup>77</sup>

### 1.3 3D SE reconstruction

For 3D SE reconstruction, previously recorded SE images are implemented into a photogrammetry software.

For this work, two commercial software solutions were used: Autodesk ReCap Photo and 3DF Zephyr Pro. In Autodesk, the reconstruction process is fully automatic, i.e. images are implemented and the software gives a 3D surface reconstruction without further configuration options (e.g., camera focal distance estimation or feature density in the image). In 3DF Zephyr Pro, the reconstruction is done step-by-step while having the possibility to change parameters, such as camera focal distance, expected feature density, density of the desired point cloud. For instance, the density of the final point cloud can be reduced to save time or increased to obtain a more accurate reconstruction.

Images presenting a high amount of surface features are more suitable for photogrammetric 3D SE reconstruction, as they have more matchable features, thus allowing to create more 3D points. For instance, samples with a high surface roughness, unevenness and/or inhomogeneities give images with more features than samples with relatively flat and homogenous surfaces. Blurry, noisy images or varying brightness/contrast settings should be avoided, as this will lead either to wrong matches or a very low amount of detected features, i.e., noise/artefacts in the 3D SE reconstruction. Thus, to produce accurate 3D SE reconstruction high-quality images are crucial to ensure a high amount of detected and matched features with low amount of noise to reduce the number of wrong matches. In preliminary reconstructions, it was shown that on average at least 60 features should be detected per image and 40 matches from one image to another to obtain a meaningful 3D SE surface representation. Yet, a distorted reconstruction can be obtained, due to erroneous camera position estimation, i.e., wrong determination of intrinsic camera parameters, including focal length, optical center, lens distortion. In the case of images taken with an optical camera, these parameters are well known, whereas for electron microscopy images these have to be estimated, which is done automatically by the photogrammetry software.<sup>78</sup>

It is worth noting that in many cases more than one trial with different intrinsic camera parameters is necessary to obtain an accurate 3D SE reconstruction. This can be done in 3DF Zephyr Pro, while Autodesk ReCap Photo does not have this option and the user is fully reliant

on the automatic performance of the software. In addition, highly concave structures introduce artefacts in 3D SE reconstructions as below big overhangs information from images cannot be recorded.

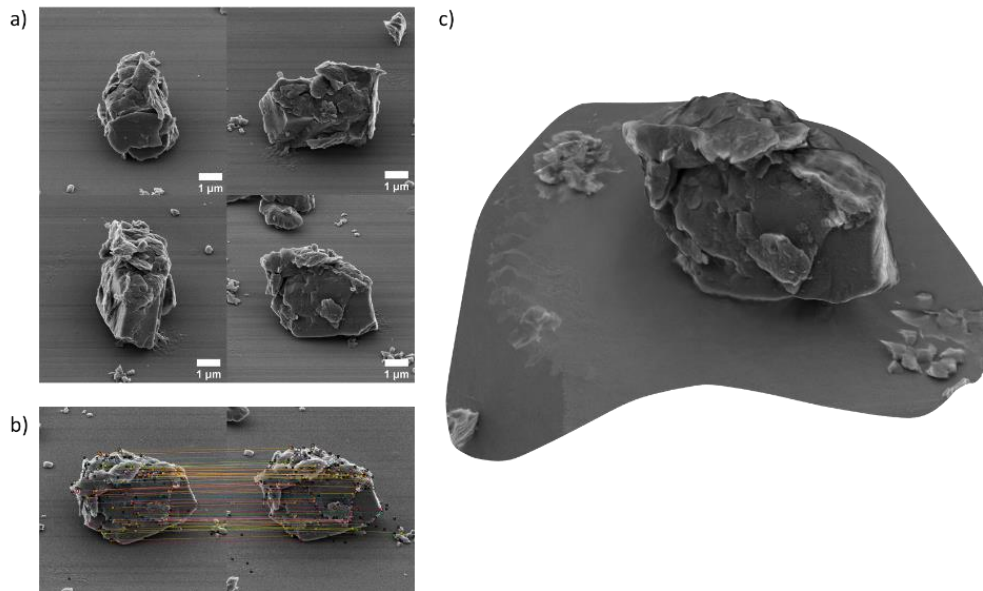


*Figure 26: Example of the 3D SE reconstruction method illustrated on a soil microaggregate. a) Exemplary SE images taken around the microaggregate (48 images in total). b) Illustration of the image feature (marked with colored dots) detection and matching process (features linked by colored lines from one image to another) between two sequential SE images. c) Capture of the 3D SE surface reconstruction (reconstruction software used here: Autodesk ReCap Photo).*

#### 1.4 Photogrammetry software performance evaluation

Since the result of a 3D SE surface reconstruction is purely reliant on the performance of the photogrammetry software, assessing the quality of a 3D SE surface reconstruction is not evident. In order to investigate the sources of artefacts of the photogrammetric 3D SE reconstruction and to find a metric to evaluate the quality of a reconstruction, a simplified mathematical algorithm for 3D reconstruction was created. The algorithm was written in MATLAB and built in a very similar way as the working principle of the commercial software, including the reconstruction steps mentioned previously (i.e., feature detection and matching, etc.). However, the main differences are that the algorithm allows to have full control on each reconstruction step and that the geometric positions, at which the images of the object are taken, are implemented exactly by the user, while the commercial solutions

perform a numerical estimation of the camera positions.<sup>78</sup> Here a summarized description of the algorithm will be provided. More details on of this algorithm can be found in the appendix. For this study, images of a simple geometric structure created in a virtual 3D space in MATLAB, in this case a cube, were used to create surface reconstructions using the MATLAB reconstruction algorithm and both commercial software, Autodesk ReCap Photo and 3DF Zephyr Pro.

In the following, 3D reconstruction of the cube was performed with the MATLAB algorithm, first with a manual feature detection/matching approach and then with a fully automatic one. In order to create the virtual cube, in MATLAB six surfaces were built in a 3-dimensional space forming the virtual cube. A texture was added on its surfaces for better visual orientation. The cube was rotated stepwise with respect its central vertical axis and four “virtual” images were produced at a polar angle of  $45^\circ$  (with respect to the lower base of the cube) and specific azimuthal angles ( $10^\circ$ ,  $20^\circ$ ,  $190^\circ$ ,  $200^\circ$ ) around the cube. Thus, each side and corner of the cube is captured by at least two of these images (Figure 27 a). The 2D xy-pixel coordinates of the cube’s corners for each image, i.e., eight corners per image, were determined manually and a matrix with the matched feature coordinates created. The matched 2D xy-pixel coordinates were implemented then into the algorithm, as well as the exact angle positions at which the used images were taken. Additionally, the coordinates of the cube’s borders (seven additional points per border) were determined from linear interpolation of the corner’s coordinates. A triangulation process, allowing to go from matched 2D pixel coordinates to 3D points, for each corner and all the border points of the cube was performed for both pairs of images. The 3D reconstructed point cloud was plotted (Figure 27 b). The angles between the borders were calculated, giving a close to  $90^\circ$  angle on average. This shows that if “camera” positions are given exactly and no post-data treatment processes are implemented, are performed, a close to perfect 3D reconstruction can be obtained, as at this point the process is reduced to linear algebra calculations. A slight deviation from  $90^\circ$  (of  $\sim 0.1\%$ ) of the side angles of the cube is resulting presumably from a slightly erroneous determination of the corner coordinates which were typically spread over an area consisting of a few pixels.

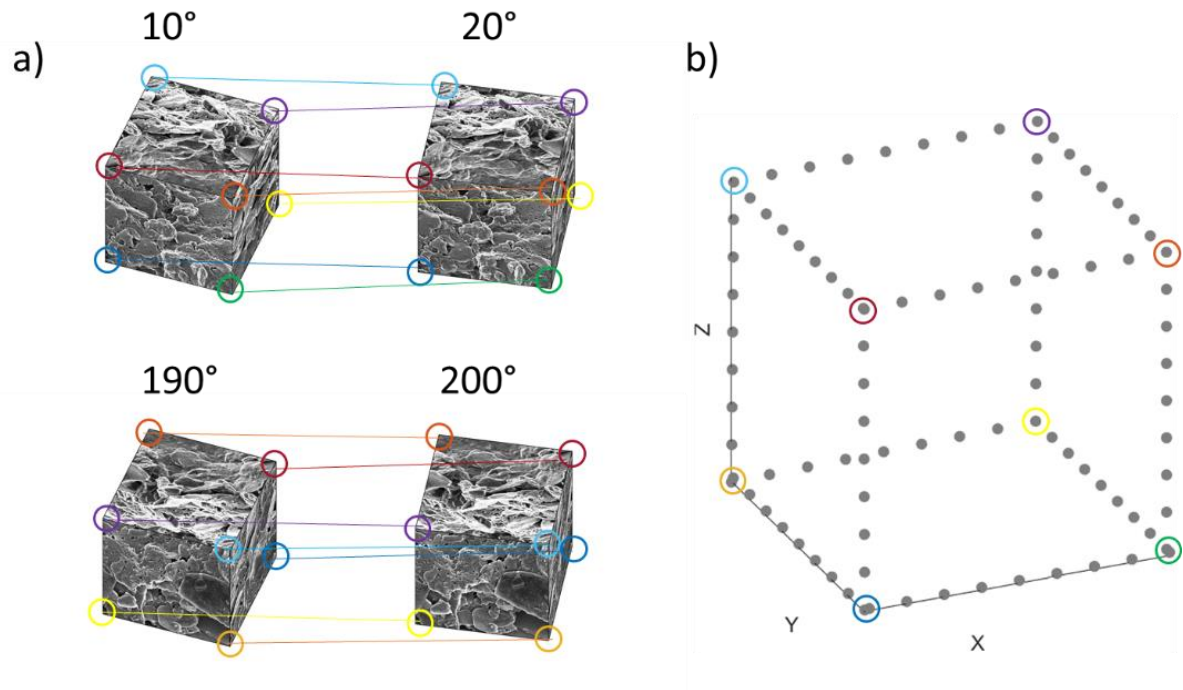
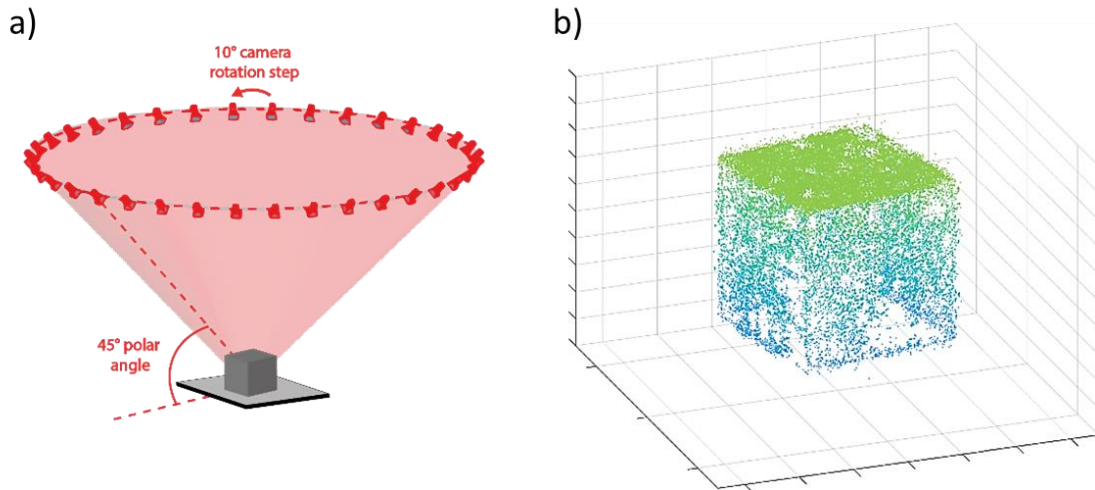


Figure 27: 3D reconstruction of a virtual cube from four images using a photogrammetric simulation algorithm. a) Manual determination of the pixel coordinates of the corners of the 4 images and their matching (marked with colored circles and lines). b) 3D point cloud reconstructed from the manually matched corner coordinates in the images and the angular camera position at which the image was taken. The corners matched in a) are marked with colored circles.

In the next step, the feature detection and matching process was automatized to approach the actual performance of a commercial photogrammetry software. A texture (overlaid with the 3D cube) was needed in this case to allow the algorithm to detect and match features automatically across the images. In total, 36 images were created showing the virtual cube at a polar angle of  $45^\circ$  and every  $10^\circ$  of azimuthal rotation (Figure 28). The exact “camera” positions were implemented, features were searched automatically (using here the SURF algorithm),<sup>70</sup> and the detected features were matched for consecutive image pairs in a for-loop. The triangulation process for each match of the considered image pair was performed in a loop to calculate the 3D coordinates of each matched feature, thus a 3D point cloud was reconstructed and plotted in space. By linear interpolation of the point cloud, connecting all the 3D points among each other with a surface, a 3D surface reconstruction was created.



*Figure 28: Photogrammetric 3D reconstruction of a virtual cube. a) Creation of 36 images around the cube at a polar angle of 45° and 10° azimuthal rotation steps (texture added to the cube is not shown here for simplicity). b) Plot of the 3D point cloud reconstructed in from the images created in a).*

It is worth noting that in order to simplify the future use of the reconstruction algorithm a simple graphical user interface was written in MATLAB (Figure 29). The user can first choose the geometrical structure to be reconstructed (cube or pyramid, with or without planar base). Then sequential 2D images around the chosen textured structure (45° polar angle, 10° azimuthal rotation step) are created and saved in the current directory. The user can choose then the accuracy of feature point detection (to speed up or slow down the process depending on the desired reconstruction quality). Once the reconstruction process is started the progress can be followed in % in the progress bar window. The reconstructed point cloud is then plotted in 3D and can be exported as a text file. The user has also the possibility to import and plot an old point cloud text file and plot it or proceed to the next step. In the final step, the reconstructed (or imported) point cloud can be converted into a surface by linear interpolation, while the accuracy can be also chosen by the user. The final 3D surface is plotted and can be exported as an .stl file. Further development of the algorithm with an exact implementation of camera positions for more accurate 3D SE reconstruction from microscopy images could be a subject for future work.

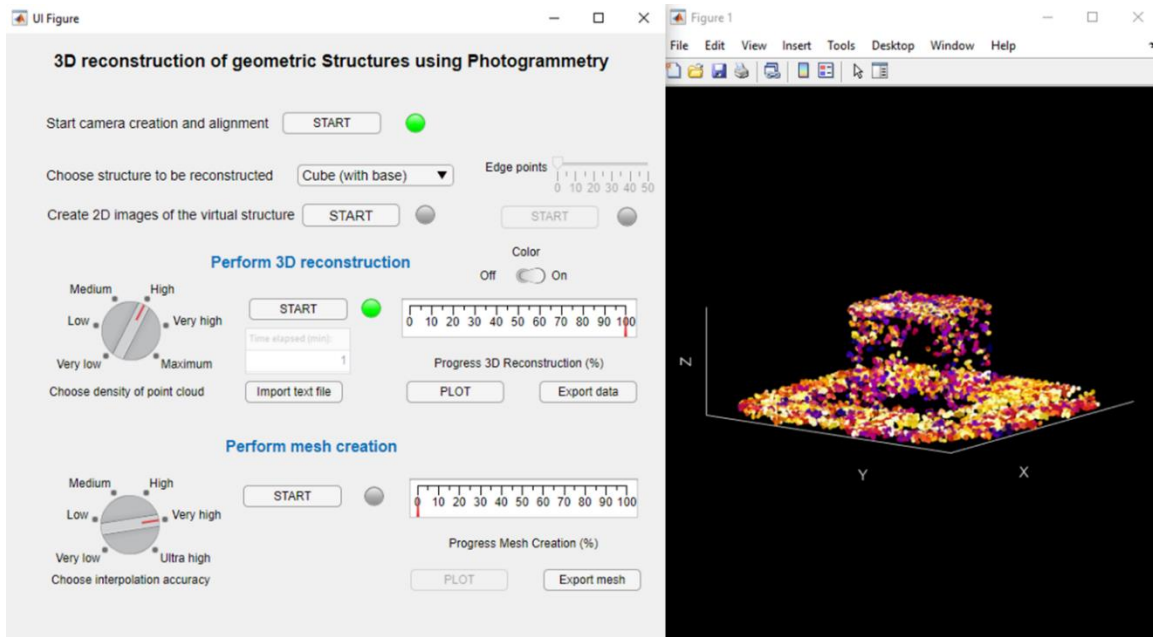


Figure 29: Capture of the graphical user interface created in MATLAB for photogrammetric 3D reconstruction of geometric structures. Here a point cloud is plotted obtained from 36 images of a virtual textured cube with a planar base.

The 36 images of the virtual textured cube created previously were implemented into the commercial photogrammetry software, Autodesk ReCap Photo and 3DF Zephyr Pro (with “default” quality options) and 3D surfaces of the cube created.

To assess the accuracy of the reconstructions, their deviations in length and height from the perfect cube were calculated. For 3DF Zephyr Pro, deviations of 25.1 % for the length and 24.3 % for its width were found, while for Autodesk ReCap Photo 1.5 % (length) and 2.5 % (width) were obtained. For the reconstruction from the MATLAB algorithm, though its surface contained a high amount of noise, a deviation of less than 1 % was measured.

The fairly high deviations for the reconstructions from the commercial solutions can be explained here by slightly misaligned camera positions. Since for the simulation algorithm the camera positions are implemented exactly, the overall reconstruction from the MATLAB algorithm is here more accurate than those from the commercial solutions and the commercial solutions. The latter are performing a numerical estimation of the camera position, which can be inaccurate in particular due to the high amount of noise in EM images. Camera misalignment can lead to local shrinkages or distortions in the reconstruction. Moreover, it is worth noting that, though noise reduction is more effective in the commercial

solutions compared to the simulation algorithm, it cannot be excluded that reconstruction artefacts can arise from removal of 3D points, which were erroneously identified as noise.

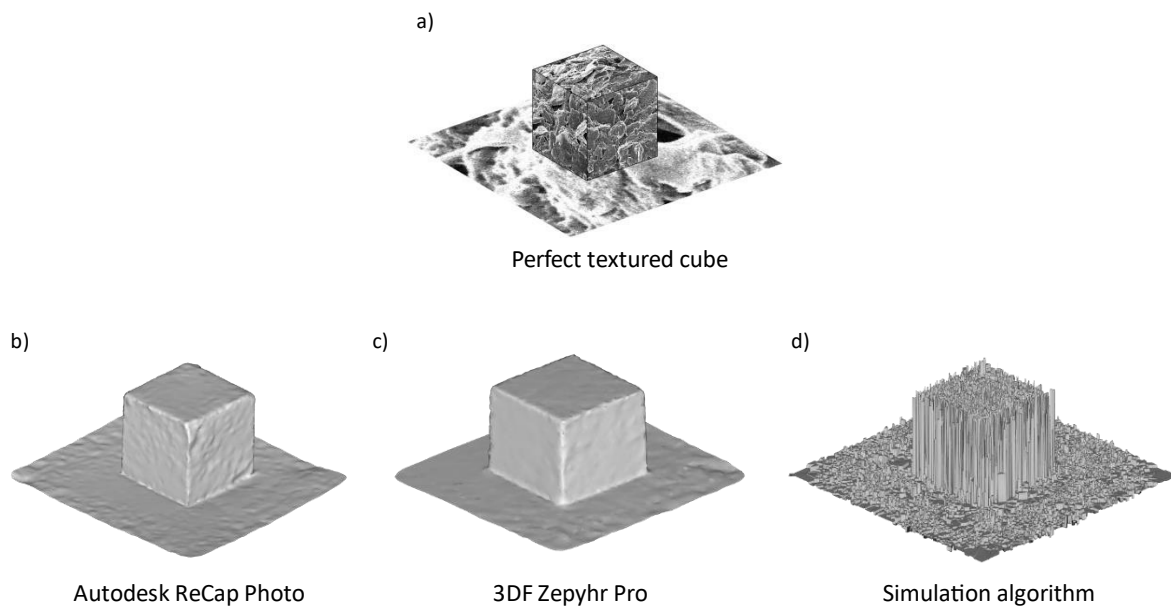


*Figure 30: Photogrammetric 3D reconstruction of a cube. A virtual cube with a planar basis was created in a). A texture was added to the cube to enhance the feature detection/matching process. Virtual images were taken at a polar angle of  $45^\circ$  and azimuthal rotation steps of  $10^\circ$  with respect to the cube. These 36 images were implemented into two commercial photogrammetry software solutions, Autodesk ReCap Photo (b) and 3DF Zephyr Pro (c), and (d) a simulation algorithm developed in MATLAB (Figure from Ost et al.).<sup>77</sup>*

Although in this simulative study the MATLAB algorithm produced overall a more accurate reconstruction of the cube than the commercial solutions, the commercial software offers a much more practical solution to perform routinely 3D reconstruction from EM images for the following reasons. First, for the simulation algorithm cameras positions need to be implemented exactly, which are not known since during the sequential HIM SE acquisitions a readjustment of the FOV is necessary to center the ROI in the image. This recentering of the FOV comes with slight deviations (minor translational shifts) of actual camera position from the designated ones (e.g.,  $45^\circ$  polar angle,  $10^\circ$  rotation steps). Therefore, a numerical estimation of the camera positions, as in the case of the commercial software, is needed to determine the actual ones. Secondly, as one can clearly see Figure 30, 3DF Zephyr Pro and Autodesk ReCap Photo offer more effective noise reduction performance, as the reconstructed surface of the cube is much smoother than in the case of the reconstruction

from the MATLAB algorithm. The key characteristics and accuracy of the reconstructed cube from the simulative study on the cube are summarized in Table 1.

*Table 1: Comparison of the key features and performances of the commercial photogrammetry software and the simulation algorithm.*

<b>Features</b>	<b>Autodesk ReCap Photo</b>	<b>3DF Zephyr Pro</b>	<b>Simulation algorithm</b>
Reconstruction process	fully automatic	stepwise	stepwise
Camera position estimation	automatic	automatic	implemented by user
Noise/outlier reduction	strong	strong	weak
Mesh reconstruction	smooth	smooth	noisy
Reconstruction time	< 15 min	< 15 min	≈ 1 h
<b>Cube reconstruction</b>			
Deviation from cuboid:			
Length	1.5 %	25.1 %	< 1 %
Width	2.5 %	24.3 %	< 1 %

In summary, to estimate the accuracy of a 3D SE reconstruction it is important to check whether the estimated camera positions correspond to the designated angles at which the images were taken. For instance, if an image series was taken at a microscope stage tilt angle (e.g., 45°) with specific sample stage rotation steps (e.g., 10°), by comparing the numerically estimated camera positions with the angles applied to the microscope stage, in many cases a reliable guess about the reconstruction accuracy can be done. Hence, if the estimated camera positions correspond from the designated ones, this indicates that the reconstruction accuracy is high. The quality can be further improved by adapting noise reduction parameters. It is worth noting that for all the reconstructions presented in this work, it was checked whether the cameras were aligned correctly and hence correspond to their designated positions.

## 1.5 3D + 1 reconstruction

In the previous sections, we discussed the 3D surface reconstruction from multi-view SE images and acquisition of chemical maps from SIMS on the same ROI. Correlating 3D topographic and SIMS information provides a better visualization of complementary data as well as a deeper understanding about the sample (upcoming section 2 of this chapter) and allows to study topography related local changes in the sputtering yield (discussed in chapter 3). To correlate both, the SIMS image is projected onto the 3D representation, giving a 3D + 1 (here also referred as “4D”)<sup>77</sup> surface reconstruction.

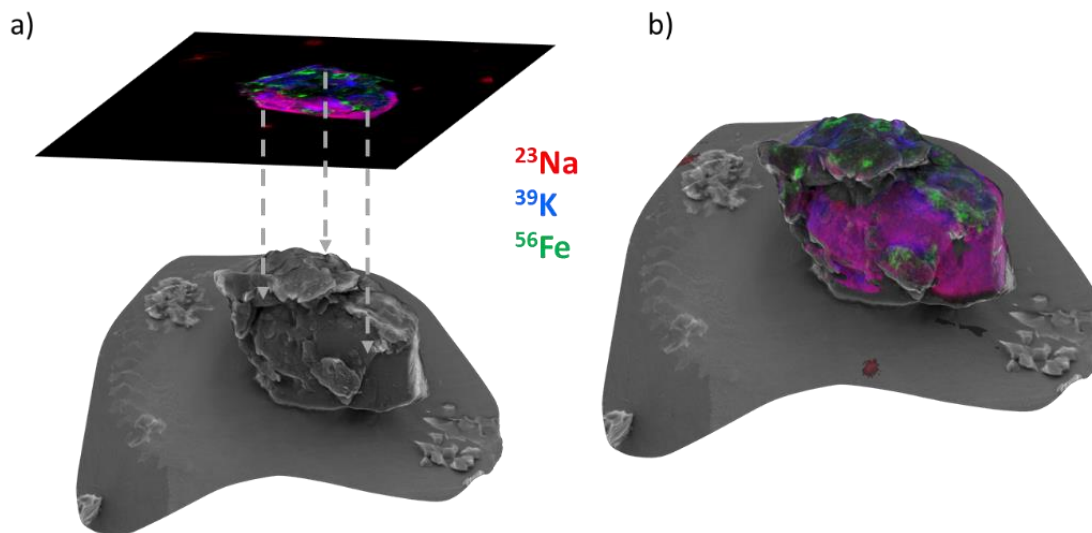


*Figure 31: Illustration of the 3D + 1 overlay to create a 4D surface reconstruction for a soil microaggregate. The SIMS RGB image (red: sodium-23, green: iron-56, blue: potassium-39) and the 3D SE model were aligned using 20 2D-3D correspondences. A top-down projection (indicated by arrows) is performed to create a new texture containing both SIMS and SE information.*

Alignment and projection of the SIMS image onto the 3D reconstruction is done in the open-source software called “MeshLab” which is a user-friendly solution for 3D surface visualization and processing. To align the (2D) SIMS image with respect to the 3D model, 2D-3D correspondences are chosen manually in the software, requiring about 20 correspondences to achieve satisfying alignment. The aligned SIMS image is then projected on the 3D SE reconstruction to create a new textured model containing both SE and SIMS information. The

development of an algorithm and graphical interface for automatic alignment and overlay of the SIMS image with the 3D SE model could significantly reduce the processing time and could be a subject for future investigations.

It is worth noting that creation of single 4D surface reconstruction takes on average about two working days, as half a day is needed to acquire the sequences of SE images around the ROI, one day to perform (HIM-)SIMS imaging and another half a day for data processing.

## 2. Application of the 3D + 1 method for sediments and soils

Once the 3D + 1 superposition has been performed, the final 4D surface model (with or without SE texture information) can be exported as a textured surface or as a colored point cloud (with its normal vector information for each 3D point) for instance for further numerical analyses in MATLAB.

The 3D + 1 method presents several advantages compared to conventional 2D image correlation. While in this section we will focus on using this method to study materials' transformation processes for sediments and soils, in chapter 3 the 3D + 1 method will be used to study local changes in the sputtering yield.

### 2.1 Diatoms

Diatoms are found in marine, estuarine and freshwater ecosystems, inhabiting a wide range of environmental conditions. Because they are found in almost any place that has, or had, water, and due to their efficient photosynthetic processes, they are important players in the global cycling of carbon and oxygen. They are responsible for around one fifth of the global photosynthesis activity.<sup>79</sup> Their cell walls ("frustules") consist of amorphous hydrated silica ( $\text{SiO}_2 \cdot \text{H}_2\text{O}$ )<sup>80</sup> and are typically laced with hole-like structures allowing nutrient and waste exchange. Among diatoms many different geometries can be found. Their surface structures on the other hand are presenting regular shapes. They are currently used for different applications including water source tracing, water quality assessment<sup>81</sup> and surface functionalization for enhancement of their photoluminescence properties<sup>82</sup> for future use in

e.g. solar cells or thin-film displays.<sup>83</sup> So far, diatoms have been mostly studied in 2D, but full 3D visualization is crucial for understanding their architecture to study and tune them for the above-mentioned applications.

Here the surface of a diatom (freshwater species *Cymbella neoleptoceros* Krammer) was reconstructed using the 3D + 1 method. First, SE images were acquired in the HIM. Images were taken in two series, at 45° polar angle (45° tilt) with stage rotation steps of 10° and at 36° polar angle (54° tilt) with 15° rotation. In *Figure 32 a*), some SE images of the acquisition series are presented exemplarily. On the same instrument, SIMS measurement performed on the diatom to map sodium (<sup>23</sup>Na), silicon (<sup>28</sup>Si) and potassium (<sup>39</sup>K) is shown in *Figure 32 b*). Since diatom cells consist of hydrated amorphous silica, in the SIMS images the <sup>28</sup>Si signal is very pronounced all over the surface of the diatom. <sup>23</sup>Na and <sup>39</sup>K secondary ions were analyzed here in order to look for possible contaminants and their distribution on the diatom surface. In fact, the surrounding particles show a pronounced signal in <sup>23</sup>Na and <sup>39</sup>K and represent indeed salt contamination. The SIMS images were then combined in a single RGB color-coded image (*Figure 32 c*).

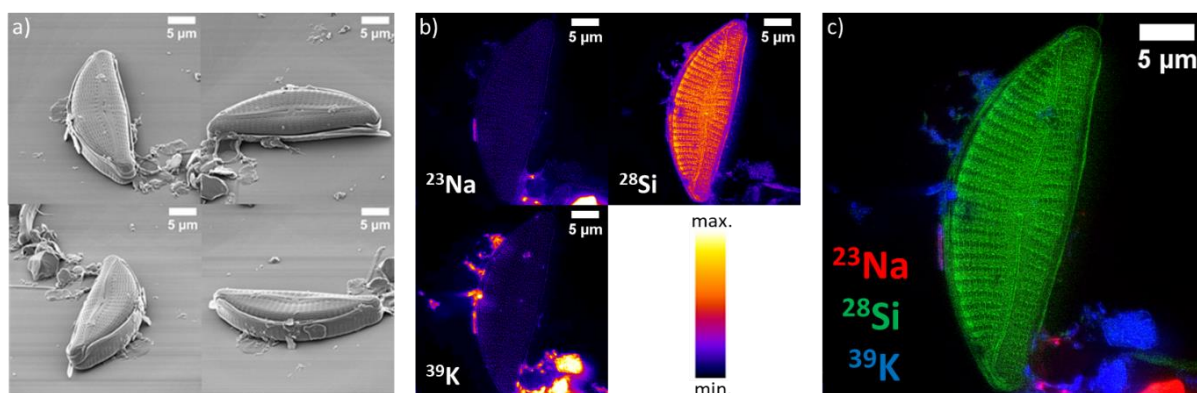


*Figure 32: HIM-SIMS imaging of a diatom. a) Exemplary SE images (25 keV He<sup>+</sup>) taken around the diatom (in total 60 images). b) SIMS images (25 keV Ne<sup>+</sup>) of <sup>23</sup>Na, <sup>28</sup>Si and <sup>39</sup>K (scale bar indicating secondary ion signal intensity) acquired in top view. c) RGB SIMS image (Red: <sup>23</sup>Na, Green: <sup>28</sup>Si, Blue: <sup>39</sup>K).*

Since the surface of the diatom is covered with many perforated structures (areolae, poroids and raphe system) allowing water and nutrient exchange with the surrounding, the 3D reconstruction gave an accurate result (*Figure 33 a*). In fact, areolae were detected as features by the reconstruction software and were matched across the image series enhancing the

reconstruction process. The 4D reconstruction obtained by projecting the RGB SIMS image (Figure 32 c) onto the 3D SE model (Figure 33 a) using 20 2D-3D correspondences is shown in Figure 33 b). The zoomed view in Figure 33 c) allows to see the frustule structures from the SE texture even though this area is covered with the SIMS image. This image has been taken with an anticlockwise azimuthal of  $120^\circ$  with respect to the view in Figure 33 b). The diatom itself has an overall convex structure favoring an accurate 3D reconstruction. However, minor concavities, e.g., on the surrounding contamination particles themselves, could not be reconstructed accurately. Moreover, on the wafer only a few surrounding defects were detected, e.g., salt particles. Hence, the flat representation of the wafer failed in this case. In Figure 33 a), a slight increase in brightness can be observed on the edges of the diatom. This effect originates from the fact that the shape of the beam-sample interaction volume is narrow at the surface of the sample for the  $\text{He}^+$  primary beam. In general, strong changes in brightness and contrast from one image to another in an acquisition series are hindering feature matching, as then the photogrammetry software is struggling to recognize the same features from one image to another.

The SIMS image overlay was done in a way that SIMS data is only displayed for areas of the 4D reconstruction where secondary ions were collected, i.e. taking into account the shadow effect and removing black pixels from the RGB SIMS image (Figure 32 c). In Figure 33 b), the SIMS texture presents a transparency of 60 % allowing to observe in Figure 33 c), although covered with the SIMS information, the areolae and raphe of the diatom wall originating from the SE texture.

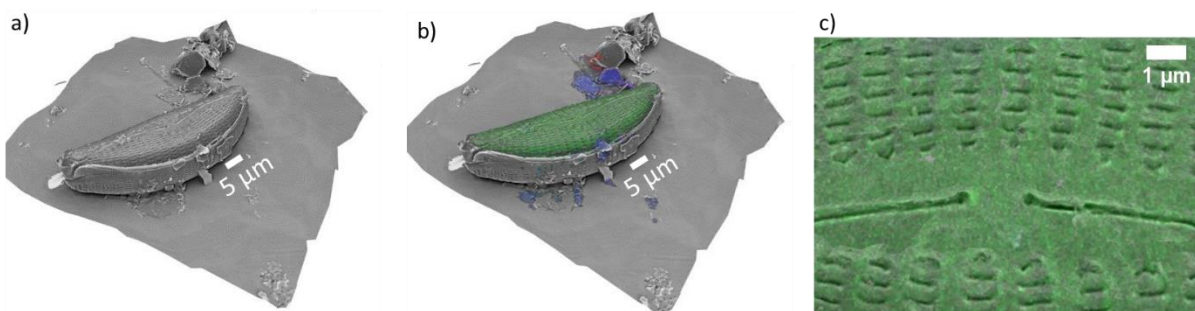


Figure 33: 3D + 1 surface reconstruction of a diatom. a) 3D SE reconstruction from 60 SE images using a photogrammetry software. b) The SIMS RGB image from Figure 32 c) projected onto the 3D SE representation. c) is a zoomed view on the 4D reconstruction of the diatom showing in detail the areolae and raphe structure.

This 3D SE reconstruction provides a more comprehensive and detailed topographic picture of the diatom structure than regular 2D SE images. The resulting maps faithfully reproduce the frustule structure revealing patterns that may help to improve data acquisition and detector sensitivity. As a long-term objective, one could imagine to create a shared database<sup>80</sup> with 3D SE reconstructions using photogrammetry of the most common diatom species to visualize and study their full structure in more details. Additional chemical analysis of functionalized diatoms with SIMS for example could elucidate the distribution of attached chemical species on cell wall and the analysis of textured 3D reconstructions or animations will help to find optimal conditions to tune diatoms, e.g. for semiconductor and solar cell applications. Furthermore, it has been shown that under exposure to heavy metals e.g. Hg, Cd, and Pb diatoms are subjected to modifications of their frustule structure resulting in a “teratological” form of the diatom.<sup>84</sup> Further analyses of such teratological forms could help to correlate the extend of a cell deformation using the 3D SE reconstruction with the amount of incorporated metal on the cell wall from SIMS information.

## 2.2 Chalks

To study the improvement of submarine oil recovery process, seawater injection into oil reservoirs is a method used initially to sustain pore pressure and hence to maintain the oil recovery efficiency. Doing so, besides achieving a constant oil flow, allowed to recover even higher amounts of oil, presumably due to alteration of the rock composition and its pore properties. The sedimentary rock material is mainly composed of chalk and additionally highly porous nanofossils, called coccolithophores which are composed of  $\text{CaCO}_3$ . To study dissolution and precipitation processes on the sample surface, a chalk sample containing coccolithophore fossils was subjected to a flow of synthetic seawater (SSW), containing among others magnesium. Coccolithophore structures from a reference sample and a structure from the SSW exposed sample, were selected and imaged first in the HIM in SE mode (Figure 34 a and d) and subsequently in-situ with SIMS (Figure 34 b and e). 4D surface reconstructions were then created (Figure 34 c and f).

Since coccolithophores consist of calcium carbonate ( $\text{CaCO}_3$ ),  $^{40}\text{Ca}^{16}\text{O}$  was detected all over the surface of both coccolithophore structures. The highly heterogeneous distribution of

coccolithophore fragments and nano-sized fossil debris on the main coccolithophore structure and the wafer, lead to a detection as well as matching of a high number of surface features, which enhanced the overall reconstruction. The SIMS image texture on the 3D SE reconstruction presents a transparency of 60 % allowing to observe both the chemical distribution and small topographical variations contained in the SE texture.

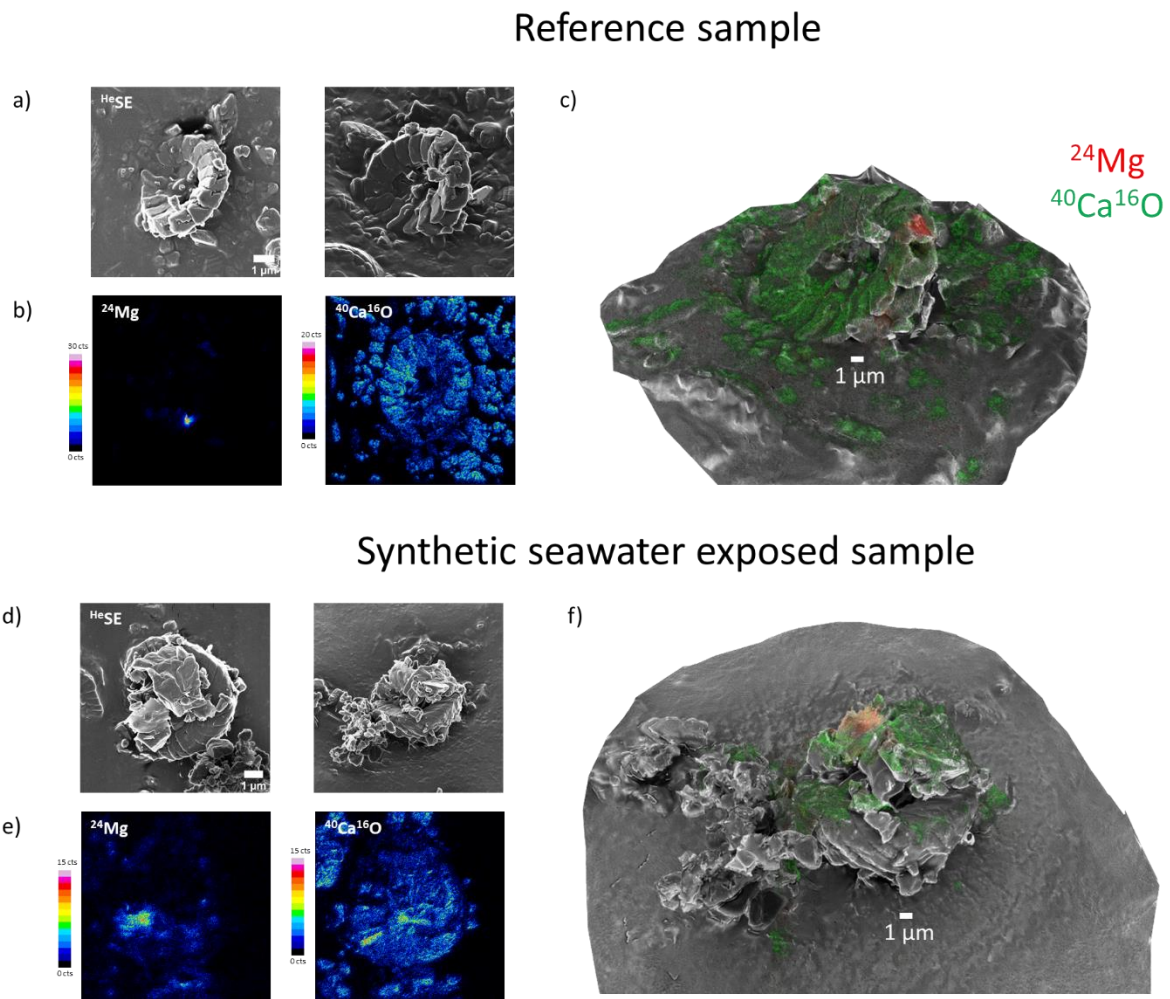


Figure 34: 4D surface reconstruction of two coccolithophore structures (reference and synthetic sea water flooded sample). a) & d) SE image (25 keV He<sup>+</sup>) in top and side view. (b) & e) SIMS images (25 keV Ne<sup>+</sup>) showing the <sup>24</sup>Mg and <sup>40</sup>Ca<sup>16</sup>O distributions. c) & f) 3D + 1 surface reconstruction with color-coded <sup>24</sup>Mg (red) and <sup>40</sup>Ca<sup>16</sup>O (green) information.

The inspection of both 4D surface reconstructions revealed that for the reference sample magnesium has precipitated very locally in the form of magnesite directly attached to the coccolith surface, at fissures and crack-like topography. On the other hand, for the SSW exposed sample magnesite precipitation took place in the form of a flat crystal on the surface

of the coccolithophore. The surface of the coccolithophore containing magnesium is about five times higher for the SSW exposed sample compared to the reference. This shows that retainment of magnesium through SSW took place successfully and induces mineral alteration of the surface and the material's porosity. Studying the distribution of magnesite (or clay minerals) through SSW injection of the samples helps eventually to increase understanding of precipitation and dissolution processes and make improvement of the oil recovery process by choosing appropriate SSW injection parameters.<sup>33</sup>

### 2.3 Soils

Soils represent one of the largest reservoirs of organic carbon on Earth. They consist of associations of organic matter and minerals of variable sizes and chemical composition. Elucidating the complex 3D structure of soil microaggregates is crucial to better understand and acquire control of soil organic carbon/matter sequestration in the future. Isotopic labelling is a commonly used method to track biogeochemical cycles of carbon in soils. A more detailed description about soil organic carbon sequestration as well as a correlative (2D) imaging study on isotopically labelled soil samples can be found in the Appendices.

Here the 3D + 1 method was applied to soil microaggregates, in a first case study with in-situ analyses on the HIM-SIMS and then ex-situ on the HIM and NanoSIMS 50L on isotopically labelled samples (<sup>13</sup>C). In the first case, the HIM-SIMS instrument was used for high lateral resolution imaging of the mineral phase, while in the second one the NanoSIMS 50L was chosen for imaging of isotopes at high mass resolving power. Finally, a numerical processing algorithm was applied to a second 4D reconstruction to localize preferential sites for organic matter (OM) deposition with respect to the soil microaggregate topography.

Serial SE images were taken in the HIM (in total 39). Figure 35 a) shows exemplary images taken around a soil microaggregate and a top view image. HIM-SIMS chemical images representing the microaggregate's mineral phase were taken in-situ (Figure 35 b). In Figure 35 c), the SIMS images were fused into a single RGB image.

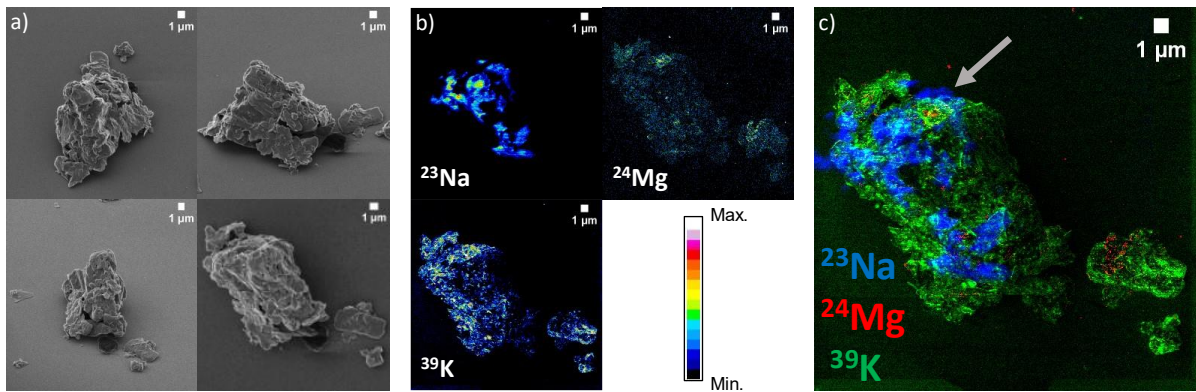


Figure 35: HIM-SIMS imaging of a soil microaggregate. a) Sequential SE images taken around the soil microaggregate (25 keV He<sup>+</sup>). The lower right SE image was taken in top view. b) SIMS images (25 keV Ne<sup>+</sup>) of <sup>23</sup>Na, <sup>24</sup>Mg, <sup>39</sup>K representing the microaggregate's mineral phase. c) RGB SIMS image (red: <sup>24</sup>Mg, green: <sup>39</sup>K, blue: <sup>23</sup>Na) (Figure adapted from Ost et al.).<sup>77</sup>

In Figure 36 a) the 39 SE images were implemented into a photogrammetry software to create a 3D SE reconstruction. While the heterogeneous distribution of clay minerals on the surface of the microaggregate favored the detection/matching of a high number of features, the homogeneous surface of the wafer with only a few minor soil particles lead to an erroneously non-flat representation of the wafer. The SIMS RGB image (Figure 35 c) was projected onto the 3D SE model (Figure 36 a) to create a 4D surface reconstruction (Figure 36 b).

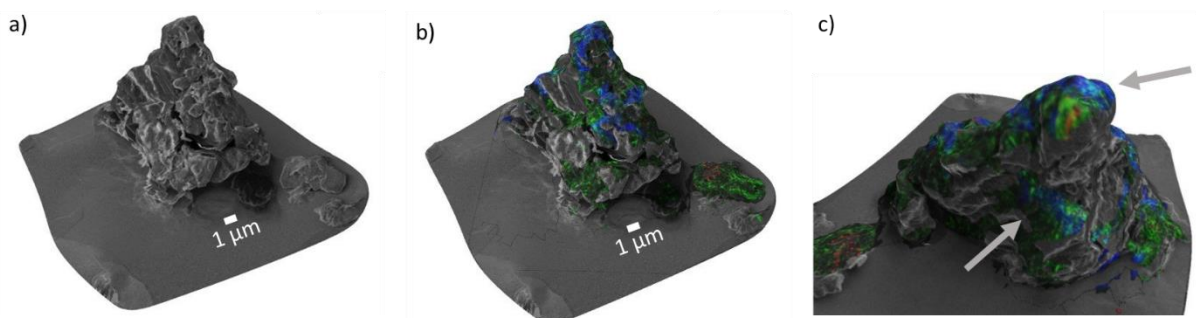


Figure 36: 4D surface reconstruction of a soil microaggregate (shown in Figure 35). a) 3D SE reconstruction obtained from 39 SE images. b) 3D + 1 surface reconstruction obtained by the alignment and subsequent top-down projection of the SIMS image in Figure 35 c) onto the 3D SE model in a). c) Zoomed view on the 4D reconstruction (azimuthal angle rotated with 180° with respect to the view in a) and b) (Figure adapted from Ost et al.).<sup>77</sup>

The arrows in Figure 35 c) and Figure 36 c) point in both cases to the same zone. While in Figure 35 c) the area of the microaggregate indicated by the arrow seems to be adjacent in space, in Figure 36 c) it becomes clear that this area is actually vertically split by regions which were not subjected to the primary ion beam due to their concave topography. Thus, with this 4D surface representation a more complete visualization is obtained compared to a 2D SIMS image.

The skeletal structure of this soil microaggregate is made of minerals. The high spatial resolution of the HIM-SIMS allowed to distinctly visualize the microscale patterns resembling pedogenic and primary minerals which constitute the microaggregate. The chemical distributions of sodium, magnesium, and potassium are the main elements forming quartz, illite, kaolinite, and chlorite, which make up by distinct proportions the microaggregate.

In a second example, a numerical analysis of a 4D surface reconstruction, obtained from ex-situ measurements performed on a HIM and a NanoSIMS 50L, was performed to study the organic carbon sequestration process.<sup>77</sup>

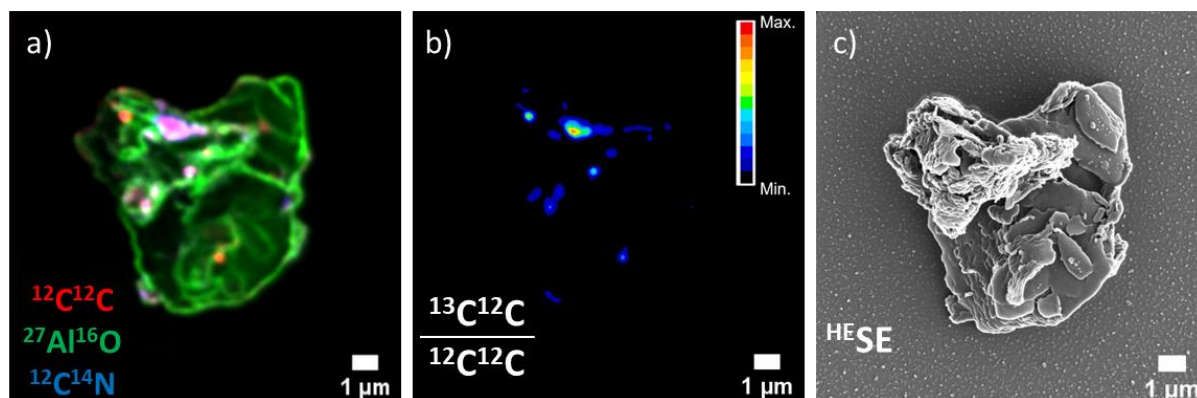


Figure 37: Correlative imaging from HIM and a NanoSIMS 50L of a soil microaggregate from a sample enriched with  $^{13}\text{C}$ . a) SIMS (16 keV  $\text{Cs}^+$ ) RGB image of the microaggregate showing the inherited OM ( $^{12}\text{C}^{12}\text{C}$ : red,  $^{12}\text{C}^{14}\text{N}$ : blue) and the mineral phase ( $^{27}\text{Al}^{16}\text{O}$ ). b) SIMS ratio image of  $^{13}\text{C}^{12}\text{C}/^{12}\text{C}^{12}\text{C}$  showing the areas enriched with  $^{13}\text{C}$ . c) HIM SE image (25 keV  $\text{He}^+$ ) of the microaggregate in top view (Figure adapted from Ost et al.).<sup>77</sup>

While for conventional correlative imaging workflows (see imaging case studies in the Appendices) the OM sequestration is investigated using 2D images, here the actual 3D surface topography of a microaggregate was used to find preferable sites for OM deposition. The soil sample was enriched with isotopic carbon ( $^{13}\text{C}$ ) with an incubation experiment to trace the

faith of the freshly introduced OM. In this case, SIMS measurements were performed before the HIM imaging to avoid sputtering of very fine OM layers on the surface of the microaggregate during the sequential SE imaging. Figure 37 a) shows the inherited OM ( $^{12}\text{C}^{12}\text{C}$ ,  $^{12}\text{C}^{14}\text{N}$ ) and the microaggregate's mineral phase ( $^{27}\text{Al}^{16}\text{O}$ ) imaged with the NanoSIMS 50L and represented in an RGB image. The enrichment of isotopic  $^{13}\text{C}$ , i.e., the ratio image between the  $^{13}\text{C}$  and  $^{12}\text{C}$  images, is shown in b). SE images around the microaggregate were acquired then ex-situ in the HIM.

Figure 37 c) shows the HIM SE image in top view. 3D SE reconstruction of the microaggregate was performed in the photogrammetry software. The reaction of the implanted  $\text{Cs}^+$  from the NanoSIMS 50L measurements led to formation of bubbles around the soil microaggregate (see Figure 37 c) which supported the reconstruction process of the wafer as these were recognized as features by the photogrammetry software. The SIMS maps of Figure 37 a) and b) were projected on the 3D SE model reconstructed from 48 SE images to obtain the 4D surface models Figure 38 a) and b). These were used for the numerical analysis of the microaggregate topography.

To mathematically characterize local topography variation in the soil microaggregate, the curvature was chosen in this case, as the latter allows to differentiate between diverse topographic structures, including plain areas and local structural features such as edges, micropores, cracks, vaults etc. and to associate this information directly with the chemical distribution from the SIMS maps.

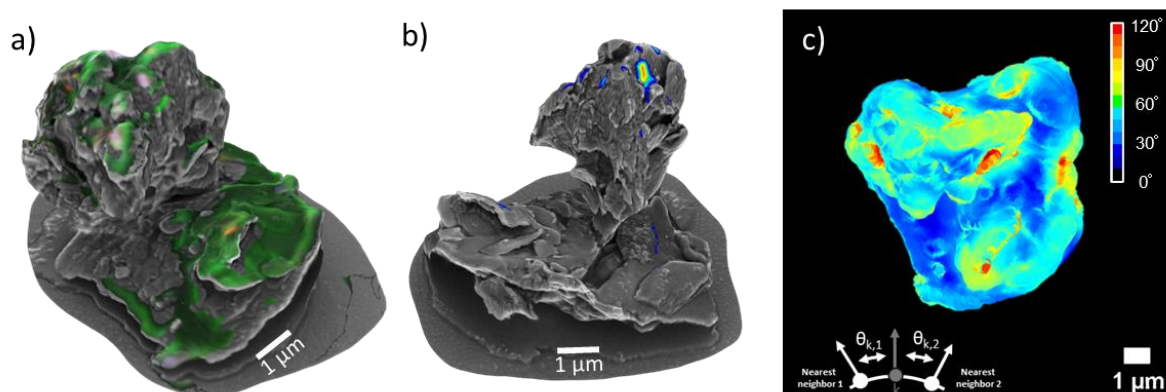


Figure 38: 4D surface reconstruction of a soil microaggregate (shown in Figure 37) and subsequent numerical analysis. a) & b) 4D surface reconstructions obtained from the overlay of the SIMS images in Figure 37 a) & Figure 37 b) onto the 3D SE model reconstructed previously. c) Top view of the color-coded visualization of the local curvature of the

*microaggregate. The schematic representation on the lower left corner illustrates the definition of the curvature parameter. (Figure adapted from Ost et al.).<sup>77</sup>*

The 4D surface models were imported as color-coded point clouds into MATLAB and for each 3D point the local surface normal vector was associated. For the entire microaggregate a surface of 197  $\mu\text{m}^2$  was found with a 3D point density of 230 data points per  $\mu\text{m}^2$ . Thus, to calculate the local  $\sigma_k$  curvature for a 3D point k the following definition was used:<sup>85</sup>

$$\sigma_k := \frac{1}{N} \sum_{i=1}^N \theta_{k,i} \quad (4)$$

Where N it the total number of nearest neighbors taken into account here (here 230, which is reasonable considering the size of the microaggregate and the point cloud density), and  $\theta_{k,i}$  is the angle between the normal vector of point k and the  $i^{\text{th}}$  nearest neighbor.  $\sigma_k$  represents thus the average angle between the normal vector k and all its nearest neighbors. A color-coded visualization of the microaggregate's local curvature is shown in Figure 38 c). It is worth noting that the curvature of the wafer is set arbitrarily to  $0^\circ$  and is not taken into account in the curvature calculation. The average curvature for a certain ion species s (e.g.,  $^{27}\text{Al}^{16}\text{O}$ ) is then given by:<sup>85</sup>

$$\sigma_s := \frac{1}{n} \sum_{j=1}^n \sigma_{s,j} \quad (5)$$

Where n is the total number of 3D points containing information of ion species s,  $\sigma_{s,j}$  the curvature of a 3D point j containing the species s. Calculating with this definition the average curvature for the mineral phase, represented by  $^{27}\text{Al}^{16}\text{O}$ , for plain areas (non-edges) an average curvature of  $14.1^\circ$  was obtained. For the inherited OM compounds, i.e.,  $^{12}\text{C}^{12}\text{C}$  and  $^{12}\text{C}^{14}\text{N}$ , curvature values of  $37.4^\circ$  and  $38.5^\circ$  were found. The curvature value corresponding to the freshly introduced OM was found to be  $37.2^\circ$ , thus very close to the inherited OM values. The standard deviations were  $4^\circ$  (mineral phase) and about  $10^\circ$  (OM) in each case. Hence, this shows that in this case the OM deposited on areas of the microaggregate with an average curvature corresponding to almost the triple of the mineral phase areas. Moreover, the freshly introduced OM was deposited on areas with a very similar topography as the inherited OM, indicating that topography is a potential driver for OM deposition in soil microaggregates which is in agreement with previous investigations on organo-mineral association.<sup>8</sup>

To improve the statistical significance of the curvature data, 6 soil samples enriched with isotopic carbon and nitrogen ( $^{13}\text{C}$ ,  $^{15}\text{N}$ ) were analyzed and for each of the samples a 3D + 1 reconstruction was created (data shown in the Appendices). A curvature analysis for the isotopic OM enrichment ( $^{13}\text{C}/^{12}\text{C}$ ,  $^{15}\text{N}/^{14}\text{N}$ ) of all the reconstructions revealed that deposition is independent of the sample treatment, as on average for each microaggregate the deposition of the OM took place on areas with a curvature in a range of  $25^\circ$  to  $40^\circ$ . It was found that carbon and nitrogen tend to deposit within the same range of medium curvature values, while highly curved and flat areas were avoided in each case.

Hence, the 4D surface reconstruction method, besides a qualitative visualization improvement, allows to study materials' transformation processes at the relevant scale and specifically for soil biogeochemistry enhances the understanding the fostering of mineral-associated OM.

### 3. Chapter summary

In this section, we presented a methodology used to create photogrammetric 3D surface representations from multi-view SE images which are correlated with analytical information to study physical properties of materials.

First, an appropriate method for 3D surface reconstruction was needed to avoid typical artefacts from classical SIMS 3D reconstruction methods. The results of traditional SIMS volumetric reconstructions generally do not represent the sample topography accurately, as the topographic information is not recorded. AFM has been used in the past to reconstruct surfaces of nanoscopic samples. However, micrometer-sized high-aspect ratio objects are particularly challenging for AFM. Photogrammetry is not limited by the size and aspect ratio of the object and was thus chosen for 3D surface reconstruction as the most appropriate method for surface reconstruction.

For photogrammetric 3D SE surface reconstruction, series of a few tens of partially overlapping images are taken around an ROI and the surface is reconstructed using a photogrammetry software. Simulative studies on geometric structures were performed to identify sources of artefacts and to find a metric for quality assessment of a 3D SE reconstruction. In the following, the photogrammetric 3D SE surface reconstruction workflow was applied to soil and sediment samples.

The key benefits of the 3D + 1 method were discussed by showing applications for sediments and soils. First, a 3D + 1 surface reconstruction offers a more complete picture of an ROI compared to simple 2D SE and SIMS images. In fact, when inspecting 2D SIMS images, for the observer it seems that all the areas where SIs were detected are adjacent to one another, i.e., since it is a 2D image vertical offsets in the 3<sup>rd</sup> dimension are not represented in this type of visualization. Thus, areas located in concave structures, which were not exposed to the primary ion beam, are not represented in a SIMS image. On the other hand, since a top-down projection of the SIMS image on the 3D model is performed, for the 4D surface model the areas exposed to the analyzing beam are separated in space. For instance, in soil biogeochemistry taking into account these vertical offsets with this 3D + 1 representation can be crucial when analyzing and concluding on the spatial distribution of clay minerals on a soil

microaggregate. Secondly, 4D models can be processed numerically to study the topography of chemical hotspots, e.g., to find preferential hotspot formation of isotopes at specific sample structures, i.e., whether this takes place on average on flat surfaces, edges, valleys etc. In the upcoming chapter the use of the 3D + 1 methodology will be further extended by studying topography induced variations of the local sputtering yield.

## Chapter 3: Advanced topographical and chemical sample characterization

### 1. Topography induced sputtering yield variation

#### 1.1 Introduction

The surface topography of the sample can strongly affect the secondary ion intensity due to local changes of the sputtering yield and edge effects. Figure 39 illustrates the different topographic effects, including variation of the sputtering yield according to the incidence angle of the primary beam and the change of the SI intensity on edges vs. plain areas.

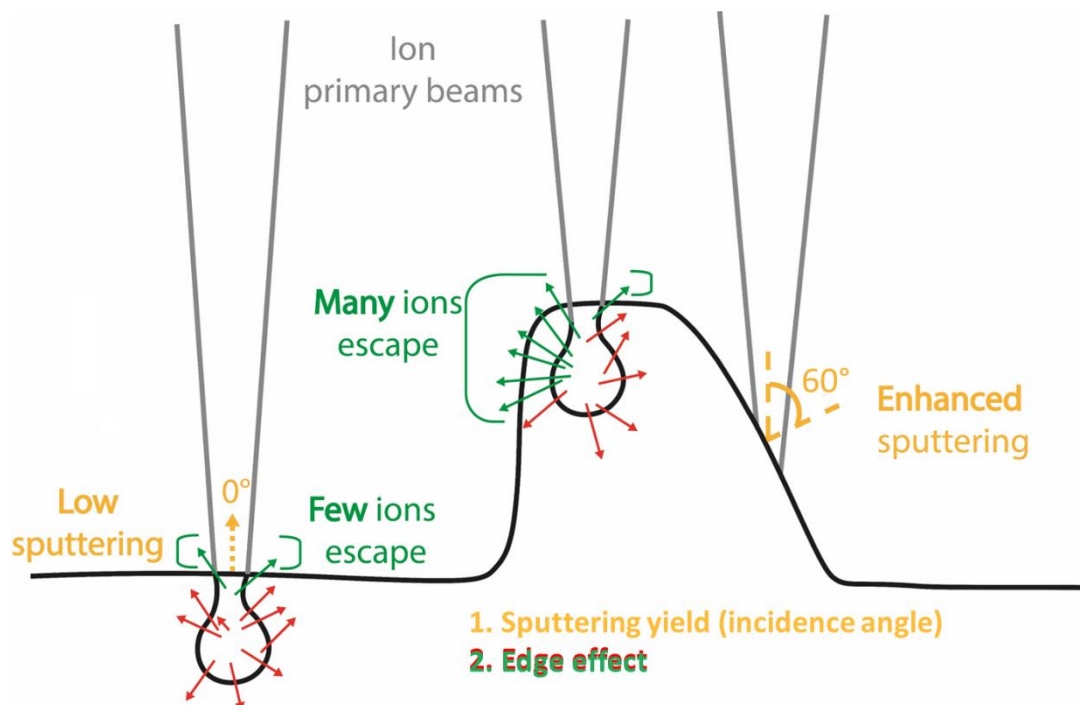


Figure 39: Schematic illustration of the topographic effects creating signal intensity variation in SIMS. 1. Increase of the sputtering yield for non-zero primary ion beam incidence angles, 2. Higher signal intensity close to edges due to lateral escape of secondary ions (“edge effect”).

First, the sputtering yield changes with the topography as the primary ion beams hit the surface with a non-constant incidence angle. Impinging on a sample with varying incidence angles creates different physical conditions with regards to momentum and energy transfer, leading to a different sputtering behavior. Numerous theoretical,<sup>19,86</sup> simulative,<sup>87,88</sup> and experimental studies<sup>21,89</sup> have been performed to study the behavior of sputtering yields with

regards to the primary ion beam incidence angle by choosing different primary ion species, acceleration energies, and target materials. These parameters were found to strongly affect sputtering properties of the materials, affecting energy and momentum transfer, collision cascade processes and penetration depth. Typically, the sputtering yield tends to increase at oblique incidence angles, reaching a maximum at about 80° incidence angle and drops at grazing angles.

Secondly, edge effects are known to have a strong impact on the secondary ion intensity.<sup>50,90</sup> In areas in the close vicinity of edge-like structures the signal intensity is typically higher, as more secondary ions can escape laterally from the edge compared to a flat surface, leading locally to a higher SI yield. Moreover, on edges and borders preferential sputtering is taking place, as in these areas atoms are bound by less nearest neighbor atoms requiring less energy to kick an atom out of the matrix, compared to plane area atoms.

Understanding SIMS images of samples with a pronounced topography is very challenging, as it is not evident to differentiate between signal variations due to concentration or topography, matrix, or/and topographic gradients. Knowing the sample topography and information about the local incidence angles will help to conclude upon the extend of topographical artefacts and to understand the origin of local signal variation. Studying experimentally and by simulations the changes of the sputtering yield with a known topography is therefore essential to gain a deeper understanding about SI variation.

In this section, first common surface sputtering models of flat and rippled surfaces will be briefly introduced and discussed with respect to simulative studies on sputtering yields. In the following, the 3D + 1 methodology (see chapter 2) was used to provide a detailed 3D reconstruction of the surface allowing to study local changes of the sputtering yield. To do so, model samples were patterned with a Ga<sup>+</sup> FIB and imaged in the HIM-SIMS to study the variation of the SI signal on the patterned surfaces vs. the corresponding incidence angle. Sputtering yields were estimated by comparing the secondary ion intensity on the patterned signal with respect to normal incidence. The experimental data was fitted with appropriate functions discussed in the first part of that section. Finally, numerical algorithms were developed used to analyze 3D + 1 reconstructions and to correct topographical artefacts in SIMS images.

Hence, here we aim to study and extend the applicability of common sputtering models on light ions ( $\text{He}^+$ ,  $\text{Ne}^+$ ) and provide novel numerical algorithms for correlative SIMS image analysis. These allow to move beyond a simple improvement of data visualization and offer an approach to study correlatively the impact of the topography on ion surface sputtering.

## 1.2 Sputtering models and Monte Carlo simulations

## 1.2.1 Flat surfaces

A qualitative description of surface ion sputtering, specifically for light ions, was provided by Bay and Bohdansky,<sup>49</sup> describing it as the sum of the contributions of two sputtering mechanisms. A schematic illustration of both mechanisms is shown in Figure 40. Mechanism 1 is described as a direct one-to-one collision (i.e., “direct knock-off”) of the incoming ion with a surface atom. Mechanism 2 refers to sputtering of ions on the surface caused by collisions from ions reflected inside the target or from (often multiple collisions series of) target atoms set into motion by the primary ions. At angles close to normal incidence mechanism 1 vanishes (almost) completely as most of the primary ions are implanted inside the target without causing ejection of surface atoms. The contribution of mechanism 2 is dominant in this case, as momentum can be transferred from the incident particle to a surface atom with a momentum vector pointing out of the surface with only a limited energy loss. At “medium” incidence angles ranging from 30° to 80°, momentum transfer of the projectile towards surface atoms becomes more effective, thus more atoms are knocked-off directly from the surface by primary ions and the contribution of mechanism 1 is more significant. Due to the inclined penetration direction of primary ions into the material collisions are shallower (Figure 41, middle: 45°, right: 75°) compared to angles close to normal incidence (Figure 41, left: 0°), i.e. the contribution of mechanism 2 is also more important, as the probability of hitting a surface atom with a reflected ion (or a target atom) is higher in this case.

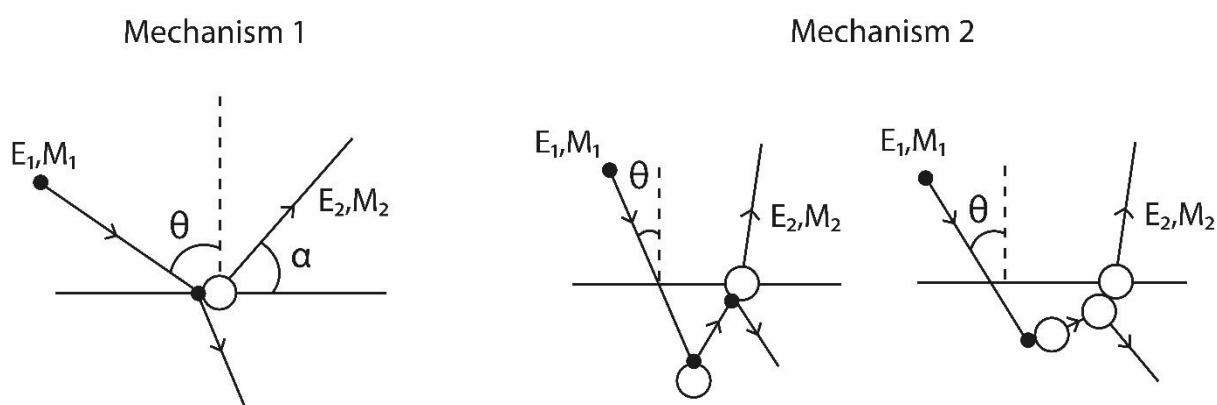
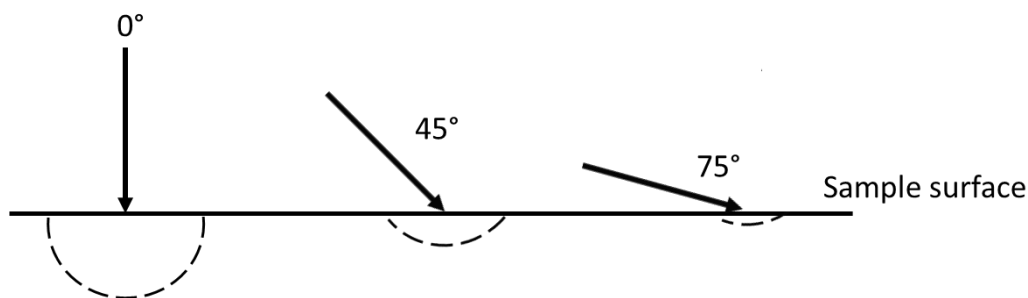


Figure 40: Schematic illustration of sputtering mechanisms for flat surfaces. Small black filled spheres represent here primary ions with energy  $E_1$  and mass  $M_1$  creating (directly or indirectly) sputtering of the surface atoms represented by white large spheres with energy  $E_2$  and mass  $M_2$  (Figure based on Bay and Bohdansky).<sup>49</sup>

At grazing angles typically  $> 85^\circ$ , the vertical component of the momentum vector of the primary ion is too low to break the surface binding forces, i.e., to eject a surface atom or to be implanted, so that the primary ion just bounces back from the surface. Therefore, the contributions of mechanisms 1 and 2 vanish progressively for incidence angles between  $\geq 85^\circ$  and  $< 90^\circ$ .



*Figure 41: Schematic view on the spatial extend of the collision cascade extend for normal ( $0^\circ$ ) and oblique incidence ( $45^\circ$ ,  $75^\circ$ ). While primary ions hitting the surface at normal incidence are mostly deeply implanted, arriving at oblique incidence angles leads to a shallower collision cascade of the primary ions favoring the sputtering of surface atoms and thus to a higher sputtering yield.*

The first theoretical description for ion sputtering of flat surfaces has been developed by Peter Sigmund<sup>10</sup> and provided a basis for numerous further investigations on sputtering. Sigmund's theory of sputtering takes into account mass, energy, and incidence angle of the primary ions, and the density, mass, and surface binding energy of the target material. Based on Boltzmann's equation of transport, a powered cosine function was derived to describe the change of the sputtering yield with respect to the incidence angle of the primary ion beam:

$$SY(\theta)/SY(\theta=0^\circ) = \cos(\theta)^{-f} \quad (6)$$

Where SY is the sputtering yield,  $\theta$  the incidence angle, and f an exponent coefficient which is a function of the projectile and target masses,  $M_1$  and  $M_2$ . The primary ion incidence angle is defined here as the angle  $\theta$  between the local surface normal vector and direction vector of the incident primary ion beam (see Figure 40). However, the theory is valid for incidence angles up to  $70^\circ$  and fails for grazing incidence angles ranges where experimentally it was

observed that sputtering yields quickly decrease for angles  $> 80^\circ$  (which cannot be reproduced by Sigmund's model).

Using the Monte Carlo simulation-based program for ion bombardment of surfaces called SRIM (Stopping and Range of Ions in Matter)<sup>91,92</sup> the sputtering yield vs. the incidence angle was simulated here for a flat silicon surface (25 keV Ne<sup>+</sup>). The sputtering yield was normalized here with respect to normal incidence to represent the change of the sputtering yield compared to the latter. The cosine function from equation 6 was fitted to the He<sup>+</sup> and Ne<sup>+</sup> sputtering yield dataset for angles  $< 70^\circ$  (as described by Sigmund's theory) showing a high agreement in this range of incidence angles with R-squared values of above 0.9 in both cases (Figure 42).

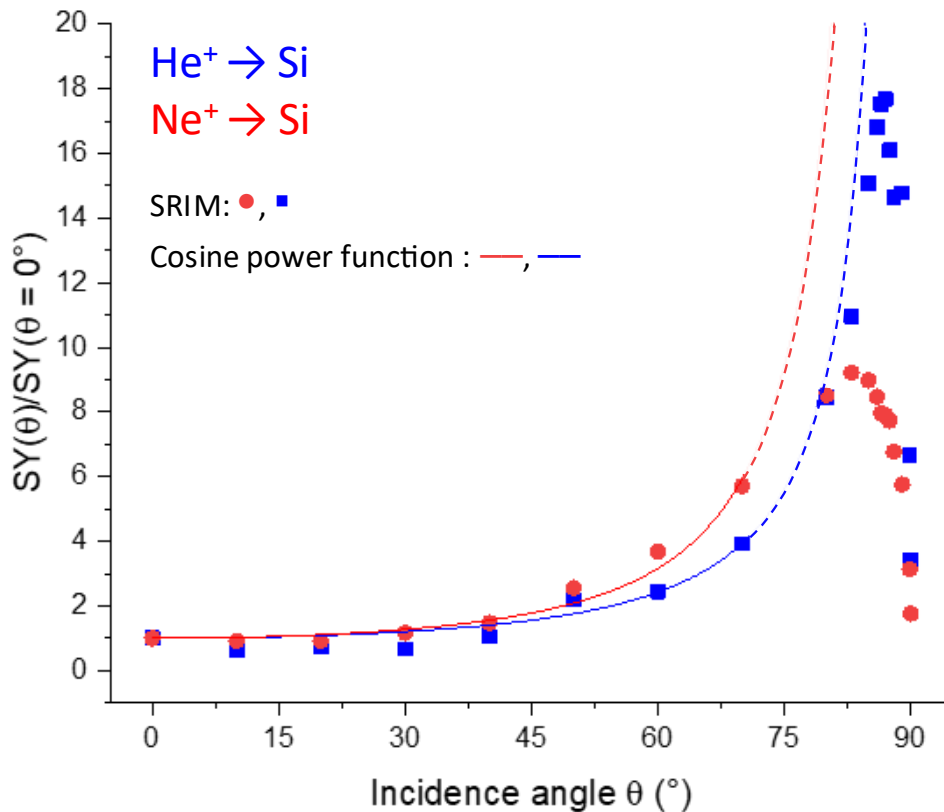


Figure 42: SRIM simulations of normalized (with respect to normal incidence) sputtering yields of He<sup>+</sup> and Ne<sup>+</sup> projectiles onto a silicon surface vs. the incidence angle at 25 keV acceleration energy (He<sup>+</sup>: blue, Ne<sup>+</sup>: red data points). A cosine power function (equation 6) was fitted to the data for incidence angles  $0^\circ \leq \vartheta \leq 70^\circ$  (blue and red lines). The fitted function for angles  $> 70^\circ$  is plotted as a dashed line.

Differences between He<sup>+</sup> and Ne<sup>+</sup> in the normalized sputtering yield arise from different penetration depth (resulting from electronic stopping power predominant for He<sup>+</sup> and nuclear stopping power for Ne<sup>+</sup>). As He<sup>+</sup> ions penetrate deeper into the material than Ne<sup>+</sup> (for silicon bombardment at 25 keV with He<sup>+</sup>: 200 nm, for Ne<sup>+</sup>: 60 nm) at normal incidence, the contribution of mechanism 2 for He<sup>+</sup> bombardment is initially very weak. However, at larger incidence angles (i.e., with an inclined primary ion beam) collisions take place in volumes closer to the surface and ejection of surface atoms are much more probable at this stage (for 75° incidence angle for He<sup>+</sup>: 100 nm, for Ne<sup>+</sup>: 30 nm). While for Ne<sup>+</sup>, due to its initially shallow penetration, the normalized sputtering yield does not change as strongly compared to He<sup>+</sup>. It is worth noting that the absolute values of the sputtering yield of Ne<sup>+</sup> are around 20 times higher as for He<sup>+</sup> (at normal incidence), while the normalized sputtering yield (with respect to normal incidence) is on average higher for He<sup>+</sup> than for Ne<sup>+</sup>, as the latter describes only the sputtering yield increase compared to normal incidence.

### 1.2.2 Rippled surfaces

So far, we considered here sputtering mechanisms for perfectly flat surfaces. However in practice, surfaces especially after high ion dose FIB milling, are far from being perfectly flat.<sup>93,94</sup> Since ripple formation of obliquely ion irradiated surfaces is observed commonly,<sup>95,96</sup> sputtering mechanisms of rough, respectively rippled, surfaces have been developed in the past.

Wittmaack<sup>97</sup> provided a simple theoretical model to describe sputtering phenomena with rippled structures. In his model, a cone-like shape of the ripples is assumed with a specific aspect ratio defined by the ripples' height and their wavelength. A schematic illustration of the sputtering model is shown in Figure 43. The expression of the sputtering yield is given by a sum of two contributions, i.e. the front and the rear side of the ripple sputtered by the primary ion beam, hitting the surface thus with two different incidence angles:

$$Y = (1 - a)Y_0(|\theta - \beta_1|) + aY_0(\theta + \beta_2) \quad (7)$$

Where  $a$  and  $(1-a)$  are the fractions of the beam irradiating the front and rear surfaces, and  $(|\theta - \beta_1|)$  and  $(\theta + \beta_2)$  the actual incidence angles of the ion beam with  $a = 1/(1+b)$  and  $b =$

$(\sin\beta_2 / \sin\beta_1)[\cos(\theta - \beta_1)/\cos(\theta + \beta_2)]$ ,  $\beta_1$  and  $\beta_2$  the inclination angle of the cone forming the rippled structure,  $Y_0$  the sputtering yield of the material at normal incidence for a flat surface.

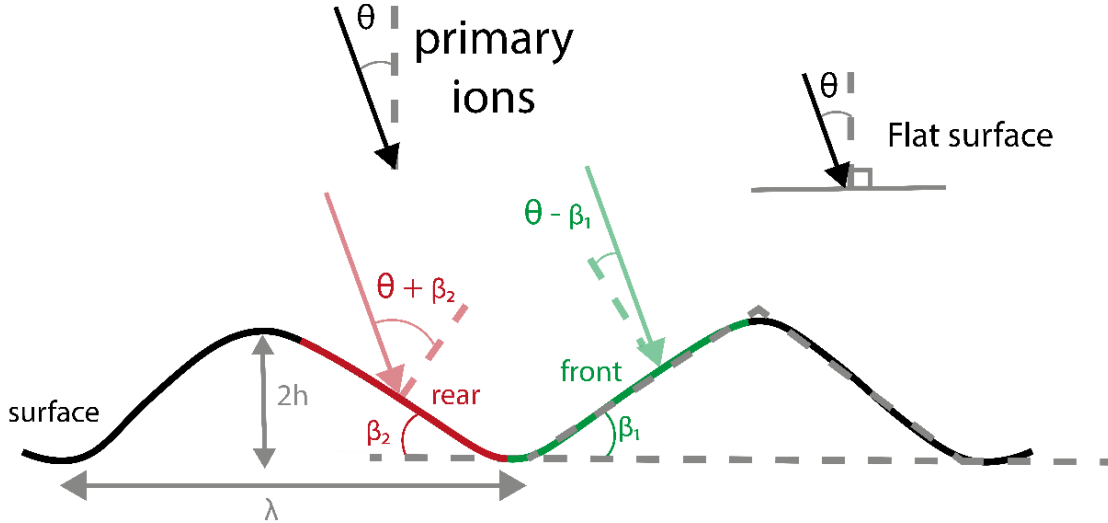


Figure 43: Schematic illustration of a sputtering model for rippled surfaces. Due to the pointed structures of the ripples, the primary ion beam is hitting the front and the rear side of the ripple in both cases with a different incidence angle (Figure based on Shulga).<sup>20</sup>

Shulga<sup>20</sup> has taken up Wittmaack's model and has added an additional condition, namely when the primary beam incidence angle is higher than a critical angle  $\theta_c$ , only the "front" surface contributes to the sputtering yield, as the rear surface is shadowed by the front surface, i.e. the rear surface is not exposed to the primary ion beam, and the corresponding term vanishes in this case. This additional condition (for equation 7) is given by the following expression:

$$Y = Y_0(|\theta - \beta_1|) \quad \text{for } \theta > \theta_c \quad (8)$$

For the ripples sinusoidal ridges are assumed here with  $\beta_1 = \beta_2 = \arctan(4h/\lambda)$ , i.e. the shadowing angle  $\theta_c = \arctan(\lambda/4h)$ , where  $\lambda$  is the wavelength and  $h$  the height of the ripple. Thus, the shadowing angle depends on the aspect ratio of the ripples.

To visualize the trend of the sputtering yield vs. the ion beam incidence angle for a rippled silicon surface, the model functions from equations 7 and 8 were implemented in an algorithm written in MATLAB. Values for the sputtering yield at normal incidence  $Y_0$  were

obtained from SRIM simulations (25 keV Ne<sup>+</sup>, 500 primary ions shot onto silicon, see Figure 42). The aspect ratio of the ripples, i.e.,  $\lambda/h$  was varied here from steep, medium to broad ripple shape ( $\lambda/h = 5, 10, \text{ and } 15$ , respectively) to show the different trend of the sputtering yield in each case.

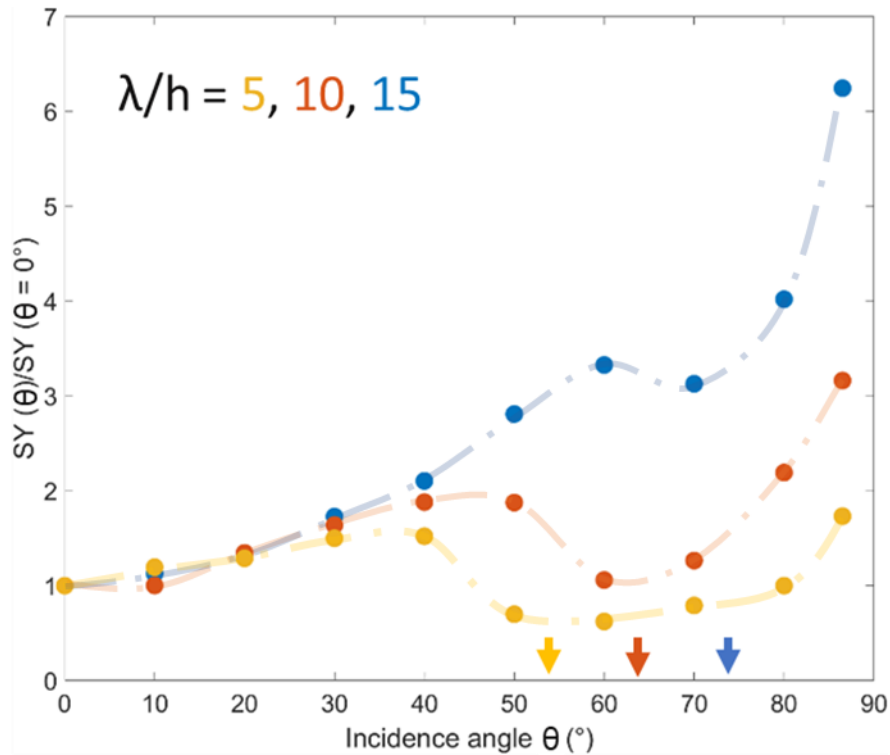


Figure 44: Implementation of Shulga's model for sputtering of rippled silicon surfaces (equations 7 and 8). SRIM simulated data for a surface bombarded with 25 keV primary Ne<sup>+</sup> ions were used to implement Shulga's model function for rippled surfaces and simulate the sputtering yield for different ripple aspect ratios ( $\lambda/h = 5, 10, \text{ and } 15$ ). Data points were connected by dashed lines to better visualize the data trend in each case. The calculated shadowing angles  $\vartheta_c$  (54°, 74°, and 65°, respectively) are indicated by arrows.

shows the sputtering yield of the silicon surface vs. the incidence angle, normalized with respect to normal incidence, for different ripple aspect ratios. The corresponding critical angles  $\theta_c$  (54°, 74°, and 65°) are indicated with arrows in each case. After passing a first maximum of the sputtering yield, it decreases as for the "front" surface the grazing angles are attained, hence the contribution from this part starts to vanish. After passing the critical angle, the front term vanishes completely and only the rear part contributes to the sputtering yield. As the latter is hit then with incidence angles favoring both mechanisms 1 and 2 with an oblique incidence angle, the sputtering yield increases again very pronouncedly. Thus, with

this first maximum just before the critical angle a typical “kink”-like shape of the curve is created. By increasing vertically the aspect ratio of the ripples, i.e., increasing  $h$  or decreasing  $\lambda$  (i.e., decreasing the ratio  $\lambda/h$ ), the value of the critical angle shifts to lower values as shadowing of the rear part becomes more important. Additionally, for low values of  $\lambda/h$ , at incidence angles above the critical angle the overall values of the normalized sputtering yield are lower as the surface of the ripples is steeper and therefore the incidence angle is closer to normal incidence. In the limit of  $\lambda/h \rightarrow \infty$ , i.e. for a flat surface, the normalized sputtering yields obtained from SRIM are recovered.

### 1.3 Experimental and simulative study on He<sup>+</sup> and Ne<sup>+</sup> sputtering yields

In this section, the aim is to study experimentally the change of the sputtering yield for different primary ion incidence angles and to understand these results with the previously discussed sputtering models. To do so, series of experiments model samples were created by FIB milling to study the change of the SIMS signal intensity for different target materials under light ion bombardment (He<sup>+</sup>, Ne<sup>+</sup>). The secondary ion intensity was correlated with respect to the real topography, using the 3D + 1 method presented in chapter 2. It is worth noting that these model samples were created here, because in the HIM-SIMS the sample stage cannot be tilted during a SIMS acquisition which would allow to study directly the signal intensity with respect to the sample orientation, i.e. stage tilt angles.

In a first step, multiple series of samples were patterned in the FIB-SEM-SIMS instrument. Two materials were used for these studies, indium phosphorus (InP) and silicon (Si) wafers. For each material and primary ion species (He<sup>+</sup>, Ne<sup>+</sup>) for the SIMS analysis later, individual sample series were prepared using the Ga<sup>+</sup> FIB.

For both materials, structures consisting of surfaces orientated at different angles with respect to the vertical direction were patterned with a Gallium ion source (in the FIB-SEM-SIMS). To do so, the sample stage was tilted with angles ranging from 2° to 47° (9 structures for one series, 36 structures in total for Si and InP materials for He<sup>+</sup>, Ne<sup>+</sup> analyses). For both samples, crater structures were milled for each stage tilt angle. Craters were created with surfaces with angles ranging from 40° to 85° of the surface normal with respect to the vertical direction, i.e. the direction of the primary ion beam for the SIMS analysis later on. The milled surfaces were analyzed subsequently in the confocal microscope to create a 3D reconstruction allowing to determine the angle and topography of the patterned surfaces. The average angles of the slopes were determined by three line scans for each structure. In addition, rippled structures on the slopes were observed and average aspect ratios (i.e.,  $\lambda/h$  ratio, cf. previous section) of 35 for Si and 16 for InP surfaces were found. A series of model samples (analyzed in the confocal microscope) patterned on the InP wafer is shown in Figure 45. Confocal microscopy was chosen here as the more appropriate method to reconstruct the surface compared to photogrammetry (see chapter 2 section 1) as confocal microscopy

presented a less time-consuming and more efficient solution for 3D surface reconstruction of the patterned craters.

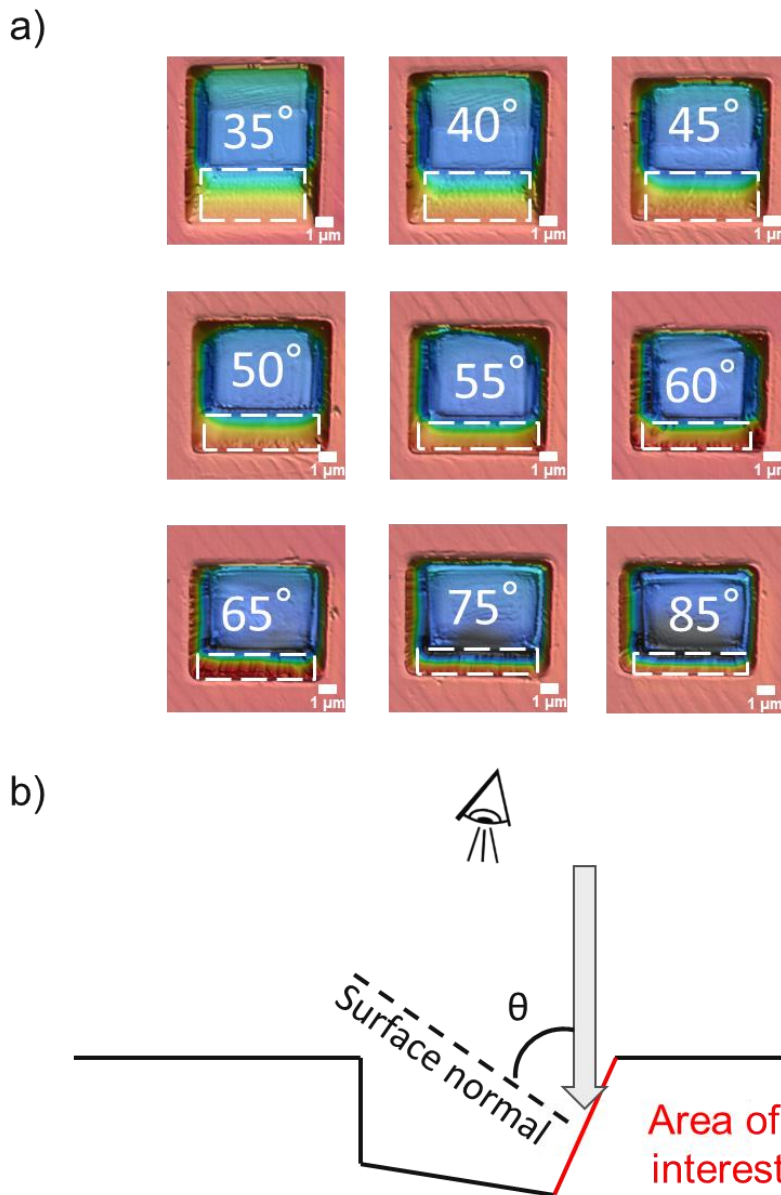


Figure 45: a) Top view on 3D surface reconstructions of Si model samples patterned in the FIB-SEM-SIMS and used for an experimental study of the sputtering yield variation. The reconstructions were obtained from confocal microscopy. b) Schematic side view of the patterned craters. The dashed squares in a) indicate the area of interest (colored in red in b) where the sputtering yield will be studied with respect to the primary ion beam incidence angle. The estimated incidence angle of the primary ion beam is specified for each structure.

The patterned InP and Si structures were analyzed in SIMS imaging mode with He<sup>+</sup> and Ne<sup>+</sup> primary beams using the HIM-SIMS instrument. Figure 46 shows the results obtained for the

Si structures under 25 keV Ne<sup>+</sup> bombardment. The images of the Si samples under He<sup>+</sup>, InP under He<sup>+</sup> and Ne<sup>+</sup> irradiation can be found in the Appendices. To determine the change of the sputtering yield on the areas of interest, the average signal on the slope was determined first, and divided then by the average signal at normal incidence, i.e., the non-patterned area. Additionally, simulations using the SRIM software were done on InP and Si surfaces with the same ion bombardment conditions (25 keV He<sup>+</sup> and Ne<sup>+</sup>) and range of incidence angles. Using an algorithm written in MATLAB, the SRIM simulation data was used (as  $Y_0$  = sputtering yield of a flat surface, see equations 7 and 8) to plot the Shulga model function. The ripple aspect ratio, i.e. the  $\lambda/h$  ratio, was varied in a for-loop, i.e. as a fitting parameter, to determine the corresponding ripple aspect ratio for each series.

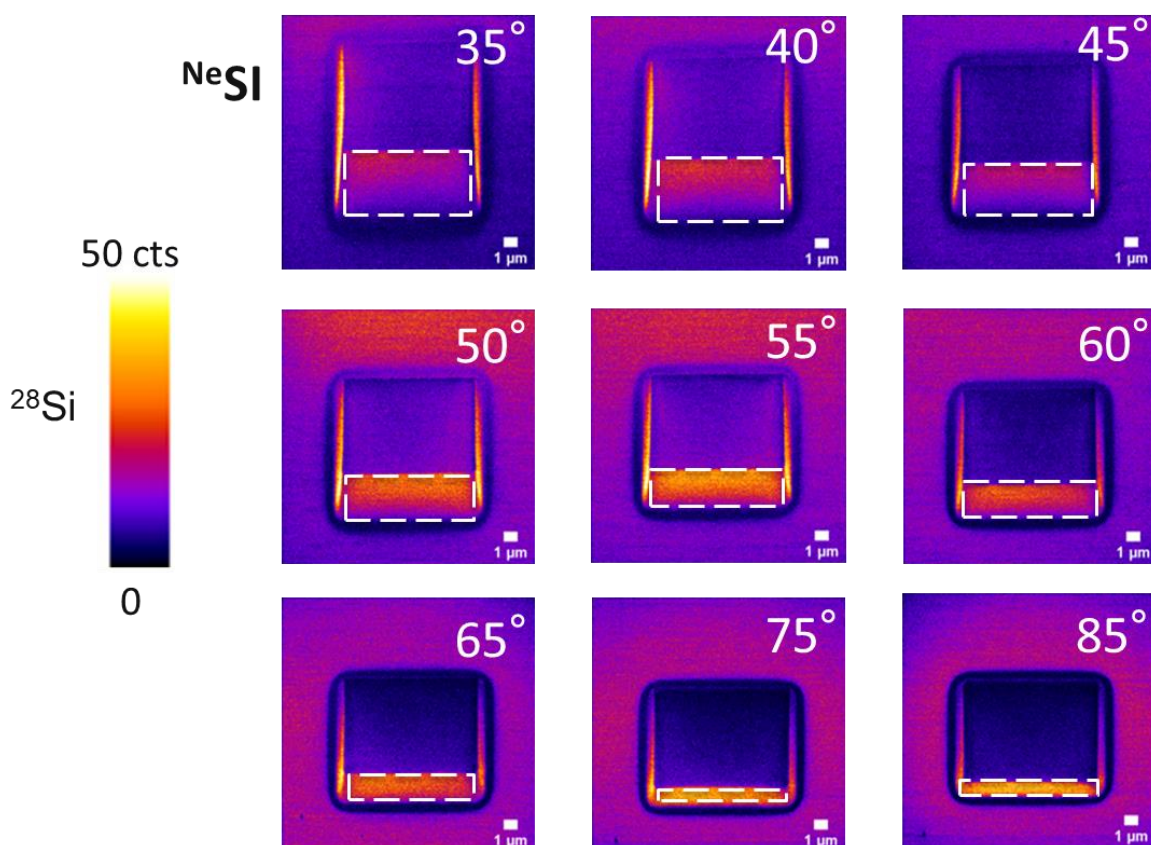


Figure 46: SIMS images of model samples in top view (series shown here: Si sample under 25 keV Ne<sup>+</sup> bombardment). Samples (Si and InP) were analyzed in the HIM-SIMS and images with a He<sup>+</sup>, Ne<sup>+</sup> primary ion beams were acquired. A dashed rectangle marks the area of interest where the signal, i.e. the sputtering yield is studied with respect to the incidence angle (indicated in the image of each structure) of the primary ion beam.

In Figure 47 experimental and simulative results as well as the fitted model functions are shown for both materials (Si, InP) and primary ion species (He<sup>+</sup>, Ne<sup>+</sup>). The SRIM data of the normalized sputtering yields was added in the plots to highlight the difference of the sputtering behavior of a rippled vs. flat surface in each case. The model function data presents in general good agreement with the experimental data and reproduces in each the “kink”-like trend of the normalized sputtering yield, emerging from the shadowing of the rear side of the ripples.

The ratio  $\lambda/h$  of the model function fitted here to the experimental data ( $\lambda/h = 30$  for Si (He<sup>+</sup>),  $\lambda/h = 8$  for Si (Ne<sup>+</sup>),  $\lambda/h = 14$  for InP (He<sup>+</sup>), and  $\lambda/h = 15$  for InP (Ne<sup>+</sup>)) and the ratios determined from the confocal microscopy data ( $\lambda/h = 35$  for Si and  $\lambda/h = 16$  for InP) were found to be in agreement in general. High ratios of  $\lambda/h$  such as measured for silicon under He<sup>+</sup>/Ne<sup>+</sup> irradiation show that rather broad ripples were formed during the Ga<sup>+</sup> milling, whereas the lower  $\lambda/h$  value for InP indicates that steeper ripple structures were created. The discrepancy for the  $h/\lambda$  ratios for the Ne<sup>+</sup> → Si series could result from a higher absolute value of the sputtering yield of Ne<sup>+</sup> vs. He<sup>+</sup> (typically 20 times higher),<sup>59</sup> leading to a change of the aspect ratio of the ripples during the SIMS analysis, i.e. ripples become steeper during the analysis (i.e.,  $\lambda/h$  decreases). Moreover, as the penetration depth of Ne<sup>+</sup> is shallower than for He<sup>+</sup>, the primary ion energy is deposited at a shallower level of the surface,<sup>19</sup> this could favor the vertical growth of the ripples during the SIMS analysis. The estimated ripple aspect ratios for each series are summarized in Table 2.

*Table 2: Estimation of the ripple aspect ratio  $\lambda/h$  determined from line scans on the 3D surface models from confocal microscopy and from fitting SIMS image data with the Shulga model function (equations 7 and 8).*

	He <sup>+</sup> → Si	Ne <sup>+</sup> → Si	He <sup>+</sup> → InP	Ne <sup>+</sup> → InP
<b>Confocal microscopy</b>	35	35	16	16
<b>Shulga model function fit</b>	30	8	14	15

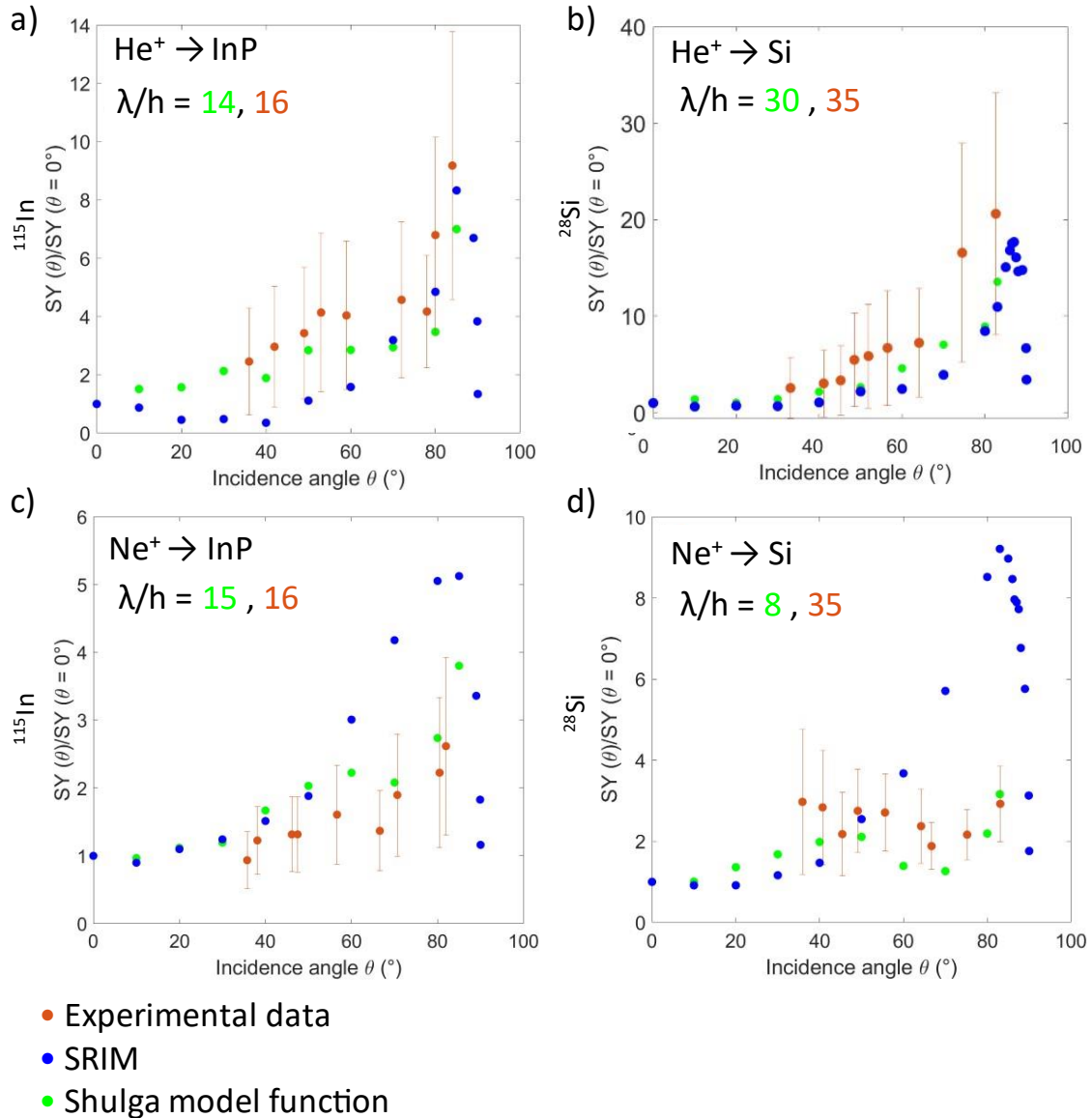


Figure 47: Synthesis of the simulative (blue data points), experimental (orange), and model fitted (green) study sputtering yields vs. incidence angle for indium phosphorus (a, c) and silicon (b, d) surface bombardment with 25 keV He<sup>+</sup> (a, b) and Ne<sup>+</sup> (c, d) primary ions. The  $\lambda/h$  ratios are indicated in each case estimated from the Shulga model fit (green) and from line scans of the confocal microscopy 3D reconstructions (orange).

Considering the SRIM data, the highest value of the normalized sputtering yield for He<sup>+</sup> vs. Ne<sup>+</sup> (e.g., for He<sup>+</sup> → Si up to 20, thus twice as high compared to Ne<sup>+</sup>, with Ne<sup>+</sup> → Si only up to 10) and for InP vs. Si targets can be explained by the penetration depth of the considered primary ion species in the target material (penetration depths from SRIM at 25 keV at normal incidence: He<sup>+</sup> → InP: 180 nm, He<sup>+</sup> → Si: 240 nm, Ne<sup>+</sup> → InP: 48 nm, He<sup>+</sup> → Si: 58 nm). As

lighter ions penetrate (in this case  $\text{He}^+$ ) deeper into the material at normal incidence the contribution of mechanism 2 for the sputtering yield (mechanisms 1 and 2 discussed in this chapter in section 1.2) is almost negligible compared to ions which are stopped in shallower levels on the surface (here  $\text{Ne}^+$ ). When bombarding at oblique incidence angles, the contribution of mechanism 2 to the sputtering yield becomes at this point much more important for the lighter ion species ( $\text{He}^+$ ) and therefore the normalized sputtering yield is higher than for ions whose penetration depth is shallow initially at small angles. Hence, for  $\text{He}^+$  on average the values of the normalized sputtering yield, particularly at oblique incidence angles, are higher than for  $\text{Ne}^+$  as the penetration depth at  $0^\circ$  incidence is higher. A similar argument can be used when considering a single primary ion species (either  $\text{He}^+$  or  $\text{Ne}^+$ ) and studying two different materials (InP, Si).  $\text{He}^+$ , respectively  $\text{Ne}^+$  ions, penetrate deeper into Si than into InP, which induces higher normalized sputtering yields at oblique incidence angles.

It is worth noting that for grazing incidence angles  $> 85^\circ$ , while for flat surfaces the simulated sputtering yield decreases, in the case of the experimental results the normalized sputter yield (of a flat surface in this kind of model samples) is expected to increase further due to lateral escaping of SIs from the edge of the patterned slope (i.e., due to the edge effect).

The variation of the SI signal on the inclined surfaces in the SIMS images led to relatively high standard deviations (on average 60 %) of the normalized sputtering yield (see experimental data in Figure 47). The relatively high noise in the SIMS images (in particular for the  $\text{He}^+$  series) was a significant factor contributing to the high standard deviations and could be improved by using oxygen flooding (see chapter 4). A reason for the high signal deviations on the slope could be an angular and/or positional dependence of the instrumental transmission with respect to the SI emission (more detailed studies will be presented later in this chapter in section 2). Another reason for this high standard deviation could be that the ripples present a non-uniform aspect ratio, leading to strong variations in the signal, whereas in Shulga's model regular pattern of ripples is assumed throughout the surface. However, it is worth noting that more series of measurements on additional model samples (data not shown here) showed that the reproducibility was quite good, as from one series to the other a standard deviation (for the normalized sputtering yield) of only 5 % was found.

Here we have used the 3D + 1 method, by correlating 3D surface information from confocal microscopy and analytical information from SIMS, to study variations of the sputtering yield

vs. the incidence angle of the primary ion beam. Sputtering yields were estimated from SIMS image data acquired on patterned samples. This experimental data was fitted with sputtering models and showed high agreement in each case. We showed that these theoretical models developed and discussed originally for heavier  $O_2^+$  (Wittmaack's model)<sup>97</sup> and  $Ar^+$  primary ions (Shulga),<sup>20</sup> are also applicable for very light projectiles, in this case  $He^+$  and  $Ne^+$ . Moreover, we have observed higher changes of the sputtering yields compared to normal incidence for  $He^+$  than for  $Ne^+$  meaning that SIMS images acquired with  $He^+$  are subjected to more pronounced artefacts, as the SI intensity varies stronger compared to normal incidence.

#### 1.4 Numerical algorithms for topographical artefact analysis in SIMS images

After studying the sputtering yield for model samples, in a next step we will move towards more complex samples. In a series of case studies, we will use numerical algorithms which analyze 3D + 1 reconstructions to study local variations of sputtering yield and to correct topographical artefacts in SIMS images.

##### 1.4.1 Ion beam incidence angle and sputtering yield estimation

In a first example, a 3D + 1 surface reconstruction of a calcite crystal was used to develop a numerical algorithm to study locally sputtering yields vs. incidence angles. A calcite crystal was chosen here, as it presents very flat rectangular surfaces and has a homogeneous concentration of  $\text{CaCO}_3$  over the entire surface of the crystal. In contrast to the model sample study in section 1.3 of this chapter, the idea was here to study the sputtering yield on a sample with a relatively flat topography (i.e., without ripples from  $\text{Ga}^+$  FIB milling).

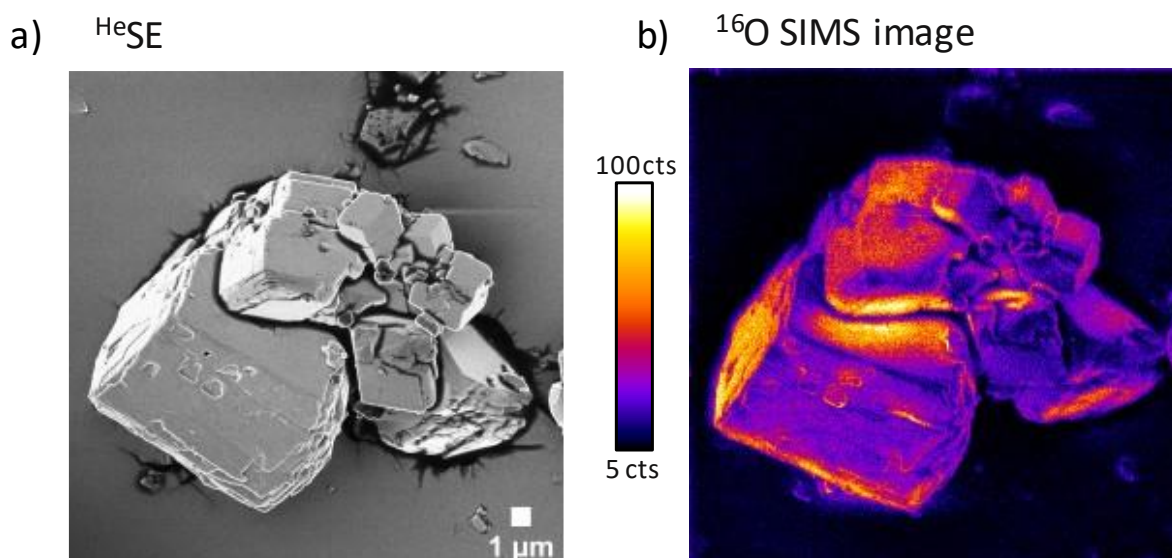


Figure 48: HIM-SIMS in-situ analysis of a calcite ( $\text{CaCO}_3$ ) structure. a) HIM SE image in top view (25 keV  $\text{He}^+$ ). b) SIMS image of  $^{16}\text{O}^-$  secondary ions (25 keV  $\text{Ne}^+$ ).

The calcite crystal was analyzed in the HIM (Figure 48 a) by acquiring a series of 48 SE images around the crystal. The crystal was then imaged in-situ with SIMS (Figure 48 b). A 3D SE reconstruction from the SE images was created using a photogrammetry software. Exemplary

SE images of the crystal as well as the 3D SE reconstruction are shown in the Appendices. The modeled 3D surface of the crystal was then used to estimate the local incidence angle of the primary ion beam.

In order to determine the local incidence angle for a specific area in the SIMS image, a 2D image containing in each pixel the incidence angle information was created using the 3D SE model. To do so, the 3D SE surface model was imported into the MATLAB environment as a point cloud. A virtual 2D image plane was positioned above the 3D model and subdivided into a given pixel raster size. For each pixel, the closest vertical 3D point to the 3D model was calculated and then the corresponding angle between the local normal vector and the vertical direction (i.e., the incidence angle of the primary ion beam) was determined (Figure 49 a). This angle information was projected onto the virtual image plane. Thus, the incidence angle image (Figure 49 b), obtained purely from the 3D SE reconstruction, contains for each pixel the estimated incidence angle of the primary ion beam during the SIMS analysis, ranging from  $0^\circ$  (normal incidence) to  $90^\circ$  (vertical surface).

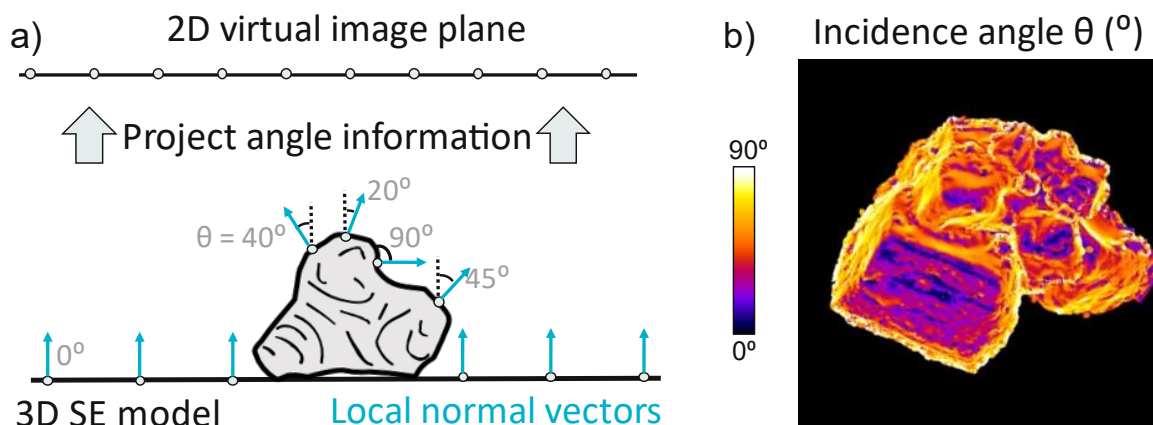


Figure 49: Estimation of the local incidence angle of the primary ion beam incidence angle using a 3D surface model a calcite crystal. a) Schematic illustration showing the creation of an incidence angle image from the 3D SE reconstruction of the crystal. b) Incidence angle image showing in each pixel the local incidence angle of primary ion beam. The incidence angle of the wafer was set arbitrarily to  $0^\circ$ .

In the following, the change of the sputtering yield of oxygen with respect to the incidence angle of the primary ion beam was studied. In the calcite structure, zones with relatively flat

surfaces were identified by inspection of the HIM SE top view image (Figure 48 a). For each zone, the pixel intensity of the SIMS image was associated to its corresponding incidence angle (determined from the incidence angle image from Figure 49 b) and collected in a single dataset. The signal was normalized with respect to the signal acquired in an area at (respectively close to) normal incidence.

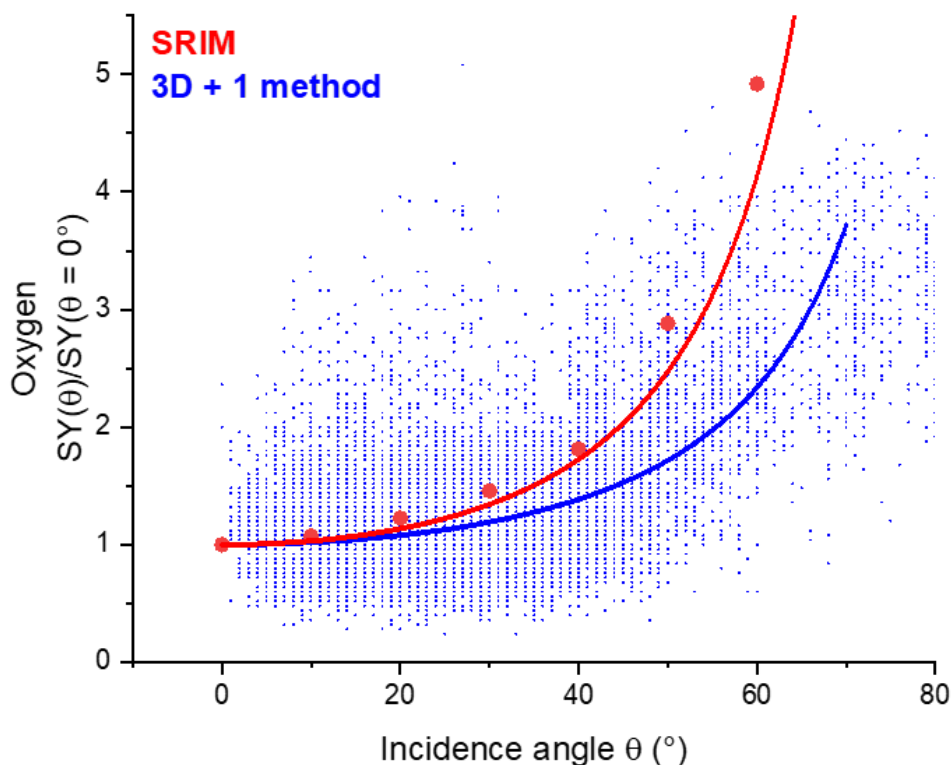


Figure 50: Plot of the estimated normalized sputtering yields,  $SY(\vartheta)/SY(\vartheta = 0^{\circ})$ , of oxygen from SRIM (25 keV  $Ne^{+}$ ) on a  $CaCO_3$  matrix (red) and using the 3D + 1 method (blue) performed on the calcite structure (shown in Figure 48). For both datasets, an inverse cosine function (equation 6) was fitted to the data for incidence angles ranging from  $0^{\circ}$  to  $70^{\circ}$ .

The plot of the normalized sputtering yield of calcium versus the incidence angle is shown in Figure 50. SRIM simulations of 25 keV  $Ne^{+}$  shot onto a  $CaCO_3$  matrix were performed for the same range of incidence angles and were added in the plot. The cosine function from equation 6 (Sigmund's theory, see section 1.2.1 earlier in this chapter) was fitted to both datasets. Comparing the overall trend, both datasets show a reasonable agreement between each other, with a tendency to underestimate the normalized sputtering yields for higher incidence

angles. The high variation of the for a given incidence angle range results presumably from noise in the SIMS image and could be improved by using higher counting. Factors leading to underestimation of the normalized sputtering yield using the 3D + 1 method could be (besides the high variation of the data) due to artefacts/distortions in the 3D SE reconstruction or locally reduced signal resulting from a restricted acceptance angle of the spectrometer (see case study later in this chapter in section 2).

As in this case the concentration of  $\text{CaCO}_3$  is expected to be homogeneous in calcite crystals and analysis parameters, including the transmission, the ionization probability, the ion beam density, and the analyzed area (see equation 1 in chapter 1) are constant, the variation of the signal in the SIMS image (Figure 48 b) is due to the changes of the sputtering yield. The agreement with Sigmund's cosine model function and the SRIM data shows that studying the sputtering yield with the 3D + 1 method is consistent and that surface modeling using the 3D + 1 method provides reasonable estimations of the angular sputtering yield.

## 1.4.2 Investigation of the SIMS signal variation in photovoltaic materials

Recent progress on CIGS solar cells allowed to reach efficiencies above 18 %.<sup>98</sup> In particular, exposition of the sample with rubidium fluoride (RbF) by a post-deposition treatment (PDT) has been shown to increase the solar cell efficiency even more, by 0.5 % as shown by Kaczynski et al.<sup>98</sup>

Studying the faith of Rb in this case is crucial to understand the reaction of the CIGS sample with Rb and further improve the efficiency of CIGS solar cells. Wirtz et al.<sup>39</sup> have shown in SIMS analyses that by correlating HIM SE and SIMS images, after RbF treatment a distinct segregation of rubidium on CIGS grain boundaries was observable as well as absence of rubidium on the surfaces of the grains (*Figure 51*). However, the correlation between the image grain boundaries and the higher <sup>85</sup>Rb SI intensity was done purely by inspection of the SE and SIMS images. However, if the segregation is less “evident”, i.e., Rb detected on both grain surfaces and grain boundaries, differentiating, whether a higher SI signal on the grain boundary is originating from a higher concentration or/and a topography effect, is not obvious.

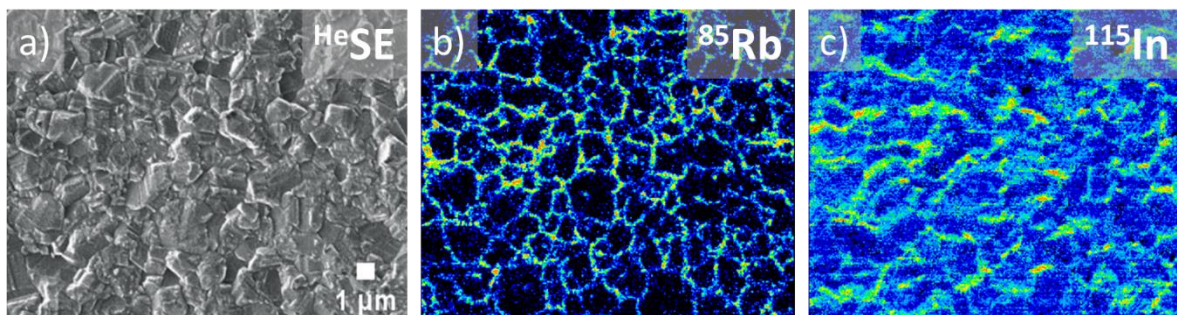


*Figure 51: A CIGS solar cell imaged in the HIM-SIMS in SE mode (a: 25 keV He<sup>+</sup>) and in SIMS (b and c: 25 keV Ne<sup>+</sup>) for the rubidium-85 (b) and indium-115 (c) signals on the same area. Inspection of both images reveals clear segregation of rubidium on the grain boundaries (data from Wirtz et al.).<sup>39</sup>*

Here the 3D + 1 method was used to study the exact topography of an RbF exposed CIGS solar cell and correlate it with the local change of the SI intensity to determine whether the preferential deposition of rubidium took place on the grain boundaries or homogeneously on the surface of the material. For a CIGS solar cell treated with RbF, indium presents a relatively

homogenous concentration on the surface of the CIGS structure<sup>99,100</sup> and will serve as a reference to compare with the rubidium signal. If a more pronounced segregation of rubidium took place on the grain boundaries, the normalized SI signal (with respect to normal incidence) is expected to be significantly higher compared to indium, as in addition to the higher sputtering yield at oblique incidence angles, a higher concentration would result in a higher SI intensity compared to grain surfaces.

The CIGS sample was deposited on a glass substrate. During the deposition process, minor cracks in the CIGS thin film were formed. An isolated CIGS structure (of about  $5 \times 5 \mu\text{m}^2$ ) was identified and in total 48 SE images were acquired around this ROI (Figure 52 a). For the SIMS analysis, the indium-115 and rubidium-85 SI were imaged (Figure 52 b). Using the SE images a 3D SE reconstruction was obtained using a photogrammetry software. SIMS images of  $^{115}\text{In}$  and  $^{85}\text{Rb}$  were overlaid with the 3D SE model to create two different 4D surface reconstructions (only the 4D model of  $^{115}\text{In}$  shown in Figure 53 a).

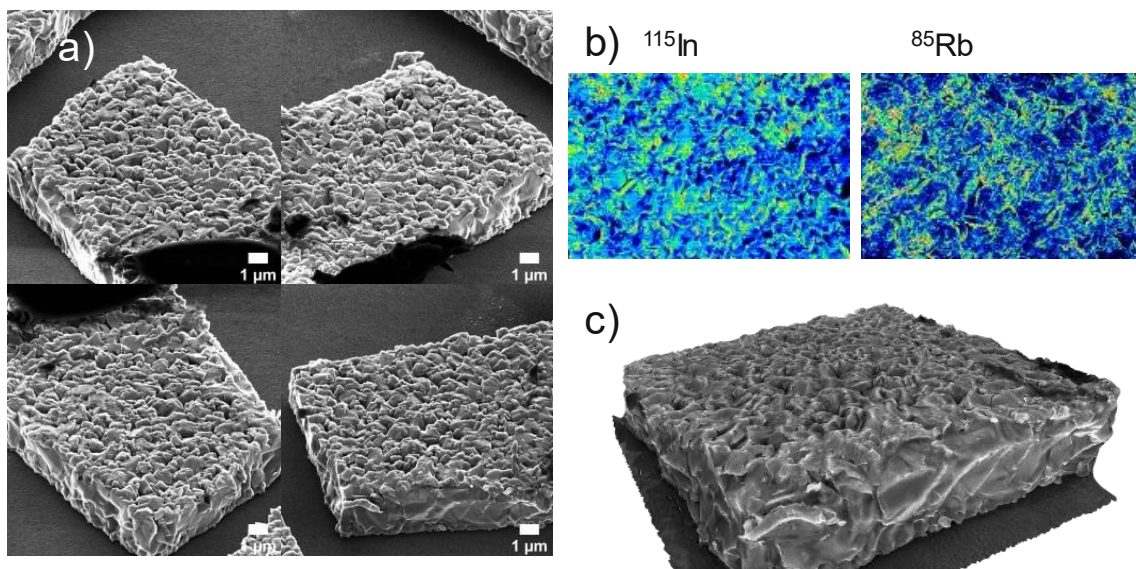


Figure 52: HIM-SIMS analysis and 3D surface reconstruction of a CIGS solar cell sample to study the rubidium distribution on the surface. a) SE image acquisition at oblique stage tilt angles. b) SIMS images of  $^{115}\text{In}$  and  $^{85}\text{Rb}$ . c) Photogrammetric 3D SE reconstruction (Figure adapted from Ost et al.).<sup>101</sup>

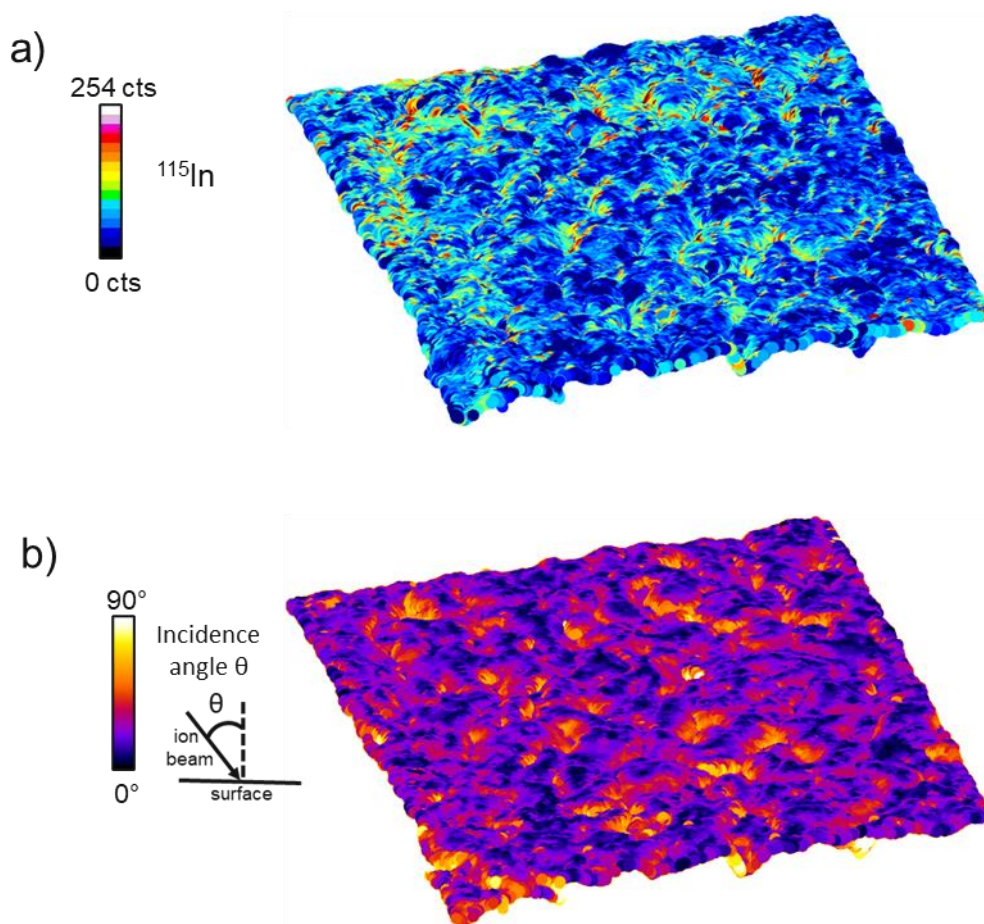


Figure 53: 3D + 1 reconstruction and numerical analysis of a CIGS structure. a) Side view of the 4D surface reconstruction obtained by the projection of the SIMS image in Figure 52 b) and the 3D SE model in Figure 52 c). e) Color coded visualization of the local incidence angle obtained from a numerical analysis of the 3D SE model from Figure 52 c).

To allow an automatized analysis process of the topography the 4D surface models were analyzed numerically. To do so, the reconstructions were imported as point clouds in a MATLAB environment. Here the local incidence angle was calculated using the local normal vectors and attributed to each reconstructed 3D point. A color-coded visualization of the local incidence angles of the reconstructed surface is shown in Figure 53 b).

Using the normal vectors, also local separation between grain surfaces and boundaries was made, allowing to compare the SI signal variation with respect to the topography. In a for-loop for each 3D point of the areas identified as grain boundaries, the incidence angle information was associated to the corresponding indium-115 and rubidium-85 signals. The average signal ( $^{115}\text{In}$  and  $^{85}\text{Rb}$ ) for defined ranges of incidence angles was calculated and

normalized with respect to the average signal at normal incidence. Table 3 contains the normalized average signal for  $^{115}\text{In}$  and  $^{85}\text{Rb}$  for specific incidence angle ranges. For both elements, it shows on average an increase of the SI intensity for oblique angles and a slight decrease for grazing angles. The standard deviation of these ratios for both  $^{115}\text{In}$  and  $^{85}\text{Rb}$  was calculated for each incidence angle binning segment and was found on average (for all the binning segments) to be equal to 0.8. The relatively high standard deviation results presumably from noise in the SIMS image and minor distortions in the 3D reconstruction leading to local artefacts for the incidence angle estimation. On average, the increase of the  $^{85}\text{Rb}$  signal at the grain boundaries compared to normal incidence on the grain surfaces follows a similar trend as for  $^{115}\text{In}$ . A slightly higher SI ratio for  $^{85}\text{Rb}$  for incidence angle ranges  $> 50^\circ$  lies within the standard deviation and therefore negligible.

As for both  $^{115}\text{In}$  and  $^{85}\text{Rb}$  the normalized SI intensity shows a very similar trend, here no particular segregation of rubidium is found on the grain boundaries of the CIGS structure, which means that here the deposition of Rb took place smoothly on both grain surfaces and boundaries of this CIGS structure and that variations in the SI intensity are due to topographical effects, i.e. changes in the sputtering yield.

*Table 3: Estimation of normalized sputtering yields (SY) of a CIGS structure for  $^{115}\text{In}$  and  $^{85}\text{Rb}$  from the 3D + 1 overlay of the 3D SE reconstructions with the corresponding SIMS images.*

$\theta$	[20°, 30°]	[40°, 50°]	[60°, 70°]	[80°, 89°]
$\text{SY}_{\text{In}}(\theta)/\text{SY}_{\text{In}}(\theta = 0^\circ)$	1.23	1.36	1.29	1.15
$\text{SY}_{\text{Rb}}(\theta)/\text{SY}_{\text{Rb}}(\theta = 0^\circ)$	1.22	1.33	1.46	1.36

1.4.3 *Topographical artefact SIMS image correction*

As we have seen earlier, sample topography has a strong influence of the sputtering yield and leads to strong changes in the secondary ion intensity in a SIMS image. Correcting topographical artefacts will help to estimate accurately concentration gradients in SIMS images and thus to acquire a deeper understanding of the sample.

In this section, an algorithm was developed to correct (or reduce) the contribution of topography in a SIMS image using a 3D + 1 reconstruction. In the following two paragraphs we present our algorithm using a reconstruction of a soil microaggregate discussed previously in chapter 2 section 2.3 (Figure 37 and Figure 38). The aluminum oxide ( $^{27}\text{Al}^{16}\text{O}$ ) image (acquired using the CAMECA NanoSIMS 50L) was studied here as it presents a homogeneous distribution on the surface of the microaggregate.

From the 3D SE model of the soil microaggregate an incidence angle image was created (Figure 54 a) using the method discussed earlier in this chapter in section 1.4.1. This angle image contains in each pixel the incidence angle information of the corresponding pixel of the  $^{27}\text{Al}^{16}\text{O}$  image. A clear correlation of the angle image (Figure 54 a) and the  $^{27}\text{Al}^{16}\text{O}$  image (Figure 54 b) can be observed as the secondary ion intensity tends to increase for higher angles, in particular at the edges of the particle. In order to give a mathematical estimate of this correlation, the Pearson's correlation coefficient between both images was calculated, giving a reasonably high correlation of 0.75. The wafer was not considered for this calculation. Thus, the high correlation between the incidence angle and SIMS image shows that the variation of the secondary ion signal intensity is mainly due here to the topography of the sample, i.e. local changes of the sputtering yield. Factors influencing the correlation could be artefacts in the 3D reconstruction, charging of the sample leading locally to reduced signal, or a restricted acceptance angle of the spectrometer leading to shadowing effects<sup>73</sup> (discussed later in this chapter in section 2).

In the following, the incidence angle information was used to perform a "correction" of the SIMS image. Each pixel of the SIMS image was divided by the normalized sputtering yield (normalized with respect to normal incidence) determined from SRIM simulations performed on an aluminum oxide matrix for a range of different incidence angles from 0° to 90°. To do so, the incidence angle of each pixel of the SIMS image was determined from the angle image.

Then, the SI intensity for this pixel was divided by the normalized sputtering yield corresponding to this incidence angle. By raster scanning the SIMS image, this process was repeated for all the pixels in the SIMS image and each pixel was divided by its corresponding normalized sputtering yield (Figure 54 c). It is worth noting that here for simplicity the change of the ionization probability resulting from locally non-constant (due to sample topography)  $\text{Cs}^+$  implantations was not taken into account. Consideration of this aspect for the image correction could be a subject for future studies.

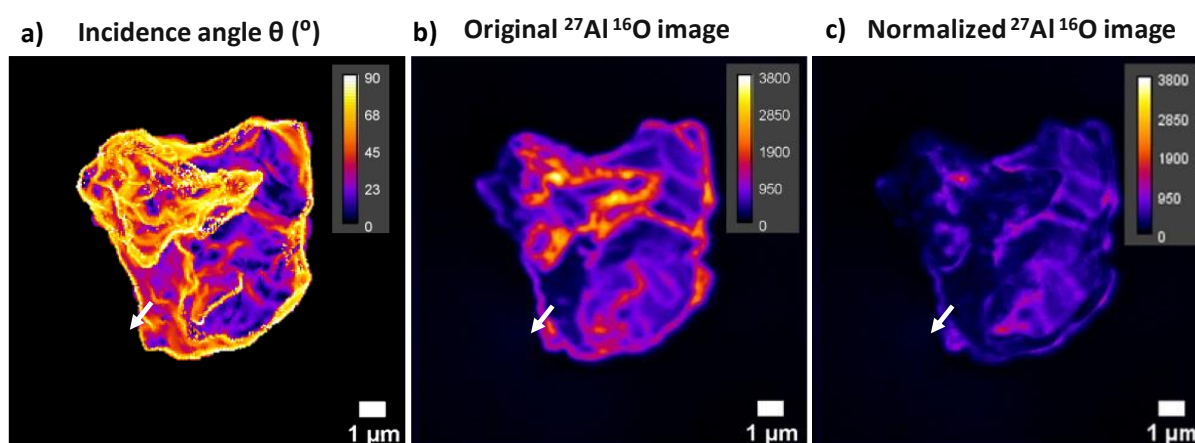


Figure 54: Topographical artefact correction of a SIMS image. a) Top view incidence angle image obtained from the 3D SE model of the soil microaggregate presented in Figure 38 a) and b). b) Raw  $^{27}\text{Al}^{16}\text{O}$  NanoSIMS 50L image. c) SIMS image after normalization with respect to the local increase of the sputtering yield. Line scans shown in the next figure are indicated here by white arrows.

To visualize the effect of the normalization, line scans on the microaggregate's edge in the images in Figure 54 were performed. For the angle image, it shows that for this segment the incidence angle increased strongly to up to  $70^\circ$  (Figure 55 a). Performing the scan on the raw SIMS image (Figure 54 b) gives the same (increasing) trend of the signal as for the incidence angle, which indicates that the signal increase is due to a purely topographic effect. As studied in the previous sections, areas with incidence angles ranging from  $65^\circ$  to  $75^\circ$  are prone to very strong topographic effects, as the sputtering yield can increase by multiple times compared to normal incidence. The line scan of the image after the normalization (Figure 54 c) shows a strong decrease of the signal for pixels (by 60 %) at the highest incidence angle, i.e. the edge of the microaggregate (Figure 55 b). On the other hand, in this segment for pixels with a low incidence angle, e.g. at  $0.2 \mu\text{m}$  of the line scan, the intensity of the image is changed slightly

as the incidence angle is only 35° in this case. Assuming that the concentration of  $^{27}\text{Al}^{16}\text{O}$  is relatively homogeneous over the surface, a homogenization of the signal is consistent, since variation of the signal is (mostly) due to topographic effects.

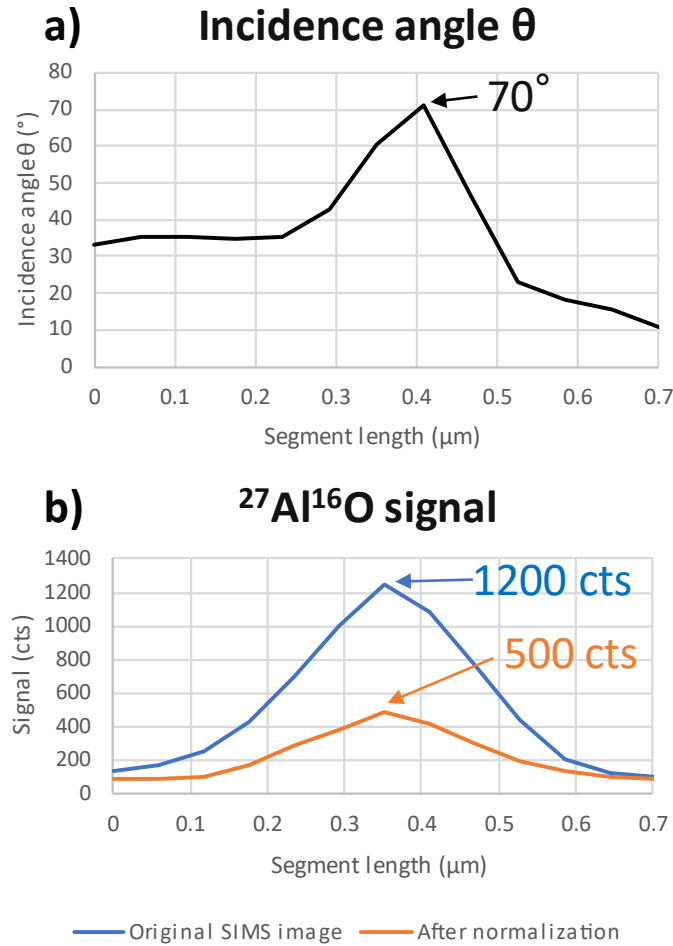


Figure 55: Line scans of (a) the incidence angle image and (b) the raw  $^{27}\text{Al}^{16}\text{O}$  SIMS image (shown in Figure 54) and after normalization with respect to the average increase of the sputtering yield due to the non-zero incidence angle of the primary ion beam.

Yet, an accurate correction of a SIMS image using the presented algorithm is restrained by certain limits, which will be discussed in the following paragraph. First, images presenting pronounced shadowing effects due to a restricted acceptance angle of the spectrometer cannot be fully corrected as signal variations are not only due to local changes in the sputtering yield but also in the spectrometer transmission<sup>73</sup> (more detailed considerations

later in this chapter in section 2). Secondly, for complex samples/matrices estimating the normalized sputtering yield using SRIM is a particularly challenging task, as the elemental composition is often not known exactly or is not homogeneous within the sample surface, which could lead to over- or underestimation of the correction coefficients. Thirdly, local topographic artefacts in the 3D SE model, resulting for instance from noise, erroneous camera alignment, lack of matches (see chapter 2 section 2) can create surface distortions. These distortions can lead to artefacts in the angle image (i.e., the incidence angles information) and thus inaccurate attribution of the normalization coefficients.

## 2. Evaluation of the mass spectrometer transmission dependency from the ion emission direction

### 2.1 Introduction

Shadowing effects in SIMS images have been observed and studied in the past by Vollnhals and Wirtz.<sup>73</sup> Figure 56 shows an example of a SIMS image of a calcite crystal agglomeration with a pronounced shadowing effect. While the HIM SE image (Figure 56 a) shows a relatively heterogeneous distribution of oblique surfaces with various surface slope angles, the SIMS image (Figure 56 b) presents on average high signal for surfaces (whose normal vector is) pointing to upper right side of the image and very low signal for surface pointing to the lower left side (areas indicated by arrows), which is clearly not due to variations in the sputtering yields. This is not due to the change of the sputtering yield, but due to a limited acceptance angle of the mass spectrometer, resulting in a lower transmission for certain ion emission directions compared to others. Studying the extend of this artefact is crucial to differentiate from local sputtering yield variations and hence for a more accurate interpretation of SIMS images.

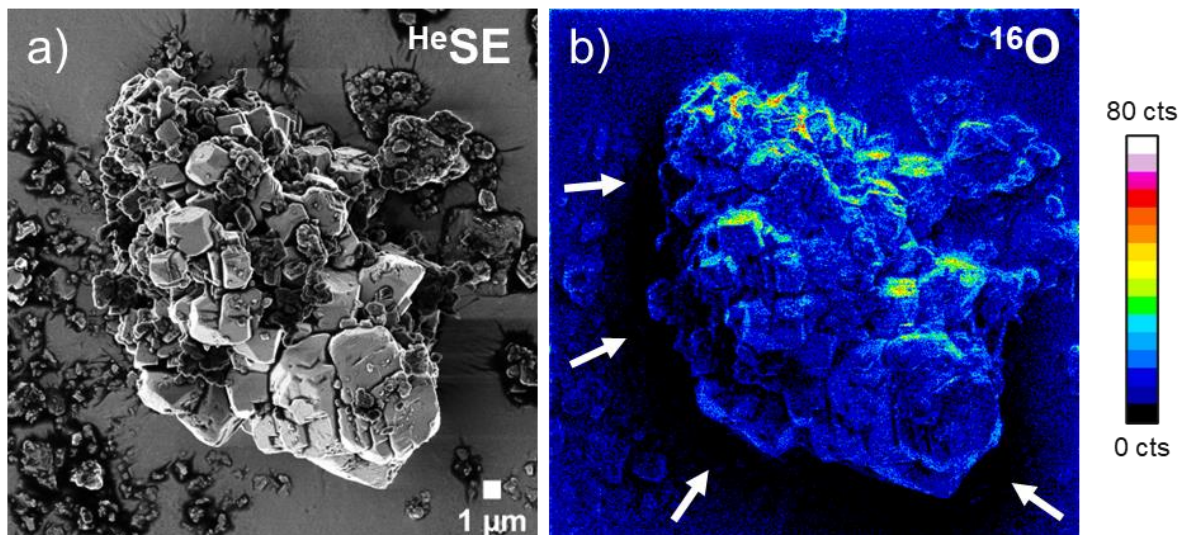


Figure 56: HIM-SIMS analysis of an agglomeration of calcite crystals. a) HIM SE image (25 keV He<sup>+</sup>), b) <sup>16</sup>O SIMS image (25 keV Ne<sup>+</sup>). The white arrows point to areas with a strong shadowing effect.

In a first step, we will investigate by simulations the influence of secondary ion emission angle on instrumental transmission. Secondly, using the 3D + 1 reconstruction of a patterned structure the SI intensity with respect to the topography will be studied.

## 2.2 Ion trajectory simulations

To study the change of the instrumental transmission vs. the secondary ion emission angle, simulations were performed with a software package called "SIMION",<sup>102,103</sup> allowing to calculate electric fields and charged particle trajectories in electric fields. Here ion trajectories were calculated in a virtual 3D space simulating the SI optics of the HIM-SIMS instrument with specific beam alignment parameters. Simulations can be done for specific azimuthal ( $\theta$ ) and polar ( $\varphi$ ) emission angles of SIs leaving the sample.

Figure 57 a) shows the simulated path of SIs in the extraction box leaving the sample at a polar angle of  $70^\circ$ , revealing that a considerable amount of SIs are hitting the walls of the extraction system and are thus lost.

In the following, the transmission was studied for different ranges of azimuthal and polar angles. Figure 57 b) shows a polar plot with the change of the transmission with respect to the azimuthal and polar emission directions. The transmission varies strongly with respect to the azimuthal and polar direction of the SI emission, i.e., the transmission is highest at  $\theta = 0^\circ$  and  $\theta = 180^\circ$  (up to 60 % for a polar angle  $\varphi = 20^\circ$ ), and lowest at  $90^\circ$  and  $270^\circ$  (down to 0.5 % for  $\varphi = 70^\circ$ ). The transmission is therefore highly non-isotropic using this specific beam alignment. The design of the electrostatic sector (spherical sector configuration with partly cut lateral sides) could favor a non-isotropy of the transmission. As inner and outer spherical deflectors located in the SIMS extraction box are aligned to the x-axis (see Figure 57 a), SIs perpendicular to the y-axis ( $\theta = 0^\circ$  or  $\theta = 180^\circ$ ) have the highest transmission, since their path is aligned and passes through the center of the spherical electrostatic sector. On the other hand, SIs leaving the sample in the orthogonal direction, i.e. with  $\theta = 90^\circ$  or  $\theta = 270^\circ$ , most of the SIs cannot be focused back to the center of the optical axis as the spherical electrostatic sector is cut partly on the sides. This design of the spherical electrostatic sector

was chosen to fit the SI extraction optics into a compact extraction box allowing to insert and retract for a more efficient workflow management.

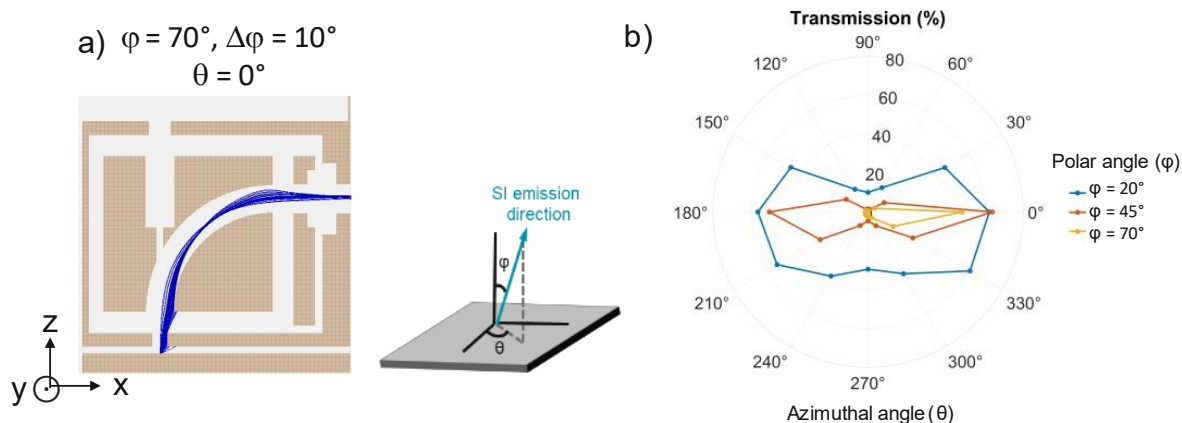


Figure 57: Ion trajectory simulations (SIMION software) of the HIM-SIMS. a) Visualization of the SI extraction system of the HIM-SIMS and the simulated path of  $^{115}\text{In}$  secondary ions leaving the sample surface (polar emission angle:  $\varphi = 70^\circ \pm 10^\circ$ , azimuthal:  $\vartheta = 0^\circ$ ). The schematic on the lower right illustrates the polar and azimuthal emission directions from the sample. b) Polar plot showing the transmission for ions for specific secondary ion emission angles.

It is worth noting that here only the angular dependence on the transmission (at center of the extraction box) was simulated here and a positional variation (i.e., different from the center of the FOV) could be a subject for future studies. Furthermore, at this stage it is not fully clear whether these transmission curves could potentially be improved/homogenized with a different beam alignment or are independent of the alignment. A simulative study on the change of the transmission by varying beam alignment could be investigated in the future.

### 2.3 3D + 1 reconstruction to study directional dependency of the transmission

Here we will study the change of the instrumental transmission on a SIMS image of a patterned structure. A pyramid was milled on an InP wafer using the  $\text{Ga}^+$  FIB of the FIB-SEM-SIMS instrument. A 3D reconstruction was obtained by confocal microscopy (Figure 58 a). Line scans performed on the 3D surface model (not shown here) confirmed that no significant

differences of the surface slope from one side of the pyramid to the other is measurable (about  $40^\circ$  incidence angle in each case). The sample was imaged ( $^{115}\text{In}$  signal) then in the FIB-SEM-SIMS instrument under 30 keV  $\text{Ga}^+$  bombardment (Figure 58 b).

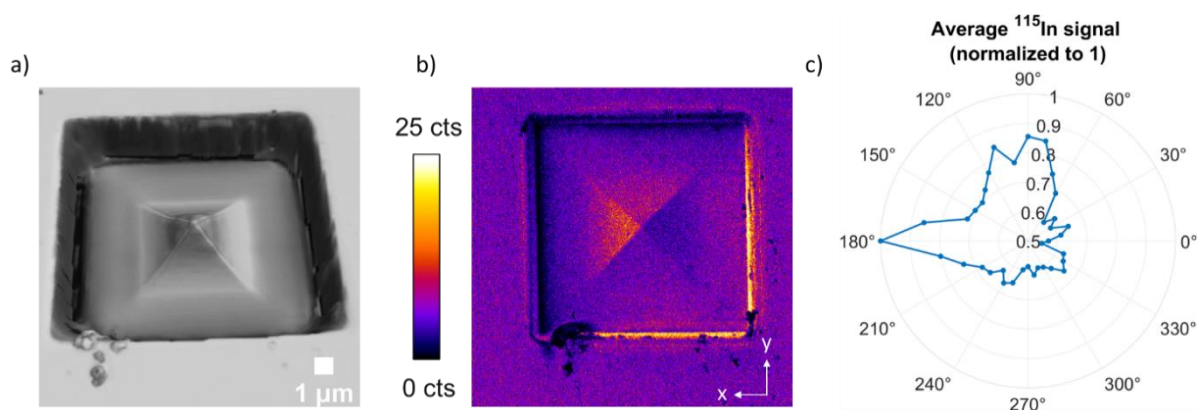


*Figure 58: Analysis of 3D + 1 reconstruction of patterned pyramid to study the directional dependence of the spectrometer transmission. a) Side view of the 3D surface model obtained from confocal microscopy analysis. b) SIMS image (30 keV  $\text{Ga}^+$ ) of the  $^{115}\text{In}$  signal acquired in the FIB-SEM-SIMS. c) Polar plot of the average signal (normalized to 1) from all the surfaces of the pyramid where the local normal vectors point in a specific (azimuthal) direction.*

In the  $^{115}\text{In}$  SIMS image one can see that the lower and right sides present on average a 55 % lower intensity compared to the upper and left sides of the pyramid. These shadowing effects are due purely due to directional changes of the transmission and not to changes in the sputtering yield, since the incidence angles are the same for all the sides of the pyramid.

In order to better estimate the extend of the non-isotropy of the transmission from this SIMS image, the 3D + 1 method was used here to correlate the SIMS image with the 3D surface model. Using a program written in MATLAB, the SI intensity of the  $^{115}\text{In}$  signal of each pixel was associated to the corresponding local topography of the 3D surface model, here represented by the local surface normal vector. The average signal for all the surfaces of the pyramid with a surface normal vector pointing in specific azimuthal directions was calculated and represented in a polar plot (see Figure 58 c). Here the surfaces with a normal vector pointing to  $90^\circ$  and  $180^\circ$  azimuthal directions have the highest transmission, while the  $0^\circ$  and  $270^\circ$  the lowest.

At this stage it is not fully understood why the “favorable” (90°, 180°) and “unfavorable” (0°, 270°) emission directions are opposite to one another, while in the SIMION simulations favorable (0°, 180°) and unfavorable (90°, 270°) directions are alternating by 90° steps. An explanation could be that here due to the relatively small size of the pyramid ( $5 \times 5 \mu\text{m}^2$ ) the secondary ions leaving the surfaces from the pyramid were focused back to the secondary ion optical axis. However, the tip of the pyramid was presumably not well aligned with respect to the center of the optical axis of the primary ion beam, i.e. the ion beam hits the left and upper side of the pyramid (almost) vertically, while for the lower and right sides the primary ion beam has to be deflected more while raster scanning, resulting in a grazing incidence of the beam on the sample, thus lower sputtering yield. It is worth noting that for this case study we have considered only a single polar emission angle ( $\varphi$  direction) as the slope of the pyramid is constant. However, a detailed experimental study on the influence of the polar emission angle could be a subject for future studies.

Here we showed that samples with pronounced topography can be prone to imaging artefacts related to non-isotropic transmission in addition to changes in the sputtering yield. A future solution to mitigate this artefact could be to find first the optimal beam alignment leading to the most isotropic transmission curve and then using this profile in combination with topographic information from a 3D + 1 reconstruction to perform a correction of the SIMS image.

### 3. Chapter summary

In this chapter, we studied changes of the secondary ion intensity in SIMS images, which are due to local variations of the sputtering yield and we proposed a solution to correct topographical artefacts in SIMS images. Here the 3D + 1 method presented in chapter 2 was used to model the sample topography and associate this local topographical information to the secondary ion intensity from SIMS images.

We reviewed briefly fundamental sputtering mechanisms for flat and rippled surfaces. Model samples with surfaces oriented at different angles with respect to the He<sup>+</sup> and Ne<sup>+</sup> primary ions were imaged to study the SI signal on these surfaces, i.e., the sputtering yield vs. the incidence angle of the primary ion beam. SRIM simulations for flat surfaces were performed under the same analytical conditions as for the model sample experimental analysis (i.e., material compositions, primary ions, acceleration energy, incidence angles) and discussed. However, the model samples presented rippled patterns on their surface produced during the milling process, reflected by the surface sputtering behavior. The data for light ions (He<sup>+</sup>, Ne<sup>+</sup>) was described successfully with a model function established by Wittmaack<sup>97</sup> and Shulga,<sup>20</sup> originally studied for surface sputtering by heavier ions (O<sub>2</sub><sup>+</sup>, Ar<sup>+</sup>).

The 3D + 1 method was then applied to micro-sized minerals and solar cell surfaces to estimate local variations of the sputtering yield from the SI intensity. From the 3D + 1 reconstruction of a calcite crystal, a numerical algorithm was built to provide the local sputtering yield which were compared to SRIM simulations. A 4D reconstruction of a CIGS solar cell was then analyzed numerically to study potential grain boundary segregation of rubidium by comparing locally the change of the SI intensity of rubidium and indium. Then, by estimating the incidence angle for each pixel of the SIMS image, a normalization process was performed to remove/reduce topographic effects from the SIMS image of a soil microaggregate. Moreover, the 3D + 1 method was used to study the directional dependency of the mass spectrometer transmission with respect to the ion emission angle.

## Chapter 4: Optimization of positive secondary ion yields in Ne<sup>+</sup> by reactive gas flooding

### 1. Introduction

As we discussed in chapter 1 (section 5), the gas field ion source in the HIM-SIMS uses Ne<sup>+</sup> as primary ions and reaches probe sizes of < 2 nm. Yet, the analyzed voxels are small (typically 20 × 20 × 10 nm<sup>3</sup>) and the ionization yield is low for non-reactive primary ions. Thus, our aim here is to improve the detection limit. Oxygen flooding is a known method to improve the ionization probability of electropositive elements by creating artificially surface oxidation. However, up to now oxygen flooding has been explored for depth profiling and imaging applications with lower resolution, thus lower brightness ion sources. In the HIM-SIMS instrument, a capillary positioned inside the SIMS box extraction above the sample (see Figure 9) allows to flood the surface with gas, e.g. oxygen. In this study, we flooded the samples with oxygen-16 (99.8 % <sup>16</sup>O<sub>2</sub>) and isotopic oxygen-18 (97.4 % <sup>18</sup>O<sub>2</sub>) while performing SIMS analyzes. All the results shown in this chapter are based on our recently submitted manuscript (Ost et al.).<sup>104</sup>

This chapter aims to study first by Monte Carlo (MC) simulations and isotopic oxygen-18 flooding experiments on the HIM-SIMS to better understand and quantify surface adsorption of residual oxygen in the analysis chamber and flooded oxygen. Second, depth profiling experiments are performed to study the improvement of the SI intensity while varying the oxygen gas flux. Third, 2D and 3D imaging was conducted to evaluate the gain of the flooding for the SIMS analysis at sub-20 nm spatial resolution. The experimental studies focus on two elements, silicon-28 on a silicon wafer, a Fin Field-effect (FinFet) transistor, and cobalt binder (<sup>59</sup>Co) in a cemented carbide sample (also called “hard metal”).

## 2. Investigating the flooding process by Monte Carlo simulations

### 2.1 Simulation setup

The presence of oxygen on the surface, in the form of a native oxide layer or through flooding of the sample with oxygen, is known to enhance of positive SI yields in SIMS.<sup>32,64</sup> MC simulations based on the binary collision approximation (BCA) were performed here using the SDTrimSP code<sup>105</sup> on a silicon surface to study the oxygen concentration, originating from a native oxide layer and from the adsorbed oxygen. Under a given primary ion fluence it allows to simulate changes in sample composition and the sputtering yields. Atomic interaction is described by the KrC potential, electronic stopping by the Oen-Robinson model, and integration was performed using the Gauss-Mehler method (sixteen pivots). The surface binding energy  $sbe$  of the target was calculated with the following expression:

$$sbe(i, j) = 0.5 \cdot (Es_i + Es_j) \quad (9)$$

where  $Es_i$  is the atomic surface binding energy of the element  $i$ . The surface binding energy was calculated for each combination of two elements studied here (oxygen, neon, silicon). The bulk densities for each species were taken as the atomic densities here.

The simulations were carried out first on a pristine silicon surface and then on pure silicon with a 2 nm thick oxide layer ( $SiO_2$ ) to simulate the presence of the native oxide layer. The thickness of this layer is in accordance with the spontaneous growth of native oxide layers under air exposure at room temperature reported in literature.<sup>106</sup> Bombardment conditions were chosen as for typical experimental conditions on the HIM-SIMS using 25 keV  $Ne^+$  with a dose per frame of  $2.3 \cdot 10^{13} \frac{ions}{cm^2}$  (dwell time: 1 s/frame), corresponding to 15 pA with a FOV of  $20 \times 20 \mu m^2$ . Flooding of oxygen was simulated by a flow of low energy oxygen atoms at 0.1 eV moving towards the silicon surface. It is worth noting that the simulations under the BCA do not allow to simulate molecules. However, in practice upon adsorption on the surface the oxygen molecules dissociate into atoms, therefore the total number of oxygen atoms on the surface is the same in both cases (i.e., whether they arrive as molecules or atoms to the surface).

## 2.2 Preliminary calculations

Using kinetic gas theory, the flux of surface adsorbed gas molecules was estimated which was necessary for the MC calculations. Here the Hertz-Knudsen equation<sup>2,107</sup> was used to approximate the number of adsorbed oxygen atoms to the material's surface per unit area and time  $j_{O_2}$ :

$$j_{O_2} = \frac{p}{\sqrt{2 \cdot \pi \cdot M \cdot R \cdot T}} \quad (10)$$

where  $p$  is the partial pressure,  $M$  the molar mass,  $R$  the molar gas constant, and  $T$  the temperature (here room temperature: 293 K). This oxygen flux was first determined for regular chamber pressure conditions ( $4 \cdot 10^{-7}$  mbar) and for the highest chamber pressure at which stable measurements can be done in the HIM-SIMS ( $4 \cdot 10^{-5}$  mbar). Using equation 10, the calculated flux of residual and flooded oxygen molecules per unit area and time is  $1.1 \cdot 10^{14} \frac{\text{molecules}}{\text{cm}^2 \cdot \text{s}}$  and  $1.1 \cdot 10^{16} \frac{\text{molecules}}{\text{cm}^2 \cdot \text{s}}$ , respectively, while the total flux  $j_O$  corresponds to the double of  $j_{O_2}$ . For depth profiling with an average ion current density of  $2.3 \cdot 10^{13} \frac{\text{ions}}{\text{cm}^2 \cdot \text{s}}$  (with 25 keV Ne<sup>+</sup> with 15 pA, FOV  $20 \times 20 \mu\text{m}^2$ ), the ratios of oxygen versus neon  $\frac{j_{O_2}}{j_{Ne}}$  correspond to 4.7 (no flooding) and  $4.7 \cdot 10^2$  (with flooding). Yet, for imaging the local primary ion density for a beam focused with a diameter of 4 nm (FW50 of the sputtered atoms),<sup>18</sup> e.g. for 3 pA, is much higher, in this case  $1.5 \cdot 10^{20} \frac{\text{ions}}{\text{cm}^2 \cdot \text{s}}$ . Thus, the  $\frac{j_{O_2}}{j_{Ne}}$  correspond to  $7.3 \cdot 10^{-7}$  at regular pressure and  $7.3 \cdot 10^{-5}$  with flooding, which represent here a lower bound, as these values do not include oxygen transport through diffusion.

In a first set of simulations, diffusion of neon was not taken into account which led to unphysically high concentrations. Subsequently, the diffusion coefficient of neon was fixed to  $10^4 \text{ \AA}^2/\text{ion}$ ,<sup>108,109</sup> and maximum peak concentration was produced in the 10 % range. Simulations with different sticking coefficients were carried out (0.1 %, 1 %, 10 %, and 100 %) and only with 0.1 % physically meaningful results were obtained. Higher sticking coefficients resulted in piling of oxygen on the surface leading to unphysical simulation conditions (0 K temperature on the surface).

## 2.3 Quantification of surface adsorbed residual and flooded oxygen

In order to better understand oxygen flooding under realistic conditions and thus to take into account the native oxide layer, simulations were done for a silicon surface with a 2 nm silicon dioxide layer (SiO<sub>2</sub>). The surface bombardment was simulated first at regular pressure conditions ( $4 \cdot 10^{-7}$  mbar) and then subjected to oxygen gas flooding ( $4 \cdot 10^{-5}$  mbar). Here we differentiated between the adsorbed and the oxygen in the native oxide layer. The surface concentration integrated over a depth of down to 5 Å and normalized to 100 atomic-%, shown in Figure 59. For simplicity Ne<sup>+</sup> implantations are not shown here. In Figure 60, we provide the depth distributions simulated for a dose of  $4 \cdot 10^{16}$  ions/cm<sup>2</sup>, corresponding to the state at final value of the fluence in Figure 59.

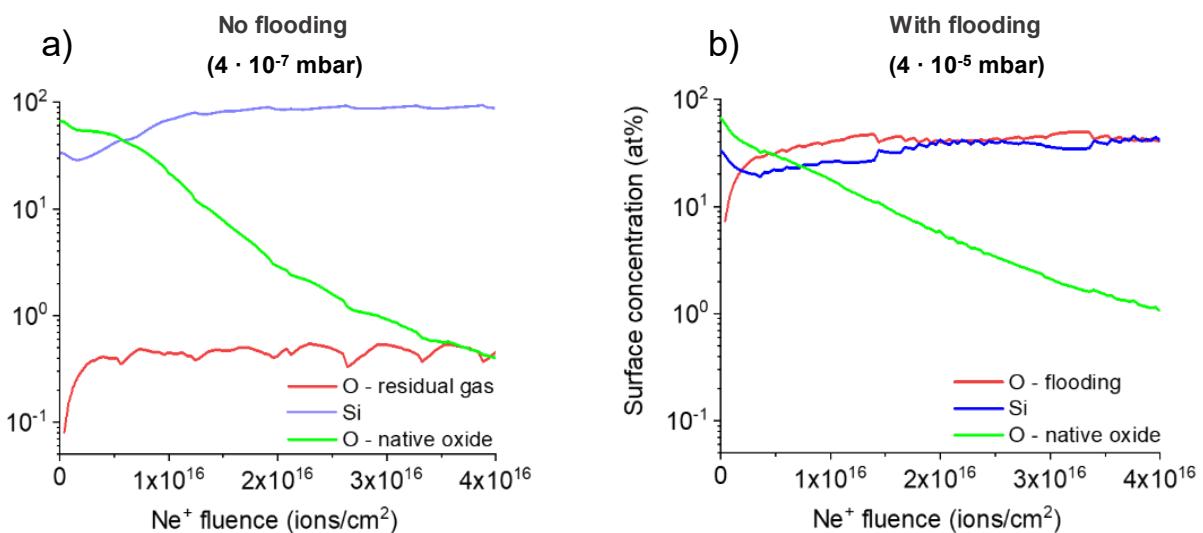


Figure 59: Concentration (normalized to 100 at%) vs. fluence profiles from SDTrimSP simulations performed on a pristine silicon sample with 2 nm thick SiO<sub>2</sub> layer (25 keV Ne<sup>+</sup> primary bombardment) at high vacuum ( $4 \cdot 10^{-7}$  mbar) and under oxygen flooding conditions ( $4 \cdot 10^{-5}$  mbar) (Figure from Ost et al.).<sup>104</sup>

In Figure 59, we observe that the surface concentration of the native oxygen decreases with the fluence in both pressure conditions (a, b) due to progressive sputtering of the oxide layer. However, residual oxygen from the chamber (no flooding) and flooded oxygen adsorbs to the surface and in the latter case allows to increase significantly and to maintain a high oxygen

concentration on the surface. Under flooding, the chosen simulation conditions lead to the creation of a nearly stoichiometric silicon dioxide.

Figure 60 a) shows clearly that without flooding at  $4 \cdot 10^{16}$  ions/cm<sup>2</sup> no residual/native oxygen is left in the matrix of the material. On the other hand, with flooding very shallow implantation of the oxygen by the highly energetic primary beam is taking place (Figure 60 d). It is worth noting that simulations of the sputtering yield under flooding (data not shown here) showed a decrease of the silicon SY, due to the high concentration of oxygen on the surface.

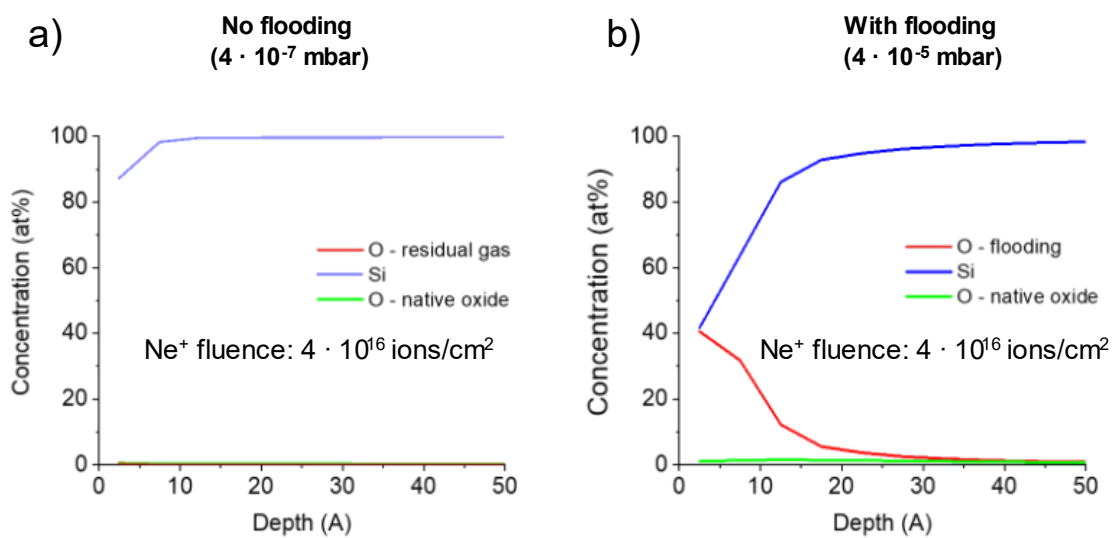


Figure 60: Depth profiles at a fluence of  $4 \cdot 10^{16}$  ions/cm<sup>2</sup> and sputtering yields vs. fluence simulated in SDTrimSP simulations performed on a silicon surface with a 2 nm thick oxide layer (25 keV Ne<sup>+</sup>, 15 pA,  $20 \times 20 \mu\text{m}^2$  FOV) without flooding ( $4 \cdot 10^{-7}$  mbar) and under oxygen flooding conditions ( $4 \cdot 10^{-5}$  mbar) (Figure adapted from Ost et al.).<sup>104</sup>

## 3. Experimental investigation for sensitivity optimization

## 3.1 Preliminary experiments: isotopic oxygen-18 flooding

In a first set of preliminary experiments, in order to differentiate between native and newly formed oxides, a silicon wafer was analyzed in depth profiling mode first at regular chamber pressure and then with isotopic oxygen-18 flooding. The studied range of fluences and chamber pressure conditions (respectively oxygen fluxes) were the same as for the simulations in Figure 59 (up to for  $4 \cdot 10^{16}$  ions/cm<sup>2</sup> at  $4 \cdot 10^{-7}$  mbar and  $4 \cdot 10^{-5}$  mbar).

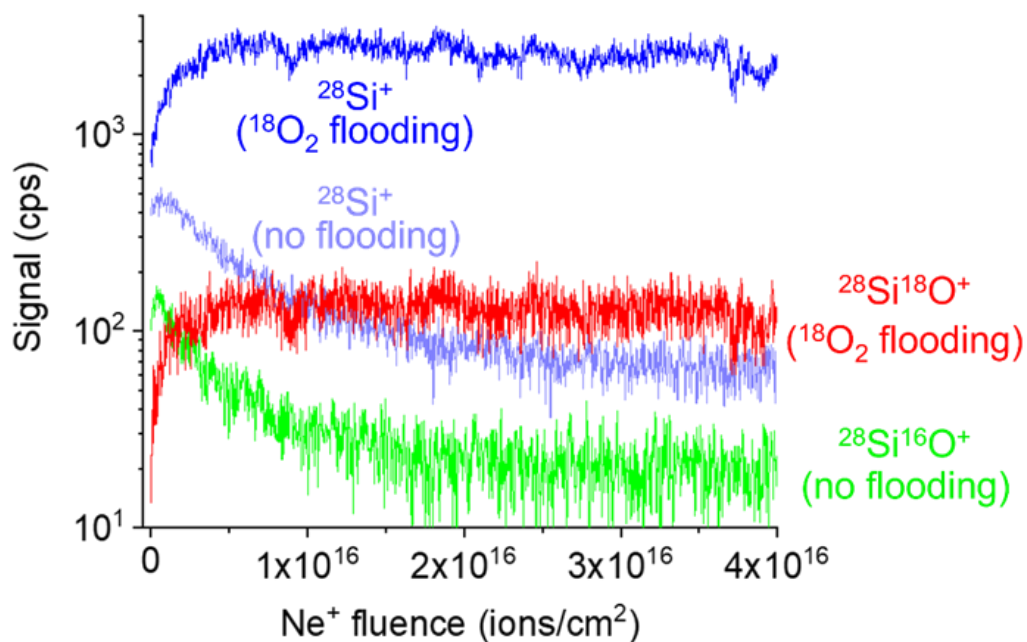


Figure 61: Depth profiling experiments performed instrument on a silicon wafer using the HIM-SIMS (25 keV Ne<sup>+</sup>) at high vacuum ( $4 \cdot 10^{-7}$  mbar) and with isotopic oxygen-18 flooding ( $4 \cdot 10^{-5}$  mbar) (Figure from Ost et al.).<sup>104</sup>

We monitored here the  $^{28}\text{Si}^+$  (Si matrix), the  $^{28}\text{Si}^{16}\text{O}^+$  (Si matrix with native oxide layer) and the  $^{28}\text{Si}^{18}\text{O}^+$  (Si matrix under  $^{18}\text{O}_2$  flooding) signals. The signal of  $\text{SiO}^+$  ions was chosen here since they are commonly used as indicators for the degree of surface oxidation.<sup>63</sup> The results of our experimental investigation are reported in Figure 61. First, without flooding once the native oxide layer is sputtered, the  $^{28}\text{Si}^{16}\text{O}^+$  signal drops. The drop of the  $^{28}\text{Si}^+$  signal is resulting from the matrix effect related to reduction of the oxygen surface concentration (i.e., sputtering of the native oxide layer). SIMS measurements were then performed with isotopic  $^{18}\text{O}_2$  flooding

on a different zone. The  $^{28}\text{Si}^+$  signal is initially at the same level as previously and increases parallelly with  $^{28}\text{Si}^{18}\text{O}^+$ , showing that here the supply of oxygen supports the ionization process of silicon. The  $^{28}\text{Si}^{18}\text{O}^+$  signal increases up to the same level as the  $^{28}\text{Si}^{16}\text{O}^+$  signal measured previously for the native oxide layer. Thus, by flooding we created similar conditions for the ionization silicon as for a silicon matrix with a native oxide layer.

Here we have seen that once the oxide layer has been sputtered, the SI signal drops, due to a reduction of the ionization yield. By assuring a constant supply of oxygen, higher detection of electropositive elements (such as silicon) is achieved.

### 3.2 Depth profiling

In the following series of experiments, oxygen flooding was performed on two different samples, a silicon wafer and a tungsten carbide sample (with cobalt binder) to analyze the  $^{28}\text{Si}$  and  $^{59}\text{Co}$  signals, respectively. The oxygen flux was varied here to find the highest SI intensity, limited up to the chamber pressure accepted by the system to prevent damage of the GFIS, i.e.  $4.5 \cdot 10^{-5}$  mbar (see chapter 1 section 4.1.1).

Figure 62 a) shows the depth profiles acquired without flooding ( $4 \cdot 10^{-7}$  mbar) and under oxygen flooding conditions ( $4 \cdot 10^{-5}$  mbar) for both ionic species. In Figure 62 b) the mean values of the depth profiles are represented at different pressures of the main chamber once the signal has reached a plateau (average over approximately 300 s for each depth profile). In each case, three measurements were performed (at different zones in the sample).

As the concentration of Co in the tungsten carbide matrix is much smaller compared to the Si matrix (localized areas rich in Co compared to homogeneous concentration on the Si wafer), one cannot compare the absolute SI signals directly, but consider the relative differences. At base pressure, the SI intensities of  $^{28}\text{Si}$  and  $^{59}\text{Co}$  drop shortly after the acquisition launch (Figure 62 a, b), which is here due to the sputtering of the native (Si or Co) oxide layer. The  $^{59}\text{Co}$  signal stabilizes at a rather high level compared to the  $^{28}\text{Si}$  signal due to the lower ionization potential (Co: 7.86 eV vs. Si: 8.15 eV)<sup>110</sup> and the higher sputtering yield (from SRIM simulations Co: 3 atoms/ion, Si: 1 atom/ion) of Co. With flooding, the enhancement factors of  $^{59}\text{Co}$  and  $^{28}\text{Si}$  are up to 5 and 1 000, respectively (Figure 62 b, c), which is in accordance with

the findings of Wirtz et al.<sup>59</sup> for Ne<sup>+</sup> irradiation of silicon. Differences in the enhancement of the <sup>28</sup>Si and <sup>59</sup>Co originate from the lower ionization potential of cobalt compared to silicon. In fact, the effect of oxygen for the ionization improvement is less effective for cobalt vs. silicon, as ionization of cobalt is a priori more probable than for silicon. In the case of <sup>28</sup>Si with flooding the signal increases with respect to the pressure (oxygen flux), which can be related to a higher coverage of oxygen on the surface<sup>111</sup> and therefore higher ionization probability of <sup>28</sup>Si. Due to the low sticking coefficient of oxygen on silicon ( $\sim 10^{-3}$  vs. 0.2 for Co),<sup>112,113</sup> the oxygen surface coverage increases with the pressure, thus also the <sup>28</sup>Si signal, and is expected to further increase at higher pressures ( $> 4 \cdot 10^{-5}$  mbar). In contrast, since the sticking coefficient for Co is much higher a maximum of the signal of <sup>59</sup>Co is reached at  $1.25 \cdot 10^{-6}$  mbar, because the surface is saturated for relatively low fluxes of oxygen. Moreover, for Co sticking of oxygen is more effective and faster oxygen surface coverage is reached, leading to a faster stabilization of the <sup>59</sup>Co signal in Figure 62 a), while for silicon more time is needed to cover the surface with oxygen, thus for the <sup>28</sup>Si signal to reach equilibrium.

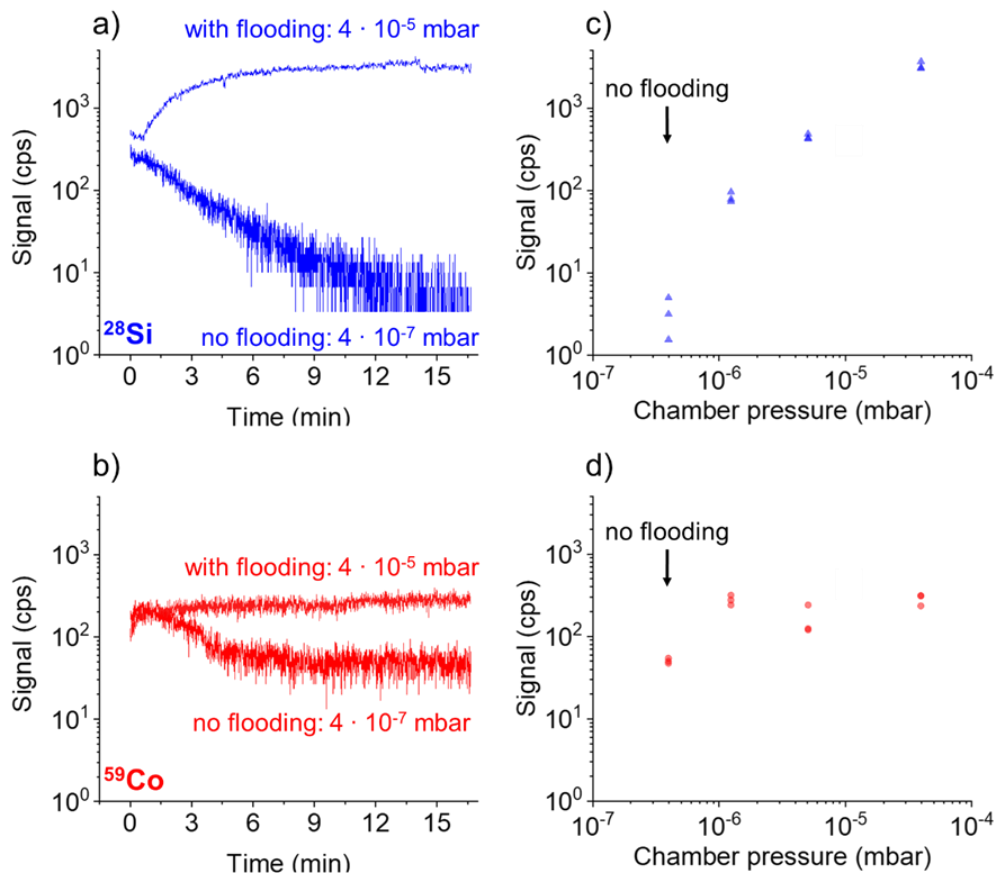


Figure 62: Depth profiling studies performed on the HIM-SIMS instrument (25 keV Ne<sup>+</sup>) on a silicon wafer (blue curves and data points) and a tungsten carbide sample with cobalt binder

*(red). a), b) Depth profiles showing the  $^{28}\text{Si}$  and  $^{59}\text{Co}$  signals, respectively, at regular chamber pressure ( $4 \cdot 10^{-7}$  mbar) and with oxygen flooding ( $4 \cdot 10^{-5}$  mbar). c), d) Average signals taken once a signal plateau was reached (3 measurements in each case) (Figure from Ost et al.).<sup>104</sup>*

### 3.3 Imaging

SIMS imaging under oxygen flooding is of high interest, as improving useful yields allows to achieve higher detection limit, which is crucial as using a GFIS with Ne<sup>+</sup> primary ion beam the number of sputtered atoms is very limited (e.g.,  $\sim 2 \cdot 10^5$  atoms for a  $20 \times 20 \times 10 \text{ nm}^3$  voxel in Si matrix). Improving the ionization probability in the context of high spatial resolution imaging is particularly important to detect and visualize nanoscopic features. In this section, applications of SIMS 2D and 3D imaging will be shown under appropriate oxygen flooding conditions, selected based on the depth profiling experiments in section 3.2.

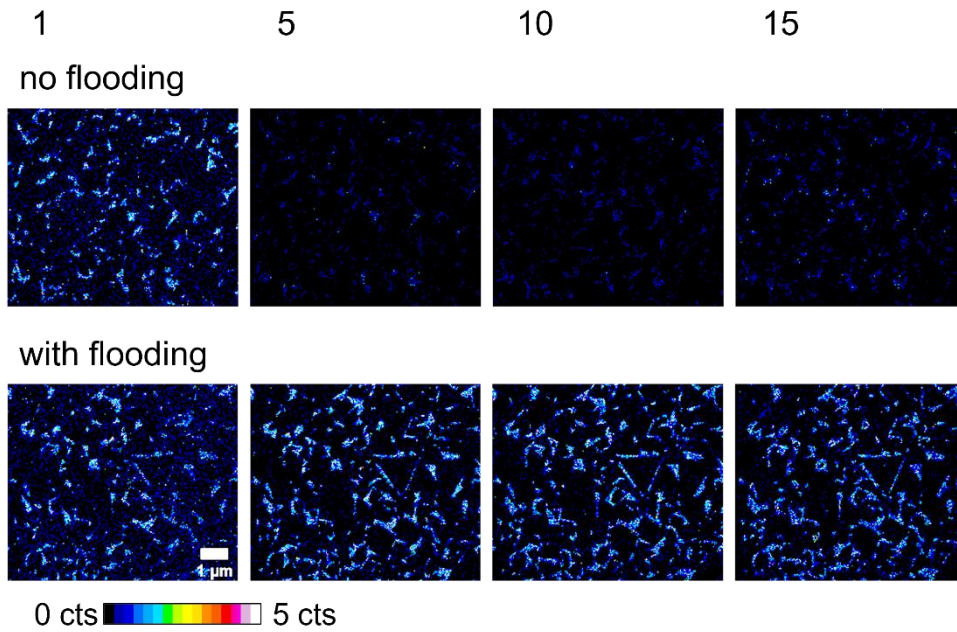
#### 3.3.1 Maintaining high ionization yields for 3D imaging

In SIMS, 3D imaging is based on the acquisition of successive slices to study the signal distribution with respect to the depth. As studied by Frache et al.<sup>64</sup> using a Ga<sup>+</sup> primary ion beam, oxygen flooding allows to maintain a high ionization and SI signal statistics throughout the series of images, and to avoid progressive signal loss due to sputtering of the native oxide layer.

The same sample (a WC cermet with cobalt binder phase) was analyzed here in 3D SIMS imaging mode in the HIM-SIMS. The  $^{59}\text{Co}$  signal, without flooding ( $4 \cdot 10^{-7}$  mbar) and under oxygen flooding ( $4 \cdot 10^{-5}$  mbar) was acquired. Experiments were performed in adjacent areas with a reasonably similar amount of cobalt binder phase sites. It is worth noting that preliminary SIMS images showed a similar density of cobalt phases over the surface of the cemented carbide sample. Figure 63 a) shows exemplary SIMS images of the series (in total 15 images). While in both cases the average image intensity of the first image is very similar, at high vacuum the intensity drops significantly (total counts drop by roughly one order of magnitude from image 1 to 3), due to the sputtering of the native oxide layer, while for oxygen flooding the intensity is kept constant throughout the series, as strong adsorption of oxygen on the surface takes place. By summing up all the counts for each image, in Figure 63 b) the

total counts are plotted against the image number. Analogously to the depth profiling experiments, a factor 5 can be gained in the case of  $^{59}\text{Co}$ . The minor increase of the total counts of  $^{59}\text{Co}$  without flooding could be due to an increase in the sputtering yield of cobalt by creation of surface roughness during the analysis.

a) Image number:



$^{59}\text{Co}$

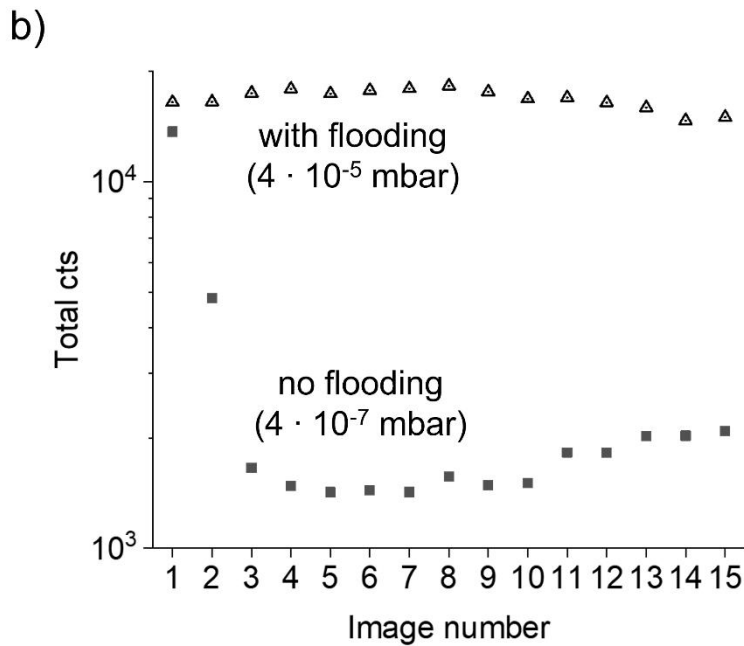


Figure 63: Serial SIMS image acquisitions of the  $^{59}\text{Co}$  signal (25 keV  $\text{Ne}^+$ ,  $10 \mu\text{m} \times 10 \mu\text{m}$ , 2.5 pA) on a WC-Co sample. a) Exemplary SIMS images under high vacuum ( $4 \cdot 10^{-7}$  mbar) and

under oxygen flooding ( $4 \cdot 10^{-5}$  mbar). b) Total sum of the counts for each image plotted against the image number for both analyses (Figure from Ost et al.).<sup>104</sup>

### 3.3.2 Perspectives for high-resolution imaging

As the latest generation of FIB-platforms allows to resolve nm-sized features, in particular microelectronic devices, we conclude our study by imaging a FinFet transistor. In this case, we focused our work on the analysis of the  $^{28}\text{Si}^+$  signal. We imaged here the transistor at a larger FOV ( $8 \mu\text{m} \times 8 \mu\text{m}$ , Figure 64) and then high magnification ( $2 \mu\text{m} \times 1.5 \mu\text{m}$ , Figure 65), in each case in adjacent zones next to one another at base pressure and flooding conditions. Flooding allowed to improve significantly the signal statistics, where the total number of counts gives in both cases an enhancement of 70 %, corresponding to the improvement of the  $^{28}\text{Si}$  signal in Figure 62 a) at  $t = 0$  min.

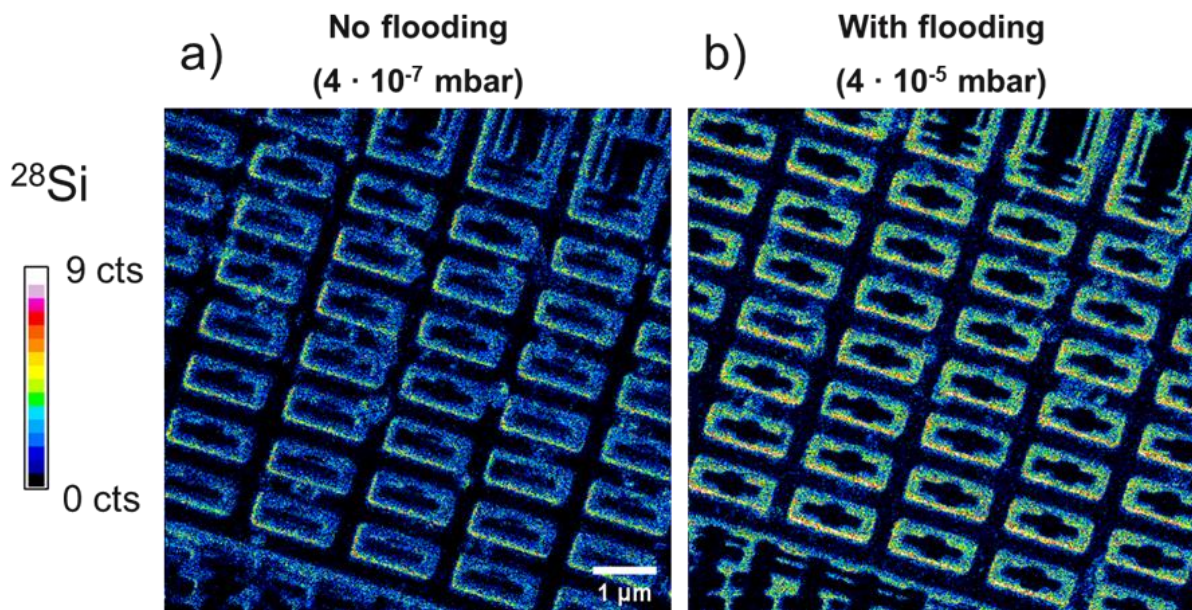


Figure 64: SIMS imaging with a 25 keV  $\text{Ne}^+$  primary ion beam at high vacuum ( $4 \cdot 10^{-7}$  mbar) and oxygen flooding ( $4 \cdot 10^{-5}$  mbar) of a FinFet transistor (FOV:  $8 \mu\text{m} \times 8 \mu\text{m}$ ) analyzed in two different (adjacent) zones. The total counts almost doubled using oxygen flooding (Figure from Ost et al.).<sup>104</sup>

The high magnification image of the transistor was acquired to directly visualize the improvement of the detection limit (Figure 65). Flooding allowed here not only to improve the total number of counts, but also to detect signal from a transistor part which was not

detected without flooding. The horizontal wire indicated with a white arrow in Figure 65 was detected thanks to the enhancement of the ionization. In this case, the concentration of silicon per voxel in this feature was so low that under regular conditions, silicon could not be detected, i.e. the SI yield was too low to create enough ions before the feature was sputtered.

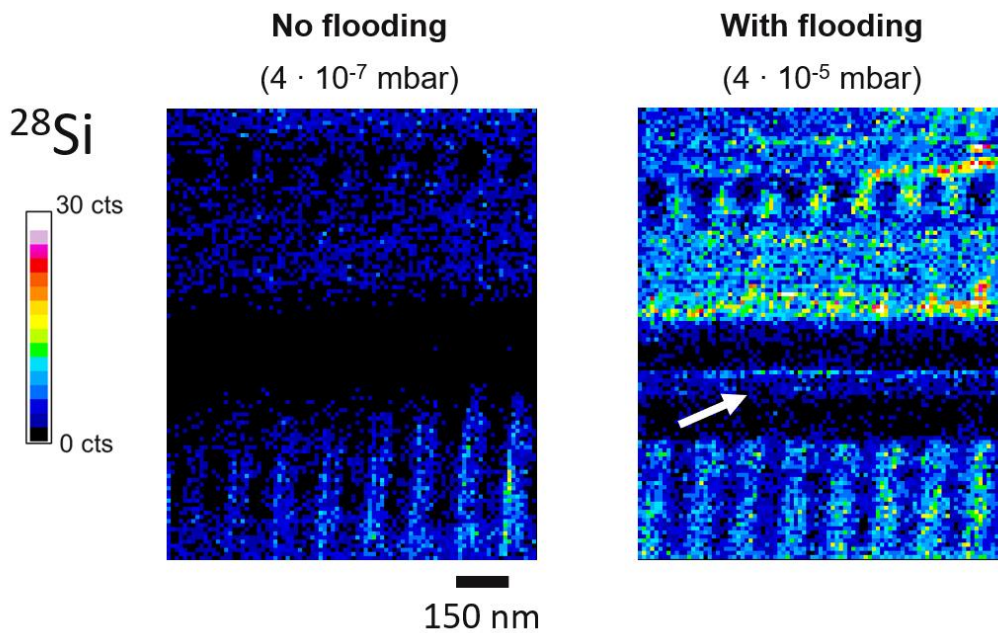


Figure 65: SIMS imaging with a 25 keV Ne<sup>+</sup> primary ion beam at high vacuum ( $4 \cdot 10^{-7}$  mbar) and oxygen flooding ( $4 \cdot 10^{-6}$  mbar) of a FinFet transistor at high magnification (field of view:  $2 \mu\text{m} \times 1.5 \mu\text{m}$ ).

Future studies for deeper understanding of the influence of the dwell time to reduce oxygen depletion on the surface due to the high bombardment density ( $\sim 10^{20} \frac{\text{ions}}{\text{cm}^2 \cdot \text{s}}$ ) will aim to further improve the enhancement factor in imaging under flooding.

#### 4. Chapter summary

Here the adsorption of residual and flooded oxygen were quantified and the improvement of SI yields under non-reactive primary light ions produced in a GFIS were studied in depth profiling and imaging modes.

First, in Monte Carlo (SDTrimSP) simulations for silicon, oxygen surface adsorption and implantation were studied for specific chamber pressure conditions. Under typical flooding conditions simulations showed a strong surface adsorption at the top surface layer of the material (40 % at a depth of  $< 5 \text{ \AA}$ ) and also sub-surface implantation at low concentration ( $< 1 \%$  at 2 nm depth). Completing our simulations with experiments using isotopic oxygen-18 flooding, we have shown that the native oxide layer allows to achieve initially relatively high ionization probability of the material, but once the native oxide is sputtered progressively the ionization probability and thus the useful yield of the material drops. Flooding the sample allows to create a surface environment rich in oxygen, allowing to maintain and even improve the ionization probability, resulting in largely higher SI intensity.

Experimental results in depth profiling by varying the oxygen flux showed improvements of up to three orders of magnitude for the  $^{28}\text{Si}$  signal. For 3D imaging, flooding allowed to maintain the SI signal for multiple acquisitions on the same area, while at regular conditions the SI yield dropped. For high resolution 2D imaging of a FinFet transistor, flooding allowed to improve the signal statistics and to detect and resolve more structural details compared to regular analysis conditions.

## General conclusions and perspectives

Current analytical challenges in imaging require the development of novel instruments and methodologies enabling the visualization of micro- and nanoscopic samples at high sensitivity and highest spatial resolution. In this work, state-of-the-art FIB platforms with add-on SIMS systems were used to develop methodologies for 3D surface reconstruction allowing to study correlatively the 3D topography and the chemistry of the sample. Reactive gas flooding was used to improve the ionization probability of electropositive elements.

A photogrammetric methodology was developed to reconstruct the surface of micro- and nanoscopic objects from multi-view SE images. Simulative studies on the reconstruction of geometric structures intended to find the main source of artefacts using the photogrammetry method. It was shown that a correct estimation of the position where the images were taken with respect to the object is essential to perform accurate reconstructions. In a next step, photogrammetric 3D surface reconstructions were overlaid with SIMS images to study correlatively topographical and chemical properties of materials. With the development of numerical analysis algorithms analyzing these 3D + 1 reconstructions it was possible to obtain a deeper understanding of the analyzed samples by studying the impact of the sample topography on its chemistry. For a 3D + 1 reconstruction of a soil microaggregate the organic carbon sequestration process was studied numerically by investigating the average curvature for areas containing inherited carbon ( $^{12}\text{C}$ ), enriched with isotopic carbon ( $^{13}\text{C}$ ), and consisting of mineral surfaces ( $^{27}\text{Al}^{16}\text{O}$ ). The analysis showed that the inherited organic carbon, was located on average on areas with medium curvatures ( $\sim 40^\circ$ ), while the mineral phase presented on average rather low curvatures ( $\sim 15^\circ$ ). Remarkably, the freshly introduced carbon deposited on areas with very similar curvatures as the inherited organic carbon. Additional analysis of reconstructions of 6 microaggregates showed that the deposition of isotopic carbon took place within a similar range of curvatures (ranging from  $25^\circ$  up to  $40^\circ$ ). Thus, our results show that chemical composition and topography are drivers of soil organic matter distribution.

To improve the efficiency of the 3D + 1 methodology, automatization algorithms for photogrammetric 3D SE acquisition for microscopy software and development of a user-friendly, possibly partially or even fully automatic, software for 3D + 1 information overlay

and analysis could be a subject of future studies. Though here only applications of the 3D + 1 surface reconstruction method were illustrated on measurements using HIM and SIMS instruments, it is certainly not limited to these two techniques, and can be used for various combinations of microscopy (e.g., optical, confocal, scanning electron, and atomic force microscopy) with spectroscopy techniques (e.g., x-ray photoelectron, energy dispersive x-ray, or Raman spectroscopy), depending on the type of sample (e.g., size of sample in  $\mu\text{m}$  or  $\text{nm}$  range) and the required information (e.g. organic, elemental, or isotopic).

As sample topography has a significant impact on sputtering processes due to changing incidence angles of the primary ion beam, this 3D + 1 method was used to study experimentally with model samples the change of the sputtering yield with respect to the incidence angles of light ions ( $\text{He}^+$ ,  $\text{Ne}^+$ ), with regards to Monte Carlo simulations and theoretical models, developed originally for heavier primary ions. Our experimental results showed that during the milling process of the model samples, rippled patterns were formed which influenced the sputtering behavior when the sputtering yield vs. incidence angle was studied. These experimental datasets were fitted with dedicated model functions and thus it was shown that these theoretical models (for sputtering of rippled surfaces) are also applicable for lower mass primary ions. Then, the 3D + 1 method was used to study the change of the sputtering yield for more complex samples and an algorithm was proposed to correct SIMS images with respect to topographical artefacts. Shadowing effects in SIMS images were investigated with ion trajectory simulations and the 3D + 1 method, showing that the ion emission angle and the primary ion beam alignment can impact the secondary ion intensity.

Topography is a key factor determining the intensity of the SI signal due to variation of the sputtering yield and non-isotropy of the spectrometer transmission. These can lead to considerable variations in the SI intensity depending on the ion emission angle. Eventually, both effects are affecting each other. While a vertical impact of primary ions leads to relatively low sputtering yields, a vertical SI emission leads to a high transmission. On the other hand, it is well known that oblique incidence leads to higher sputtering yields. However, if this surface is oriented in an “unfavorable” direction it can lead to a reduced transmission of the spectrometer. Further investigations specifically on SIMS image corrections with respect to both, the sputtering yield and instrumental transmission, could be subjects of further studies. Knowing the specimen topography and the exact instrumental transmission profile are key

factors which will allow to draw more reliable conclusions on SIMS images and interpret accurately analytical results in the future. By improving the 3D SE reconstruction model quality (e.g., by reducing noise in SE images, using more SE image acquisitions with even higher quality/higher spatial resolution to capture more surface features) and the signal statistics in a SIMS image (e.g., by using oxygen flooding), the image correction algorithm could be used in the future to perform more accurate correction of SIMS images. With the development of automatic workflows for 3D surface reconstruction, SIMS images could be normalized/corrected on a routine basis for an artefact-free visualization and deeper understanding of the analyzed material.

Finally, experimental studies using oxygen flooding performed on the HIM-SIMS instrument were shown to improve detection limits under high  $\text{Ne}^+$  bombardment densities ( $\sim$  up to  $10^{20} \frac{\text{ions}}{\text{cm}^2 \cdot \text{s}}$ ). In a first step, MC simulations were performed for a silicon matrix with a native oxide layer under oxygen flooding to quantify oxygen surface concentration and to better understand the extend of oxygen sub-surface implantation. It was found that under the studied conditions (oxygen flux of  $1.1 \cdot 10^{16} \frac{\text{molecules}}{\text{cm}^2 \cdot \text{s}}$ ), while the native oxide layer was sputtered, flooded oxygen adsorbed to the surface, creating an “artificial” oxide layer and also shallow sub-surface implantation of oxygen took place (up to a depth of 2 nm). Depth profiling experiments on a silicon wafer under isotopic oxygen-18 flooding showed that sputtering of the native oxide led to a strong reduction of the ionization probability, thus the secondary ion intensity, while under flooding the creation of an artificial oxide layer allowed to improve significantly the SI intensity. By varying the oxygen flux, depth profiling experiments on a silicon wafer and a cobalt binder phase in a cemented carbide revealed that the ionization potential of the main element in the matrix is a key factor determining the extend of the enhancement effect of the flooding, while sticking coefficients of oxygen to the material determine the oxygen surface adsorption kinetics. Enhancement factors of up to  $10^3$  and 5 were found for silicon and cobalt, respectively. Results on SIMS imaging showed that flooding allows to enhance the signal statistics, thus image quality, as well as to maintain a high ionization probability, when sequential image acquisitions are taken on a single ROI.

Further experimental investigation will focus on studying the influence of the scanning dwell time. Using high beam densities in combination with high pixel dwell times led presumably to

oxygen depletion and thus a lower enhancement factor of the  $^{28}\text{Si}$  signal in imaging compared to depth profiling. Therefore, further investigations with multiple acquisitions of a same ROI at lower dwell times could elucidate the influence of the exposure time on the enhancement factors. Once these conditions are optimized this will allow to detect and to image trace elements at a sub-20nm spatial resolution. In this context, it is worth noting that in this work for the imaging of transistors we focused on the analysis of silicon. However, common elements present in transistors include aluminum, titanium, nickel, copper, and tungsten. Further investigations on the improvement of the detection of these elements (and more elements of the periodic table) under flooding in particular for SIMS imaging could be a subject for further studies. Finally, since Frache et al.<sup>64</sup> demonstrated successfully SIMS applications of flooding on a CAMECA IMS-6f with a  $\text{Ga}^+$  primary ion beam, the installation of an oxygen flooding system on the FIB-SEM-SIMS is currently in consideration. The advantage of performing reactive gas flooding under  $\text{Ga}^+$  bombardment is to sputter samples surfaces at higher rates, compared to light ions such as  $\text{He}^+$  or  $\text{Ne}^+$ .

## References

- (1) Zalm, P. Secondary Ion Mass Spectrometry. *Vacuum* **1994**, *45* (6–7), 753–772. [https://doi.org/10.1016/0042-207X\(94\)90113-9](https://doi.org/10.1016/0042-207X(94)90113-9).
- (2) Van der Heide, P. *Secondary Ion Mass Spectrometry*; John Wiley & Sons, Inc.: Hoboken, NJ, USA, 2014. <https://doi.org/10.1002/9781118916780>.
- (3) Williams, P. Secondary Ion Mass Spectrometry. *Annu. Rev. Mater. Sci.* **1985**, *15* (1), 517–548. <https://doi.org/10.1146/annurev.ms.15.080185.002505>.
- (4) McPhail, D. S. Applications of Secondary Ion Mass Spectrometry (SIMS) in Materials Science. *J. Mater. Sci.* **2006**, *41*, 873–903. <https://doi.org/10.1007/s10853-006-6568-x>.
- (5) Fragu, P.; Briançon, C.; Fourré, C.; Clerc, J.; Casiraghi, O.; Jeusset, J.; Omri, F.; Halpern, S. SIMS Microscopy in the Biomedical Field. *Biol. Cell* **1992**, *74*, 5–18. [https://doi.org/10.1016/0248-4900\(92\)90004-K](https://doi.org/10.1016/0248-4900(92)90004-K).
- (6) Agüi-Gonzalez, P.; Jähne, S.; Phan, N. T. N. SIMS Imaging in Neurobiology and Cell Biology. *J. Anal. At. Spectrom.* **2019**, *34*, 1355. <https://doi.org/10.1039/c9ja00118b>.
- (7) Remusat, L.; Hatton, P. J.; Nico, P. S.; Zeller, B.; Kleber, M.; Derrien, D. NanoSIMS Study of Organic Matter Associated with Soil Aggregates: Advantages, Limitations, and Combination with STXM. *Environ. Sci. Technol.* **2012**, *46* (7), 3943–3949. <https://doi.org/10.1021/es203745k>.
- (8) Vogel, C.; Mueller, C. W.; Höschen, C.; Buegger, F.; Heister, K.; Schulz, S.; Schlöter, M.; Kögel-Knabner, I. Submicron Structures Provide Preferential Spots for Carbon and Nitrogen Sequestration in Soils. *Nat. Commun.* **2014**, *5*, 2947. <https://doi.org/10.1038/ncomms3947>.
- (9) Zimmermann, U.; Madland, M. V.; Nermoen, A.; Hildebrand-Habel, T.; Bertolino, S. A. R.; Hiorth, A.; Korsnes, R. I.; Audinot, J. N.; Grysan, P. Evaluation of the Compositional Changes during Flooding of Reactive Fluids Using Scanning Electron Microscopy, Nano-Secondary Ion Mass Spectrometry, x-Ray Diffraction, and Whole-Rock

- Geochemistry. *Am. Assoc. Pet. Geol. Bull.* **2015**, *99* (5), 791–805.  
<https://doi.org/10.1306/12221412196>.
- (10) Sigmund, P. Theory of Sputtering. I. Sputtering Yield of Amorphous and Polycrystalline Targets. *Phys. Rev.* **1969**, *184* (2), 383–416.  
<https://doi.org/https://doi.org/10.1103/PhysRev.184.383>.
- (11) Oechsner, H. Sputtering - a Review of Some Recent Experimental and Theoretical Aspects. *Appl. Phys.* **1975**, *8*, 185–198. <https://doi.org/10.1007/BF00896610>.
- (12) *Sputtering by Particle Bombardment: Experiments and Computer Calculations from Threshold to MeV Energies*; Behrisch, R., Eckstein, W., Eds.; 2007; Vol. 110.
- (13) Gillen, G.; Fahey, A.; Wagner, M.; Mahoney, C. 3D Molecular Imaging SIMS. *Appl. Surf. Sci.* **2006**, *252* (19), 6537–6541. <https://doi.org/10.1016/j.apsusc.2006.02.235>.
- (14) De Castro, O.; Audinot, J.-N.; Hoang, Q.; Coulbary, C.; Bouton, O.; Barrahma, R.; Ost, A.; Stoffels, C.; Jiao, C.; Dutka, M.; Geryk, M.; Wirtz, T. Magnetic Sector Secondary Ion Mass Spectrometry on FIB-SEM Instruments for Nanoscale Chemical Imaging. *Anal. Chem.* **2022**. <https://doi.org/https://doi.org/10.1021/acs.analchem.2c01410>.
- (15) Son, J. G.; Yoon, S.; Shon, H. K.; Moon, J. H.; Joh, S.; Lee, T. G. Ar-Gas Cluster Ion Beam in ToF-SIMS for Peptide and Protein Analysis. *Biointerphases* **2020**, *15* (2), 021011.  
<https://doi.org/10.1116/6.0000105>.
- (16) Audinot, J. N.; Philipp, P.; De Castro, O.; Biesemeier, A.; Hoang, Q. H.; Wirtz, T. Highest Resolution Chemical Imaging Based on Secondary Ion Mass Spectrometry Performed on the Helium Ion Microscope. *Reports on Progress in Physics*. August 17, 2021, p 105901. <https://doi.org/10.1088/1361-6633/ac1e32>.
- (17) Vickerman, J. C.; Brown, A.; Reed, N. M. *Secondary Ion Mass Spectrometry : Principles and Applications*; Vickerman, J. C., Brown, A. (Alan), Reed, N. M., Eds.; The International series of monographs on chemistry ; 17; Clarendon Press: Oxford, 1989.
- (18) Wirtz, T.; Philipp, P.; Audinot, J. N.; Dowsett, D.; Eswara, S. High-Resolution High-Sensitivity Elemental Imaging by Secondary Ion Mass Spectrometry: From Traditional 2D and 3D Imaging to Correlative Microscopy. *Nanotechnology* **2015**, *26* (43), 434001.

- <https://doi.org/10.1088/0957-4484/26/43/434001>.
- (19) Makeev, M. A.; Barabási, A. L. Effect of Surface Morphology on the Sputtering Yields. I. Ion Sputtering from Self-Affine Surfaces. *Nucl. Instruments Methods Phys. Res. Sect. B Beam Interact. with Mater. Atoms* **2004**, *222* (3–4), 316–334. <https://doi.org/10.1016/j.nimb.2004.02.027>.
- (20) Shulga, V. I. Angle-Dependent Sputter Yield of Rippled Surfaces. *Appl. Surf. Sci.* **2018**, *458* (April), 18–23. <https://doi.org/10.1016/j.apsusc.2018.07.059>.
- (21) Küstner, M.; Eckstein, W.; Hechtel, E.; Roth, J. Angular Dependence of the Sputtering Yield of Rough Beryllium Surfaces. *J. Nucl. Mater.* **1999**, *265* (1–2), 22–27. [https://doi.org/10.1016/S0022-3115\(98\)00648-5](https://doi.org/10.1016/S0022-3115(98)00648-5).
- (22) Lindsey, S.; Hobler, G. Sputtering of Silicon at Glancing Incidence. *Nucl. Instruments Methods Phys. Res. Sect. B Beam Interact. with Mater. Atoms* **2013**, *303*, 142–147. <https://doi.org/10.1016/j.nimb.2012.12.087>.
- (23) Manova, D.; Schreck, M.; Mändl, S.; Stritzker, B.; Rauschenbach, B. Orientation Dependent Sputter Yield of Aluminium. *Surf. Coatings Technol.* **2002**, *151–152*, 72–75. [https://doi.org/10.1016/S0257-8972\(01\)01595-X](https://doi.org/10.1016/S0257-8972(01)01595-X).
- (24) Meyer, D. O. *Sputtering by Particle Bombardment, Vol. I: Physical Sputtering of Single-Elements Solids*; 1982; Vol. 107. [https://doi.org/10.1016/0022-3115\(82\)90441-x](https://doi.org/10.1016/0022-3115(82)90441-x).
- (25) Behrisch, R. First-Wall Erosion in Fusion Reactors. *Nucl. Fusion* **1972**, *12* (6), 695–713. <https://doi.org/10.1088/0029-5515/12/6/011>.
- (26) Taglauer, E. Fundamental Processes in Sputtering of Atoms and Molecules (SPUT92). In *Sputtering and Surface Science*; Sigmund, P., Ed.; 1993; Vol. 43, p 643.
- (27) Frost, F.; Rauschenbach, B. Nanostructuring of Solid Surfaces by Ion-Beam Erosion. *Appl. Phys. A Mater. Sci. Process.* **2003**, *77* (1). <https://doi.org/10.1007/s00339-002-2059-3>.
- (28) Frost, F.; Fechner, R.; Flamm, D.; Ziberi, B.; Frank, W.; Schindler, A. Ion Beam Assisted Smoothing of Optical Surfaces. *Appl. Phys. A Mater. Sci. Process.* **2004**, *78* (5), 651–654. <https://doi.org/10.1007/s00339-003-2274-6>.

- (29) Gulbiński, W. Deposition of Thin Films by Sputtering. In *Chemical Physics of Thin Film Deposition Processes for Micro- and Nano-Technologies*; Pauleau, Y., Ed.; Springer, Dordrecht, 2002; pp 309–333. [https://doi.org/10.1007/978-94-010-0353-7\\_13](https://doi.org/10.1007/978-94-010-0353-7_13).
- (30) Benninghoven, A.; Rudenauer, F. G.; Werner, H. W. *Secondary Ion Mass Spectrometry: Basic Concepts, Instrumental Aspects, Applications and Trends.*; Wiley-Interscience: New York, 1987.
- (31) Williams, P. The Sputtering Process and Sputtered Ion Emission. *Surf. Sci.* **1979**, *90* (2), 588–634. [https://doi.org/10.1016/0039-6028\(79\)90363-7](https://doi.org/10.1016/0039-6028(79)90363-7).
- (32) Pillatsch, L.; Vanhove, N.; Dowsett, D.; Sijbrandij, S.; Notte, J.; Wirtz, T. Study and Optimisation of SIMS Performed with He<sup>+</sup> and Ne<sup>+</sup> Bombardment. *Appl. Surf. Sci.* **2013**, *282*, 908–913. <https://doi.org/10.1016/j.apsusc.2013.06.088>.
- (33) Bredal, T. V.; Zimmermann, U.; Madland, M. V.; Minde, M. W.; Ost, A. D.; Wirtz, T.; Audinot, J.; Korsnes, R. I. High-Resolution Topographic and Chemical Surface Imaging of Chalk for Oil Recovery Improvement Applications. *Minerals* **2022**, *12* (3), 1–10. <https://doi.org/https://doi.org/10.3390/min12030356>.
- (34) *Science of Microscopy*, Volume 1.; Hawkes, P. W., Spence, J. C. H., Eds.; Springer, New York, NY, 2007. <https://doi.org/10.1007/978-0-387-49762-4>.
- (35) Van Vaeck, L.; Adams, F. *Encyclopedia of Spectroscopy and Spectrometry*, 3rd editio.; Lindon, J. C., Tranter, G. E., Koppenaar, D. W., Eds.; Elsevier Ltd., 2017. <https://doi.org/10.1016/B978-0-12-803224-4.00370-8>.
- (36) Winograd, N. The Magic of Cluster SIMS. *Analytical Chemistry*. April 1, 2005, p 142 A–149 A. <https://doi.org/10.1021/ac053355f>.
- (37) Vollnhals, F.; Audinot, J. N.; Wirtz, T.; Mercier-Bonin, M.; Fourquaux, I.; Schroepel, B.; Kraushaar, U.; Lev-Ram, V.; Ellisman, M. H.; Eswara, S. Correlative Microscopy Combining Secondary Ion Mass Spectrometry and Electron Microscopy: Comparison of Intensity-Hue-Saturation and Laplacian Pyramid Methods for Image Fusion. *Anal. Chem.* **2017**, *89* (20), 10702–10710. <https://doi.org/10.1021/acs.analchem.7b01256>.
- (38) Moore, K. L.; Lombi, E.; Zhao, F. J.; Grovenor, C. R. M. Elemental Imaging at the

- Nanoscale: NanoSIMS and Complementary Techniques for Element Localisation in Plants. *Anal. Bioanal. Chem.* **2012**, *402* (10), 3263–3273.  
<https://doi.org/10.1007/s00216-011-5484-3>.
- (39) Wirtz, T.; De Castro, O.; Audinot, J. N.; Philipp, P. Imaging and Analytics on the Helium Ion Microscope. *Annu. Rev. Anal. Chem.* **2019**, *12*, 523–543.  
<https://doi.org/https://doi.org/10.1146/annurev-anchem-061318-115457>.
- (40) Hlawacek, G.; Götzhäuser, A. *Helium Ion Microscopy*; Springer Nature: Basel, Switzerland, 2016. <https://doi.org/10.1007/978-3-319-41990-9>.
- (41) Dowsett, D.; Wirtz, T. Co-Registered In-Situ Secondary Electron and Mass Spectral Imaging on the Helium Ion Microscope Demonstrated Using Lithium Titanate and Magnesium Oxide Nanoparticles. *Anal. Chem.* **2017**, acs.analchem.7b01481.  
<https://doi.org/10.1021/acs.analchem.7b01481>.
- (42) Burt, P. J.; Adelson, E. H. The Laplacian Pyramid as a Compact Image Code. *IEEE Trans. Commun.* **1983**, *31* (4), 532–540. <https://doi.org/10.1109/tcom.1983.1095851>.
- (43) Dowsett, D.; Wirtz, T. Co-Registered in Situ Secondary Electron and Mass Spectral Imaging on the Helium Ion Microscope Demonstrated Using Lithium Titanate and Magnesium Oxide Nanoparticles. *Anal. Chem.* **2017**, *89* (17), 8957–8965.  
<https://doi.org/10.1021/acs.analchem.7b01481>.
- (44) Anderle, M.; Barozzi, M.; Bersani, M.; Giubertoni, D.; Lazzeri, P. Ultra Shallow Depth Profiling by Secondary Ion Mass Spectrometry Techniques. In *AIP Conference Proceedings*; 2003; Vol. 683, pp 695–704. <https://doi.org/10.1063/1.1622547>.
- (45) De Chambost, E.; Merkulov, A.; Peres, P.; Rasser, B.; Schuhmacher, M. Latest Developments for the CAMECA ULE-SIMS Instruments: IMS Wf and SC-Ultra. *Appl. Surf. Sci.* **2004**, *231–232*, 949–953. <https://doi.org/10.1016/j.apsusc.2004.03.202>.
- (46) Artemov, V. V.; Khmelinin, D. N.; Mamonova, A. V.; Gorkunov, M. V.; Ezhov, A. A. Microscopic Studies of Alignment Layers Processed by a Focused Ion Beam for the Creation of Liquid Crystal Metasurfaces. *Crystallogr. Reports* **2021**, *66* (4), 673–681.  
<https://doi.org/10.1134/S1063774521040039>.

- (47) De Castro, O.; Biesemeier, A.; Serralta, E.; Bouton, O.; Barrahma, R.; Hoang, Q. H.; Cambier, S.; Taubitz, T.; Klingner, N.; Hlawacek, G.; Pinto, S. D.; Gnauck, P.; Lucas, F.; Bebeacua, C.; Wirtz, T. NpSCOPE: A New Multimodal Instrument for in Situ Correlative Analysis of Nanoparticles. *Anal. Chem.* **2021**, *93* (43), 14417–14424. <https://doi.org/10.1021/acs.analchem.1c02337>.
- (48) Likonen, J.; Hautala, M.; Koponen, I. The Ultimate Depth Resolution in SIMS Profiting : Low-Energy Ion Beam Mixing of Au -Pt Interface. *Nucl. Instruments Methods Phys. Res. Sect. B Beam Interact. with Mater. Atoms* **1993**, *81*, 151–155.
- (49) Bay, H. L.; Bohdansky, J. Sputtering Yields for Light Ions as a Function of Angle of Incidence. *Appl. Phys.* **1979**, *19* (4), 421–426. <https://doi.org/10.1007/BF00930106>.
- (50) Lee, J. L. S.; Gilmore, I. S.; Fletcher, I. W.; Seah, M. P. Topography and Field Effects in the Quantitative Analysis of Conductive Surfaces Using ToF-SIMS. *Appl. Surf. Sci.* **2008**, *255* (4), 1560–1563. <https://doi.org/10.1016/j.apsusc.2008.05.164>.
- (51) Koch, S.; Ziegler, G.; Hutter, H. ToF-SIMS Measurements with Topographic Information in Combined Images. *Anal. Bioanal. Chem.* **2013**, *405*, 7161–7167. <https://doi.org/10.1007/s00216-013-6850-0>.
- (52) Terlier, T.; Lee, J.; Lee, K.; Lee, Y. Improvement of the Correlative AFM and ToF-SIMS Approach Using an Empirical Sputter Model for 3D Chemical Characterization. *Anal. Chem.* **2018**, *90* (3), 1701–1709. <https://doi.org/10.1021/acs.analchem.7b03431>.
- (53) Wucher, A.; Cheng, J.; Winograd, N. Protocols for Three-Dimensional Molecular Imaging Using Mass Spectrometry. *Anal. Chem.* **2007**, *79* (15), 5529–5539. <https://doi.org/10.1021/ac070692a>.
- (54) Fleming, Y.; Wirtz, T.; Gysin, U.; Glatzel, T.; Wegmann, U.; Meyer, E.; Maier, U.; Rychen, J. Three Dimensional Imaging Using Secondary Ion Mass Spectrometry and Atomic Force Microscopy. *Appl. Surf. Sci.* **2011**, *258* (4), 1322–1327. <https://doi.org/10.1016/j.apsusc.2011.09.029>.
- (55) Akhtar, I.; Rehman, M. A.; Choi, W.; Kumar, S.; Lee, N.; Cho, S. J.; Park, H. H.; Park, K. H.; Seo, Y. Three-Dimensional Atomic Force Microscopy for Ultra-High-Aspect-Ratio Imaging. *Appl. Surf. Sci.* **2019**, *469*, 582–592.

- <https://doi.org/10.1016/j.apsusc.2018.11.030>.
- (56) Eulitz, M.; Reiss, G. 3D Reconstruction of SEM Images by Use of Optical Photogrammetry Software. *J. Struct. Biol.* **2015**, *191* (2), 190–196.  
<https://doi.org/10.1016/j.jsb.2015.06.010>.
- (57) Gontard, L. C.; Schierholz, R.; Yu, S.; Cintas, J.; Dunin-borkowski, R. E. Photogrammetry of the Three-Dimensional Shape and Texture of a Nanoscale Particle Using Scanning Electron Microscopy and Free Software. *Ultramicroscopy* **2016**, *169*, 80–88. <https://doi.org/10.1016/j.ultramic.2016.07.006>.
- (58) Tan, S.; Livengood, R.; Shima, D.; Notte, J.; McVey, S. Gas Field Ion Source and Liquid Metal Ion Source Charged Particle Material Interaction Study for Semiconductor Nanomachining Applications. *J. Vac. Sci. Technol. B, Nanotechnol. Microelectron. Mater. Process. Meas. Phenom.* **2010**, *28* (6), C6F15–C6F21.  
<https://doi.org/10.1116/1.3511509>.
- (59) Wirtz, T.; Vanhove, N.; Pillatsch, L.; Dowsett, D.; Sijbrandij, S.; Notte, J. Towards Secondary Ion Mass Spectrometry on the Helium Ion Microscope: An Experimental and Simulation Based Feasibility Study with He + and Ne + Bombardment. *Appl. Phys. Lett.* **2012**, *101* (4). <https://doi.org/10.1063/1.4739240>.
- (60) Franzreb, K.; Lörinčík, J.; Williams, P. Quantitative Study of Oxygen Enhancement of Sputtered Ion Yields. I. Argon Ion Bombardment of a Silicon Surface with O<sub>2</sub> Flood. *Surf. Sci.* **2004**, *573* (2), 291–309. <https://doi.org/10.1016/j.susc.2004.10.001>.
- (61) Williams, P.; Evans, C. A. J. Anomalous Enhancement of Negative Sputtered Ion Emission by Oxygen. *Surf. Sci.* **1978**, *78* (2), 324–338.  
[https://doi.org/https://doi.org/10.1016/0039-6028\(78\)90084-5](https://doi.org/https://doi.org/10.1016/0039-6028(78)90084-5).
- (62) Zalm, P. C.; Vriezema, C. J. Oxygen Bleed-in during SIMS Depth Profiling: Curse or Blessing? *Nucl. Inst. Methods Phys. Res. B* **1992**, *64* (1–4), 626–631.  
[https://doi.org/10.1016/0168-583X\(92\)95546-4](https://doi.org/10.1016/0168-583X(92)95546-4).
- (63) Tian, C.; Vandervorst, W. Effects of Oxygen Flooding on Sputtering and Ionization Processes during Ion Bombardment. *J. Vac. Sci. Technol. A Vacuum, Surfaces, Film.* **1997**, *15* (3), 452–459. <https://doi.org/10.1116/1.580873>.

- (64) Frache, G.; Adib, B. El; Audinot, J. N.; Migeon, H. N. Evaluation of Ionization Yields under Gallium Bombardment. *Surf. Interface Anal.* **2011**, *43* (1–2), 639–642. <https://doi.org/10.1002/sia.3418>.
- (65) Williams, P.; Franzreb, K.; Sobers, R. C.; Lörinčík, J. On the Effect of Oxygen Flooding on the Detection of Noble Gas Ions in a SIMS Instrument. *Nucl. Instruments Methods Phys. Res. Sect. B Beam Interact. with Mater. Atoms* **2010**, *268* (17–18), 2758–2765. <https://doi.org/10.1016/j.nimb.2010.05.037>.
- (66) *Multiple View Geometry in Computer Vision*, 2nd ed.; Hartley, R., Zisserman, A., Eds.; Cambridge University Press: Cambridge, 2004. <https://doi.org/https://doi.org/10.1017/CBO9780511811685>.
- (67) Galantucci, R. A.; Fatiguso, F. Advanced Damage Detection Techniques in Historical Buildings Using Digital Photogrammetry and 3D Surface Analysis. *J. Cult. Herit.* **2019**, *36*, 51–62. <https://doi.org/10.1016/j.culher.2018.09.014>.
- (68) Peter Heng, B. C.; Chandler, J. H.; Armstrong, A. Applying Close Range Digital Photogrammetry in Soil Erosion Studies. *Photogramm. Rec.* **2010**, *25* (131), 240–265. <https://doi.org/10.1111/j.1477-9730.2010.00584.x>.
- (69) Agisoft. Community Articles. <https://www.agisoft.com/community/articles/cultural-heritage/> (accessed Jul 3, 2019).
- (70) Bay, H.; Ess, A.; Tuytelaars, T.; Van Gool, L. Speeded-Up Robust Features (SURF). *Comput. Vis. Image Underst.* **2008**, *110* (3), 346–359. <https://doi.org/10.1016/j.cviu.2007.09.014>.
- (71) Mussabayev, R. R.; Kalimoldayev, M. N.; Amirgaliyev, Y. N.; Tairova, A. T.; Mussabayev, T. R. Calculation of 3D Coordinates of a Point on the Basis of a Stereoscopic System. *Open Eng.* **2018**, *8* (1), 109–117. <https://doi.org/10.1515/eng-2018-0016>.
- (72) Hartley, R. I.; Sturm, P. Triangulation. *Comput. Vis. Image Underst.* **1997**, *68* (2), 146–157. <https://doi.org/10.1006/cviu.1997.0547>.
- (73) Vollnhals, F.; Wirtz, T. Correlative Microscopy in 3D: Helium Ion Microscopy-Based

- Photogrammetric Topography Reconstruction Combined with in Situ Secondary Ion Mass Spectrometry. *Anal. Chem.* **2018**, *90* (20), 11989–11995.  
<https://doi.org/10.1021/acs.analchem.8b02530>.
- (74) Herrmann, A. M.; Ritz, K.; Nunan, N.; Clode, P. L.; Pett-Ridge, J.; Kilburn, M. R.; Murphy, D. V.; O'Donnell, A. G.; Stockdale, E. A. Nano-Scale Secondary Ion Mass Spectrometry - A New Analytical Tool in Biogeochemistry and Soil Ecology: A Review Article. *Soil Biol. Biochem.* **2007**, *39* (8), 1835–1850.  
<https://doi.org/10.1016/j.soilbio.2007.03.011>.
- (75) Mueller, C. W.; Weber, P. K.; Kilburn, M. R.; Hoeschen, C.; Kleber, M.; Pett-Ridge, J. *Advances in the Analysis of Biogeochemical Interfaces: NanoSIMS to Investigate Soil Microenvironments*, 1st ed.; Elsevier Inc., 2013; Vol. 121.  
<https://doi.org/10.1016/B978-0-12-407685-3.00001-3>.
- (76) Höschen, C.; Höschen, T.; Mueller, C. W.; Lugmeier, J.; Elgeti, S.; Rennert, T.; Kögel-Knabner, I. Novel Sample Preparation Technique To Improve Spectromicroscopic Analyses of Micrometer-Sized Particles. *Environ. Sci. Technol.* **2015**, *49* (16), 9874–9880. <https://doi.org/10.1021/acs.est.5b01636>.
- (77) Ost, A. D.; Wu, T.; Höschen, C.; Mueller, C. W.; Wirtz, T.; Audinot, J.-N. 4D Surface Reconstructions to Study Microscale Structures and Functions in Soil Biogeochemistry. *Environ. Sci. Technol.* **2021**, *55* (13), 9384–9393.  
<https://doi.org/10.1021/acs.est.1c02971>.
- (78) De la Escalera, A.; Armingol, J. M. Automatic Chessboard Detection for Intrinsic and Extrinsic Camera Parameter Calibration. *Sensors* **2010**, *10* (3), 2027–2044.  
<https://doi.org/10.3390/s100302027>.
- (79) Armbrust, E. V. The Life of Diatoms in the World's Oceans. *Nature* **2009**, *459* (7244), 185–192. <https://doi.org/10.1038/nature08057>.
- (80) Mansilla, C.; Novais, M. H.; Faber, E.; Martínez-Martínez, D.; De Hosson, J. T. On the 3D Reconstruction of Diatom Frustules : A Novel Method , Applications , and Limitations. *J. Appl. Phycol.* **2016**, *28*, 1097–1110. <https://doi.org/10.1007/s10811-015-0653-y>.

- (81) Chen, X.; Ostadi, H.; Jiang, K. Three-Dimensional Surface Reconstruction of Diatomaceous Frustules. *Anal. Biochem.* **2010**, *403* (1–2), 63–66. <https://doi.org/10.1016/j.ab.2010.04.003>.
- (82) Townley, H. E. Diatom Frustules: Physical, Optical, and Biotechnological Applications. In *The Diatom World. Cellular Origin, Life in Extreme Habitats and Astrobiology*; Seckbach, J., Kociolek, J. P., Eds.; Springer: Dordrecht, 2011; pp 273–289. [https://doi.org/10.1007/978-94-007-1327-7\\_12](https://doi.org/10.1007/978-94-007-1327-7_12).
- (83) Parker, A. R.; Townley, H. E. Biomimetics of Photonic Nanostructures. *Nanosci. Technol.* **2009**, 230–238. [https://doi.org/10.1142/9789814287005\\_0024](https://doi.org/10.1142/9789814287005_0024).
- (84) Falasco, E.; Bona, F.; Badino, G.; Hoffmann, L.; Ector, L. Diatom Teratological Forms and Environmental Alterations: A Review. *Hydrobiologia* **2009**, *623* (1), 1–35. <https://doi.org/10.1007/s10750-008-9687-3>.
- (85) Wilke, W. Segmentierung Und Approximation Großer Punktwolken, Technical University of Darmstadt, 2002.
- (86) Makeev, M. A.; Barabási, A. L. Effect of Surface Morphology on the Sputtering Yields. II. Ion Sputtering from Rippled Surfaces. *Nucl. Instruments Methods Phys. Res. Sect. B Beam Interact. with Mater. Atoms* **2004**, *222* (3–4), 335–354. <https://doi.org/10.1016/j.nimb.2004.02.028>.
- (87) Yamamura, Y.; Mössner, C.; Oechsner, H. The Bombarding-Angle Dependence of Sputtering Yields under Various Surface Conditions. *Radiat. Eff.* **1987**, *103* (1–4), 25–43. <https://doi.org/10.1080/00337578708221239>.
- (88) Shulga, V. I. Note on the Artefacts in SRIM Simulation of Sputtering. *Appl. Surf. Sci.* **2018**, *439*, 456–461. <https://doi.org/10.1016/j.apsusc.2018.01.039>.
- (89) Szabo, P. S.; Chiba, R.; Biber, H.; Stadlmayr, R.; Berger, B. M.; Mayer, D.; Mutzke, A.; Doppler, M.; Sauer, M.; Appenroth, J.; Fleig, J.; Foelske-Schmitz, A.; Hutter, H.; Mezger, K.; Lammer, H.; Galli, A.; Wurz, P.; Aumayr, F. Solar Wind Sputtering of Wollastonite as a Lunar Analogue Material – Comparisons between Experiments and Simulations. *Icarus* **2018**, *314*, 98–105. <https://doi.org/10.1016/j.icarus.2018.05.028>.

- (90) Huang, D.; Hua, X.; Xiu, G. L.; Zheng, Y. J.; Yu, X. Y.; Long, Y. T. Secondary Ion Mass Spectrometry: The Application in the Analysis of Atmospheric Particulate Matter. *Anal. Chim. Acta* **2017**, *989*, 1–14. <https://doi.org/10.1016/j.aca.2017.07.042>.
- (91) Ziegler, J. SRIM and TRIM <http://www.srim.org/> (accessed May 13, 2022).
- (92) Castaldo, V.; Hagen, C. W.; Kruit, P. Simulation of Ion Imaging: Sputtering, Contrast, Noise. *Ultramicroscopy* **2011**, *111* (8), 982–994. <https://doi.org/10.1016/j.ultramic.2011.03.019>.
- (93) Bradley, R. M.; Harper, J. M. E. Theory of Ripple Topography Induced by Ion Bombardment. *J. Vac. Sci. Technol. A Vacuum, Surfaces, Film.* **1988**, *6* (4), 2390–2395. <https://doi.org/10.1116/1.575561>.
- (94) Adams, D. P.; Mayer, T. M.; Vasile, M. J.; Archuleta, K. Effects of Evolving Surface Morphology on Yield during Focused Ion Beam Milling of Carbon. *Appl. Surf. Sci.* **2006**, *252* (6), 2432–2444. <https://doi.org/10.1016/j.apsusc.2005.06.013>.
- (95) MacLaren, S. W.; Baker, J. E.; Finnegan, N. L.; Loxton, C. M. Surface Roughness Development during Sputtering of GaAs and InP: Evidence for the Role of Surface Diffusion in Ripple Formation and Sputter Cone Development. *J. Vac. Sci. Technol. A Vacuum, Surfaces, Film.* **1992**, *10* (3), 468–476. <https://doi.org/10.1116/1.578173>.
- (96) Iacob, E.; Demenev, E.; Giubertoni, D.; Barozzi, M.; Gennaro, S.; Bersani, M. Development of Nano-Roughness under SIMS Ion Sputtering of Germanium Surfaces. *Surf. Interface Anal.* **2013**, *45* (1), 409–412. <https://doi.org/10.1002/sia.4997>.
- (97) Wittmaack, K. Effect of Surface Roughening on Secondary Ion Yields and Erosion Rates of Silicon Subject to Oblique Oxygen Bombardment. *J. Vac. Sci. Technol. A Vacuum, Surfaces, Film.* **1990**, *8* (3), 2246–2250. <https://doi.org/10.1116/1.576744>.
- (98) Kaczynski, R.; Lee, J.; Alsbury, J. Van; Wang, Y.; Sang, B. Inline Rubidium Fluoride Treatment of (A)CIGS Absorbers Deposited onto Flexible Substrates in a Production-Scale Process Tool. *Conf. Rec. IEEE Photovolt. Spec. Conf.* **2019**, 1420–1423. <https://doi.org/10.1109/PVSC40753.2019.8981303>.
- (99) Vilalta-Clemente, A.; Raghuwanshi, M.; Duguay, S.; Castro, C.; Cadel, E.; Pareige, P.;

- Jackson, P.; Wuerz, R.; Hariskos, D.; Witte, W. Rubidium Distribution at Atomic Scale in High Efficient Cu(In,Ga)Se<sub>2</sub> Thin-Film Solar Cells. *Appl. Phys. Lett.* **2018**, *112* (10). <https://doi.org/10.1063/1.5020805>.
- (100) Keller, J.; Aboufadel, H.; Stolt, L.; Donzel-Gargand, O.; Edoff, M. Rubidium Fluoride Absorber Treatment for Wide-Gap (Ag,Cu)(In,Ga)Se<sub>2</sub> Solar Cells. *Sol. RRL* **2022**, *6* (6). <https://doi.org/10.1002/solr.202200044>.
- (101) Ost, A. D.; Audinot, J.; Wirtz, T. 4D Reconstructions from Microscale Photogrammetry : Correlation of 3D Surface Representations with SIMS to Link Microstructural Topography and Chemical Information. *Microsc. Microanal.* **2022**, *28* (Suppl 1), 252–254. <https://doi.org/10.1017/S1431927622001830>.
- (102) *Handbook of Charged Particle Optics*, 2nd editio.; Orloff, J., Ed.; CRC Press, 2009. <https://doi.org/10.1201/9781420045550>.
- (103) Dahl, D. A. SIMION for the Personal Computer in Reflection. *Int. J. Mass Spectrom.* **2000**, *200* (1–3), 3–25. [https://doi.org/10.1016/S1387-3806\(00\)00305-5](https://doi.org/10.1016/S1387-3806(00)00305-5).
- (104) Ost, A. D.; Vollnhals, F.; Philipp, P.; Wirtz, T.; Audinot, J.-N. Improvement of SIMS Analyses under Ne<sup>+</sup> Bombardment by Oxygen Flooding. *Beilstein J. Nanotechnol.* **2022**, submitted.
- (105) Mutzke, A.; Schneider, R.; Eckstein, W.; Dohmen, R.; Schmid, K.; von Toussaint, U.; Bandelow, G. *SDTrimSP Version 6.00*; 2019.
- (106) Morita, M.; Ohmi, T.; Hasegawa, E.; Kawakami, M.; Suma, K. Control Factor of Native Oxide Growth on Silicon in Air or in Ultrapure Water. *Appl. Phys. Lett.* **1989**, *55* (6), 562–564. <https://doi.org/10.1063/1.102435>.
- (107) Barlett, R. W.; McCamont, J. W. The Influence of Crystal Orientation on the Volume Plasmon of Germanium. *J. Electrochem. Soc.* **1965**, *112* (2), 148–152. <https://doi.org/https://doi.org/10.1149/1.2423484>.
- (108) Mutzke, A.; Eckstein, W. Ion Fluence Dependence of the Si Sputtering Yield by Noble Gas Ion Bombardment. *Nucl. Instruments Methods Phys. Res. Sect. B Beam Interact. with Mater. Atoms* **2008**, *266* (6), 872–876.

<https://doi.org/10.1016/j.nimb.2008.01.053>.

- (109) Rzeznik, L.; Fleming, Y.; Wirtz, T.; Philipp, P. Experimental and Simulation-Based Investigation of He, Ne and Ar Irradiation of Polymers for Ion Microscopy. *Beilstein J. Nanotechnol.* **2016**, *7*, 1113–1128. <https://doi.org/10.3762/bjnano.7.104>.
- (110) Haynes, W. M. *CRC Handbook of Chemistry and Physics*, 95th ed.; Haynes, W. M., Lide, D. R., Bruno, T. J., Eds.; CRC Press: Boca Raton, FL, 2014.
- (111) Sander, P.; Kaiser, U.; Jede, R.; Lipinsky, D.; Ganschow, O.; Benninghoven, A. Secondary Ion and Sputtered Neutral Formation from Oxygen Loaded Si(100). *J. Vac. Sci. Technol. A Vacuum, Surfaces, Film.* **1985**, *3* (5), 1946–1954. <https://doi.org/10.1116/1.572949>.
- (112) Benitez, G.; Carelli, J. L.; Heras, J. M.; Viscido, L. Interaction of Oxygen with Thin Cobalt Films. *Langmuir* **1996**, *12*, 57–60. <https://doi.org/10.1021/la940743w>.
- (113) Barbee, T. W.; Keith, D. L.; Nagel, L.; Tiller, W. A. Controlled Reactive Sputter Synthesis of Refractory Oxides: , The Silicon-Oxygen System. *J. Electrochem. Soc.* **1984**, *131* (2), 434–439. <https://doi.org/10.1149/1.2115599>.
- (114) Yu, M. L.; Lang, N. D. Mechanisms of Atomic Ion Emission during Sputtering. *Nucl. Inst. Methods Phys. Res. B* **1986**, *14* (4–6), 403–413. [https://doi.org/10.1016/0168-583X\(86\)90135-7](https://doi.org/10.1016/0168-583X(86)90135-7).
- (115) Slodzian, G. Some Problems Encountered in Secondary Ion Emission Applied to Elementary Analysis. *Surf. Sci.* **1975**, *48* (1), 161–186. [https://doi.org/10.1016/0039-6028\(75\)90315-5](https://doi.org/10.1016/0039-6028(75)90315-5).
- (116) Slodzian, G. Remarks on Some Factors Influencing the Charge State of Sputtered Particles. *Phys. Scr.* **1983**, *1983* (T6), 54–66. <https://doi.org/10.1088/0031-8949/1983/T6/009>.
- (117) Hagen, C. W.; Fokkema, E.; Kruit, P. Brightness Measurements of a Gallium Liquid Metal Ion Source. *J. Vac. Sci. Technol. B Microelectron. Nanom. Struct.* **2008**, *26* (6), 2091–2096. <https://doi.org/10.1116/1.2987958>.
- (118) Malherbe, J.; Penen, F.; Isaure, M. P.; Frank, J.; Hause, G.; Dobritsch, D.; Gontier, E.;

- Horréard, F.; Hillion, F.; Schaumlöffel, D. A New Radio Frequency Plasma Oxygen Primary Ion Source on Nano Secondary Ion Mass Spectrometry for Improved Lateral Resolution and Detection of Electropositive Elements at Single Cell Level. *Anal. Chem.* **2016**, *88* (14), 7130–7136. <https://doi.org/10.1021/acs.analchem.6b01153>.
- (119) Alton, G. D. 3 - Sources of Low-Charge-State Positive-Ion Beams. In *Atomic, Molecular, and Optical Physics: Charged Particles*; Dunning, F. B., Hulet, R. G., Eds.; 1995; Vol. 29, pp 69–168. [https://doi.org/https://doi.org/10.1016/S0076-695X\(08\)60654-7](https://doi.org/https://doi.org/10.1016/S0076-695X(08)60654-7).
- (120) Kumar, P.; Pfeffer, M.; Willsch, B.; Eibl, O.; Yedra, L.; Eswara, S.; Audinot, J. N.; Wirtz, T. Direct Imaging of Dopant Distributions across the Si-Metallization Interfaces in Solar Cells: Correlative Nano-Analytics by Electron Microscopy and NanoSIMS. *Sol. Energy Mater. Sol. Cells* **2017**, *160* (November 2016), 398–409. <https://doi.org/10.1016/j.solmat.2016.11.004>.
- (121) Bischoff, L.; Mazarov, P.; Bruchhaus, L.; Gierak, J. Liquid Metal Alloy Ion Sources - An Alternative for Focussed Ion Beam Technology. *Appl. Phys. Rev.* **2016**, *3* (2). <https://doi.org/10.1063/1.4947095>.
- (122) Kollmer, F.; Paul, W.; Krehl, M.; Niehuis, E. Ultra High Spatial Resolution SIMS with Cluster Ions - Approaching the Physical Limits. *Surf. Interface Anal.* **2013**, *45*, 312–314. <https://doi.org/10.1002/sia.5093>.
- (123) IONTOF GmbH. The all new M6 TOF Analyser <https://www.iontof.com/m6-tof-sims-technical-details.html> (accessed Aug 24, 2022).
- (124) Knuffman, B.; Steele, A. V.; McClelland, J. J. Cold Atomic Beam Ion Source for Focused Ion Beam Applications. *J. Appl. Phys.* **2013**, *114* (4). <https://doi.org/10.1063/1.4816248>.
- (125) Nanoscale Stripe Pattern for Testing of Lateral Resolution and Calibration of Length Scale. In *Certified Reference Material - BAM-L200 - Certification Report*; Berlin, Germany, 2007; pp 1–4.
- (126) Newey, B. *ORION NanoFab. HIM-FIB for Nanofabrication and Microscopy. Operator's Manual*; Carl Zeiss Group: Oberkochen, Germany, 2018.

- (127) Wu, T.; Ost, A. D.; Audinot, J. N.; Wiesmeier, M.; Wirtz, T.; Buegger, F.; Häusler, W.; Höschen, C.; Mueller, C. W. Association of Fresh Low-Molecular-Weight Organic Compounds with Clay-Sized Mineral Fraction in Soils of Different Organic Carbon Loading. *Geoderma* **2022**, *409*. <https://doi.org/10.1016/j.geoderma.2021.115657>.
- (128) Wu, C. Normalized Spectral Mixture Analysis for Monitoring Urban Composition Using ETM+ Imagery. *Remote Sens. Environ.* **2004**, *93* (4), 480–492. <https://doi.org/10.1016/j.rse.2004.08.003>.
- (129) Rennert, T.; Höschen, C.; Rogge, D.; Steffens, M. Small-Scale Distribution of Copper in a Technosol Horizon Studied by Nano-Scale Secondary Ion Mass Spectrometry. *Rapid Commun. Mass Spectrom.* **2018**, *32* (11), 851–861. <https://doi.org/10.1002/rcm.8111>.
- (130) Steffens, M.; Rogge, D. M.; Mueller, C. W.; Höschen, C.; Lugmeier, J.; Kölbl, A.; Kögel-Knabner, I. Identification of Distinct Functional Microstructural Domains Controlling C Storage in Soil. *Environ. Sci. Technol.* **2017**, *51* (21), 12182–12189. <https://doi.org/10.1021/acs.est.7b03715>.

## Appendices

### Appendix A: Ionization models

In this section, a brief description of the two most common ionization models will be provided.

In the electron tunneling model (Figure A. 1 a) the ionization process is described by the resonance electron transfer of the atomic level of an atom leaving the surface and the delocalized state of the valence band of the metal matrix through the electron tunneling effect.<sup>114</sup> The ionization probability depends on the electron work function  $\phi$  which is defined as the difference between the Fermi energy  $e_F$ , i.e., the separation level between the occupied and unoccupied states in the metal, and the vacuum level. However, charge transfer is suppressed by a potential barrier between the electronic states in the metal and the leaving atom. At a distance  $z_c$  from the metal the electron can tunnel through the barrier, where the potential barrier level equals the Fermi level.

For positive and negative ions the ionization probabilities  $\beta^+$  and  $\beta^-$  are given by:

$$\beta^+ = 1, \text{ if } \phi > I \qquad \beta^- = 1, \text{ if } \phi < A \qquad (\text{A.1})$$

$$\beta^+ = e^{-\left(\frac{I-\phi}{\varepsilon_p}\right)}, \text{ if } \phi < I \qquad \beta^- = e^{-\left(\frac{\phi-A}{\varepsilon_n}\right)}, \text{ if } \phi > A \qquad (\text{A.2})$$

where  $I$  is the ionization energy,  $A$  the electron affinity of the sputtered atom, and  $\varepsilon_p$  and  $\varepsilon_n$  are local sample property parameters.

For chemical compounds with highly localized (ionic or covalent) bonds, e.g. for oxides, the bond breaking model is applied, which was first introduced by Slodzian.<sup>115,116</sup> In this model, during the sputtering process, an ion  $M^+$  departs from the surface and leaves a vacant cation with an electron affinity  $A$  (Figure A. 1 b). The site keeps the electron for the sputtering time interval ( $10^{-13}$  s). A transfer of the electron between the sample and the sputtered ion  $M^+$  can take place at a distance  $R_c$  from the sample surface. At  $R_c$  the curves of the covalent potential energy and ionic potential energy cross each other. The charge transfer probability is given by the Landau-Zener relation, stating that with lower ionization energy the ionization probability increases.<sup>18</sup>

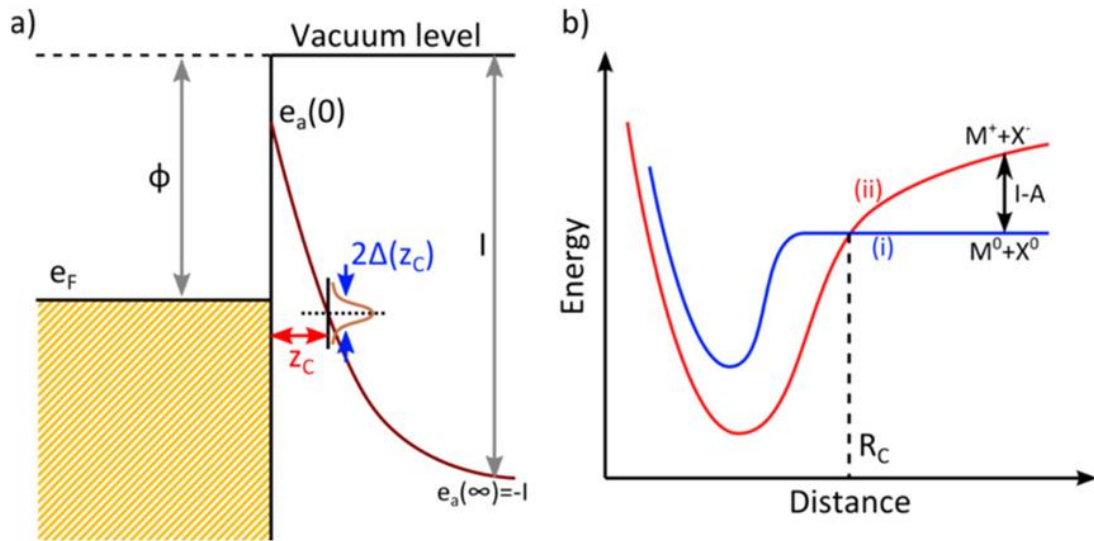


Figure A. 1: Illustration of the a) electron tunnelling and b) the bond breaking models (Figure from Wirtz et al.).<sup>18</sup>

## Appendix B: Ion sources

In this section, a brief overview of the characteristics of the most common ion sources will be given: the electron impact, duoplasmatron, surface ionization, RF-plasma, and liquid metal ion sources (LMIS) (see Table B. 1).

In the electron impact source highly energetic electrons are directed towards the gas molecules which are ionized upon impact and accelerated towards the sample. This source allows to use any gas (e.g., argon, oxygen) or vapor after evaporating a liquid/solid compound to produce monoatomic ions ( $\text{Ar}^+$ ,  $\text{O}^+$ ) or cluster ions (e.g.,  $\text{Ar}_{2000}^+$  or  $\text{C}_{60}^+$ ). The source brightness and current densities are relatively low, and the virtual source size (referring to the apparent source size when looking backwards through the primary ion optics)<sup>102,117</sup> is large. Monoatomic ions are mainly used for the cleaning of the surface and record mass spectra with time-of-flight (ToF) mass spectrometers. Cluster ions can be used also for recording of mass spectra and depth profiling (also in x-ray photoelectron spectroscopy) because the energy impact per atom is reduced minimizing the fragmentation, which is especially useful for organic chemistry and life science applications.<sup>36</sup>

The duoplasmatron source also works with gases but uses in this case a plasma environment to ionize injected gas molecules. This leads to a more efficient ionization process and leads to a higher brightness and reduced beam diameters. However, usage of this source is limited to monoatomic ions or small gas molecules, e.g. oxygen (to produce  $\text{O}_2^+$  and  $\text{O}^-$ ), and is suited for depth profiling and imaging applications. The typical lateral resolution of the duoplasmatron source ( $\text{O}^-$ ) can vary from 100 nm to 400 nm, depending on the current density.<sup>118</sup>

In a surface ionization source, a salt (e.g.,  $\text{CaCO}_3\text{Cs}$ ,  $\text{KCs}$ ) is used to produce a primary ion beam ( $\text{Cs}^+$ ) by heating and guiding the heated atomic vapor through a closed tube. After its deposition on a hot tungsten plate the atomic vapor becomes ionized.<sup>119</sup>  $\text{Cs}^+$  primary ions are of high interest for SIMS since they allow to significantly improve both sputtering and ionization yields (i.e., useful yields) of negative ion species by reducing the work function of the material. This source is able to operate with high currents and has the lowest energy spread of those discussed in this section, making it highly suitable for depth profiling and

imaging applications at high spatial resolution (down to 50 nm),<sup>120</sup> in particular for the detection of trace elements.

*Table B. 1: Most common primary ion sources used in SIMS with their characteristics (table from Audinot et al.).<sup>16</sup>*

Source type/ Characteristics	Electron impact ion source	Duoplasma- tron ion source	Surface ionization ion source	Liquid metal ion source	Gas field ion source	RF plasma source	Cold atom ion source
<b>Species</b>	Ar, Xe, O <sub>2</sub> , SF <sub>6</sub> , C <sub>60</sub> , ...	Ar, Xe, O <sub>2</sub> , ...	Cs	Ga, In, Au <sub>n</sub> , Bi <sub>n</sub> , ...	He, Ne, N <sub>2</sub>	H, He, O <sub>2</sub> , Ar, Ne, Kr, Xe	Li, Na, Rb, Cs, Ga, ...
<b>Virtual source size</b>	1 mm	200 μm	50 μm	3 nm	~ 3 Å	15 μm	10 μm
<b>Ion energy for singly charged ions (keV)</b>	0.1-20	0.1-20	0.3-20	2-30	5-45	3-30	2 – 30
<b>Beam current</b>	1-1000 μA	1-1000 mA	10 μA – 100 mA	1 – 1000 μA	1 fA – 100 pA	1 pA – 1 μA	1 pA – 10 nA
<b>Brightness (A cm<sup>-2</sup> sr<sup>-2</sup>)</b>	1	10 <sup>2</sup>	10 <sup>2</sup>	10 <sup>7</sup>	10 <sup>9</sup>	10 <sup>3</sup>	> 10 <sup>7</sup>
<b>Energy dispersion (eV)</b>	1-10	5-20	0.2-0.5	5-50	<1	5-6	0.01 – 10

The liquid metal ion source is a field ion emission source and uses a sharp needle covered by metal or metal alloy (e.g., AuGeSi or recently also GaBiLi).<sup>121</sup> The needle is heated until the melting point of the metal (alloy) and a high electric field is applied with an extractor electrode to emit primary single or cluster ions. Ga<sup>+</sup> is very commonly used for this type of source for nano-patterning and milling applications in FIB-SEM microscopes. In a SIMS instrument, the LMIS is mainly used for imaging and mass spectrum acquisitions. For instance, the bismuth cluster LMIS Bi<sub>n</sub><sup>+</sup> allows to perform imaging at a lateral resolution under 50 nm.<sup>122,123</sup>

The gas field ion source is able to produce ultra-high brightness using He<sup>+</sup> and Ne<sup>+</sup> primary ions, particularly useful for high spatial resolution (< 20 nm) imaging in SIMS.<sup>16,39</sup> More details about the GFIS are given in chapter 1 in section 4.1.

The most recent progress on ion sources was made on radio frequency (RF) and cold ion sources.

In the RF source, a high-frequency discharge in a dielectric bottle is used to create gas (e.g., oxygen) ionization in a dielectric bottle. Ions (e.g., O<sub>2</sub><sup>+</sup>) are extracted with an electric field through the bottle.<sup>2</sup> Advantages of the RF source are the possibility to obtain high source brightness, allowing imaging with a higher lateral resolution and higher sputtering rates, and longer lifetimes compared to regular plasma sources.

The cold ion source uses laser-cooling to create ultra-cold atoms, e.g. Cs. In this source, first a slow atomic beam is produced with a magneto-optical trap and then the atomic beam is ionized by passing through the overlapping region of two highly focused laser beams. The focus of the lasers can be changed to increase/reduce the overlap volume in order to adapt the ion beam diameter and current. Advantages of this source are the low energy spread and a very high brightness.<sup>16,124</sup>

## Appendix C: Lateral resolution of the HIM-SIMS and FIB-SEM-SIMS

Here the results on the determination of the SIMS imaging resolution of the HIM-SIMS and FIB-SEM-SIMS instruments performed by Dowsett and Wirtz<sup>43</sup> and De Castro et al.<sup>14</sup> will be shown.

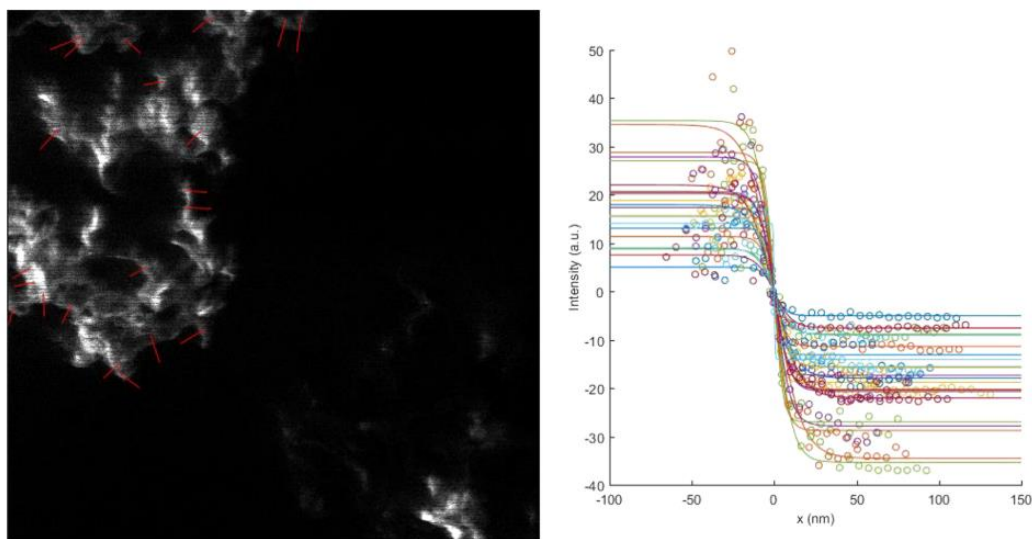


Figure C. 1:  ${}^6\text{Li}^+$  image (FOV  $1.5\ \mu\text{m} \times 1.5\ \mu\text{m}$ , 25 keV  $\text{Ne}^+$ , 1.1 pA) of lithium titanate nanoparticles acquired on a HIM-SIMS instrument (Figure from Dowsett and Wirtz).<sup>43</sup>

Figure C. 1 shows the lithium-6 image of lithium titanate nanoparticles analyzed by Dowsett and Wirtz<sup>43</sup> using the HIM-SIMS instrument. The mean (21 line scans) edge resolution (75 % - 25 %) corresponded to  $10 \pm 3.6\ \text{nm}$ , i.e. close to the fundamental limit defined by the collision cascade.

In Figure C. 2 De Castro et al.<sup>14</sup> analyzed the BAM-200 sample<sup>125</sup> in SIMS imaging mode using the FIB-SEM-SIMS. Performing the rising-edge resolution determination (80 % - 20 % maximum intensity drop criterion)<sup>122</sup> on the P9 and P10 periods (Figure C. 2), a lateral resolution of 15 nm is obtained.

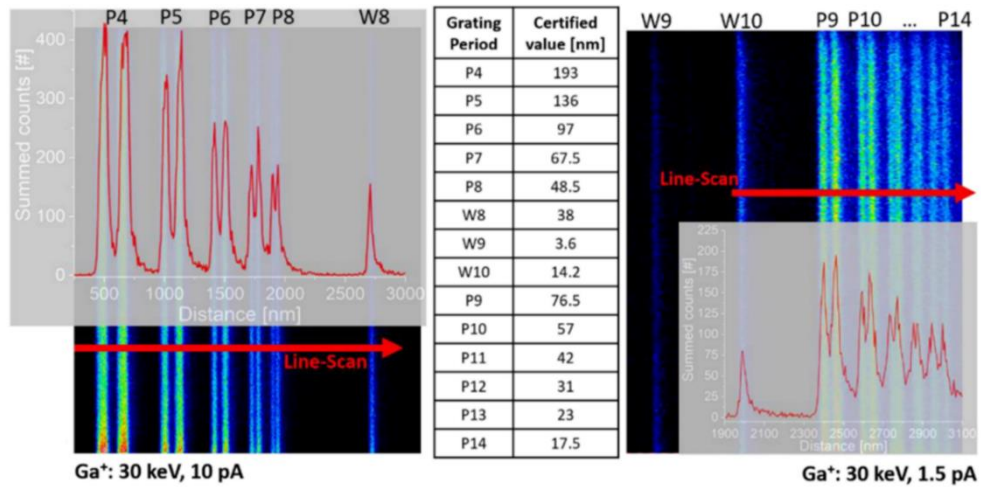


Figure C. 2: Determination of the lateral resolution of the FIB-SEM-SIMS in SI imaging mode on a BAM-200 sample.<sup>125</sup> Left:  $^{27}\text{Al}^+$  image with FOV  $3.5\ \mu\text{m} \times 3.5\ \mu\text{m}$ , 30 keV  $\text{Ga}^+$ , 10 pA, right:  $^{27}\text{Al}^+$  image with FOV  $5.2\ \mu\text{m} \times 5.2\ \mu\text{m}$ , 30 keV  $\text{Ga}^+$ , 1.5 pA (Figure adapted from De Castro et al.).<sup>14</sup>

## Appendix D: Brief primary and secondary ion optics description of the HIM-SIMS instrument

In this section, a brief description of the primary and secondary ion optics of the HIM-SIMS instrument will be given. Further information about the primary ion optics can be found in the official Zeiss ORION NanoFab HIM manual.<sup>126</sup> As the primary ion source of the HIM-SIMS the GFIS represents a rather recent ion source development compared to the liquid metal ion source (LMIS) of the FIB-SEM-SIMS and secondary optics of the HIM-SIMS are similar (with some fundamental differences discussed in chapter 1 section 4.2.1) to those of the FIB-SEM-SIMS, we will limit ourselves here to a description of the HIM-SIMS only. The role of the source and primary optics is to create a stable and aligned primary ion beam focused onto the sample. In Table D. 1 the ion optics components of the GFIS column are listed with a brief description and characteristic parameters, such as typically applied voltage or aperture diameter.

*Table D. 1: Summarized description of the source and primary ion optics of the HIM.*

<b>Component</b>	<b>Description and Function</b>	<b>Characteristic values</b>
	Source – made of a tungsten filament creating positive gas ions. A (positive) bias is applied to the source to allow extraction of the primary ions.	Ranging from 10 kV to 35 kV
	Extractor electrode biased to create a (negative) potential difference with the source creating an electric field used to ionize gas atoms and extract the ions.	Ranging from - 25 kV to - 35 kV
	Lens 1 (also known as condenser lens) used to bring the primary beam into a single point (called crossover). Value changed in most cases only in source view mode and to change spot size.	Ranging from 0 kV to 40 kV
	Quadrupoles – positioned under lens 1 to realign the beam on the x-axis and center on lens 2.	n/a

	Beam limiting apertures used to narrow down the beam for better imaging. In total 14 apertures with different diameter sizes available.	Typically in - SE mode: 10 $\mu\text{m}$ , 5 $\mu\text{m}$ - SIMS: 70 $\mu\text{m}$ , 40 $\mu\text{m}$ , 20 $\mu\text{m}$
	Octupole deflectors – deflect the primary ion beam to scan over the surface of the sample for imaging purposes and to correct astigmatism.	n/a
	Lens 2 (objective lens) focusses the beam on the sample and controls position of the focal point (working distance).	Ranging from 0 kV to 40 kV

The SI optics collects the created ions from the sample and transfers them towards the mass spectrometer, while optimal transmission is achieved by aligning the SI beam. Table D. 2 summarizes the main components of the SI extraction system and the mass spectrometer.

*Table D. 2: Summarized description of the secondary ion optics and mass spectrometer components of the SIMS part of the HIM-SIMS instrument.*

<b>Device</b>	<b>Description and Function</b>	<b>Characteristic values</b>
	Movable sample stage under positive/negative bias for enhanced extraction of positive/negative SIs.	$\pm 500 \text{ V}$
	Spherical electrostatic sector electrodes used to bend the SI beam by 90°. Consists of an inner and outer spherical sector.	Inner: 365 V – 385 V Outer: 425 V
	Lens 1 transfers the ion beam towards the mass spectrometer and used for beam alignment.	800 V – 1600 V
	Quadrupoles – a four-plate deflector centering the SI beam.	n/a

	Lens 2 transfers the ion beam towards the mass spectrometer and used for beam alignment.	800 V – 1600 V
	Quadrupoles – a four-plate deflector centering the SI beam.	n/a
	Beam limiting apertures (in total 5 of variable diameters) used to align the SI beam to the center of the SI optics axis.	Diameter ranging from 2 $\mu\text{m}$ to 0.1 $\mu\text{m}$
	Spherical electrostatic sector electrodes used to bend the SI beam by 60° and acts as an energy separator. Consists of an inner and outer spherical sector.	Inner: ~ 670 V Outer: ~ 550 V
	Double-plate magnetic field sector used to deviate and separate the SIs according to their charge-to-mass ratio with a magnetic field.	0 mT – 500 mT
	Channeltron detectors: 3 movable ones, 1 fixed (CH1-4), and 1 total ion count (TIC) detector.	CH1-4: 2100 V TIC: 2500 V

The design of the secondary ion optics system of the FIB-SEM-SIMS is similar to one of the HIM-SIMS with some fundamental differences. For practical reasons, three lenses are used to transfer the SI beam to the mass analyzer and an additional electrostatic sector between the spherical electrostatic sector and lens 1 needed to be added to bend the beam due to the 52° orientation of the FIB with respect to the vertical direction.

## Appendix E: Correlative microscopy case studies in soil biogeochemistry

This section aims to present two case studies in soil biogeochemistry where the HIM-SIMS and a CAMECA NanoSIMS 50L were correlated.

In the following case study, HIM-SIMS results were correlated with those acquired with the CAMECA NanoSIMS 50L for a study in the field of soil biogeochemistry (Figure E. 1). Soils represent one of the largest carbon storage pools on Earth, since they are capable of incorporating (and releasing) organic carbon from (and into) the atmosphere which is known as the organic carbon sequestration process. Soils consist mainly of an association of organic matter (OM) and different mineral substances. To study the OM sequestration in soils, isotope labeling is a known method to trace the fate of freshly introduced carbon in soil samples. In this study, samples of soil microaggregates were enriched with isotopic carbon ( $^{13}\text{C}$ ) and nitrogen ( $^{15}\text{N}$ ) in an incubation experiment.<sup>127</sup> Here the aim was to find preferable sites of OM deposition.

The HIM-SIMS was used to image the microaggregate's topography in SE and its mineral phase at high spatial resolution and the NanoSIMS 50L to image OM compounds at appropriate MRP to avoid mass interferences.

First, an SE image of a soil microaggregate was taken in the HIM (Figure E. 1 a). In-situ high-resolution (HIM-) SIMS imaging of the soil mineral phase was performed on the same microaggregate (Figure E. 1 b). Subsequently, the sample was transferred to the NanoSIMS 50L instrument to image the inherited and isotopically labelled OM phase of the microaggregate (Figure E. 1 c). By correlating SIMS images (magnesium, aluminum, potassium) with HIM using the Laplace fusion method (Figure E. 1 d and e) allowed to identify mineral phase areas of the microaggregate with a high/low surface roughness.

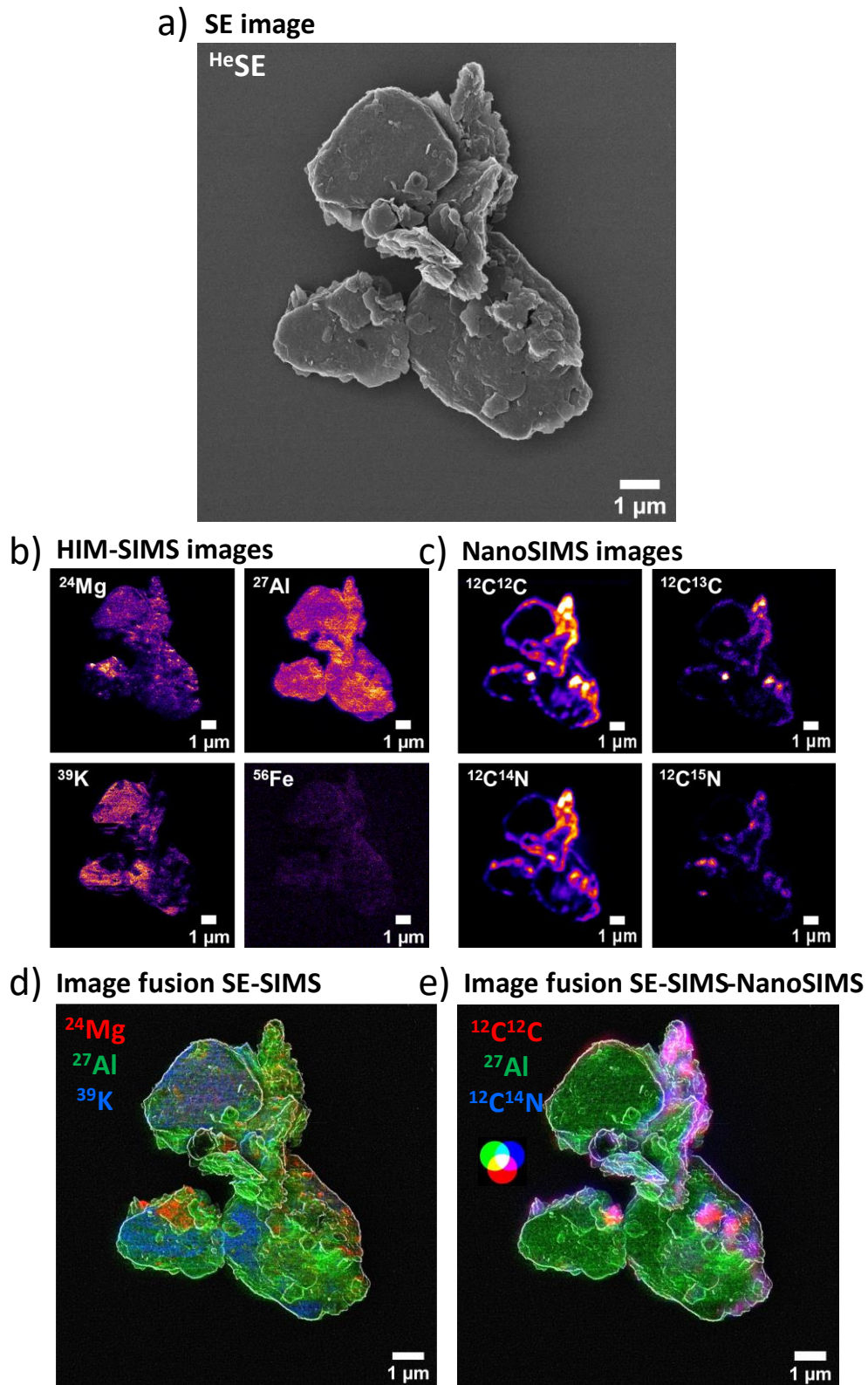


Figure E. 1: Correlative imaging study on a soil microaggregate combining HIM-SIMS and NanoSIMS 50L measurements. a) HIM SE image (25 keV He<sup>+</sup>, 2 pA, 10 μs/pixel, 4 line average). b) HIM-SIMS images of the microaggregate's mineral phase (25 keV Ne<sup>+</sup>, 6 pA, 5 ms/pixel). c) NanoSIMS 50L images of the OM compounds (16 keV Cs<sup>+</sup>, 2 pA, 1 ms/pixel). d) Laplace image

fusion of the HIM SE image in a) and (HIM-)SIMS images of b). e) fusion of HIM-SIMS images from a), b) and NanoSIMS 50L images from c).

Additionally, correlating images from both instruments (HIM-SIMS, NanoSIMS 50L) revealed that in this case the OM is located on surfaces with a high rugosity, while flat surfaces were avoided, which was first observed by Vogel et al.<sup>8</sup> Moreover, the freshly introduced OM deposited on areas which contained already inherited one.

The aim of the next case study was precisely to analyze in detail structures with OM hotspots (Figure E. 2). NanoSIMS 50L images were correlated here with ultra-high resolution HIM SE images. First, a soil sample presenting a high OM content was analyzed in the NanoSIMS 50L. SIMS analyses were performed for a chosen soil microaggregate for its mineral phase, represented by  $^{16}\text{O}$ , and OM, shown by the  $^{12}\text{C}^{14}\text{N}$  distribution. SIMS was performed here first to identify first OM hotspots and areas without OM distribution.

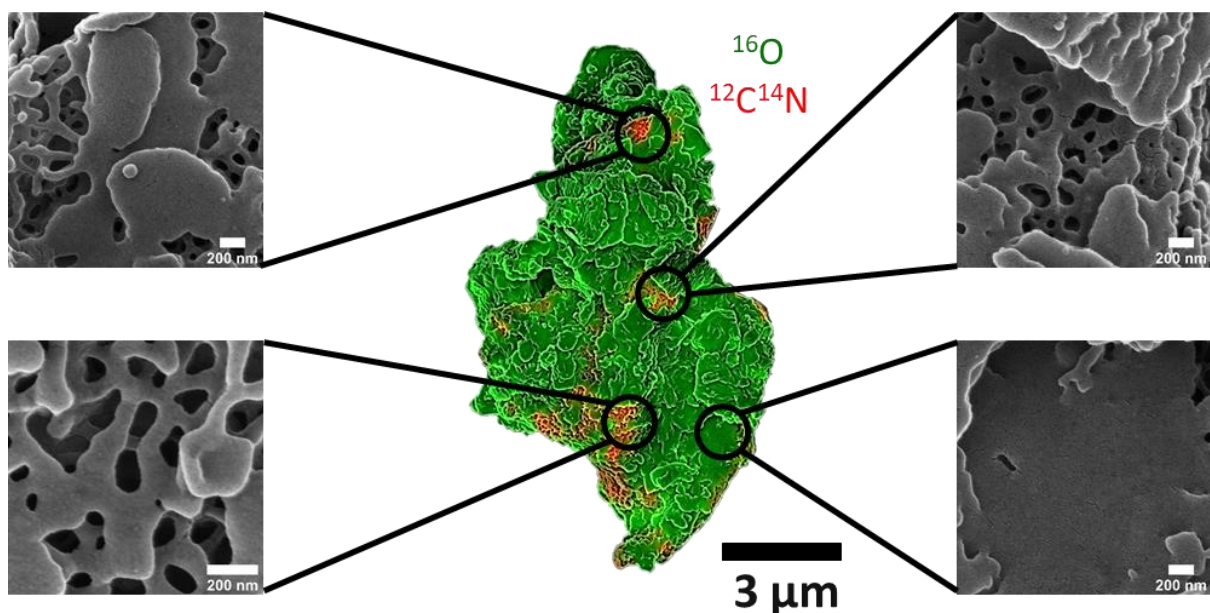


Figure E. 2: Correlative NanoSIMS 50L and HIM study on a soil microaggregate to find preferable topographic sites for OM hotspots. The soil microaggregate was imaged first in SIMS (25 keV  $\text{Ne}^+$ , 6 pA, 5 ms/pixel) to localize locations of hotspots and absence of OM (red:  $^{12}\text{C}^{14}\text{N}$ ) on the mineral phase (green:  $^{16}\text{O}$ ). The microaggregate was imaged then in HIM (25 keV  $\text{He}^+$ , 1 pA, 10  $\mu\text{s}$ /pixel, 4 line average) at specific locations presenting a high concentration and absence of OM.

These ROIs were imaged then in the HIM in SE mode at high magnification (fields of view of  $2.5\ \mu\text{m} \times 2.5\ \mu\text{m}$  and  $1\ \mu\text{m} \times 1\ \mu\text{m}$ ). OM hotspots were found on structures with a high porosity and irregular topography, while flat mineral surfaces did not present OM hotspots. This shows that chemical composition and topography are drivers for OM deposition in soils which helps to understand the organic carbon sequestration process and eventually to control it in the future.

While in this study 2D images were used and correlated to link topographical and analytical information to conclude on preferential sites for OM deposition just from inspection of the images, more representative conclusions can be taken when knowing the exact 3D topography of the microaggregate. In chapter 2 section 1, a novel photogrammetric methodology for 3D surface reconstruction was presented used to analyze topologically the surface and to statistically evaluate the distribution of OM with respect to its topography.

In this context, it is worth noting that in the framework of this thesis first experiments were performed on the HIM-SIMS to identify pixel-wise different clay mineral species (kaolinite, chlorite, illite, muscovite, each consisting of different compositions of magnesium, aluminum, silicon, and potassium) in SIMS images of chalk rock or soil samples. By calculating characteristic ratios (“mean normalized counts”, MNCs)<sup>128–130</sup> from the SI signals of  $^{24}\text{Mg}$ ,  $^{27}\text{Al}$ ,  $^{28}\text{Si}$ , and  $^{39}\text{K}$  signals, measured in depth profiling mode on reference mineral samples, the aim was to map the distribution of these minerals in SIMS images of mixed samples. However, due to a widespread and overlap of the MNCs, an accurate mineral identification was not possible at this stage. The results about this study can be found in the next section of the Appendices. More detailed investigations could be a subject of future studies.

## Appendix F: Mineral identification by comparing mean normalized counts

In this study, the aim was to identify pixel-wise different clay minerals (illite, kaolinite, muscovite, and chlorite) in SIMS images. To do so, characteristic values of each mineral were needed to allow the identification of a mineral in a given pixel in the image.

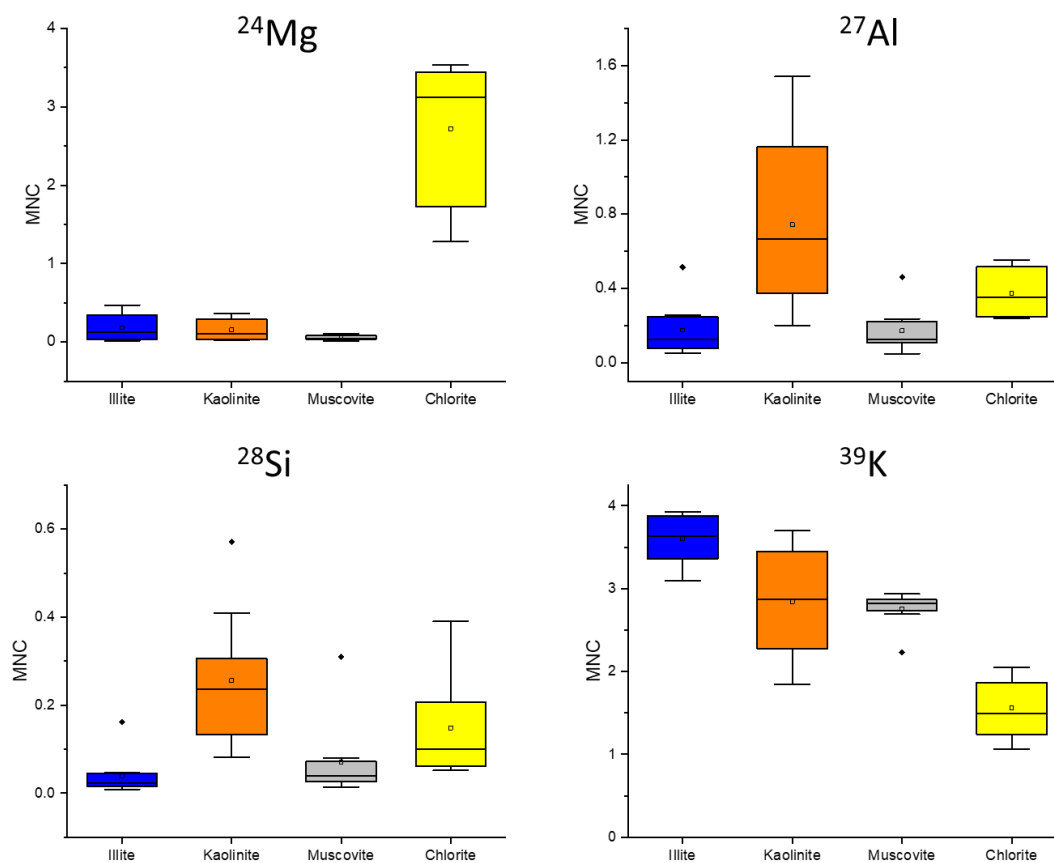


Figure F. 1: Boxplots of the MNCs determined from depth profiles (10 measurements acquired for each box) for  $^{24}\text{Mg}$ ,  $^{27}\text{Al}$ ,  $^{28}\text{Si}$ , and  $^{39}\text{K}$  SI signals measured on pure reference mineral samples (illite, kaolinite, muscovite, and chlorite) consisting of different chemical compositions containing magnesium, aluminum, silicon, and potassium.

Therefore, depth profiling experiments (25 keV  $\text{Ne}^+$ , 10 pA primary current,  $20 \times 20 \mu\text{m}^2$ , 60 % gating, dwell time 1s/frame) were performed on pure reference clay mineral samples (10 measurements for each mineral), monitoring the  $^{24}\text{Mg}$ ,  $^{27}\text{Al}$ ,  $^{28}\text{Si}$ , and  $^{39}\text{K}$  SI signals in positive mode. The average number of counts was determined once the signal stabilized (signal taken

at  $t = 100$  s in each case). The mean normalized counts (MNC)<sup>128–130</sup> for a species  $i$  were then calculated for each mineral using the following equation:

$$MNC_i = \frac{cts_i}{(\sum_{i=1}^n cts_i)/n} \quad (F.1)$$

Where  $cts_i$  is the average number of counts for a detected secondary ion  $i$ , and  $n$  is the number of considered SIs (i.e.,  $n = 4$  here). The calculated MNCs are represented as boxplots in Figure F. 1. In order to map the distribution of the minerals, a MATLAB algorithm was written based on the flowchart shown in Figure F. 2. The algorithm imports first the  $^{24}\text{Mg}$ ,  $^{27}\text{Al}$ ,  $^{28}\text{Si}$ , and  $^{39}\text{K}$  SIMS images taken of a sample with mixed distributions of clay minerals. It raster scans through all the pixels of the images calculates for each pixel the MNC for a given SI and identifies the clay mineral based on the MNC found from the measurements on the pure minerals (Figure F. 2). As the boxplots for  $^{27}\text{Al}$  and  $^{28}\text{Si}$  showed a very similar distribution, the MNC of  $^{28}\text{Si}$  was chosen here as the boxplots presented a lower spread of the MNCs compared to  $^{27}\text{Al}$ .

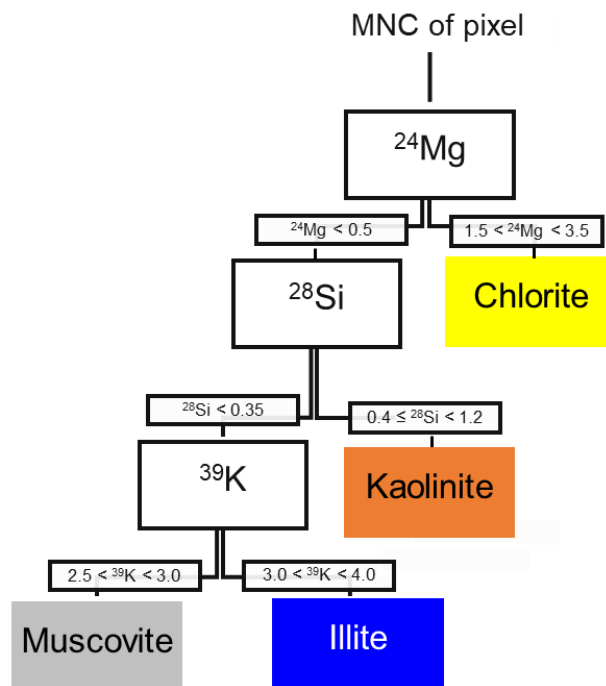


Figure F. 2: Flow chart implemented in a MATLAB program to map clay minerals in a mixed sample.

However, tests on SIMS images acquired on mixed mineral samples presented a significant number of artefacts (e.g., alleged accumulation of illite on the borders of a microaggregate which did not make sense from the geological point of view) and an accurate identification of the minerals was not possible. Reasons for this could be the partial overlap of the boxplots resulting from poor statistics resulting and/or impurities of the reference mineral samples, as for instance for the kaolinite reference sample  $^{24}\text{Mg}$  and  $^{39}\text{K}$  was detected although pure kaolinite does not contain magnesium nor potassium. Further trials with a statistically more relevant number of datasets and longer depth profiling acquisition times as are encouraged for future studies.

## Appendix G: Study on topographical influence on soil organic matter deposition on multiple soil microaggregates

In this study, to improve the statistical relevance of the curvature data, soil samples were isotopically labelled with  $^{13}\text{C}$  and  $^{15}\text{N}$  in incubation experiments with glucose and amino acid solutions. Microaggregates were selected (for each sample one microaggregate) and series of image acquisitions were performed around the ROIs (48 images taken at  $1024 \text{ pixels} \times 1024 \text{ pixels}$  in each case) in the HIM. For SIMS analyses, the NanoSIMS 50L instrument was used to image OM compounds at appropriate MRP. 3D SE reconstructions were created using the 3DF Zephyr Pro software (Figure G. 1) and the SIMS images overlaid to create 3D + 1 reconstructions.

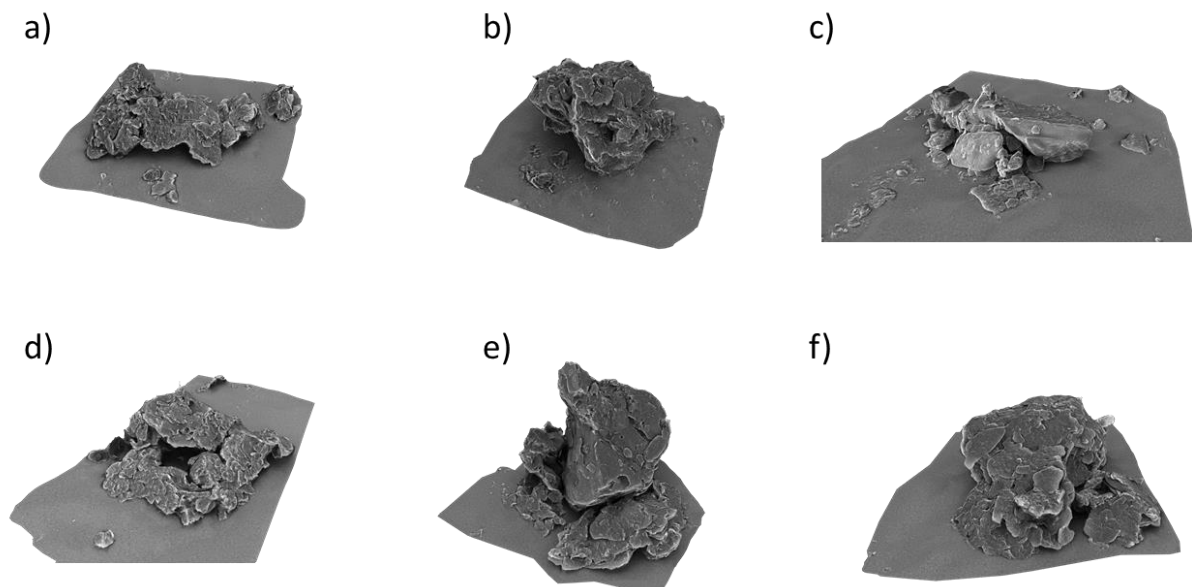


Figure G. 1: Side view on 3D SE reconstructions of 6 soil microaggregates taken from isotopically enriched samples ( $^{13}\text{C}$ ,  $^{15}\text{N}$ ).

Curvature analyses of each microaggregate for  $^{13}\text{C}$  and  $^{15}\text{N}$  hotspots ( $^{13}\text{C}/^{12}\text{C}$  and  $^{15}\text{N}/^{14}\text{N}$  ratio images taken here) was performed in MATLAB according to the calculations discussed in chapter 2 section 2. The results of the curvature analyses are shown in Figure G. 2. The OM deposition took place in a relatively narrow range of curvature values, from  $25^\circ$  to  $40^\circ$ . The average curvature of the mineral phase (represented areas where  $^{16}\text{O}$  was detected) is shown with a red bar in each case in Figure G. 2. The average curvature of the OM tends to be slightly

higher than the average mineral surfaces of the soil microaggregate. Our 3D (+1) results show that topography is a driver for OM sequestration which is in accordance with the findings of Vogel et al. on soil organo-mineral structures.<sup>8</sup>

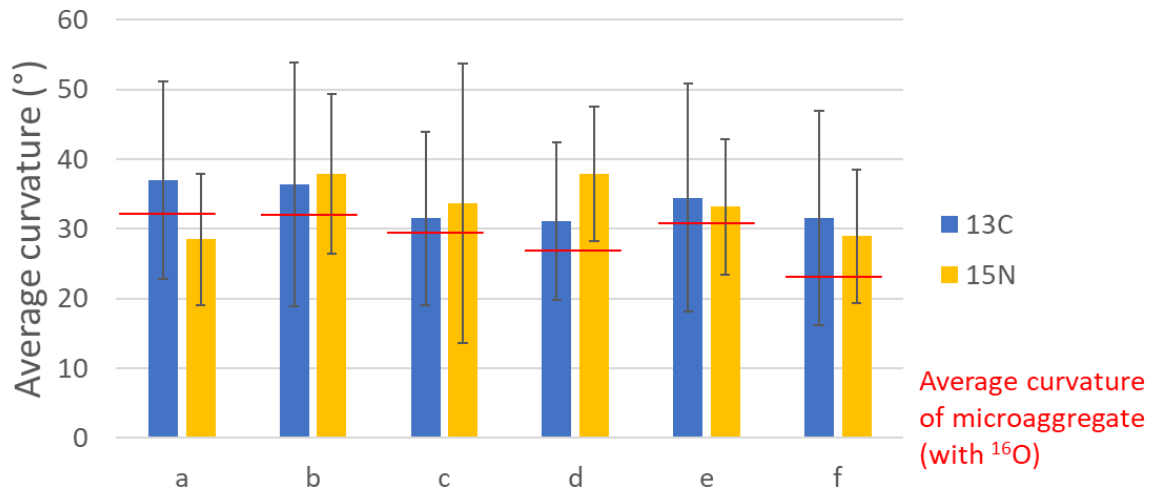


Figure G. 2: Average curvature of 6 reconstructed soil microaggregates (labelled from a – f) for areas identified <sup>13</sup>C and <sup>15</sup>N hotspots.

## Appendix H: Description of the photogrammetric MATLAB 3D reconstruction algorithm

This section aims to give more details about the simulation algorithm for photogrammetric 3D surface reconstruction (with automatic feature detection and matching) used for the reconstruction of a cube described in chapter 2 section 1.4. The codes were written using the MATLAB 2019b version while MATLAB's Computer Vision Toolbox is required (purchased in 2019).

### H.1 Cube creation and image acquisition

In a first step, a geometric structure (in this case a cube on a plateau) is created in a 3D space, by defining the coordinates of the corners of the cube and the plateau. Separate texture images (e.g., in .jpeg format) are loaded and projected on each surface of the cube. The texture images should present a high amount of features and reduced amount of noise to facilitate the feature detection and matching process later on. In the following, virtual images of the cube are acquired. Therefore, the textured 3D cube is plotted with given polar and azimuthal angles ( $45^\circ$  polar and  $0^\circ$  azimuthal angles) of the observer's perspective. A first image of the plot is saved in the current directory (e.g. also in .jpeg format). In a for-loop the observer's perspective is changed (from  $0^\circ$  to  $360^\circ$ ), thus by changing the azimuthal angle (with  $10^\circ$  steps) and an image of the plot is saved in each case, so that in the end 36 images are saved.

### H.2 Camera alignment

For the point cloud reconstruction later on, a precise camera position and orientation of each of the acquired images is required. For the camera positions, cameras are distributed in a circular arrangement (from 0 to  $360^\circ$ ) with given azimuthal, polar angles, and the distance from the center with coordinates (0,0,0). A coordinate transformation from spherical to cartesian coordinates is then performed to obtain the xzy-coordinates of each camera. For

the camera orientations, all the cameras are aligned initially to the z-axis (i.e., camera's direction vector with yaw, pitch, and roll = 0°). In a for-loop all the cameras are aligned then to their designated orientation by multiplying the default direction vector with two rotation matrices, first to rotate around the z-axis and secondly around a defined xy-axis, tangent to the circular curve connecting all the camera positions at the position of the considered camera. All the camera positions and orientations are stored in a table file.

### H.3 Point cloud creation

For 3D point cloud reconstruction, the virtual images and the camera positions and orientations are loaded first. A feature searching process is then launched for all the images using the SURF algorithm. These are matched from one image to the next in the series and stored. At this stage the triangulation process is performed for all the matched features. This process runs in a for-loop over all the images and all the pairs of matched features. Thus, the pixel coordinates of each match, the camera position and orientations of both cameras, and the camera/image intrinsic parameters (focal length, principal point, image size) are implemented. The output is a 3D-coordinate of the matched feature with an associated color coming from the pixel color of the matched feature. All the reconstructed 3D points with their color information are stored in a point cloud file which is plotted and exported as a .txt file in the current directory.

### H.4 Mesh reconstruction

To create a surface from the point cloud, a mesh grid with spanned over the entire range of x and y coordinates of the point cloud. The local z-coordinates of the mesh are determined from linear interpolation on the 3D points of the point cloud. The color information of the mesh considered mesh points is determined by finding the nearest neighbor in the 3D point cloud and by storing this color accordingly. Noise is removed at this stage by removing outliers. The colored mesh is plotted and the 3D surface is exported as an .stl file (no color information).

## Appendix I: Experimental study on sputtering yields of silicon and indium under He<sup>+</sup> and Ne<sup>+</sup> bombardment

Here additional SIMS image data is shown to study the sputtering yield vs. the primary ion beam (He<sup>+</sup>, Ne<sup>+</sup>) incidence angle for indium phosphorus (Figure I. 1, Figure I. 2) and silicon (Figure I. 3). Model samples imaged here were created using a Ga<sup>+</sup> FIB in the FIB-SEM(-SIMS) instrument.

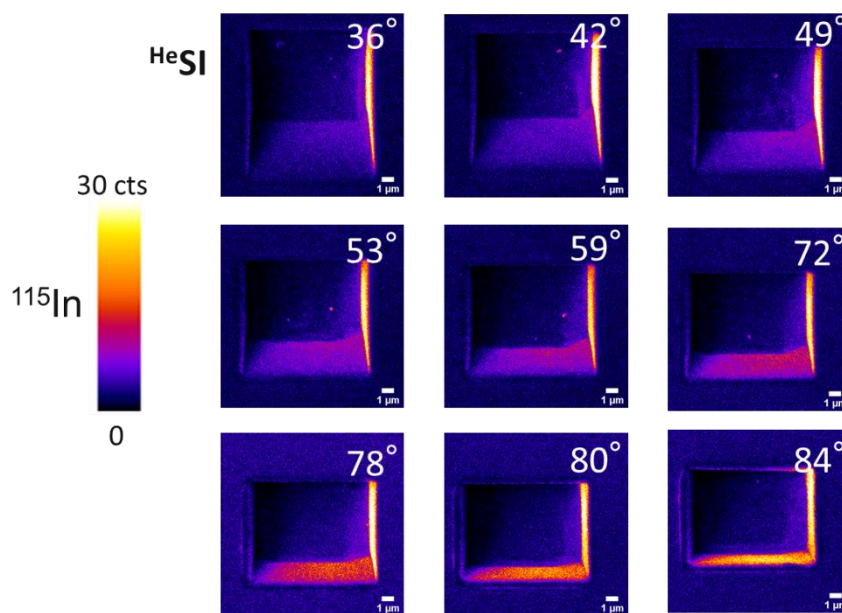


Figure I. 1: SIMS images of InP model samples to study the <sup>28</sup>Si signal under 25 keV He<sup>+</sup> bombardment.

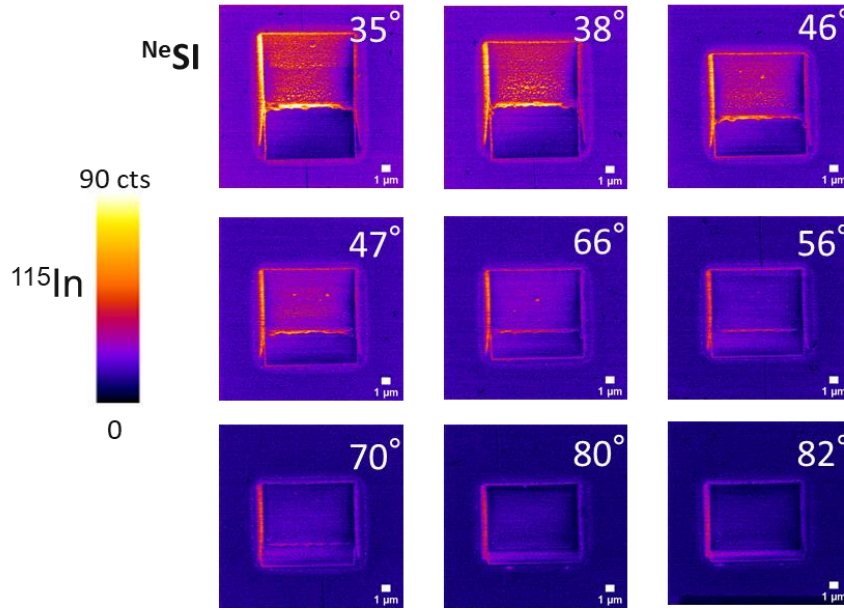


Figure I. 2: SIMS images of InP model samples to study the  $^{115}\text{In}$  signal under 25 keV  $\text{Ne}^+$  bombardment.

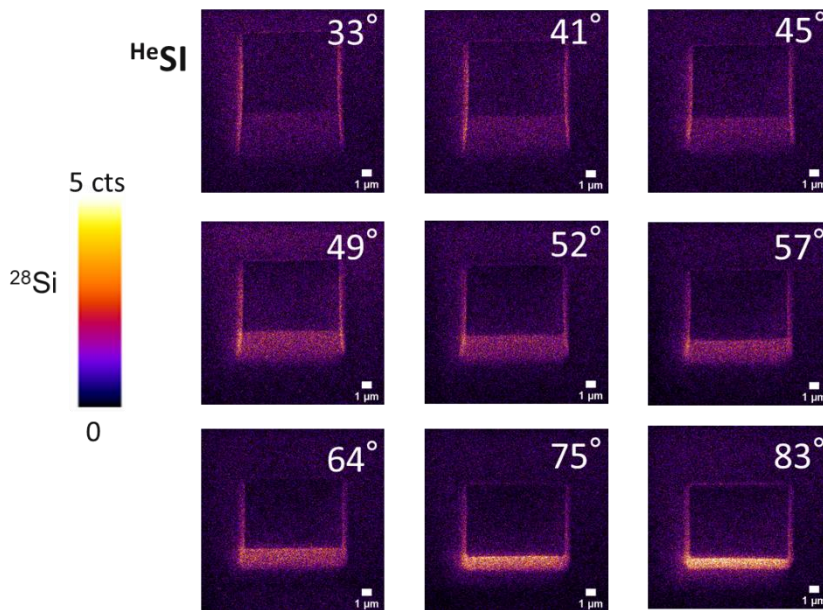
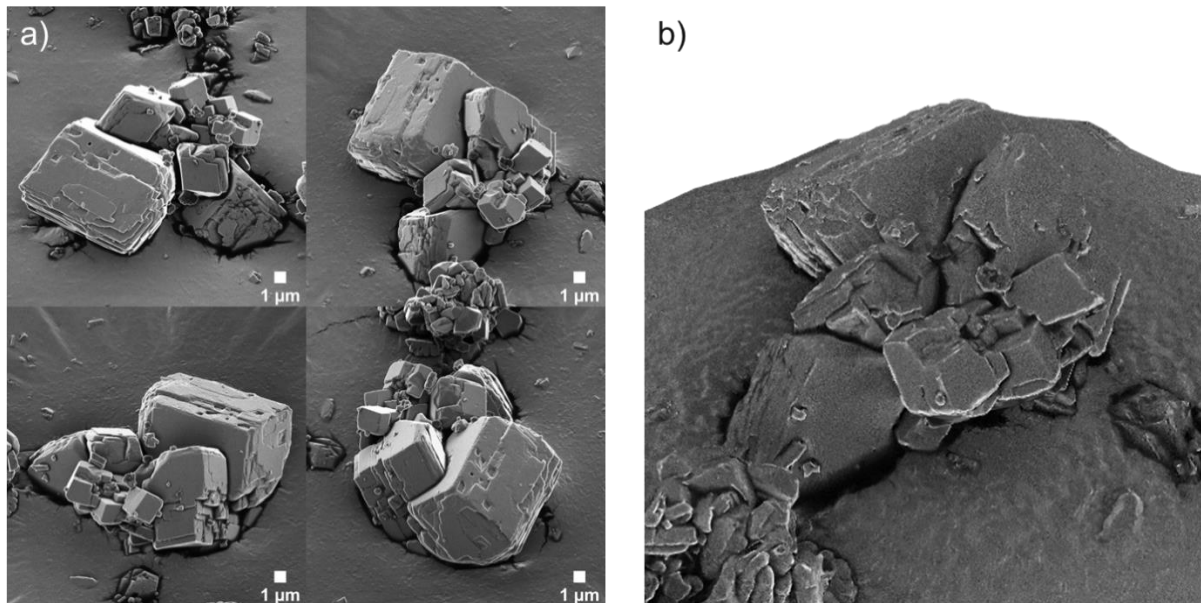


Figure I. 3: SIMS images of Si model samples to study the  $^{28}\text{Si}$  signal under 25 keV  $\text{He}^+$  bombardment.

## Appendix J: 3D SE surface reconstruction of a calcite crystal

In this section, exemplary SE images of the calcite crystal (Figure J. 1 a) discussed in chapter 3 section 1.4.1 as well as the corresponding 3D SE surface reconstruction (Figure J. 1 b) are shown.



*Figure J. 1: Photogrammetric 3D SE reconstruction of a calcite crystal. a) Exemplary SE images taken around the crystal (in total 48 images). b) 3D SE surface reconstruction.*